

**WET OXIDATION PERFORMANCE OF TYPE
310S STAINLESS STEEL**

WET OXIDATION PERFORMANCE OF TYPE 310S STAINLESS STEEL

BY: SHOOKA MAHBOUBI, M.A.Sc.

A Thesis Submitted to the School of Graduate Studies in Partial
Fulfilment of the Requirements for the Degree Doctor of Philosophy in
Materials Science and Engineering

McMaster University © Copyright by Shooka Mahboubi, April 2018

Title: Wet Oxidation Performance of Type 310S Stainless Steel

Author: Shooka Mahboubi, M.A.Sc. (McMaster University)

Supervisors: Dr. Joseph R. Kish and Dr. Gianluigi A. Botton

Pages: xxiv-269

Lay Abstract

The effects of total gas pressure, water vapour partial pressure, temperature and minor alloying elements (Mn and Si in particular) on the wet oxidation performance of Type 310S stainless steel were examined within the context of the stability of the protective chromia (Cr_2O_3) scale formed. Focus was placed on examining factors that influence the onset of accelerated linear oxidation associated with the Fe-rich oxide formation and oxide thickening. Links between changes in structure and composition of the protective Cr_2O_3 scale and breakaway oxidation as exhibited in water vapour-containing environments are made using advanced electron microscopy techniques. Si addition up to ~6 wt.% assists the formation of a continuous silica (SiO_2) barrier layer under the Cr_2O_3 scale as well as Cr-rich silicide intermetallic phases that act as reservoirs to supply for the oxidized Cr lost to volatilization. Si addition is proposed to be a promising way of prohibiting Fe-rich oxide formation albeit modifications to the morphology of the silicide intermetallic phases are required.

Abstract

High-temperature wet oxidation resistance of Type 310S stainless steel arises from the formation of a thin, adherent and compact external Cr_2O_3 scale that is more protective compared with the other oxides. Stability of the Cr_2O_3 scale is often at risk in the presence of water vapour at higher temperatures, which promotes the loss of oxidized Cr to volatilization. Continuous volatilization of the Cr_2O_3 scale accelerates the rate of oxidation and increases the risk of non-protective Fe-rich oxide formation that immensely contributes to the oxide thickening (breakaway oxidation). In this study, the possibility of surrogating high-pressure supercritical water with an ambient pressure air-10% H_2O mixture is studied at temperatures associated with the predicted coolant outlet conditions in the current GEN IV design concepts. Factors influencing structure and composition of the Cr_2O_3 scale during wet oxidation are then examined in the wet environments. An increase in the total gas pressure, water vapour partial pressure and temperature is shown to accelerate the Fe-rich oxide formation by increasing the rate of oxidized Cr loss. A more complete physical description of the oxidation kinetics in terms of the evolution of the oxide scale structure and composition at the various exposure conditions is also reported. Presence of small amount of Mn in the alloy is shown herein to be beneficial as it assists the formation of a MnCr_2O_4 layer on top of the Cr_2O_3 scale, which serves to reduce the volatilization rate. It is shown however that the MnCr_2O_4 layer itself is only temporary protective and becomes prone to volatilization (loss of oxidized Cr) at relatively high temperatures, pressures and

exposure times. The formation of a MnCr_2O_4 cap is therefore, only a temporary solution for delaying the onset of accelerated Fe-rich oxide formation. Addition of Si is proposed to be a more promising way of controlling the onset of the Fe-rich oxide formation. Increase in the Si content to ~6 wt.% results in the formation of a continuous SiO_2 barrier layer under the Cr_2O_3 scale as well as Cr-rich silicide intermetallic phases in the starting microstructure that serve as effective Cr reservoirs in helping to maintain the structure and composition of the compact protective Cr_2O_3 scale despite the continued loss of oxidized Cr to volatilization.

Acknowledgements

I will forever be thankful to my supervisors Dr. Joseph Kish and Dr. Gianluigi Botton who expertly guided me throughout my graduate studies, unconditionally supported and encouraged me and set examples of excellence as mentors and role models for me. I would like to express my gratitude to Dr. Hatem Zurob for patiently assisting me with my experiments and Dr. Joseph McDermid for kindly sitting in my supervisory committee meetings and having helpful discussions with me throughout my project. I would also like to thank Dr. Bruce Pint for sitting in my Ph.D. thesis defence and sharing valuable thoughts with me. Thanks are also expressed to Dr. Carmen Andrei, Dr. Glynis de Silveira, Chris Butcher, Andy Duft, and Travis Casagrande for electron microscopy training, Victoria Jarvis for X-ray diffraction measurements and Doug Culley, Xiaogang Li, Connie Barry, Mukesh Sharma, Dr. Yinan Jiao and Dr. Beth McNally for their technical assistance at the Materials Science and Engineering (MSE) laboratories. I would like to acknowledge that the funding for the this study was provided by Natural Resources Canada through the Office of Energy Research and Development, Canadian Nuclear Laboratories (formerly Atomic Energy of Canada Limited), and Natural Sciences and Engineering Research Council of Canada under the Discovery Grant Program.

At last but not least, I wish to thank my family for their constant loving, inspiration and support and dedicate this thesis to them without whom my life's pursuits would have not been accomplished.

Table of Contents

| | |
|--|----|
| Preface | 1 |
| 1. Introduction..... | 2 |
| 1.1. Overall Context | 2 |
| 1.2. Research Objectives and Hypothesis | 4 |
| 1.3. Thesis Layout..... | 8 |
| 1.4. References..... | 12 |
| 2. Literature Review | 15 |
| 2.1. Cr ₂ O ₃ Scale Formation..... | 15 |
| 2.1.1. Thermodynamics of Cr ₂ O ₃ Scale Formation | 16 |
| 2.1.2. Cations Diffusivity in the Cr ₂ O ₃ Scale and Austenitic Matrix | 21 |
| 2.2. Wet Oxidation | 24 |
| 2.2.1. Thermodynamics of Wet Oxidation | 24 |
| 2.2.2. Relevant Wet Oxidation Environments | 25 |
| 2.2.2.1. Supercritical Water (SCW) | 26 |
| 2.2.2.2. Wet Air..... | 28 |
| 2.2.3. Wet Oxidation Kinetics..... | 30 |
| 2.3. Stresses in the Oxides | 39 |
| 2.4. Proposed Mechanisms of Wet Oxidation | 41 |
| 2.4.1. Dissociative Mechanism | 43 |
| 2.4.2. Penetration Mechanism of Gas Oxidants | 45 |
| 2.4.3. Hydrogen Dissolution..... | 46 |

| | |
|--|----|
| 2.4.4. Formation of Fe-Hydroxides | 46 |
| 2.4.5. Formation of Volatile Cr-Oxy-Hydroxides | 47 |
| 2.5. Cr ₂ O ₃ Volatilization Mechanism | 48 |
| 2.5.1. Effect of Temperature | 48 |
| 2.5.2. Effect of Pressure | 49 |
| 2.5.3. Effect of Gas Velocity | 51 |
| 2.5.4. Effect of Alloy Cr Supply Rate..... | 54 |
| 2.5.5. Effect of Minor Alloying elements..... | 57 |
| 2.5.5.1. Mn Effects | 57 |
| 2.5.5.2. Si Effects | 60 |
| 2.6. References..... | 63 |
| 3. Stability of Chromia (Cr ₂ O ₃)-Based Scales Formed During Corrosion of Austenitic Fe-Cr-Ni Alloys in Flowing Oxygenated Supercritical Water | 71 |
| 3.1. Abstract..... | 72 |
| 3.2. Introduction | 73 |
| 3.3. Experimental Procedures..... | 75 |
| 3.4. Results | 80 |
| 3.5. Discussion..... | 91 |
| 3.5.1. Scale Evolution | 91 |
| 3.5.2. Mechanism of Scale Volatilization | 92 |
| 3.6. Conclusions | 98 |
| 3.7. Acknowledgements | 99 |

| | |
|---|-----|
| 3.8. References..... | 100 |
| 4. Environment Effects on the Stability of Chromia (Cr ₂ O ₃) Scale Formed on Type 310S Stainless Steel during Wet Oxidation | 103 |
| 4.1. Abstract..... | 104 |
| 4.2. Introduction | 105 |
| 4.3. Experimental Procedures..... | 108 |
| 4.3.1. Oxidation Testing Apparatus and Conditions..... | 108 |
| 4.3.2. Electron Microscopy Characterization of the Oxidized Coupons | 109 |
| 4.4. Results | 112 |
| 4.5. Discussion..... | 122 |
| 4.5.1. Oxidation Kinetics | 122 |
| 4.5.2. Scale Evolution | 125 |
| 4.5.3. Significance to SCW Testing | 130 |
| 4.6. Conclusions | 131 |
| 4.7. Acknowledgements | 132 |
| 4.8. References..... | 133 |
| 5. Effect of Water Vapour Partial Pressure on the Chromia (Cr ₂ O ₃)-Based Scale Stability..... | 138 |
| 5.1. Abstract..... | 139 |
| 5.2. Introduction | 140 |
| 5.3. Experimental Procedures..... | 143 |
| 5.3.1. Material..... | 143 |
| 5.3.2. Wet Oxidation Testing | 143 |

| | |
|---|-----|
| 5.3.3. Oxide Scale Characterization | 144 |
| 5.4. Results and Discussion..... | 146 |
| 5.5. Conclusions | 159 |
| 5.6. Acknowledgements | 160 |
| 5.7. Disclosure Statement..... | 160 |
| 5.8. Funding | 160 |
| 5.9. References..... | 160 |
| 6. Temperature Effect on the Wet Oxidation Performance of Type 310S Stainless Steel | 163 |
| 6.1. Abstract..... | 164 |
| 6.2. Introduction | 165 |
| 6.3. Experimental Procedures..... | 167 |
| 6.4. Results | 170 |
| 6.4.1. Wet Oxidation Kinetics..... | 170 |
| 6.4.2. Oxide Scales Characterization..... | 175 |
| 6.5. Discussion..... | 191 |
| 6.6. Conclusions | 205 |
| 6.7. Acknowledgements | 206 |
| 6.8. Appendix A..... | 207 |
| 6.9. References..... | 210 |
| 7. Silicon Effects on the Wet Oxidation of Type 310S Stainless Steel..... | 216 |
| 7.1. Abstract..... | 217 |

| | |
|--|-----|
| 7.2. Introduction | 218 |
| 7.3. Experimental Procedures | 222 |
| 7.3.1. Materials | 222 |
| 7.3.2. Wet Oxidation Exposure | 223 |
| 7.4. Results | 227 |
| 7.4.1. Starting Material Characterization..... | 227 |
| 7.4.2. Wet Oxidation Kinetics..... | 230 |
| 7.4.3. Oxide Scale Characterization | 232 |
| 7.5. Discussion..... | 245 |
| 7.5.1. Parabolic Kinetic Regime..... | 246 |
| 7.5.2. Linear Kinetic Regime..... | 248 |
| 7.6. Conclusions | 254 |
| 7.7. Acknowledgements | 255 |
| 7.8. References..... | 256 |
| 8. Conclusions and Outlooks..... | 261 |

List of Figures

| | |
|---|----|
| Figure 2-1. Physical description of internal and external oxidation for a binary Fe-Cr alloy. ²³⁻²⁵ | 18 |
| Figure 2-2. Physical description of the binary Fe-Cr alloy after long exposure times. ^{25,27} | 19 |
| Figure 2-3. Comparison, in an Arrhenius plot, of bulk and grain boundary diffusion of cations in Cr ₂ O ₃ scales after A.C.S. Sabioni et al. ³² | 23 |
| Figure 2-4. Water phase diagram. | 27 |
| Figure 2-5. Saturation pressure (P _s) of H ₂ O. ⁴⁶ | 29 |
| Figure 2-6. Common high-temperature oxidation rate laws governing the oxidation kinetics. ²⁵ | 30 |
| Figure 2-7. Physical description of oxide scale formation according to Wagner's theory. ⁵¹ | 33 |
| Figure 2-8. Oxidation kinetic of breakaway rate law. ⁵⁸ | 36 |
| Figure 2-9. Description of the oxide protectiveness based on the scale kinetics. | 38 |
| Figure 2-10. Schematic illustration of the breakaway oxidation for Fe-Cr-Ni alloys proposed by T. Jonsson et al. ⁸⁸ in H ₂ O- and O ₂ -containing gases with high and low pO ₂ at 600°C. | 42 |
| Figure 2-11. Dissociative mechanism proposed by Fujii and Meussner. ⁹² | 44 |
| Figure 2-12. Fe(OH) ₂ formation proposed by J. Ehlers et al. ⁹⁷ | 47 |
| Figure 2-13. Thermodynamically calculated equilibrium pCrO ₂ (OH) ₂ in ppm as a function of temperature (°C). ¹⁰¹ | 49 |
| Figure 2-14. CrO ₂ (OH) ₂ vapour pressure-temperature diagram for different steam/air-H ₂ O mixture environments. ²⁰ | 51 |
| Figure 2-15. Schematic illustration of Cr mass loss rate (g/s) over Cr ₂ O ₃ in different flow velocities reproduced after C. Key et al. ¹⁰³ | 52 |

Figure 2-16. Effect of gas velocity of the weight change of Type 304L stainless steel exposed in a O₂ - 40% H₂O mixture for 168 h, after H. Asteman et al.⁵⁴ 53

Figure 2-17. Calculated Cr loss fluxes as a function of (v/l)^{1/2} for air + 5% H₂O at 650–800°C. Dashed lines mark conditions in the laboratory test compared to the approximate conditions in a micro turbine recuperator, after D. Young and B. Pint.⁶⁶ 54

Figure 2-18. Schematic illustration of oxidation of Type 304/310 and Alloy X20 after 168 h exposure in O₂/H₂O.¹⁰⁴ 56

Figure 2-19. Maximum metal loss calculated based on Ebbingham’s data.¹⁰⁷ ... 58

Figure 2-20. Physical description of the MnCr₂O₄ scale volatilization..... 60

Figure 2-21. Physical description of the Cr₂O₃ volatilization in the presence of SiO₂. 62

Figure 2-22. Comparison of the average effective interdiffusion coefficients of Cr in the cast alloys after 7 days isothermal air oxidation at 1000°C.¹¹⁰..... 63

Figure 3-1. Images of the etched (a) Alloy 33 and (b) Type 310S stainless steel in the rolling direction (RD)-through thickness (TT) plane. 77

Figure 3-2. (a) Weight change data after 100 h, 250 h, and 542 h exposure and (b) single weight loss data for the descaled coupon of each alloy after 542 h exposure (longest exposure time) in 25 MPa and 550°C flowing oxygenated SCW. 81

Figure 3-3. Secondary electron images of (a), (b), and (c) Alloy 33 after exposure for 100 h, 250 h, and 542 h, respectively, and (d), (e), and (f) Type 310S stainless steel after exposure for 100 h, 250 h, and 542 h, respectively, in 25 MPa and 550°C flowing oxygenated SCW. Type I oxide nodules in all cases and Type II oxide nodules formed on Type 310S stainless steel coupons after 250 h and 542 h exposure ([e] and [f]) can also be seen. 83

Figure 3-4. Average atomic concentration profile of O, Cr, Fe, Ni, and Mn measured across the base scale/alloy interface of Alloy 33 after (a) 100 h, (b) 250 h, and (c) 542 h exposure and Type 310S stainless steel after (d) 100 h, (e) 250 h, and (f) 542 h exposure in 25 MPa and 550°C flowing oxygenated SCW. 85

Figure 3-5. Secondary electron images of the FIB-prepared thin cross-section TEM foil of oxide scale formed on (a) Alloy 33 and (b) Type 310S stainless steel after 542 h exposure in 25 MPa and 550°C flowing oxygenated SCW..... 86

Figure 3-6. BF-STEM image of the substrate and the base scale formed after 542 h exposure in 25 MPa and 550°C flowing oxygenated SCW on (a) Alloy 33 and (b) Type 310S stainless steel in cross section along with their O, Cr, Mn, Fe, and Ni STEM-EDS maps. 87

Figure 3-7. DF-STEM image of the base scale formed on (a) Alloy 33 and (b) Type 310S stainless steel after 542 h exposure in 25 MPa and 550°C flowing oxygenated SCW. (c) EELS spectra of Areas 1, 2, and 3 across the base scale on Alloy 33. (d) EELS spectra of Areas 4 and 5 across the base scale on Type 310S stainless steel. 89

Figure 3-8. (a) DF-STEM image of Type II oxide nodules formed on Type 310S stainless steel after 542 h exposure in flowing oxygenated SCW. (b) EELS spectra of superimposed Areas 1 and 2 in (a), and (c) SAD pattern of Area 2 in (a)..... 90

Figure 3-9. Schematic of the scale evolution with time for (a) Alloy 33 and (b) Type 310S stainless steel after exposure in 25 MPa and 550°C flowing oxygenated SCW for 100 h, 250 h, and 542 h. The thicknesses of layers are not to scale. 92

Figure 3-10. Comparison of the average Cr/Fe atomic concentration ratio after 100 h, 250 h, and 542 h exposure in 25 MPa and 550°C flowing oxygenated SCW, 500 h exposure of Alloy 33 in 25 MPa and 550°C stagnant SCW,³⁵ and 542 h exposure of Type 310S stainless steel in 25 MPa and 550°C stagnant SCW..... 95

Figure 4-1. Layout of the wet oxidation testing apparatus for exposures in flowing 0.1 MPa air-10% H₂O. 109

Figure 4-2. Weight gain data of the coupons exposed for up to 1000 h in flowing 0.1 MPa air-10% H₂O at 550°C (dashed red line). Weight gain data of the coupons exposed in flowing oxygenated 25 MPa SCW at 550°C for up to 542 h are also shown for comparison (dashed black line).¹⁹ 113

Figure 4-3. Plan-view secondary electron images of the Type 310S stainless steel surface after (a) 100 h, (b) 250 h, (c) 500 h, and (d) 1000 h exposure in flowing 0.1 MPa air-10% H₂O at 550°C. A corresponding set of images obtained after

| | |
|--|-----|
| exposure in flowing oxygenated 25 MPa SCW at 550°C for (e) 100 h, (f) 250 h, and (g) 542 h are also shown for comparison. ¹⁹ | 114 |
| Figure 4-4. Average atomic concentration depth profile of Fe, Cr, Ni, Mn, O, and Si across the scale/alloy interface after (a) 100 h, (b) 250 h, (c) 500 h, and (d) 1000 h exposure in flowing 0.1 MPa air-10% H ₂ O at 550°C..... | 116 |
| Figure 4-5. BF-STEM cross-sectional image and associated STEM-EDS elemental maps of Cr, Mn, O, Fe, Ni, Si, and C of the oxide scale formed after 1000 h exposure flowing 0.1 MPa air-10% H ₂ O at 550°C. | 118 |
| Figure 4-6. HAADF-STEM cross-sectional image of the oxide scale formed after 1000 h exposure in flowing 0.1 MPa air-10% H ₂ O at 550°C and the corresponding EELS spectra from the areas identified. | 119 |
| Figure 4-7. (a) EELS spectrum from Area 6 in Figure 6 and (b) HRTEM image of the SiO ₂ layer. | 120 |
| Figure 4-8. (a) BF-STEM cross-sectional image and associated SAD pattern of a Cr-carbide Cr ₂₃ C ₆ precipitate formed in the Cr depleted zone in the coupon exposed for 1000 h in flowing 0.1 MPa air-10% H ₂ O at 550°C and (b) the STEM-EDS intensity profiles from the precipitate and its adjacent matrix. | 121 |
| Figure 4-9. Plot of the time required to sputter completely through the minutes of the Cr ₂ O ₃ scale as a function of time required to sputter completely through the minutes of the Cr-depleted substrate (obtained from the AES depth profiles data), for the coupons exposed in flowing 0.1 MPa air-10% H ₂ O at 550°C and flowing 25 MPa SCW at 550°C. ¹⁹ | 125 |
| Figure 4-10. Summary of the scale structure and wet oxidation mechanism in flowing 0.1 MPa air-10% H ₂ O at 550°C. Thicknesses are not set to scale. Note that the SiO ₂ layers beneath the Cr-rich scales are not shown..... | 126 |
| Figure 5-1. EELS spectra in reference compounds for (a) Cr ₂ O ₃ and MnCr ₂ O ₄ , and (b) MnO, MnO ₂ , Mn ₂ O ₃ , Mn ₃ O ₄ . ²⁴⁻²⁹ The red arrow in (a) shows the characteristic feature of a spinel MnCr ₂ O ₄ structure. | 145 |
| Figure 5-2. Weight gain data of coupons exposed to 0.1 MPa and 550°C air-10% H ₂ O and air-70% H ₂ O for up to 500 h. The error bars show the 95% confidence interval for five coupons per data point. | 147 |

| | |
|--|-----|
| Figure 5-3. Plan-view secondary electron images of coupons exposed to 0.1 MPa and 550°C air-10% H ₂ O and air-70% H ₂ O for up to 500 h..... | 148 |
| Figure 5-4. Cross-section HAADF-STEM images of coupons after 500 h exposure in 0.1 MPa and 550°C (a) air-10% H ₂ O and (b) air-70% H ₂ O for 500 h..... | 149 |
| Figure 5-5. Cross-section HAADF-STEM image and EELS Fe, Cr, Mn, Ni, and O elemental maps of the base scale formed on Type 310S stainless steel after 500 h exposure in 0.1 MPa and 550°C air-10% H ₂ O..... | 150 |
| Figure 5-6. EELS spectra of <i>Areas</i> 1, 2, and 3 in the HAADF-STEM image in Figure 5-5. | 151 |
| Figure 5-7. Cross-section HAADF-STEM image and EELS Fe, Cr, Mn, Ni, and O elemental maps of the base scale formed on Type 310S stainless steel after 500 h exposure in 0.1 MPa and 550°C air-70% H ₂ O..... | 152 |
| Figure 5-8. EELS spectra of <i>Areas</i> 1, 2, and 3 in the HAADF-STEM image in Figure 5-7. | 153 |
| Figure 5-9. (a) Cross-section HAADF-STEM image of Type 310S stainless steel after 500 h exposure in 0.1 MPa and 550°C air-70% H ₂ O, (b) the corresponding EELS spectra from points 1-6 in (a), and (c) the corresponding EELS spectra from points 7-12 in (a)..... | 155 |
| Figure 5-10. HRTEM images of the alloy/oxide interface and the EELS spectra of the amorphous regions (obtained in DF-STEM mode), in Type 310S stainless steel after 500 h exposure in 0.1 MPa and 550°C air-10% H ₂ O (a) and (b), and air-70% H ₂ O (c) and (d). | 156 |
| Figure 5-11. Summary of the scale characterization after 500 h exposure of Type 310S stainless steel coupons in 0.1 MPa and 550°C air-10% H ₂ O and air-70% H ₂ O. The thicknesses are not set to scale..... | 157 |
| Figure 6-1. Weight gain of Type 310S stainless steel exposed for 24 h, 50 h, 100 h, 250 h, 500 h, and 1000 h in flowing air-10% H ₂ O at (a) 550°C, (b) 675°C, and (c) 800°C. | 172 |
| Figure 6-2. Weight loss of Type 310S stainless steel exposed for 24 h, 50 h, 100 h, 250 h, 500 h, and 1000 h in flowing air-10% H ₂ O at (a) 550°C, (b) 675°C, and (c) 800°C. | 174 |

| | |
|---|-----|
| Figure 6-3. Plan-view secondary electron images of coupons exposed for 100 h, 250 h, 500 h, and 1000 h in flowing 0.1 MPa air-10% H ₂ O at 550°C, 675°C, and 800°C. | 177 |
| Figure 6-4. Cross-sectional back-scattered electron images of the oxidized coupons exposed for 100 h, 250 h, 500 h, and 1000 h in flowing 0.1 MPa air-10% H ₂ O at 800°C, and the corresponding SEM-EDS elemental maps of O, Cr, Ni, Si, Mn, and Fe. | 181 |
| Figure 6-5. Secondary electron images of the FIB-prepared cross-sectional TEM samples of the oxide scale formed after 500 h exposure in flowing air-10% H ₂ O at (a) 550°C, (b) 675°C, and (c) 800°C..... | 183 |
| Figure 6-6. Cross-sectional HAADF-STEM image of the oxide scale formed after 500 h exposure in flowing air-10% H ₂ O at 550°C along with an associated set of STEM-EELS elemental maps and spectra. | 184 |
| Figure 6-7. Cross-sectional HAADF-STEM image of the oxide scale formed after 500 h exposure in flowing air-10% H ₂ O at 675°C along with an associated set of STEM-EDS elemental maps and EELS spectra (acquired from Areas 4, 5, 6 and 7 shown on the image). | 186 |
| Figure 6-8. Cross-sectional HAADF-STEM image of the outer layer of the scale formed after 500 h exposure at 800°C along with an associated set of STEM-EDS elemental maps, an EELS spectrum (acquired from Area 8 shown on the image) and a SAD pattern (acquired from Area 9 shown on the image). | 188 |
| Figure 6-9. Cross-sectional HAADF-STEM image of the outer layer/inner layer interface in the scale formed after 500 h exposure at 800°C along with an associated set of STEM-EDS elemental maps and EELS spectra (acquired from Area 10 and 11 shown on the image). | 189 |
| Figure 6-10. Cross-sectional HAADF-STEM image of the inner layer (near the scale/metal interface) of the scale formed after 500 h exposure at 800°C along with an associated set of STEM-EDS elemental maps and EELS spectra (acquired from Area 12, 13 and 14 shown on the image). | 191 |
| Figure 6-11. Simplified physical description of the oxidation and volatilization mechanistics for Type 310S stainless steel after up to 500 h exposure in flowing 0.1 MPa air-10% H ₂ O at 550°C, 675°C and 800°C. | 194 |

| | |
|---|-----|
| Figure 6-12. Average minimum Cr content (wt.%) present in the Cr-depleted zone as a function of exposure time at 550°C, ³⁶ 675°C, and 800°C. | 199 |
| Figure 6-13. Graph of the Cr-depleted depth (µm) formed in Type 310S stainless steel matrix after up to 1000 h exposure in flowing 0.1 MPa air-10% H ₂ O at (a) 550°C, ³⁶ (b) 675°C, and (c) 800°C. | 201 |
| Figure 6-14. Variation in the thickness of the oxide scale formed on Type 310S stainless steel after up to 1000 h exposure in flowing 0.1 MPa air-10% H ₂ O at 675°C. | 202 |
| Figure 7-1. Images of the etched (a) as-cast Type 310-6Si stainless steel in the axial direction (AD)-radial direction (RAD) plane and (b) cold rolled and mill annealed Type 310S stainless steel in the rolling direction (RD)-through thickness (TT) plane. | 228 |
| Figure 7-2. (a) Low and (b) high magnification back-scattered electron images and an associated set of EDS maps of the starting microstructure of the as-cast Type 310-6Si stainless steel. | 229 |
| Figure 7-3. XRD pattern of Type 310-6Si stainless steel in the as-cast condition. | 230 |
| Figure 7-4. Average (a) weight gain and (b) weight loss of coupons exposed for up to 500 h in flowing 0.1 MPa air-10% H ₂ O at 800°C. The error bars represent 95% confidence interval for replicate set of coupons exposed. | 232 |
| Figure 7-5. Low magnification plan-view secondary electron images of the oxidized surfaces of (a) Type 310-6Si and (c) Type 310S stainless steel after exposure for up to 500 h in flowing 0.1 MPa air-10% H ₂ O at 800°C. (b) High magnification plan-view secondary electron images of the oxidized surfaces of Type 310-6Si stainless steel obtained from the superimposed boxes in Figure 7-5(a). | 233 |
| Figure 7-6. Cross-sectional secondary electron images of the oxidized coupons exposed for 24 h, 50 h, 100 h, 250 h, and 500 h in flowing 0.1 MPa air-10% H ₂ O at 800°C, and the corresponding SEM-EDS elemental maps of O, Cr, Ni, Si, Mn, and Fe. | 235 |
| Figure 7-7. XRD patterns of Type 310-6Si stainless steel coupons exposed for 24 h, 50 h, 100 h, 250 h, and 500 h in flowing 0.1 MPa air-10% H ₂ O at 800°C. | 240 |

Figure 7-8. (a) Plan-view secondary electron image of the coupon exposed for 500 h in flowing 0.1 MPa air-10% H₂O at 800°C. The red box on the image shows the area from which a TEM thin foil was extracted by FIB. (b) Secondary electron image of the as-prepared TEM sample in cross-section. 241

Figure 7-9. BF-STEM image of the scale formed on Type 310-6Si stainless steel after 500 h exposure in flowing 0.1 MPa air-10% H₂O at 800°C and the STEM-EDS elemental maps of O, Cr, Ni, Si, Mn, Fe and C..... 242

Figure 7-10. The corresponding EELS spectra from the numbers superimposed on the BF-STEM image in Figure 7-9. 243

Figure 7-11. Cross-sectional HAADF-STEM image of the scale formed on the oxide surface on Type 310-6Si stainless steel exposed for 500 h in flowing 0.1 MPa air-10% H₂O at 800°C and the O, Cr, Ni, Si, and Fe EELS elemental maps. The corresponding EELS spectra from the areas identified with numbers superimposed on the HAADF-STEM image are also shown..... 244

Figure 7-12. Schematic diagrams showing the composition and structure of the oxide scale formed on the (a) high-Si Type 310-Si stainless steel and (b) low-Si Type 310S stainless steel¹⁵ associated with the parabolic kinetic regime. 247

Figure 7-13. Schematic diagrams showing the composition and structure of the oxide scale formed on the (a) high-Si Type 310-6Si stainless steel and (b) low-Si Type 310S stainless steel¹⁵ associated with the linear kinetic regime. 249

Figure 7-14. Variation in the Fe/Cr concentration ratio (at.%) as a function of exposure time in the flowing air-10% H₂O mixture at 800°C..... 250

Figure 7-15. Variation in the thickness of the Cr₂O₃ intermediate layer formed on the high-Si Type 310-6Si stainless steel as a function of exposed time in the flowing air-10% H₂O mixture at 800°C..... 252

List of Tables

| | |
|--|-----|
| Table 2-1 Lattice diffusion coefficient values for Fe, Cr and Ni in austenitic Fe-Cr-Ni alloys at 963°C after ~24 h exposure in vacuum | 22 |
| Table 2-2 Values of water dew point for different vol.% H ₂ O present in air. | 29 |
| Table 3-1 Composition (wt.%) of Alloy 33 and Type 310S Stainless Steel | 76 |
| Table 4-1 Elemental composition (at.%) of each of the oxide layers, obtained from AES | 117 |
| Table 4-2 Energy positions (eV) for the major peaks in each of the oxide compounds with ±0.2 eV error. A comparison of the integrated L ₃ /L ₂ peaks ratio in this study with those reported in the literature is also shown. | 119 |
| Table 6-1 k _p and k _i oxidation rate constants (within the 95% CI) for Type 310S stainless steel after up to 1000 h exposure in flowing air-10% H ₂ O | 175 |
| Table 6-2 Average elemental composition (at.%) obtained from the oxide scale surface formed in flowing air-10% H ₂ O | 179 |
| Table 6-3 Estimated and measured Cr loss flux (g/cm ² /s) in air-10% H ₂ O | 204 |
| Table 7-1 Chemical composition (wt.%) of the stainless steels | 222 |
| Table 7-2 Comparison of the integrated L ₃ /L ₂ peaks ratio in this study with those reported in the literature..... | 243 |
| Table 7-3 Kinetic rate constants determined in flowing air-10% H ₂ O mixture at 800°C. Previously published k _p and k _i values are also shown for comparison . | 246 |

List of Abbreviations

| | |
|-------|---|
| AES | A uger E lectron S pectroscopy |
| AD | A xial D irection |
| BF | B right F ield |
| CI | C onfidence I nterval |
| CTE | C oefficient of T hermal E xpansion |
| DF | D ark F ield |
| DO | D issolved O xygen |
| EDS | E nergy D ispersive S pectroscopy |
| EELS | E lectron E nergy L oss S pectroscopy |
| FIB | F ocused I on B eam |
| FEG | F ield E mission G un |
| GIF | G eneration-IV I nternational F orum |
| HAADF | H igh A ngle A nnular D ark F ield |
| ICP | I nductively C oupled P lasma |
| MTC | M ill T est C ertificate |
| PBR | P illing- B edworth R atio |
| RAD | R adial D irection |
| RD | R olling D irection |
| TT | T hrough T hickness |
| SS | S tainless S teel |

| | |
|------|---|
| SAD | S electe A A rea D iffraction |
| SCC | S tress C orrosion C racking |
| SEM | S canning E lectron M icroscopy |
| SCW | S upercritical W ater |
| SCWR | S upercritical W ater-Cooled R eactor |
| STEM | S canning T ransmission E lectron M icroscopy |
| SHS | S uperheated S tream |
| TEM | T ransmission E lectron M icroscopy |
| WG | W eight G ain |
| WL | W eight L oss |

Declaration of Academic Achievements

This dissertation is written to fulfill the requirement for the degree Doctor of Philosophy in Materials Science and Engineering at McMaster University. The research project was undertaken between September 2014 and January 2018. Over the course of this study, I designed a wet oxidation testing apparatus to work at ambient pressure and high temperatures. This design was then used to investigate the wet oxidation performance of Type 310S stainless steel. The investigation first enabled a comparison between the wet oxidation mechanism exhibited by Type 310S stainless steel in ambient pressure wet air and in high-pressure supercritical water (SCW) and then enabled an investigation of the factors that control the transition from protective to non-protective performance, including the partial pressure of water vapour, temperature and minor alloying elements (Mn and Si in particular). The major contribution of this study came from myself, with helpful discussions with my supervisors. The results of my studies will be published in a set of five peer-reviewed journal articles that I prepared as the lead author. I was also the second author in a peer-reviewed journal article that was published in 2015, which involved collaboration between McMaster University and Trent University on examining the high-temperature oxidation resistance of candidate alloys to be used in SCW. The five journal articles that comprise this “sandwich” thesis include the following:

1. S. Mahboubi, Y. Jiao, W. Cook, W. Zheng, D.A. Guzonas, G.A. Botton and J.R. Kish: Stability of Chromia (Cr_2O_3)-Based Scales Formed during Corrosion of Austenitic Fe-Cr-Ni Alloys in Flowing Oxygenated Supercritical Water, ***Corrosion***, Vol. 72, No. 9 (2016), pp: 1170-1180, <https://doi.org/10.5006/1982>
2. S. Mahboubi, H.S. Zurob, G.A. Botton, and J.R. Kish: Environment Effects on the Stability of Chromia (Cr_2O_3) Scale Formed on Type 310S Stainless Steel during Wet Oxidation, *Submitted to ***Corrosion****, Jan. 30th, 2018.
3. S. Mahboubi, H.S. Zurob, G.A. Botton, and J.R. Kish: Effect of Water Vapour Partial Pressure on the Chromia (Cr_2O_3)-Based Scale Stability, ***Journal of Canadian Metallurgical Quarterly (CMQ)***, Vol. 57, No. 1 (2018), pp.89-98, <https://doi.org/10.1080/00084433.2017.1373968>
4. S. Mahboubi, H.S. Zurob, G.A. Botton, and J.R. Kish: Temperature Effect on the Wet Oxidation Performance of Type 310S Stainless Steel, *Submitted to ***Corrosion Science****, Mar. 25th, 2018.
5. S. Mahboubi, H.S. Zurob, G.A. Botton, and J.R. Kish: Silicon Effects on the Wet Oxidation of Type 310S Stainless Steel, *Submitted to ***Corrosion Science****, Feb. 13th, 2018.

Preface

In this collective work, the effects of temperature, total pressure, water vapour partial pressure and minor alloying elements (Mn and Si in particular) on the wet oxidation performance of Type 310S stainless steel were examined within the context of the stability of the protective Cr_2O_3 scale formed. This thesis is written as a “sandwich” thesis and consists of eight Chapters. Chapter 1 (Introduction) describes the overall context, research objectives and hypotheses and the layout of the “sandwich” thesis. Chapter 2 (Literature Review) summarizes the enabling theories and the current knowledge states regarding the wet oxidation performance of Cr_2O_3 -forming high-temperature alloys. Chapters 3-7 present the five journal articles that have been written capturing the research conducted. Chapter 8 summarizes the major conclusions drawn for the collective work and provides a commentary on the outlook that is presented in view of these conclusions.

1. Introduction

1.1. Overall Context

Deterioration of materials used in service at high temperatures due to oxidation has been a matter of concern for decades and the high-temperature oxidation behaviour of these materials is of paramount importance in various fields of technology.¹⁻³ The practical consequences associated with the high-temperature oxidation include the devastating impacts on the failure of the structural components, which puts the reliable and efficient operation of equipment at risk.^{4,5} For those components that are used as heat exchangers for example, continuous oxidation and an increase in the oxide scale thickness can reduce the heat transfer rate, decrease efficiency, and lead to an overheated microstructure and increased thermal stresses within both the alloy and the oxide scale.^{1,6,7} Another major issue with the oxide scale thickening is the possibility of oxide scale spallation.^{5,8,9} The latter becomes an important problem during the long-term service, as spalled oxide scales can deposit downstream in undesirable (heat transfer) locations and induce erosion corrosion of the downstream components.^{5,1,10-12}

One method to increase the high-temperature oxidation resistance of the alloy structural components is the application of oxidation resistant coatings.¹³⁻¹⁵ However, many problems can arise with the coating application such as: thermal expansion mismatch with the substrate, high stress levels at the coating/alloy interface (especially at the stress raiser points in the component design such as

edges), intermetallic phase formation close to the coating/alloy interface (specifically for the diffusion coating process), coating delamination due to imperfections exist at the interface, and localized composition inhomogeneities (e.g. defects and pores) that enhances ion diffusion through the coating.¹⁶⁻¹⁸

Another major limitation of the high-temperature oxidation resistance coatings, as well as of many alloys that are known to form relatively protective scales such as Cr_2O_3 or SiO_2 , is the possibility of the oxide scale volatilization (sublimation).¹⁹⁻²¹ Reaction of the oxidizing gas species with the oxide scale could result in the loss of the protective scale and, thus, a loss in protection.¹⁹⁻²¹ The rate of scale volatilization becomes significant when the scale reaches a limiting thickness, after which the rate of oxide growth and the rate of oxide volatilization becomes comparable.^{19,22} Oxide scale volatilization results in rapid consumption of the alloy to compensate for the loss of the scale.¹⁹⁻²¹ Generally, the concern with volatilization increases with an increase in the gas flow rate, temperature, and partial pressures of the oxidizing gas components.²³⁻²⁵

While a sound understanding of pure metal oxidation fundamentals has been achieved over the years, same cannot be said of alloys as oxidation is more complicated because of the various alloying effects. Among the common engineering alloys that are currently being used or are candidates to be used in high-temperature oxidizing applications, high Cr-containing austenitic Fe-Cr-Ni alloys are attractive due to improved high-temperature creep resistance and oxidation resistance compared with that of the ferritic alloys.^{1,26-28} The high-

temperature oxidation resistance of such engineering alloys that are currently in service typically relies on the formation of a thin, adherent and compact external Cr_2O_3 scale compared with the other oxide scale types.^{1,19-21}

Stability of the Cr_2O_3 scale is often threatened due to the tendency to volatilization in the presence of water vapour.¹⁹⁻²¹ The addition of the minor alloying elements such as Mn and Si in the Cr_2O_3 scale forming alloys can help promote the formation of a more protective scale: one that is more resistant to volatilization.^{18,29,30} Such improvement in performance is of practical importance for structural components used in steam-generating applications such as: steam boiler power plants, solid oxide fuel cells, nuclear reactors and geothermal power plants.^{14,31-36} The role of water vapour in changing the oxidant transport into the Cr_2O_3 scale, particularly in the presence of Mn and Si minor alloying elements, and the extent to which the Cr_2O_3 scale remains protective, is still not well understood.

1.2. Research Objectives and Hypothesis

The overarching objective of the research conducted was to investigate links between changes in the structure and composition of the protective Cr_2O_3 scale and breakaway oxidation as exhibited in water vapour-containing environments using advanced electron microscopy techniques. Focus was placed specifically on the role played by the minor alloying elements Mn and Si on the onset of the linear kinetics (non-protective). The development of a more complete physical description of the parabolic and linear oxidation is needed to identify the promising

alloying strategies that could improve the wet oxidation performance of this important class of high-temperature engineering materials. One particular point of interest is the onset of the domination of the linear oxidation during parabolic or breakaway kinetics. It is believed that if the onset is somehow delayed, the accelerated oxidation rate is outlawed which then can result in increase in the lifetime of components used at high temperatures. Some attempts have been done thus far to examine the effects of temperature, gas velocity, and oxygen and water vapour partial pressures on the mechanism of breakaway kinetics.^{25,37-40} The effect of total gas pressure on the change in the oxidation kinetics and mechanisms is not yet well understood.¹ This is mostly because most laboratories do not have access to both high-pressure testing facilities, for examples those that operate at pressures over 20 MPa, and low-pressure testing facilities, therefore cannot make a direct comparison between the oxidation kinetics of the two environments and study the effect of total gas pressure on the parabolic or breakaway kinetics. Not to mention that most studies only focus on the environmental oxidizing parameters that affect the kinetics rather than finding a possible permanent elucidation for example modification of the chemical compositions of the alloys to delay the onset of accelerated oxidation.

It is argued that in the presence of even small amount of Mn in high Cr-containing austenitic stainless steels a Mn-rich spinel oxide cap (MnCr_2O_4) forms on top of the Cr_2O_3 scale.^{29,41,42} The rate of Cr loss over the MnCr_2O_4 and Cr_2O_3 has been thermodynamically measured and it is implied that it is much smaller in

the former.⁴³ If the volatilization rate of the scale is somehow reduced by the presence of a MnCr_2O_4 layer, it then follows that the onset of accelerated oxidation that is induced by high volatilization rates can be delayed. Examining the effects of MnCr_2O_4 on delaying the formation of a Fe-rich scale during accelerated linear oxidation therefore deserves further investigation. Another minor alloying element in high Cr-containing austenitic stainless steels that deserves further consideration with regards to studying the parabolic or breakaway kinetics is Si. Most stainless steels have some amount of Si and it is well known that depending on the alloy Si content and oxidizing conditions, Si tends to form a SiO_2 layer or precipitates underneath the Cr_2O_3 scale.^{28,44,45} SiO_2 is most often amorphous at high-temperatures and is known to reduce the diffusion rates of cations through.^{46,47} Studying the effects of Si on the mechanism of linear (non-protective) oxidation kinetics associated with the Fe-rich oxide formation therefore merits further attention.

The effect of total gas pressure on the wet oxidation kinetics of Type 310S stainless steel is studied herein particularly because accelerated Fe-rich oxidation is a performance concern for alloys used in SCW environment. This was achieved by first screening the performance of Type 310S stainless steel in SCW using the high-pressure testing facility at the University of New Brunswick, results of which are discussed in Chapter 3. The wet oxidation kinetics of Type 310S stainless steel was then examined at ambient pressure yet at the same testing temperature as that for SCW testing. A physical description of accelerated Fe-rich oxidation due to

the change in the total gas pressure is then proposed. Another important knowledge gap that exists is the possibility of surrogating high-pressure SCW with ambient pressure wet air. Thermodynamic measurements show that the partial pressure of Cr-gas species is the same in both environments. The effect of total gas pressure as well as examining the possibility of using ambient pressure wet air instead of high-pressure SCW are discussed in Chapter 4. Furthermore, effects of water vapour partial pressure and gas temperature on the volatilization rate and breakaway kinetics were examined (as shown in Chapters 5 and 6). This process involved developing a more complete physical description of the role played by minor alloying elements, particularly Mn and Si, in stabilizing C_2O_3 scale against volatilization by a detailed examination linking the wet air oxidation kinetics of Type 310S stainless steel to the structure and composition of the oxide scale formed.

In the next phase of this research a custom-made high Si-containing Type 310 stainless steel (~6 wt.% Si) with more promising stability against volatilization was selected for examinations followed by a detailed study linking the wet air oxidation kinetics of custom-made experimental alloy to the structure and composition of the oxide scales formed. The oxidation and volatilization tests were done to examine the oxidation kinetics of austenitic Type 310S stainless steel.

1.3. Thesis Layout

The remainder of this “sandwich” thesis consists of seven Chapters. A description of each Chapter contents and the specific contribution to the overarching research objective is described as below:

- **Chapter 2** presents a literature review of the current state of knowledge of thermodynamics and kinetics of high-temperature wet oxidation. Proposed mechanisms of Cr_2O_3 scale volatilization are described and critiqued. The effects of Mn and Si, as minor alloying elements in the high-temperature Cr_2O_3 -forming Fe-Cr-Ni alloys, on the stability of the Cr_2O_3 scale is discussed and critiqued within the current knowledge base. A discussion of the effects of stresses on the scale mechanical spallation is also included. The knowledge gaps that currently exist in the literature, which serve as motivation for the research conducted, are addresses throughout this Chapter.
- **Chapter 3** reproduces a journal article published in *Corrosion* in 2016 that documents the research conducted investigating the performance of Cr_2O_3 forming candidate fuel cladding materials in SCW. This article is a first authored paper and the main contribution of this study is the evidence in support that accelerated Fe-rich oxidation is indeed a performance concern for Cr_2O_3 forming engineering alloys in SCW that needs to be considered in the selection of a suitable material for fuel claddings.

- **Chapter 4** reproduces a journal article submitted to ***Corrosion***, which documents the research conducted investigating the suitability of using an ambient pressure air-10% H₂O mixture as a surrogate for the high-pressure SCW by directly comparing the oxidation kinetics exhibited by, and the structure and composition of the oxide scale formed on, Type 310S stainless steel in the two oxidizing H₂O-containing environments. This article is the first in the literature that makes such a direct comparison to validate such a prediction based on thermodynamic calculations. The major contribution of this work is that the rate of Cr-oxy-hydroxide formation is significantly lower in the air-10% H₂O mixture which is attributed to the much lower total pressure of the wet air, serving to prolong the stability of a protective MnCr₂O₄ outer layer. An air-10% H₂O mixture therefore is suggested not to be used as a surrogate for SCW at temperatures associated with the predicted coolant outlet conditions in the current GEN IV design concepts.
- **Chapter 5** reproduces an invited article published in ***Canadian Metallurgical Quarterly*** in 2018 that documents the research conducted to investigate the effect of water vapour partial pressure on the wet oxidation kinetics of Type 310S stainless steel. The major contribution of this work is that the vapour pressure of Cr-oxy-hydroxides over the MnCr₂O₄ is significantly important as it increases considerably with the increase in percent water vapour of the wet air and is responsible for the linear oxidation rate constant observed. This article was invited for publication by ***Canadian***

Metallurgical Quarterly after it was accepted for presentation at the 2017 Conference of Metallurgists that was held on August 27-30, 2017 in Vancouver, BC, CA.

- **Chapter 6** reproduces a journal article submitted to ***Corrosion Science*** that documents the research conducted to examine the effect of temperature on the high-temperature wet oxidation kinetics of Type 310S stainless steel. A more complete physical description of the oxidation kinetics was developed at each of the temperatures considered by linking the structure and composition of the oxides formed to their kinetics. The mechanism of the linear oxidation is discussed considering the roles of Mn and Si minor alloying elements. It was shown that the MnCr_2O_4 formed on Cr_2O_3 only has a temporary effect on reducing the rate of scale volatilization and becomes more prone to loss of oxidized Cr at higher temperatures. Addition of Si in order to form a uniform continuous SiO_2 barrier layer under Cr_2O_3 was identified as a possible promising solution for delaying the accelerated Fe-rich oxide formation.
- **Chapter 7** reproduces a journal article submitted to ***Corrosion Science*** that documents the research conducted to validate the prediction based on the physical descriptions of the scales formation that alloyed Si will improve the wet oxidation performance of Type 310 stainless steel. A modified Type 310 stainless casting alloyed with ~6 wt.% silicon (Type 310-6Si stainless steel) was used for this purpose. The major contribution of this work is that the Fe-

rich oxides are not seen because of the formation of a uniform continuous SiO_2 layer under Cr_2O_3 as well as the presence of Cr-rich silicide intermetallic phases in the starting as-cast microstructure which serve as reservoirs to sufficiently supply Cr from the alloy to replace the oxidized Cr lost to volatilization.

- **Chapter 8** summaries the major conclusions extracted from the research conducted and discusses the significance of these conclusions in terms of the current state of knowledge regarding the fundamentals and practical implications of the wet oxidation performance of Cr_2O_3 -forming Fe-Cr-Ni engineering alloys. An outlook in view of these conclusions is also presented herein.

1.4. References

1. I.G. Wright and R.B. Dooley, *Int. Mater. Rev.* 55 (2010): pp. 129–167.
2. K. Matsui, A. Ogawa, J. Kikuma, M. Tsunashima, T. Ishikawa, and S. Matsuno, *Denver X-Ray Conf. Appl. X-Ray Anal.* (1999): pp. 170–178.
3. D. Lee, Y. Jang, and M. Nakamura, *Mater. Trans.* 43 (2002): pp. 2531–2535.
4. A. Fry, S. Osgerby, and M. Wright, *NPL Rep. MATC 90* (2002): pp. 1–39.
5. P.J. Ennis, and W.J. Quadackers, *Int. J. Press. Vessel. Pip.* 84 (2007): pp. 82–87.
6. A.S. Sabau, I.G. Wright, and J.P. Shingledecker, *Mater. Corros.* 63 (2012): pp. 896–908.
7. M. Lukaszewicz, N.J. Simms, T. Dudziak, and J.R. Nicholls, *Mater. High Temp.* 29 (2012): pp. 210–218.
8. J.P. Shingledecker, B.A. Pint, A.T. Fry, and I.G. Wright, *Adv. Mater. Process.* (2013): pp. 23–25.
9. J. Rujisomnapa, P. Seechompoo, P. Suwannachaoat, S. Suebca, and P. Wongpanya, *Technology* 20 (2010): pp. 31–36.
10. M. Schütze, *Corros. Eng. Sci. Technol.* 48 (2013): pp. 303–312.
11. Q.W. Li, and G.H. Yao, *Adv. In Materials Sci. Eng.* 2015 (2015): pp. 1–11.
12. M.T. Cheng, *Adv. Mater. Res.* 516–517 (2012): pp. 524–529.
13. A. Agüero, R. Muelas, A. Pastor, and S. Osgerby, *Surf. Coatings Technol.* 200 (2005): pp. 1219–1224.
14. N. Shaigan, W. Qu, D.G. Ivey, and W. Chen, *J. Power Sources* 195 (2010): pp. 1529–1542.
15. A. Agüero, M. Gutiérrez, and R. Muelas, *Mater. Sci. Forum* 522–523 (2006): pp. 205–212.

16. M. Martena, D. Botto, P. Fino, S. Sabbadini, M.M. Gola, and C. Badini, *Eng. Fail. Anal.* 13 (2006): pp. 409–426.
17. G.W. Goward, and D.H. Boone, *Oxid. Met.* 3 (1971): pp. 475–495.
18. T. Sundararajan, S. Kuroda, K. Nishida, T. Itagaki, and F. Abe, *ISIJ Int.* 44 (2004): pp. 139–144.
19. E.J. Opila, *J. Am. Ceram. Soc.* 86 (2003): pp. 1238–1248.
20. G. Ecer, and G. Meier, *Scr. Metall.* 7 (1973): pp. 1189–1194.
21. V. Peres, L. Favergeon, M. Andrieu, J.C. Palussire, J. Balland, C. Delafoy, and M. Pijolat, *J. Nucl. Mater.* 423 (2012): pp. 93–101.
22. D.J. Young, and B.A. Pint, *Oxid. Met.* 66 (2006): pp. 137–153.
23. H. Asteman, J.-E. Sevensson, and L.-G. Johansson, *Oxid. Met.* 57 (2002): pp. 193–216.
24. S. Mahboubi, Y. Jiao, W. Cook, W. Zheng, D.A. Guzonas, G.A. Botton, and J.R. Kish, *Corros.* 72 (2016): pp. 1170–1180.
25. H. Asteman, J. Svensson, M. Norell, and L. Johansson, *Oxid. Met.* 54 (2000): pp. 11–26.
26. A. Sabioni, A.-M. Huntz, E. Conceição da Luz, M. Mantel, and C. Haut, *Mat. Res.* 6 (2003): p. 179.
27. R. Plaut, C. Herrera, and D. Escriba, *Mat. Res.* 10 (2007): pp. 453–460.
28. Z. Yang, J. tao Lu, Z. Yang, Y. Li, Y. Yuan, and Y. Feng Gu, *Corros. Sci.* 125 (2017): pp. 106–113.
29. K.A. Al-Hatab, F.S. Alariqi, M.A. Al-Bukhaiti, U. Krupp, and M. Kantehm, *Oxid. Met.* 76 (2011): pp. 385–398.
30. H.E. Evans, D.A. Hilton, R.A. Holm, and S.J. Webster, *Oxid. Met.* 19 (1983): pp. 1–18.
31. N. Otsuka, Y. Shida, and H. Fujikawa, *Oxid. Met.* 32 (1989): pp. 13–45.

32. J. Stringer, and I.G. Wright, *Oxid. Met.* 44 (1995): pp. 265–308.
33. W.H. Yeo, A.T. Fry, J. Purbolaksono, S. Ramesh, J.I. Inayat-Hussain, H.L. Liew, and M. Hamdi, *J. Supercrit. Fluids* 92 (2014): pp. 215–222.
34. Z. Shen, L. Zhang, R. Tang, and Q. Zhang, *J. Nucl. Mater.* 458 (2015): pp. 206–215.
35. S.N. Karlsdottir, K.R. Ragnarsdottir, I.O. Thorbjornsson, and A. Einarsson, *Geothermics* 53 (2015): pp. 281–290.
36. Y. Liu, and D.Y. Chen, *Int. J. Hydrogen Energy* 34 (2009): pp. 9220–9226.
37. X. Cheng, Z. Jiang, B.J. Monaghan, D. Wei, R.J. Longbottom, J. Zhao, J. Peng, M. Luo, L. Ma, S. Luo, and L. Jiang, *Corros. Sci.* 108 (2016): pp. 11–22.
38. T. Jonsson, S. Karlsson, H. Hooshyar, M. Sattari, J. Liske, J.E. Svensson, and L.G. Johansson, *Oxid. Met.* 85 (2016): pp. 509–536.
39. K. Segerdahl, J.E. Svensson, M. Halvarsson, I. Panas, and L.G. Johansson, *Mater. High Temp.* 22 (2005): pp. 69–78.
40. J.E. Tang, F. Liu, H. Asteman, J.E. Svensson, L.G. Johansson, and M. Halvarsson, *Mater. High Temp.* 24 (2007): pp. 27–55.
41. A.N. Hansson, and M.A.J. Somers, *Mater. High Temp.* 22 (2005): pp. 223–229.
42. A.C.S. Sabioni, A.M. Huntz, L.C. Borges, and F. Jomard, *Philos. Mag.* 87 (2007): pp. 1921–1937.
43. G.R. Holcomb, and D.E. Alman, *Scr. Mater.* 54 (2006): pp. 1821–1825.
44. X.H uang, J. Li, B.S. Amirkhiz, and P. Liu, *J. Nucl. Mater.* 467 (2015): pp. 758–769.
45. T.D. Nguyen, J. Zhang, and D.J. Young, *Oxid. Met.* 81 (2014): pp. 549–574.
46. K. Schulmeister, and W. Mader, *J. Non. Cryst. Solids* 320 (2003): pp. 143–150.
47. R. Bauer, M. Baccalaro, L.P.H. Jeurgens, M. Pohl, and E.J. Mittemeijer, *Oxid. Met.* 69 (2008): pp. 265–285.

2. Literature Review

2.1. Cr₂O₃ Scale Formation

Formation of a Cr₂O₃ scale has paramount significance from the high-temperature oxidation resistance perspective of alloys used in wet environments such as steam turbines, solid oxide fuel cells, and power plants.^{1,2} Cr₂O₃ is a dense protective scale and, if formed uniformly, can reduce the diffusion rate of other alloying elements through.³⁻⁵ Cr₂O₃ is known to be a metal deficit p-type semiconductor, one that forms vacancies in cation lattice sites along with electron holes.⁵⁻⁷ The deviation of Cr₂O₃ from stoichiometry is however, almost neglectable compared to, for example, defective FeO or NiO.^{8,9} The protectiveness of the Cr₂O₃ scale arises from this low concentration of defects present in its structure.^{8,9} Protectiveness of Cr₂O₃ is often compared with Fe-rich oxides as the latter also tend to form in high-temperature wet environments in the absence of sufficient alloyed Cr content and/or high oxidizing temperature and pressure.¹⁰⁻¹² Generally Fe-rich oxide compounds particularly Fe chromate (FeCr₂O₄) and hematite (Fe₂O₃) (relevant to this study) are considered to be less protective than Cr₂O₃, as their more defective nature can easily allow outward transport of Fe cations and inward transport of O anions.¹³ FeCr₂O₄ is still a p-type semiconductor and is metal deficit, whereas Fe₂O₃ is a n-type semiconductor in the temperature range of ~600-800°C in which either an excess of cations interstitials or oxygen vacancies are the main ionic defects.¹⁴⁻¹⁶ The sequence of scales based on their protectiveness can then be

considered as: $\text{Cr}_2\text{O}_3 > \text{FeCr}_2\text{O}_4 > \text{Fe}_2\text{O}_3$.¹³ It is evident that Cr_2O_3 is considered to be the most desirable form of oxide in many of the high-temperature applications.^{17,1,2} Both Cr_2O_3 and Fe_2O_3 have similar corundum-type structure and can be easily dissolved in one another to form a solid solution of $(\text{Fe}_x\text{Cr}_{1-x})_2\text{O}_3$.¹⁸ Also, Ni, Cr, Mn, and Fe have roughly similar atomic size.¹⁹ In order to make links between structure and composition of oxide scales formed to the oxidation mechanisms of alloys used in high-temperature applications, it is important to differentiate the oxide types formed. This matter becomes important for relatively thin scales in particular. Characterization of these mixed oxides is, however, only possible using advanced electron microscopy techniques as will be presented in this thesis.

2.1.1. Thermodynamics of Cr_2O_3 Scale Formation

First consider a simplified chemical reaction of a pure Cr metal reacting with the gas containing only O_2 as shown in **Equation 2-1**:²⁰



The Gibbs free energy change, ΔG , (J/mol) for **Equation 2-1** is shown in **Equation 2-2** in which ΔG° is the equilibrium Gibbs free energy of the reaction (J/mol), R is the universal gas constant (J/mol/K), T is the reaction temperature (K), p_{O_2} is the O_2 partial pressure of the environment, and a_{Cr} and $a_{\text{Cr}_2\text{O}_3}$ are the activities of solid Cr and Cr_2O_3 , respectively:²⁰

$$\Delta G = \Delta G^\circ + RT \ln \left[\frac{a_{\text{Cr}_2\text{O}_3}}{(a_{\text{Cr}})^2 \cdot (p\text{O}_2)^2} \right] \quad \text{Equation 2-2}$$

Considering the activities of the solids are invariant (equal to 1), at equilibrium ($\Delta G = 0$) **Equation 2-2** can be written as:²⁰

$$\Delta G^\circ = -RT \ln \left[\frac{1}{(p\text{O}_2)^2} \right] = \frac{3}{2} RT \ln p\text{O}_2 \quad \text{Equation 2-3}$$

Thermodynamically, formation of the Cr_2O_3 scale depends on the $p\text{O}_2$ and occurs when $p\text{O}_2$ is greater than the dissociation O_2 partial pressure of the scale $(p\text{O}_2)_{\text{dissoc.}}$. [$p\text{O}_2 > (p\text{O}_2)_{\text{dissoc.}}$].^{20,21}

Formation of a protective adherent Cr_2O_3 scale in alloys depends on the alloyed Cr content.²² For simplicity, consider a binary Fe-Cr alloy in which Cr is more reactive for oxidation. According to Wagner's theory of oxidation,²³⁻²⁵ if the flux of Cr cations is less than that for O anions, internal oxidation of Cr_2O_3 occurs. The depth of the internal oxidation ($x[t]$) depends on the concentration of the solute Cr in the alloy through **Equation 2-4** where D_{Cr} and D_{O} are diffusion coefficients of Cr and O, respectively, $N_{\text{O}}^{(s)}$ is the O_2 solubility in Fe (mole fraction), $N_{\text{Cr}}^{(0)}$ is the bulk alloy concentration of Cr in Fe-Cr (mole fraction), D_{O} is the diffusivity of O_2 (cm^2/s) and t is the time (s):²³⁻²⁵

$$x(t) = \left[\frac{2N_O^{(s)} D_{Ot}}{N_{Cr}^{(O)}} \right]^{\frac{1}{2}} \quad \text{Equation 2-4}$$

Equation 2-4 shows that an increase in the bulk alloy concentration of Cr decreases the depth of the internal oxidation. If the concentration of Cr reaches some critical value, $N_{Cr}^{crit.}$ (mole fraction), (**Figure 2-1**) a continuous external layer of Cr_2O_3 , one that is known to be protective, forms.²³⁻²⁵

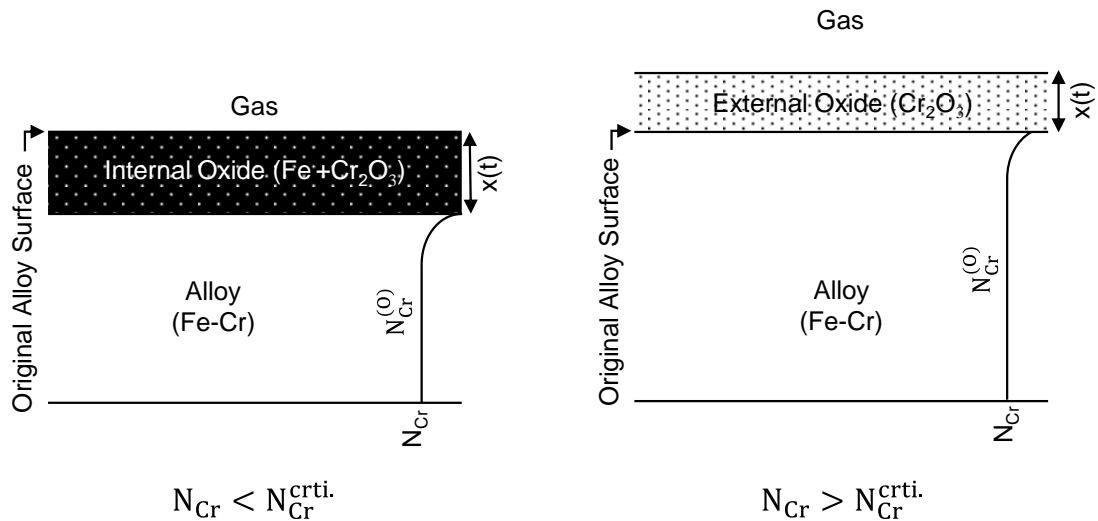


Figure 2-1. Physical description of internal and external oxidation for a binary Fe-Cr alloy.²³⁻²⁵

Equation 2-5 shows that $N_{Cr}^{crit.}$ depends on the molar volume of Cr (V_{Cr}) and Cr_2O_3 (V_O) in dm^3/mol , critical volume fraction of oxide for transition (g^*), and diffusivity of Cr in the oxide (D_{Cr}) in cm^2/s .²³⁻²⁵

$$N_{Cr}^{crit.} = \left[\frac{\pi g^*}{2} N_O^{(s)} \frac{D_O V_{Cr}}{D_{Cr} V_O} \right]^{\frac{1}{2}} \quad \text{Equation 2-5}$$

It is important to note that after relatively longer exposure times, with continued depletion of Cr, the amount of Cr available at the alloy/oxide interface reaches a critical minimum value required to sustain external oxidation.²² Activity of Fe at the original alloy surface increases in this case and easier mobility of Fe into the Cr₂O₃ scale more readily assists formation of Fe-rich oxides (e.g. Fe₂O₃ at high pO₂), **Figure 2-2**.²⁶

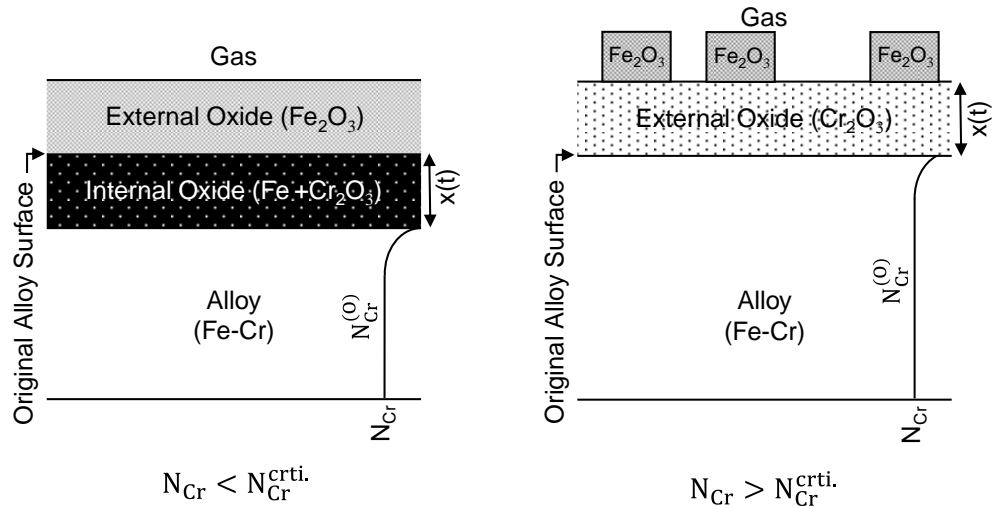


Figure 2-2. Physical description of the binary Fe-Cr alloy after long exposure times.^{25,27}

For an external oxide scale to be considered protective not only the Cr concentration needs to exceed $N_{Cr}^{crit.}$ (mole fraction) as shown by **Equation 2-5**, but also the parabolic diffusion of Cr in the alloy needs to remain rapid so that its content in the oxide is provided at least at the same rate as it is consumed by the

oxide scale growth.²⁷ The relation between the Cr content in the alloy and the parabolic oxidation rate for the oxide scale growth is shown by **Equation 2-6** in which N_{Cr}^* (mole fraction) is the second critical Cr value for maintaining the parabolic oxidation rate in the external scale, D_L is the Cr lattice diffusion coefficient (cm^2/s), D' is the Cr grain boundary diffusion coefficient (cm^2/s), s is the alloy grain size (cm) and δ is the grain boundary thickness (cm).²⁷ As can be inferred from **Equation 2-6**, the N_{Cr}^* depends on the alloy grain size, grain boundary thickness, lattice and grain boundary diffusion of Cr, molar volumes of Cr and Cr_2O_3 , and parabolic rate constant for oxidation.²⁷

$$N_{Cr}^* = [2\pi^{\frac{1}{4}} \frac{V_{Cr}}{V_O \cdot 3\sqrt{2}}] \left\{ \frac{sk_p^{\frac{1}{2}}}{D_L^{\frac{1}{4}} (\delta D')^{\frac{1}{2}} t^{\frac{1}{4}}} \right\} \quad \text{Equation 2-6}$$

Selective oxidation of elements in an alloy with more than two elements is more complex; however, the concept remains the same. High-temperature alloys used in the structural components need to have acceptable high-temperature mechanical properties, creep resistance, and oxidation resistance from a service performance perspective. In the temperature range of 550-900°C, high Cr-containing austenitic Fe-Cr-Ni alloys are preferred from a material selection perspective since: (i) they have relatively good high-temperature mechanical integrity, (ii) they have much better creep resistivity at high temperatures compared with ferritic alloys, and (iii) they tend to form a protective external Cr_2O_3 scale that decreases the alloy oxidation rate.^{20,22,28} It is well established that the critical Cr

content required for the formation of an external Cr_2O_3 scale in austenitic Fe-Cr-Ni alloys is ~20 wt.%.^{20,22,28} R. Peraldi et al.²⁹, however, discussed that the critical Cr content in Fe-Cr-Ni alloys is a function of the alloy Ni content as well as its grain size. It is often seen that even when the Cr content of the alloy is higher than the critical value required to promote the formation of an external Cr_2O_3 layer, the oxide still has small amounts Fe and Mn dissolved. Most high Cr-containing austenitic Fe-Cr-Ni alloys contain other elements such as Si, Mn, Ti, and Al that each can selectively oxidize. The amount of these alloying elements is usually low in the alloy, therefore, from thermodynamics, all are expected to oxidize to some extent during exposure at high temperature. The so-called Ellingham diagram, which plots the variation of the standard Gibbs free energies of oxide formation as a function of temperature, illustrates the relative stability of an oxide as a function of both temperature and $p\text{O}_2$.²¹ The sequence of oxide formation in H_2O -containing environments related to this study (as discussed later), from the most to the least thermodynamically stable oxides is: Al_2O_3 , TiO_2 , SiO_2 , MnO , Cr_2O_3 , FeO , Fe_3O_4 , Fe_2O_3 , and NiO .²¹ For alloys containing Si for instance (relevant to this study), formation of SiO_2 underneath the Cr_2O_3 is expected, whereas Fe-rich oxides are expected to form above Cr_2O_3 .²¹

2.1.2. Cations Diffusivity in the Cr_2O_3 Scale and Austenitic Matrix

The values of Fe, Cr, and Ni lattice diffusion coefficients [D_L (cm^2/s)] in austenitic Fe-Cr-Ni alloys in vacuum at 963°C and after ~24 h are compared in **Table 2-1**. In all cases, D_L decreases in the order of: $D_{L,\text{Cr}} > D_{L,\text{Fe}} > D_{L,\text{Ni}}$.³⁰ Z. Tokei³¹ argued that

the alloy boundary transport is far more important than lattice transport for the formation of the Cr₂O₃ scale. The grain boundary diffusion coefficient values of Fe, Cr and Ni in Fe-15Cr-20Ni alloys was also compared at 963°C and it was shown that $D_{Cr} > D_{Fe} \geq D_{Ni}$.³⁰ It is evident that Cr has the highest lattice and grain boundary diffusion coefficient values between the three major alloying elements (Fe, Cr and Ni) in austenitic Fe-Cr-Ni alloys and also forms the most stable oxides among the three element, therefore, the concentration change in the alloy Cr content plays an important role in the formation of a protective oxide scale.³⁰

Table 2-1 Lattice diffusion coefficient values for Fe, Cr and Ni in austenitic Fe-Cr-Ni alloys at 963°C after ~24 h exposure in vacuum

| Trace | Lattice Diffusion Coefficient , D_L (cm ² /s) | | | |
|-------|--|------------------------|------------------------|------------------------|
| | Fe-15Cr-20Ni | Fe-15Cr-45Ni | Fe-22Cr-45Ni | Fe-15Cr-20Ni-1.4Si |
| Fe | 3.98×10^{-13} | 1.43×10^{-12} | 1.32×10^{-12} | 6.76×10^{-13} |
| Cr | 5.21×10^{-13} | 1.71×10^{-12} | 1.46×10^{-12} | 9.74×10^{-13} |
| Ni | 2.92×10^{-13} | 7.21×10^{-13} | 7.17×10^{-13} | 4.33×10^{-13} |

A large amount of literature has studied the diffusion of cations through a Cr₂O₃ scale.³²⁻³⁴ A.C.S. Sabioni et al.^{26,32} compared the values of bulk and grain boundary diffusion coefficients in the Cr₂O₃ scales that were oxidized in the temperature range of 700-1100°C under an oxygen partial pressure of 10⁻⁴ atm.

Figure 2-3 shows an Arrhenius plot of bulk and grain boundary diffusion for Fe, Mn, and Cr reported in the A.C.S. Sabioni et al.³² study. They argued that Fe and Cr cations diffusion is slower than that for Mn in both bulk and grain boundaries, while Mn cations diffusion is the fastest in the bulk but depends on the temperature for the grain boundaries. On their graph they also compared their own values with

those previously measured by R.E. Lobnig et al.³³ and showed that their measured values are greater than those for R.E. Lobnig et al.³³. They rationalized this difference implying that most probably the values reported by R.E. Lobnig et al.³³ are effective diffusion coefficients which include both the grain boundary diffusion coefficient and bulk diffusion coefficients.

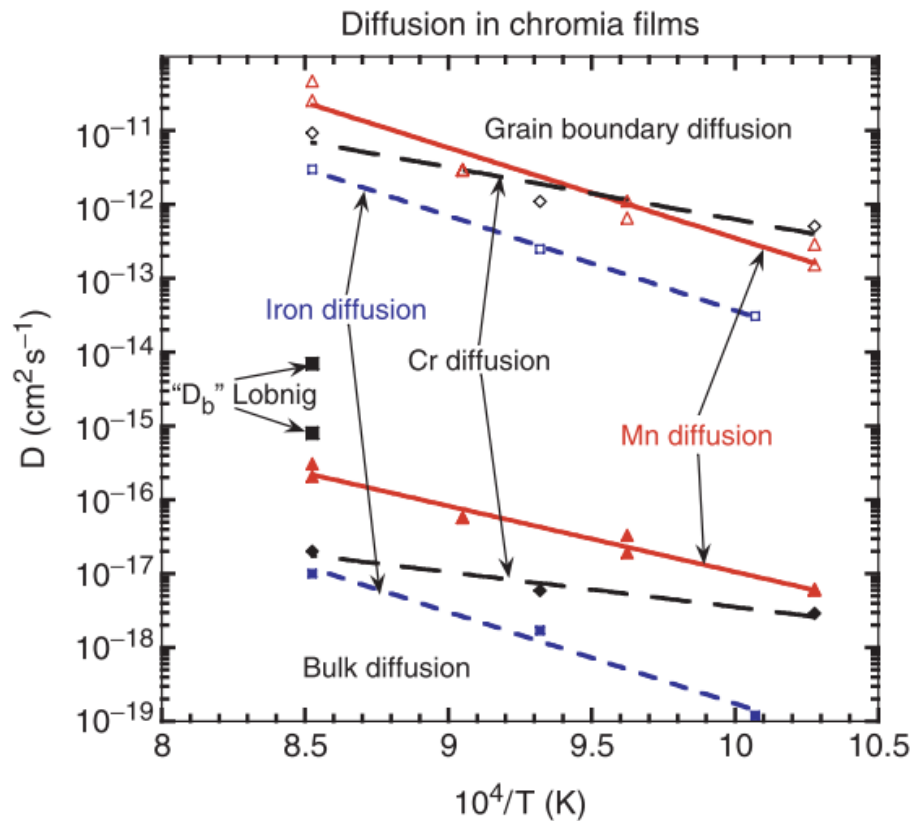


Figure 2-3. Comparison, in an Arrhenius plot, of bulk and grain boundary diffusion of cations in Cr_2O_3 scales after A.C.S. Sabioni et al.³²

There are still some discrepancies in the values reported in the literature for the diffusion coefficients of cations in the Cr_2O_3 scale mainly due to the different thermal processes used to attain the Cr_2O_3 scale and different oxidizing temperatures and pressures used for the diffusion measurements. Regardless,

most literatures still agree with the relative comparison of Fe, Mn, and Cr cations diffusion coefficients reported by A.C.S. Sabioni et al. stating that Mn has the highest diffusivity in the Cr₂O₃ scale.^{33,35,36}

2.2. Wet Oxidation

Wet environments are considered as those containing water vapour (H₂O). The wet oxidation behaviour of alloys significantly vary in wet air and dry air. The following sections discuss the available literature on the thermodynamics and kinetics of wet oxidation along with the proposed theories of wet oxidation.

2.2.1. Thermodynamics of Wet Oxidation

In the case where the environment is pure steam (100 vol.-% H₂O), the O₂ required for the oxidation reaction (Cr₂O₃ formation) to happen is provided from the steam dissociation (**Equation 2-7**).²⁰



The pO₂ in **Equation 2-7** is related to the total steam pressure, P, via **Equation 2-8** in which k₂ is the equilibrium constant for the steam dissociation at a given temperature. As P increases, also pO₂ increases, which favors the forward reaction in **Equation 2-7** (complete oxidation).²⁰ For ambient pressure (0.1 MPa), the value of pO₂ is relatively small, however, as P increases, specifically in the pressures above 24-25 MPa, the effect of pO₂ becomes important.²⁰

$$p_{O_2} = \left(\frac{k_2}{2}\right)^{\frac{2}{3}} P^{\frac{2}{3}} \quad \text{Equation 2-8}$$

In the case where the environment is not pure steam, e.g. wet air, p_{O_2} is provided by both O_2 from the air and H_2O dissociation. p_{O_2} in this case is related to the total wet air pressure (P^*) via **Equation 2-9** in which w is the volume percent H_2O in air considering 21% of air is oxygen.²⁰ Therefore, the amount of O_2 available for the oxidation reaction to occur highly depends on the vol.% H_2O existing in the mixture.²⁰

$$p_{O_2} = (1-w)0.21 P^* \quad \text{Equation 2-9}$$

The calculated equilibrium dissociation pressure (p_{O_2})_{dissoc.} of most metal oxides, particularly Cr_2O_3 , is below the p_{O_2} in the high-pressure steam [$(p_{O_2})_{dissoc.} < p_{O_2}$], low-pressure (ambient) steam, and wet air environments meaning Cr_2O_3 is thermodynamically stable in the aforementioned conditions.²⁰

2.2.2. Relevant Wet Oxidation Environments

The two particular wet environments of interest to the research presented in this thesis are (i) supercritical water (SCW) and (ii) wet air, which is a mixture of air and a certain volume percent H_2O . Both wet environments are described in some detail in the following sections.

2.2.2.1. Supercritical Water (SCW)

According to the pressure-temperature water phase diagram (**Figure 2-4**), a critical pressure ($P_c = 22.1$ MPa) and temperature ($T_c = 374.0^\circ\text{C}$) exists above which the densities of liquid and gas phases become identical resulting in the existence of one single phase.³⁷⁻³⁹ In other words, above the critical point, any increase in the pressure and/or temperature of water does not change its state and only one phase exists known as “supercritical water (SCW)”.³⁷⁻³⁹ This unique characteristic of SCW can increase the efficiency of a power plant from ~36% to possibly as high as ~50%. Consequently, it forms the basis of one of the six Generation IV nuclear reactor designs being considered worldwide as part of the Generation IV Forum.⁴⁰⁻⁴² As a coolant in a Supercritical Water-Cooled Reactor (SCWR) design, the SCW heated to such a condition within the reactor core will drive the turbines.⁴⁰ Due to the very high average thermal energy of the water molecules at temperatures above T_c , regardless of the pressure value, the liquid phase cannot be formed.³⁷⁻

39

It has been discussed that the oxidation performance of structural materials in SCW is very much similar to that in superheated steam ($T > T_c$ and $P < P_c$), in that the corrosion mechanism in both environments is chemical because of the absence of an electrolyte necessary for the electrochemical corrosion.^{39,43}

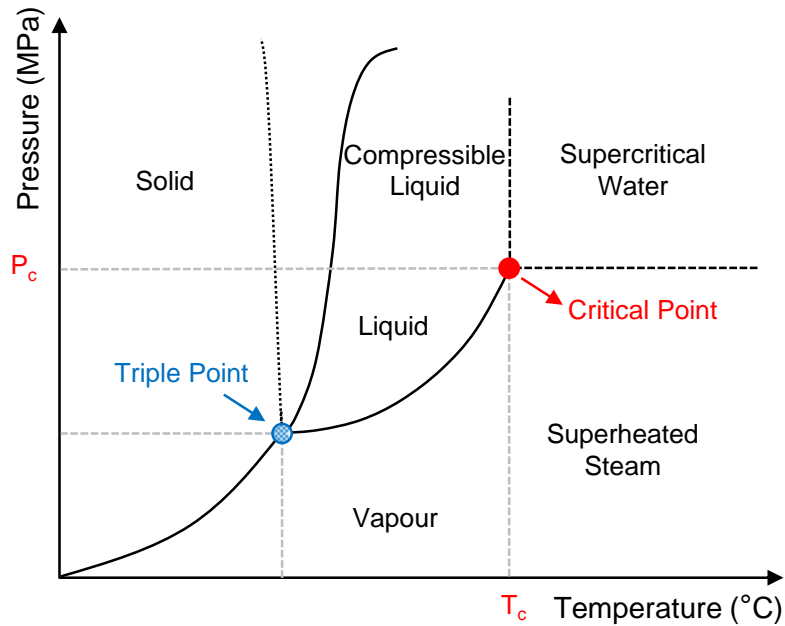


Figure 2-4. Water phase diagram.

SCW has a relatively low dielectric constant, which allows it to contain more uncharged, neutral water molecules at the expense of its ionic dissociation products: H^+ and OH^- .^{44,45} This feature of SCW therefore decreases the water ionic products of SCW.^{39,44,45} It has been discussed that SCW behaves similar to a nonpolar solvent, meaning many of the oxide-hydroxides (e.g. $Me(OH)_{n(aq)}$) that are hardly soluble in subcritical water are highly soluble in SCW.^{39,45} As a result, one major concern regarding the use of SCW in SCWR is the possibility of release and transport of oxide-hydroxide corrosion products from the surface of oxides.³⁹ The oxidation products that are carried away can deposit on the fuel cladding of SCWR, decrease heat transfer rates, and result in the failure of components.³⁹

2.2.2.2. Wet Air

The atmospheric dry air consists of approximately 78.1% nitrogen, 21.0% oxygen, 0.93% argon, 0.03% carbon dioxide, and minor amount of other gases (e.g. neon, methane, and hydrogen).⁴⁶ The volume percent (vol.-%) of each gas changes with the presence of H₂O in the air. The vol.-% H₂O is related to the number of H₂O molecules per unit volume divided by the total number of gas molecules per unit volume, as shown in **Equation 2-10**, where P_w and P_T are the partial pressures of water vapour and total gas, respectively.⁴⁶

$$\text{vol.}\%_{(\text{H}_2\text{O})} = \frac{P_w}{P_T} \qquad \text{Equation 2-10}$$

The amount of H₂O that air can hold increases with temperature. The vol.-% H₂O is often measured using the water dew point, which is the temperature at which air is saturated with H₂O.⁴⁶ The dew point can be calculated from the saturation pressure (P_s)-temperature diagram (**Figure 2-5**). For example, for an air-10 vol.-% H₂O mixture, the P_s is 10% of the atmospheric pressure (1 atm), which is 0.1 atm with ~46°C dew point.⁴⁶

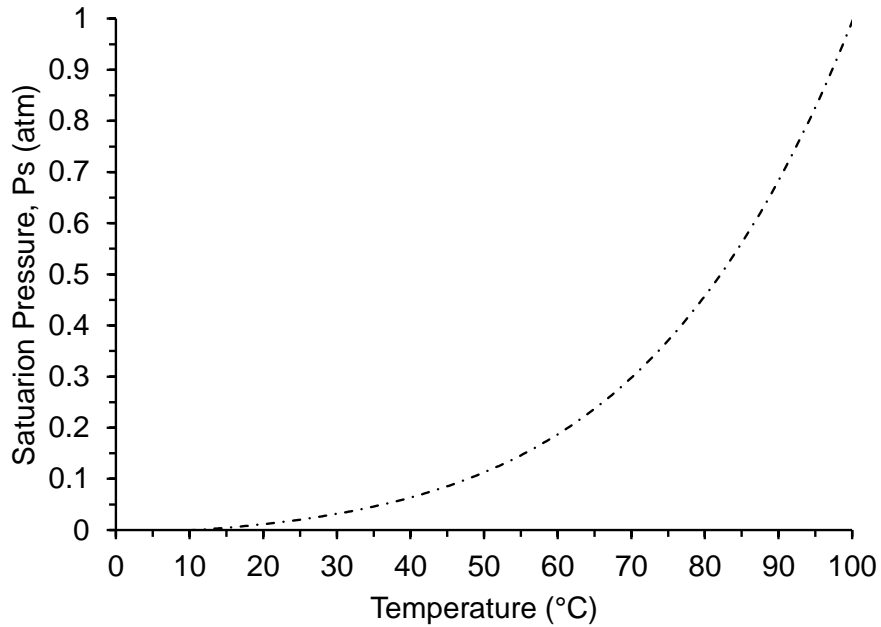


Figure 2-5. Saturation pressure (P_s) of H_2O .⁴⁶

Table 2-2 shows the vol.-% H_2O and the corresponding water dew points.⁴⁶

Table 2-2 can be used in the experimental designs to achieve a certain mixture of an air-x vol.-% H_2O (relevant to this study).

Table 2-2 Values of water dew point for different vol.% H_2O present in air.

| Vol.-% H_2O | Dew point (°C) |
|---------------|----------------|
| 0 | -273.3 |
| 10 | 46.1 |
| 20 | 60.6 |
| 30 | 69.4 |
| 40 | 76.1 |
| 50 | 81.7 |
| 60 | 86.1 |
| 70 | 90.0 |
| 80 | 93.9 |
| 90 | 97.2 |
| 100 | 100.0 |

2.2.3. Wet Oxidation Kinetics

Knowledge of oxidation reaction rates is essential to understand the rate-controlling oxidation steps in the wet environments. **Figure 2-6** shows the simplest empirical oxidation reaction kinetics in the presence of O_2 . The oxidation kinetics in the presence of both O_2 and H_2O , known as the wet oxidation kinetics, are also discussed in this section.

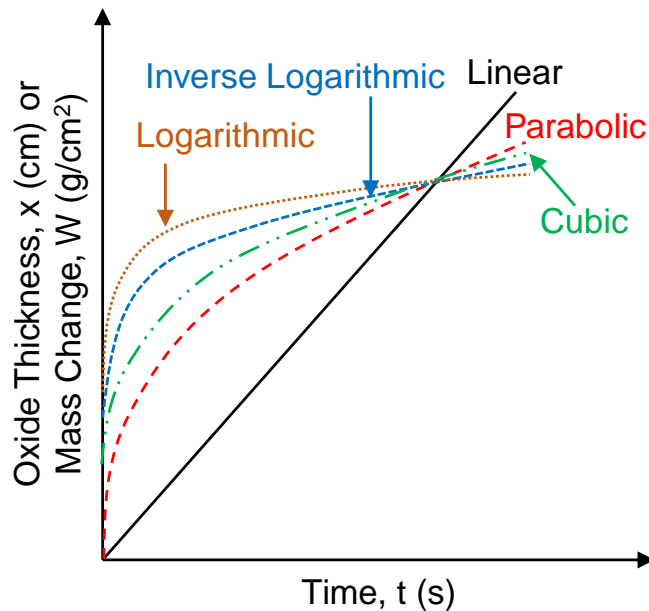


Figure 2-6. Common high-temperature oxidation rate laws governing the oxidation kinetics.²⁵

The logarithmic or inverse logarithmic oxidation rate laws are applicable to the thin oxide scales (typically below ~100 nm) formed at relatively low temperatures (~400°C or less).⁴⁷ The driving force for oxidation exhibiting logarithmic or inverse logarithmic kinetics is the presence of an electric field across a thin oxide scale, which is first formed by the O_2 adsorption on the surface.^{48,49}

Lots of research has been conducted to better understand the fundamentals of logarithmic and inverse logarithmic oxidation. However, obtaining reliable experimental data in the initial stage of oxidation is very difficult. Consequently, mechanistic aspects are still not well-understood. Logarithmic and inverse logarithmic functions are shown in **Equation 2-11** and **Equation 2-12**, respectively, where x is the oxide thickness (cm) or mass per surface area (g/cm^2), t is the oxidation time (s), k_e and k_i are the logarithmic and inverse logarithmic rate constants, respectively (cm^2/s or $\text{g}^2/\text{cm}^4/\text{s}$), and a and b are equation constants.^{47,49}

$$x = k_e \log(at + 1) \qquad \text{Equation 2-11}$$

$$\frac{1}{x} = b - k_i \log t \qquad \text{Equation 2-12}$$

The linear kinetics in dry O_2 mainly applies to the case where the metal surface is not protected with an oxide scale.⁴⁷ The oxidation reaction occurs at the metal surface or phase boundary, and the steady state reaction is limited by the reactant supply at the metal surface.^{47,50} The oxidation rate in the linear kinetics increases linearly with time as shown in **Equation 2-13**, where k_l is the linear rate constant (cm/s or $\text{g}/\text{cm}^2/\text{s}$).^{47,50}

$$x = k_l t \qquad \text{Equation 2-13}$$

Oxides that follow the linear kinetics usually have at least one of the following characteristics:

1. High volatility and/or dissolution in the oxidizing environment
2. Pilling-Bedworth¹ ratio of less than one
3. Spalled or cracked
4. Porous and non-protective

Wagner⁵¹ developed the theory of high-temperature oxidation of metals in which he described the diffusion-controlled (parabolic) oxidation process considering the following assumptions:

1. The oxide scale is compact, adherent and relatively thick
2. The rate-controlling oxidation process is the volume diffusion of reactive ions or corresponding electronic defects across the scale
3. Thermodynamic equilibrium is established at all interfaces and across the scale
4. The oxide scale is close to stoichiometric (similar ionic flux across the scale)
5. Oxide has close to zero solubility in the metal

¹ The concept of Pilling-Bedworth ratio is discussed in details later.

Figure 2-7 shows the scale formation diagram according to the Wagner's theory. Diffusion of ions across the scale forms an electric field, which will cause the transport of electrons. The rate of cations, anions and electrons diffusion across the scale is balanced such that there exists no net charge (electroneutrality of the scale). The rate-controlling process in the parabolic kinetics is the ions diffusion through a uniform, compact, and adherent oxide scale.⁵¹ The driving force for the parabolic kinetics is the chemical potential gradient across the scale as shown in **Figure 2-7**.

Figure 2-7.

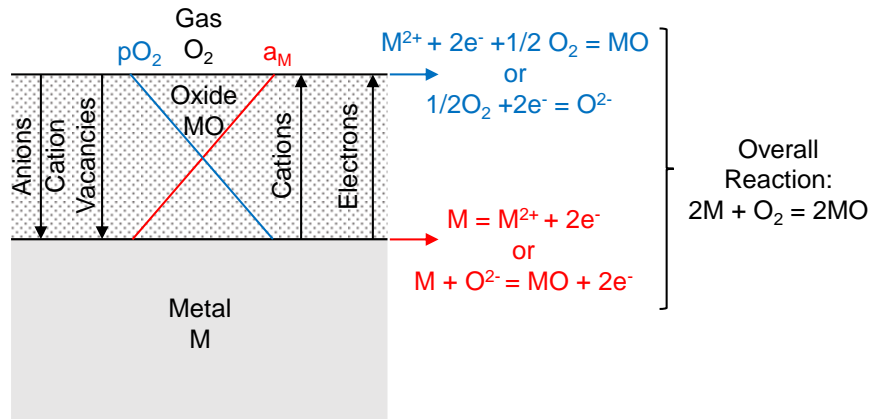


Figure 2-7. Physical description of oxide scale formation according to Wagner's theory.⁵¹

With the oxide thickening, the diffusion distance increases. The oxidation rate is inversely proportional to the scale thickness through **Equation 2-14**, in which k_p is the parabolic rate constant (cm^2/s or $g^2/cm^4/s$).

$$\frac{dx}{dt} = \frac{k_p}{x}$$

Equation 2-14

The parabolic oxidation kinetic reaction is shown below upon the integration of **Equation 2-14**:

$$x^2 = \frac{k_p}{2} t \quad \text{Equation 2-15}$$

The parabolic rate constant increases exponentially with temperature as shown in the Arrhenius **Equation 2-16** where Q is the activation energy of oxide growth (J/mol), R is the universal gas constant (J/mol/K), and T is the oxidation temperature (K). k_0 is the Arrhenius equation constant (**Equation 2-16** and **Equation 2-17**) that is dependent on the pO_2 of the gas, oxide composition, and the exponent constant (n) dependent on the deficit nature of the oxide (p-type or n-type).²⁰

$$k_p = k_0 \exp\left(-\frac{Q}{RT}\right) \quad \text{Equation 2-16}$$

$$k_0 = \text{const.} pO_2^{\frac{1}{n}} \quad \text{Equation 2-17}$$

Under high oxide growth stress⁵² and/or oxide grain growth⁵³ a cubic rate law might be governed. The reaction rate is approximated using **Equation 2-18** in which k_3 is the cubic rate constant. Cubic kinetics is mostly seen in Cu, Zr, and Ti alloys in dry air.²⁵

$$x^3 = k_3 t \quad \text{Equation 2-18}$$

Both parabolic and linear oxidation kinetics are commonly exhibited by alloys exposed in wet environments at high temperatures.⁵⁴⁻⁵⁶ Mechanistic aspects of the parabolic and linear rate laws individually have been explained above. Often in wet environments, a combination of the parabolic and linear kinetic is observed.⁵⁴⁻⁵⁶ It is argued that the combination of parabolic and linear kinetic regimes occurs due to accelerated Fe-rich oxide formation, which in some literature, is known as “breakaway” kinetics.⁵⁴⁻⁵⁶ An example of breakaway kinetic is shown in **Figure 2-8**.⁵⁴⁻⁵⁶ A parabolic rate law governs the initial stage of oxidation and a linear rate law governs the final stage of oxidation.⁵⁴⁻⁵⁶ Initial parabolic oxidation is controlled by ions diffusion through the scale.⁵⁷ The rate-controlling step of the linear stage is still not well understood and the current knowledge in this regard is discussed later. A note must be made here regarding the terminologies used when reporting the combination of parabolic and linear kinetics. In a large amount of articles breakaway kinetics is used when Fe-rich oxides are formed.^{38,54,58} Some others report the combination of parabolic and linear kinetics using the paralinear terminology.⁵⁹⁻⁶¹ Values of metal loss of the alloy (if measured using a descaling procedure as shown in this thesis) in both of these cases follow the kinetics similarly (combination of parabolic and positive linear rate constants). Therefore, paralinear and breakaway kinetic terms in the metal loss curves are used interchangeably.⁶²

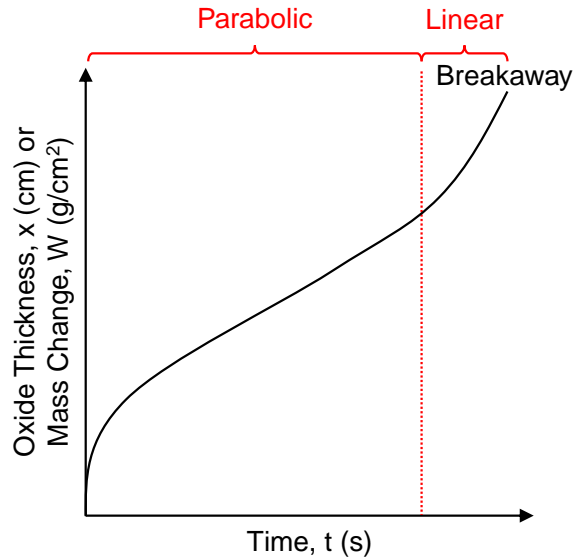


Figure 2-8. Oxidation kinetic of breakaway rate law.⁵⁸

The change in the oxidation rate laws typically occurs with a concomitant decrease in the protectiveness of the oxide scale due to either mechanical spallation or chemical volatilization.⁶¹ Often, the oxide scale is comprised of an inner oxide layer, which remains protective with a constant thickness, and an outer layer that is porous and non-protective.⁶³ The mass of the metal consumed (m) in grams in the breakaway rate law is related to the parabolic and linear rate laws, with the units of $\text{g}^2/\text{cm}^4/\text{s}$ and $\text{g}/\text{cm}^2/\text{s}$, respectively through **Equation 2-19**.⁶⁴ The parabolic kinetics herein reflect the accumulation (growth) of an oxide scale and the linear kinetics reflect loss of the accumulated oxide scale due to volatilization.⁶⁴

$$m = \frac{k_p}{k_l} \ln \frac{k_p}{k_p - k_l(m - k_l t)}$$

Equation 2-19

It has been shown that the mass change during scale accumulation and subsequent volatilization follows **Equation 2-20** in which W is the mass change per unit surface area (g/cm^2).^{65,66}

$$W\left(\frac{dW}{dt}\right) = k_p - m \times k_l \quad \text{Equation 2-20}$$

It has also been proposed that a limiting oxide thickness [x_l (cm)] exists at which the metal cation diffusion rate into the oxide scale equals the metal cation loss due to oxide scale spallation/volatilization (**Equation 2-21**).^{65,66} Note that the units for k_p and k_l in **Equation 2-21** are cm^2/s and cm/s , respectively.

$$x_l = \frac{k_p}{2k_l} \quad \text{Equation 2-21}$$

Figure 2-9 illustrates the common high-temperature oxidation kinetics that have been described above. An oxide is considered to be protective at high temperatures when the rate of oxidation decreases with time and is typically governed by a parabolic rate law.^{5,67} For relatively thick scales or scales that are formed and spalled during thermal cycling, the oxide is considered somewhat protective depending on the extent of spallation.⁶⁸ For the breakaway rate law, the oxide scale formed is considered to be protective during the initial parabolic oxidation stage and much less protective during the final linear oxidation stage.^{61,69} It is possible that as a consequence of the balance between the two parabolic and linear governing rate laws, the scale thickness reaches a maximum value

(Equation 2-21) after which the scale volatilization becomes dominant.⁶⁶ The latter is shown in **Figure 2-9** as scale growth with superimposed volatilization curve and is considered to be temporary protective.

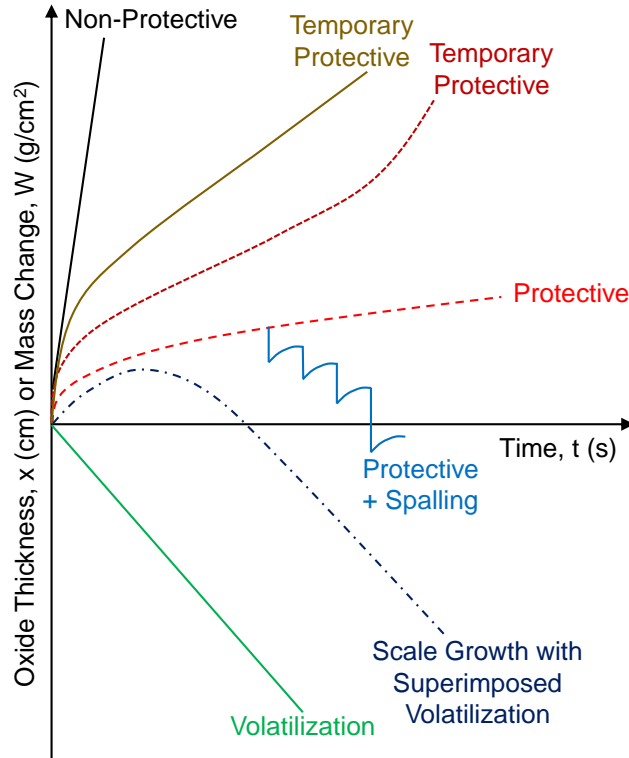


Figure 2-9. Description of the oxide protectiveness based on the scale kinetics.

Most often during cyclic oxidation and sometimes during wet oxidation, a linear negative rate is observed as shown in **Figure 2-9**.^{59,70} It is reported that the negative rate constant can also be a consequence of oxide spallation at the temperature of exposure or during cooling.^{69,71}

2.3. Stresses in the Oxides

Oxidation of Cr₂O₃-forming alloys can generate two major types of stresses: growth stress and thermal stress.^{72,73} Growth stresses are created during oxide scale formation at a constant temperature whereas thermal stresses are often generated when the alloy is subjected to thermal cycles during exposure.^{25,71,74} It follows then that the difference between the coefficient of thermal expansion (CTE) of the oxide scale and the underlying substrate becomes important.⁷⁵ The major contribution to the growth stress arises from the difference between the volume of the oxide and its underlying substrate.⁷⁶ **Equation 2-22** shows the ratio of the specific volumes of oxide (V_{ox}) and alloy (V_A) known as Pilling-Bedworth ratio (PBR).⁷⁶

$$PBR = \frac{V_{ox}}{V_A} \qquad \text{Equation 2-22}$$

In most cases, PBR is greater than one, meaning the oxide is under compressive stresses and is considered to be more protective than those oxides that are in tension (PBR of less than one).⁷⁶ The reason that oxides with a PBR of less than one (under tensile stresses) are not considered to be protective is that tensile stresses assist the formation of cracks in the oxides.⁷⁶ In the conditions that the PBR is greater than one, the compressive stresses might not be of concern if the value of the oxidizing solute metal is high enough that the oxide is formed externally at the oxide/gas interface.⁷⁶ If the oxidizing solute metal concentration is however, relatively low and the oxide is formed internally, relatively large compressive stresses might generate.⁷⁶ Growth stresses can also generate if there is any

change in the composition of the oxide and/or its substrate.⁷⁷ The change in composition, changes the lattice parameter of the oxide and/or substrate, and can result in the difference in their volumes and amount of O₂ solubility, therefore, increasing the compressive stresses.⁷⁷ Also, recrystallization of the scale, presence of additional point defects, and formation of new oxides within the old ones can incorporate into the formation of growth stresses.⁷⁸⁻⁸⁰ The specimen geometry is of great important here as sharper edges in the specimen can increase the value of stress intensity leaving the alloy and oxide at higher risk of stresses.⁸¹ As mentioned before, the growth stresses specifically for the oxides that form uniform layers at the oxide/gas interface are not considered to play a role in mechanical spallation or crack induction into the scale.⁷⁶ When the oxide scale formed on the alloy is subjected to a temperature change (mostly during sample cooling), the difference between CTE of the oxide and the alloy results in the formation of thermal stresses.¹² If the thickness of the oxide is relatively thin compared to the underlying substrate (which is often the case) and no bending deformation occurs, the value of thermal stress (σ_{ox}) can be estimated by **Equation 2-23** where E_{ox} is the modulus of elasticity of the oxide (GPa), α_{ox} and α_M are the linear CTE of the oxide and metal, respectively (1/K), ν is the Poisson's ratio of the oxide and ΔT is the difference between the final and initial oxidation temperature (K).⁸²

$$\sigma_{Ox} = \frac{-E_{Ox} (\alpha_{Ox} - \alpha_M) \Delta T}{(1 - \nu)} \quad \text{Equation 2-23}$$

In most cases, thermal stresses cause oxide spallation, especially when the material undergoes a cyclic oxidation.^{68,83,84} The necessary criterion for the oxide spallation and its failure to happen is when the elastic energy stored in the oxide scale is greater than the fracture resistance of the interface (G_c).⁸⁵ **Equation 2-24** shows this criterion in which σ is the oxide biaxial residual stress (MPa), and h is the oxide thickness.⁸⁶ It can be concluded that for thicker oxides or those that have higher stresses, spallation occurs more rapidly.

$$\frac{(1 - \nu) \sigma^2 h}{E} > G_c \quad \text{Equation 2-24}$$

2.4. Proposed Mechanisms of Wet Oxidation

The magnitude of parabolic and linear rate constants dictates the onset of the intersection between the parabolic and linear kinetic regimes and has paramount importance as if the onset is delayed, accelerated oxidation is prohibited.⁶⁹ Therefore, understanding factors that may delay this point is crucial from the high-temperature oxidation performance perspective. Research has been conducted to evaluate the onset of the intersection between parabolic and linear kinetic regimes as a function of exposure time, temperature, oxygen partial pressure and alloyed Cr content.^{54,58,61,87} However, little attention has been given to the role played by those minor alloying elements that can readily oxidize as well. Mechanistic aspects of the parabolic and breakaway rate laws, the rate-controlling step in particular, are still being debated. T. Jonsson et al.⁸⁸ proposed the breakaway oxidation model

for Fe-Cr-Ni alloys exposed in H₂O- and O₂-containing gases with high and low pO₂ at 600°C (**Figure 2-10**). It is implied that a protective Cr₂O₃ scale, with some dissolved Fe, initially forms on the alloy surface, which leaves behind a Cr-depleted zone in the substrate underneath the scale. With increasing the exposure time, the Cr-depleted zone becomes sufficiently large to trigger the outward diffusion of Fe cations, which promotes the formation of outer Fe-rich oxides: Fe₃O₄ in low pO₂ wet environments and Fe₂O₃ in high pO₂ wet environments. At the same time, inward diffusion of the oxidant component promotes the formation of inward-growing Fe-Cr spinel regions, which leaves behind Fe and Ni regions within the metal. Their model however does not identify the rate-controlling step that is responsible for the linear volatilization of the oxidized Cr and formation of Fe-rich oxides.

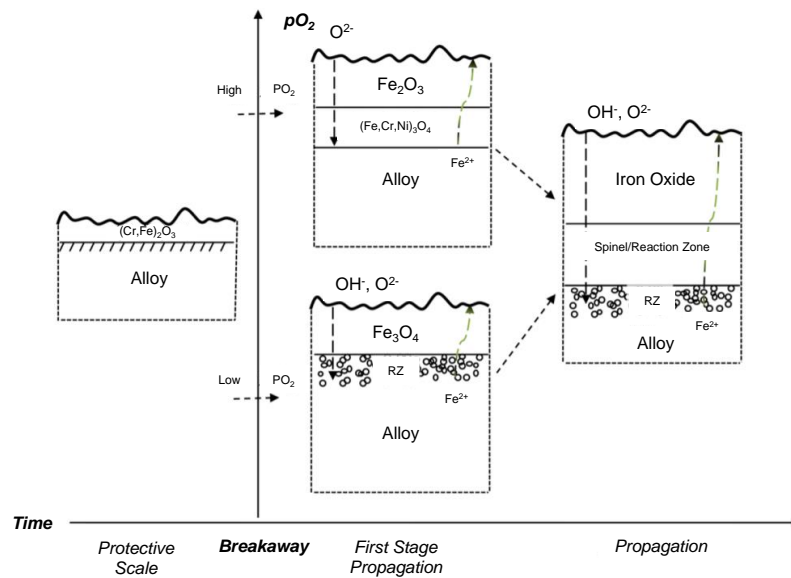
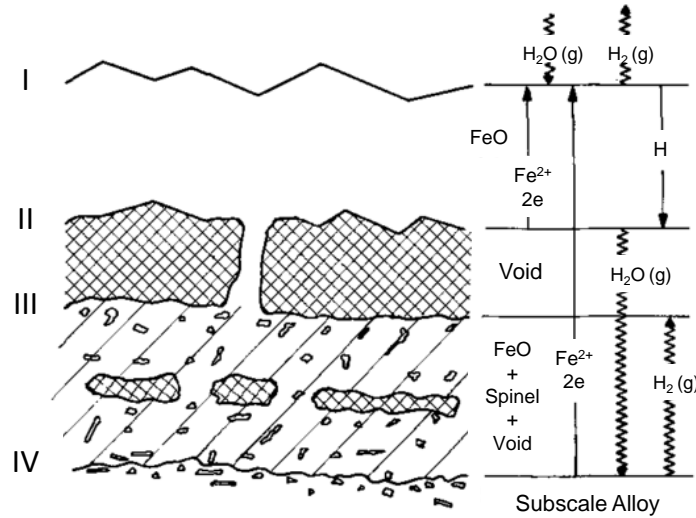


Figure 2-10. Schematic illustration of the breakaway oxidation for Fe-Cr-Ni alloys proposed by T. Jonsson et al.⁸⁸ in H₂O- and O₂-containing gases with high and low pO₂ at 600°C.

It is implied that breakaway oxidation occurs after a large Cr depleted zone is formed.^{56,87,89} Once the oxidant component reaches the alloy/oxide interface, Fe-rich oxides nucleate.²⁵ Other studies suggest that the double-layered scale grows simultaneously both at the alloy/oxide and oxide/gas interface and the interface between the two layers is the original alloy surface.⁹⁰ There is still little information regarding which oxidizing species controls the oxidation rate in the wet air. It is implied that in the O₂/H₂O environments, competitive adsorption of O₂ and H₂O species on the surface of the alloy directly influences the accelerated linear oxidation.⁹¹ Mechanistic aspects of oxidation in Fe-Cr alloys in the presence of H₂O and O₂ are still not understood. There are generally five main mechanisms proposed to describe the effect of water vapour on the oxidation of Fe-Cr alloys as described below:

2.4.1. Dissociative Mechanism

Fujii and Meussner⁹² proposed the dissociative mechanism for Fe-Cr alloys exposed in low pO₂ containing Ar-10% H₂O at 800-1100°C illustrated in **Figure 2-11**. The scale that forms in this condition is an outer wustite (FeO) with relatively large voids on an internal porous FeO and Fe-spinel layer. They argued that even though the lattice transfer of Fe cations is limited by the small bridges between the internal and external oxide layers, the surface reactions are rate controlling, not the cations diffusion. Dissociation of H₂O gases in the voids provide O₂ required for growth of the inner layer and releases Fe cations for maintaining the surface reactions on the external oxide layer.⁹²



$$p_{H_2O_I} > p_{H_2O_{II}} \geq p_{H_2O_{III}}$$

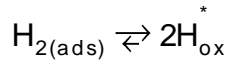
Figure 2-11. Dissociative mechanism proposed by Fujii and Meussner.⁹²

The reactions occurring during the growth of FeO are now described. At the outer interface (I) H₂O molecules are adsorbed (**Equation 2-25**) and react with the Fe cations that have diffused to the interface (**Equation 2-26**) leading to the formation of FeO, oxide defects and adsorbed H₂. Fe_□ and ⊕ stand for vacant Fe sites and electronic defects, respectively.



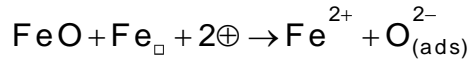
Hydrogen adsorbed from **Equation 2-26** can either form gas H₂ (H₂ evolution), **Equation 2-27**, or dissolve into the oxide forming H* (**Equation 2-28**).





Equation 2-28

At interface II, FeO dissociates consuming lattice defects and generating Fe²⁺ and adsorbed O²⁻ (**Equation 2-29**). **Equation 2-27** and **Equation 2-28** are reverted at this interface. The adsorbed O²⁻ then reacts with the H₂ adsorbed to form H₂O gas molecules at interface II.



Equation 2-29

Reactions similar to interface I then occur at interface III. At Interface IV, the predominant reaction is Fe²⁺ production and electron release. It was argued that some oxygen must be removed from the oxide and dissolved into the metal to allow the formation of internal oxides.

2.4.2. Penetration Mechanism of Gas Oxidants

It is implied that transport of H₂O and O₂ can directly occur through relatively large micro-cracks and pores formed in the Cr₂O₃ scale.⁹³ It is suggested that Cr loss during scale volatilization or growth stresses during isothermal exposure can lead to micro cracks or pores formation in the scale.⁹³ These species can then directly reach out to the alloy surface through these defects. It is implied that once a Cr₂O₃ scale forms, transport of gases through micro-cracks and pores in the scale increases pO₂ in the voids resulting in formation of Fe-rich oxides. The mixed Fe- and Cr-rich scale is not protective as the diffusion rate of Fe cations is high in a

mixed defective Fe- and Cr- rich scale.⁹⁴ The scale eventually becomes rich in Fe.⁹³

2.4.3. Hydrogen Dissolution

It is argued that H₂O is a source of H₂ (from dissociation), which can easily dissolve into both the oxide and the alloy forming atomic H.^{95,96} If true, then it is possible that H₂ dissolution in the oxide increases the number of defects, which in turn would serve to assist the transport of H₂O and metallic cations through the oxide and thus, increase the oxidation rate.^{95,96}

2.4.4. Formation of Fe-Hydroxides

J. Ehlers et al.⁹⁷ proposed that the growth of non-protective Fe-rich scale depends on the competitive adsorption of O₂ on the external oxide surface and absorption of H₂O on the internal oxide surface. The pO₂ is lower at the inner layer surface and inside the pores, therefore, Fe-hydroxide (Fe(OH)₂) gas species are produced. Fe(OH)₂ is not stable at the external oxide/gas interface since the pO₂ is relatively high there, therefore they deposit to form solid Fe-rich oxides (**Figure 2-12**). It has been suggested that the rate-controlling step in this mechanism can be either outward diffusion of Fe cations into the oxide/gas interface, inward diffusion of O anions to the alloy/oxide interface or transport of Fe(OH)₂ gas to the oxide/gas interface. The rate-controlling steps suggested herein do not however explain the linear oxidation kinetics which is controlled by chemical reactions at the surfaces.

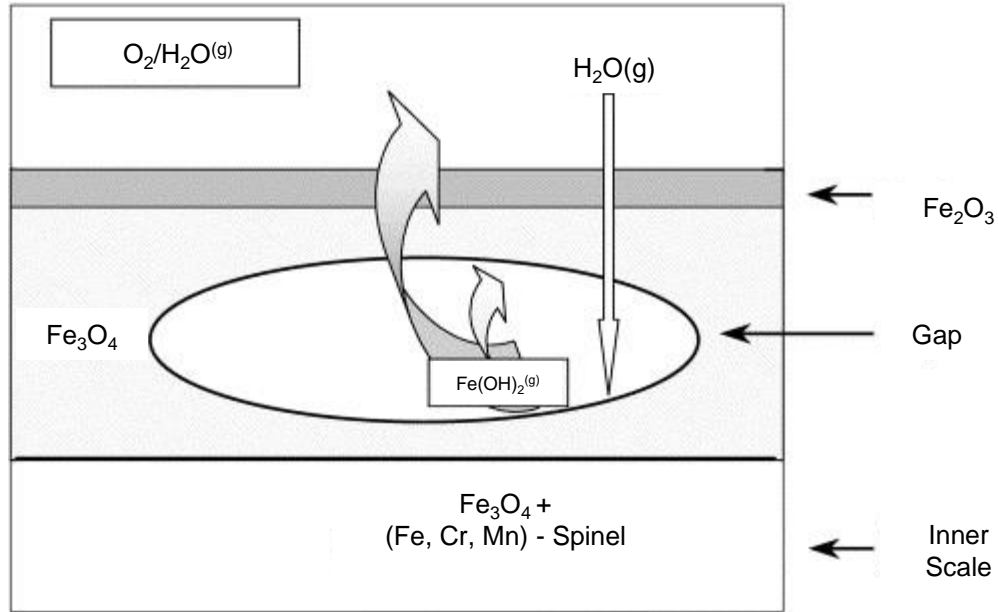


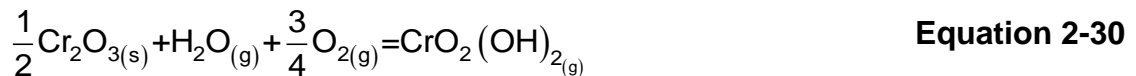
Figure 2-12. $Fe(OH)_2$ formation proposed by J. Ehlers et al.⁹⁷

2.4.5. Formation of Volatile Cr-Oxy-Hydroxides

Several authors have discussed the formation of gaseous Cr-hydroxides over a Cr_2O_3 scale and the associated effects of H_2O on this formation (volatilization) rate.^{98,99} Experimental results confirm the formation of Cr-oxide hydroxides.^{20,98,99} In addition, the aforementioned theories do not explain the volatilization mechanisms associated with the compact adherent Cr_2O_3 scales that have relatively few pores and are free of cracks. The following sections discuss the mechanism of Cr_2O_3 scale volatilization and the associated critical factors in more detail.

2.5. Cr₂O₃ Volatilization Mechanism

It is now well accepted that in the presence of H₂O and O₂ (and an appreciable gas flow rate) Cr₂O₃ reacts with the H₂O and O₂ and forms volatile oxidized Cr compounds such as CrO₂(OH), Cr(OH)₃, CrO₃, CrO(OH)₂ and CrO₂(OH)₂ that easily get carried away in the gas flow.¹⁰⁰ Thermodynamic calculations of volatile oxidized Cr compound partial pressures have shown that the most stable compound (phase) at temperatures below ~1000°C is chromium oxy-hydroxide [CrO₂(OH)₂] (**Equation 2-30**), whereas at temperatures above ~1000°C, significant formation of CrO₃ occurs.^{87,98,100}



In the research conducted as part of this thesis, experiments were carried out at temperatures below ~1000°C, therefore, the CrO₂(OH)₂ volatilization product is of particular interest. The volatilization rate of Cr₂O₃ depends on the gas temperature, pressure, velocity, and the rate of alloy Cr supply to the scale as is discussed in further detail below.^{54,66,91}

2.5.1. Effect of Temperature

Figure 2-13 shows the effect of temperature change on the equilibrium partial pressure of CrO₂(OH)₂ (pCrO₂(OH)₂).¹⁰¹ It is shown that at temperatures below

~600°C, the volatilization rate of Cr₂O₃ is relatively low. With the increase in the gas temperature however, the pCrO₂(OH)₂ increases exponentially.

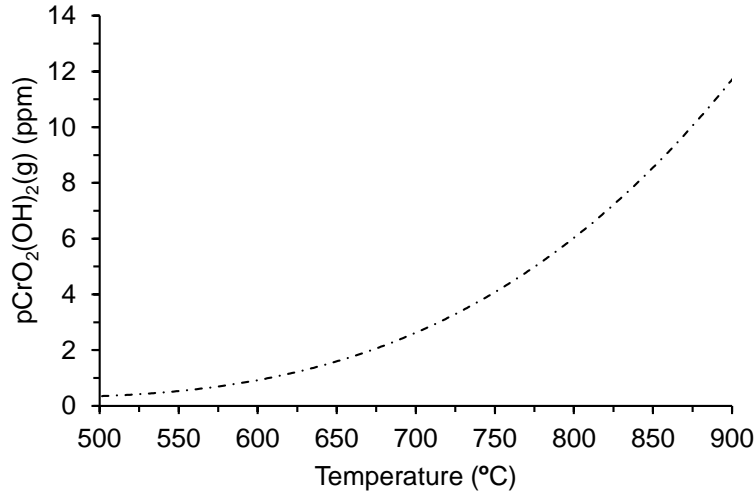


Figure 2-13. Thermodynamically calculated equilibrium pCrO₂(OH)₂ in ppm as a function of temperature (°C).¹⁰¹

2.5.2. Effect of Pressure

The ΔG° for **Equation 2-30** considering an activity of one for the solid Cr₂O₃ is:²⁰

$$\Delta G^\circ = -RT \ln \left(\frac{p_{\text{CrO}_2(\text{OH})_2}}{p_{\text{O}_2}^4 \cdot p_{\text{H}_2\text{O}}} \right) \quad \text{Equation 2-31}$$

From **Equation 2-32**, it can be seen that the pCrO₂(OH)₂ is related to the pO₂ and pH₂O in the wet gas mixture, therefore the total gas pressure. K is the temperature dependent constant in **Equation 2-32**.

$$p_{\text{CrO}_2(\text{OH})_2} = K p_{\text{O}_2}^4 \cdot p_{\text{H}_2\text{O}} \quad \text{Equation 2-32}$$

It must be noted that the $p_{\text{CrO}_2(\text{OH})_2}$ shows a power law dependence of 1 for $p_{\text{H}_2\text{O}}$ compared with $\frac{3}{4}$ for p_{O_2} . It can be concluded that the Cr_2O_3 volatilization rate at a constant temperature is strongly dependent on the volume percent of H_2O present in the wet gas mixture.²⁰

The predicted vapour pressures of $\text{CrO}_2(\text{OH})_2$ for different total steam pressures, and an air-10% H_2O mixture, are shown in **Figure 2-14** as a function of temperature. The vapour pressure of $\text{CrO}_2(\text{OH})_2$ in steam at higher pressures, e.g. 240 bar (24 MPa) or 340 bar (34 MPa) is significantly higher than that in steam at low pressure (~0.1 MPa). However, in an air-10% H_2O gas mixture, an even higher vapour pressure of $\text{CrO}_2(\text{OH})_2$ is predicted.²⁰ It has been argued that the vapor pressure of $\text{CrO}_2(\text{OH})_2$ in a low-pressure (0.1-10 MPa) air-10% H_2O gas mixture is suitable as a reasonable surrogate for high-pressure (24 or 34 MPa) steam and SCW.^{20,66,102} A limited number of studies have been done to characterize the evolution in the structure and composition of Cr_2O_3 during wet oxidation. Consequently, a detailed mechanistic description of the $\text{CrO}_2(\text{OH})_2$ formation and the role played by the underlying alloy is lacking. As mentioned above, the predicted $p_{\text{CrO}_2(\text{OH})_2}$ in a low-pressure air-10% H_2O gas mixture is similar to that predicted in high-pressure steam. However, for SCW conditions, the non-polar characteristics of SCW increases the solubility of oxy-hydroxides, which casts some doubts about the suitability of a low-pressure air-10% H_2O gas mixture as an appropriate surrogate for SCW.³⁹ The hypothesis that a low-pressure air-10% H_2O gas mixture is an appropriate surrogate for SCW is addressed by the research

conducted and presented in Chapter 4, as a full-length article submitted to **CORROSION** for publication consideration.

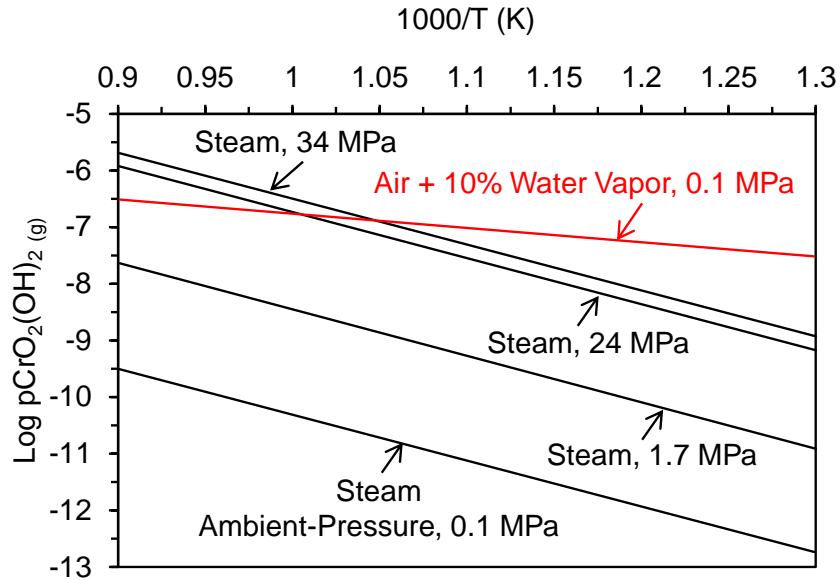


Figure 2-14. $\text{CrO}_2(\text{OH})_2$ vapour pressure-temperature diagram for different steam/air- H_2O mixture environments.²⁰

2.5.3. Effect of Gas Velocity

It is often seen that the data regarding the gas flow rate is reported in terms of the volumetric gas rate (mL/min).¹⁰³ However, with no information regarding the cross-sectional area of the gas reactor, it is not possible to compare the effect of flow rate on the oxidation in different experiments.^{39,103} The most accurate way to report the gas flow rate is to state it as the linear gas velocity (cm/s).¹⁰³ **Figure 2-15** shows the calculated Cr loss as a function of the gas velocity reproduced after C. Key et al.¹⁰³ Initially (region A), the oxidized Cr mass loss rate is quite small since the gas becomes saturated with the oxidized gaseous Cr compound. With the increase in

the flow rate (region B), the Cr mass loss rate increases linearly. The latter reaches a plateau under laminar flow conditions because of limited rate of Cr transport. With the flow transition from laminar to turbulent, (region D), even more Cr is lost due to oxide volatilization. The volatilization rate reaches a plateau in the turbulent region again (region E) and is now limited by the diffusion of Cr gas species into the turbulent flow.

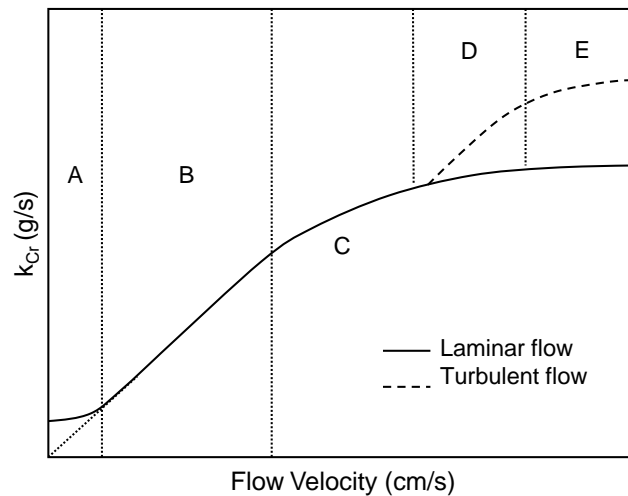


Figure 2-15. Schematic illustration of Cr mass loss rate (g/s) over Cr_2O_3 in different flow velocities reproduced after C. Key et al.¹⁰³

H. Asteman et al.⁵⁴ studied the effect of gas velocity on the wet oxidation of Type 304L stainless steel exposed in a O_2 -40% H_2O mixture at 500-800°C for 168 h. The gas velocity was varied from 0.02 cm/s to 13 cm/s. **Figure 2-16** shows a summary of their results. They argued that at 500°C, the mass change of the alloy is negligible over this range of gas velocities. They showed that at a gas velocity of ~3 cm/s the mass change at higher temperatures reaches a plateau and the oxidation becomes independent of the gas velocity.

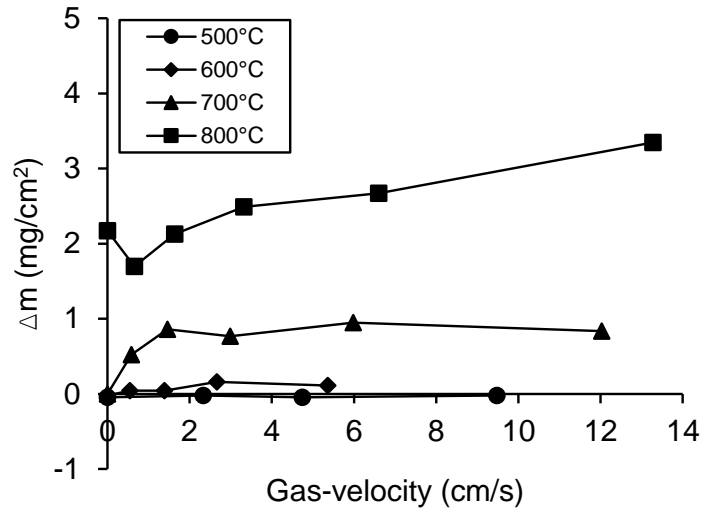


Figure 2-16. Effect of gas velocity of the weight change of Type 304L stainless steel exposed in a O₂ - 40% H₂O mixture for 168 h, after H. Asteman et al.⁵⁴

D. Young and B. Pint⁶⁶ argued that the ratio of velocity (v) over sample length (l) used in laboratory tests are much smaller than the actual values used for example, in recuperator. They showed that even though the flux of oxidized Cr lost to volatilization increases with temperature (**Figure 2-17**) regardless of the flow velocities, values reported in the laboratories are often much smaller than those expected in high-temperature applications. This implies that volatilization of the Cr₂O₃ scale is a very important concern that needs to be fully studied when examining structural alloys used in high-temperatures wet environments.

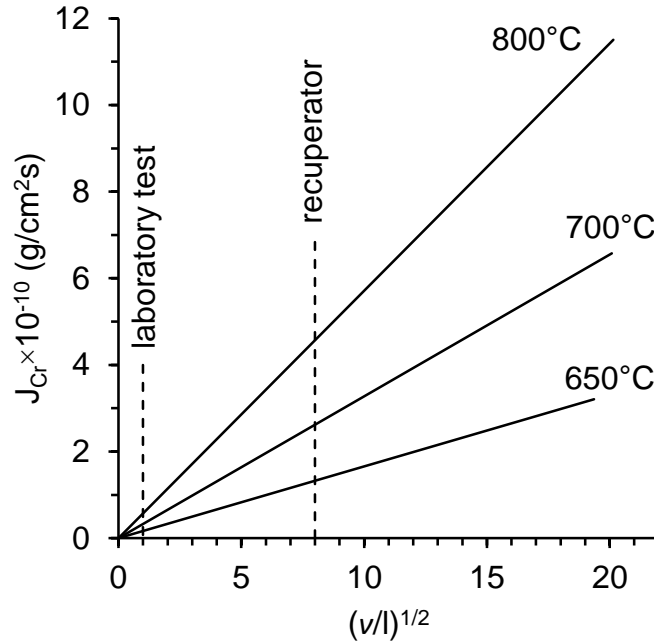


Figure 2-17. Calculated Cr loss fluxes as a function of $(v/l)^{1/2}$ for air + 5% H₂O at 650–800°C. Dashed lines mark conditions in the laboratory test compared to the approximate conditions in a micro turbine recuperator, after D. Young and B. Pint.⁶⁶

2.5.4. Effect of Alloy Cr Supply Rate

For the Cr₂O₃ to maintain its protectiveness (structure and composition), the rate of Cr supply from the alloy to the scale must be sufficiently high to offset oxidized Cr loss due to volatilization. If the Cr supply rate from the alloy is relatively small, or there is not enough Cr in the alloy to compensate for the Cr lost during scale volatilization, Fe present at the alloy/oxide interface diffuses through the vacant lattice sites of Cr in the oxide scale and changes the Cr/Fe ratio, which results in the formation of a less protective, more Fe-rich, Cr₂O₃ scale. Continuous Fe diffusion into a Cr depleted Cr₂O₃ scale can either result in the scale breakaway and formation of Fe-rich oxide nodules and/or eventually formation of a less-

protective porous Fe₂O₃ scale (**Equation 2-33**).⁵⁴ Fe₂O₃ is known to be less-protective than Cr₂O₃ as ionic diffusion rates through this oxide are typically much higher than that in Cr₂O₃.⁵⁴ Formation of Fe₂O₃ is therefore not desirable from the oxidation resistance perspective of the alloy.

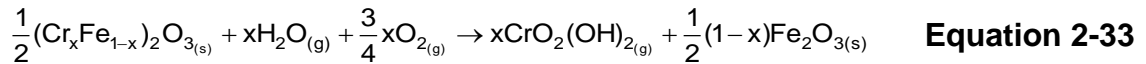


Figure 2-18 shows a schematic of oxide scale transformation for the low Cr-containing Alloy X20 (12 wt.% Cr) and high Cr-containing Types 304L and 310S stainless steels (18 wt.% and 24 wt.% Cr, respectively). As discussed above, volatilization of Cr₂O₃ results in diffusion of Fe into the scale and accelerated formation of Fe-rich oxides as a result of oxidized Cr volatilization (breakaway kinetics). As a result, further scale protectiveness relies on the Cr supply rate from the alloy to the scale.

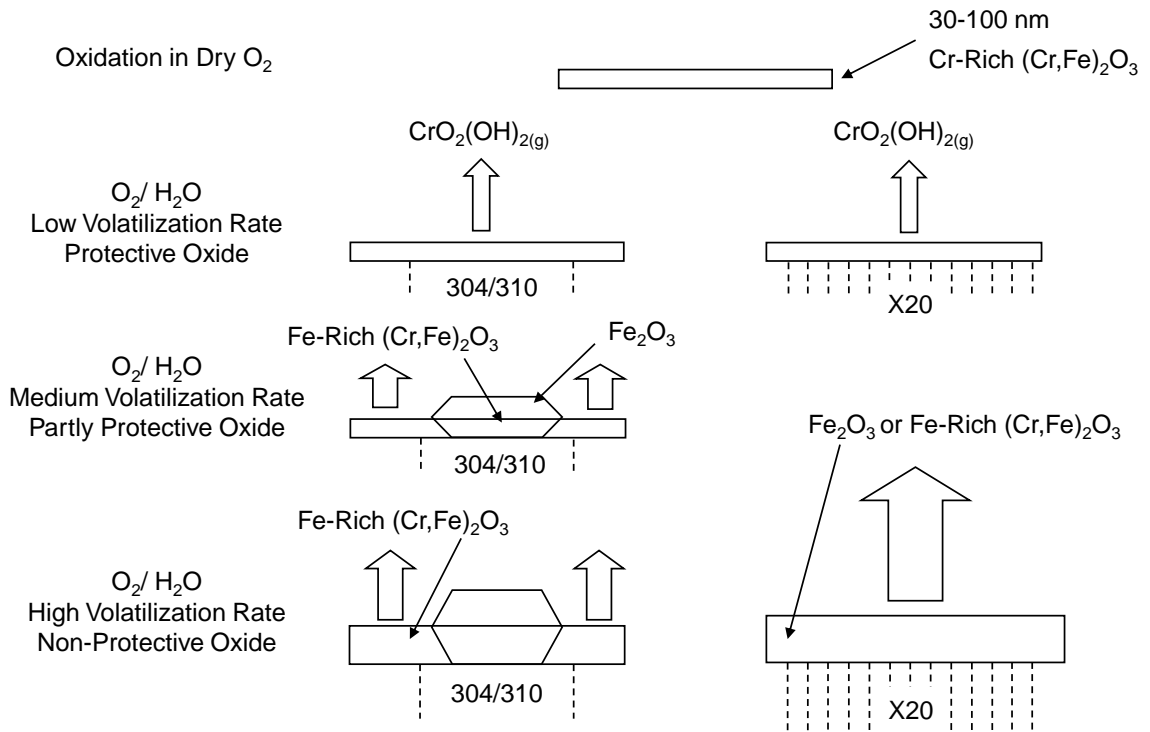


Figure 2-18. Schematic illustration of oxidation of Type 304/310 and Alloy X20 after 168 h exposure in O_2/H_2O .¹⁰⁴

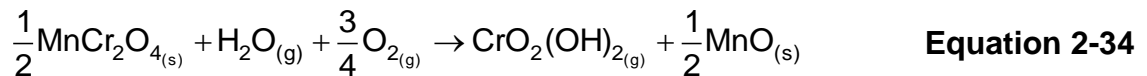
It must be pointed out that factors such as residual surface stress and structural changes to the subsurface grain size from cold working have large impacts on the rate of Cr supply from the alloy to the scale.³⁹ The surface finish prior to oxidation testing therefore has paramount importance influencing the oxidation kinetics. In this thesis, the surface finish is kept at 400-800 grit SiC. These relatively rough surface finishes have been suggested by the Canadian Gen IV International Forum for studying the SCW oxidation of alloys as it has been shown that surface finishes resulting in severe cold work reduce the oxidation rate in SCW.³⁹

2.5.5. Effect of Minor Alloying elements

Other than Cr₂O₃ and Fe₂O₃, oxides that can form as reaction products involved in the wet oxidation of stainless steel which are relevant to this thesis are Mn-rich and Si-rich oxides. Due to very low diffusivity of Ni in Cr₂O₃, it is often observed that Ni is enriched at the alloy/oxide interface and does not incorporate into the oxide scale.^{58,94,105,106} This sub-section focuses on the formation of Mn-rich and Si-rich oxides during wet oxidation and discusses their roles on protecting Cr₂O₃ against volatilization.

2.5.5.1. Mn Effects

The role of Mn in the wet oxidation performance of stainless steel is often overlooked due to its relatively small concentration in the alloy. Mn has relatively high diffusivity in Cr₂O₃ scale and, thus, is readily found to be present in the oxide scales formed.³² This rapid diffusion of Mn typically results in the formation of a Mn spinel (MnCr₂O₄) oxide layer (cap) on top of Cr₂O₃.^{1,32,53} However, this phase is still susceptible to oxidized Cr loss due to volatilization (**Equation 2-34**). From **Equation 2-34**, MnCr₂O₄ volatilization leaves behind a MnO product, which can further oxidize into other types of Mn-rich oxides namely Mn₂O₃ and Mn₃O₄.¹⁰⁷



The maximum volatilization rate (g/cm²/s) of Cr₂O₃ or MnCr₂O₄ has been approximated using **Equation 2-35** where p is the vapour pressure of the gas species, M is the molecular mass of the vapour species (g/mol) and T is the

temperature (K).¹⁰⁷ **Equation 2-35** is reported to provide a reasonable estimate of the maximum Cr loss rate from each layer.¹⁰⁷

$$\text{Evaporation} \left(\frac{\text{g}}{\text{cm}^2 \text{s}} \right) = 44.33p \sqrt{\frac{M}{T}} \quad \text{Equation 2-35}$$

Figure 2-19 shows the calculated maximum Cr loss rate from Cr_2O_3 and MnCr_2O_4 as a function of temperature for exposure in an air-3% H_2O mixture.¹⁰⁷ The square data points in the graph were determined experimentally. It has been shown that the presence of a MnCr_2O_4 cap on top of Cr_2O_3 decreases the surface contact area between Cr_2O_3 with the wet gas mixture. This serves to reduce the rate of Cr loss due to oxide volatilization. In addition, as shown in **Figure 2-19**, the rate of Cr loss from MnCr_2O_4 is less than that from Cr_2O_3 by a factor of 35 at 800°C .

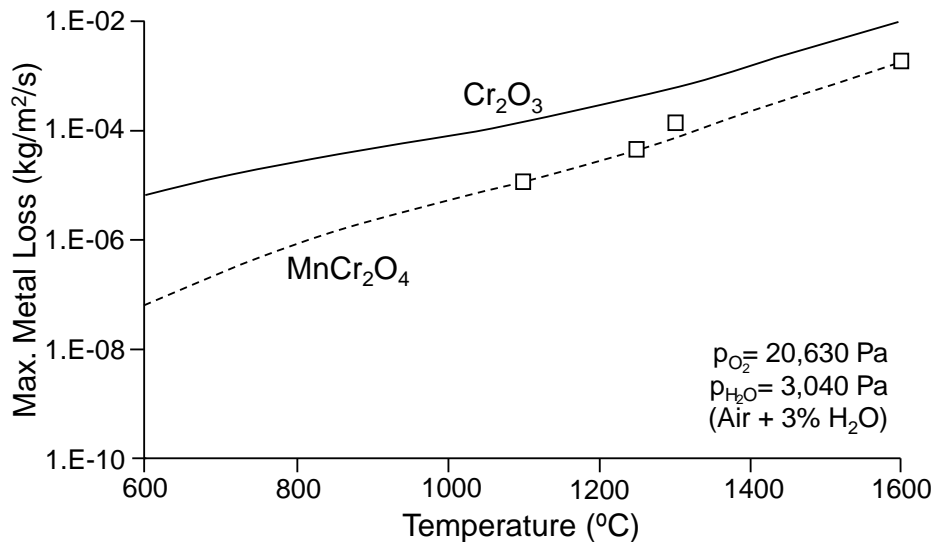


Figure 2-19. Maximum metal loss calculated based on Ebbingham's data.¹⁰⁷

Figure 2-20 illustrates a physical description of Cr loss due to volatilization from MnCr_2O_4 that has been prepared based on thermodynamic predictions and previously published articles. When the volatilization rate is quite small (e.g. relatively small $p\text{O}_2$ or shorter exposure times), the MnCr_2O_4 remains intact and adherent with almost negligible Cr loss from the scale.¹⁰⁷ With the increase in the scale volatilization rate, the MnCr_2O_4 layer tends to form a Cr-free or Cr-lean, Mn-rich oxide.⁶¹ This reaction may not occur continuously on the surface, as it is generally observed to initiate locally.⁶² For the relatively high scale volatilization rates, the transformation of MnCr_2O_4 into a Mn-rich oxide occurs at a faster rate and Cr loss continues from the underlying Cr_2O_3 scale resulting in the formation of a mixed layer rich in Fe (**Equation 2-33**). It follows then that the volatilization susceptibility of a MnCr_2O_4 cap formed on Cr_2O_3 likely plays a key role in controlling the wet oxidation performance of stainless steel. This hypothesis is addressed by the research conducted and presented in Chapter 6, as a full-length article submitted to **Corrosion Science** for publication consideration.

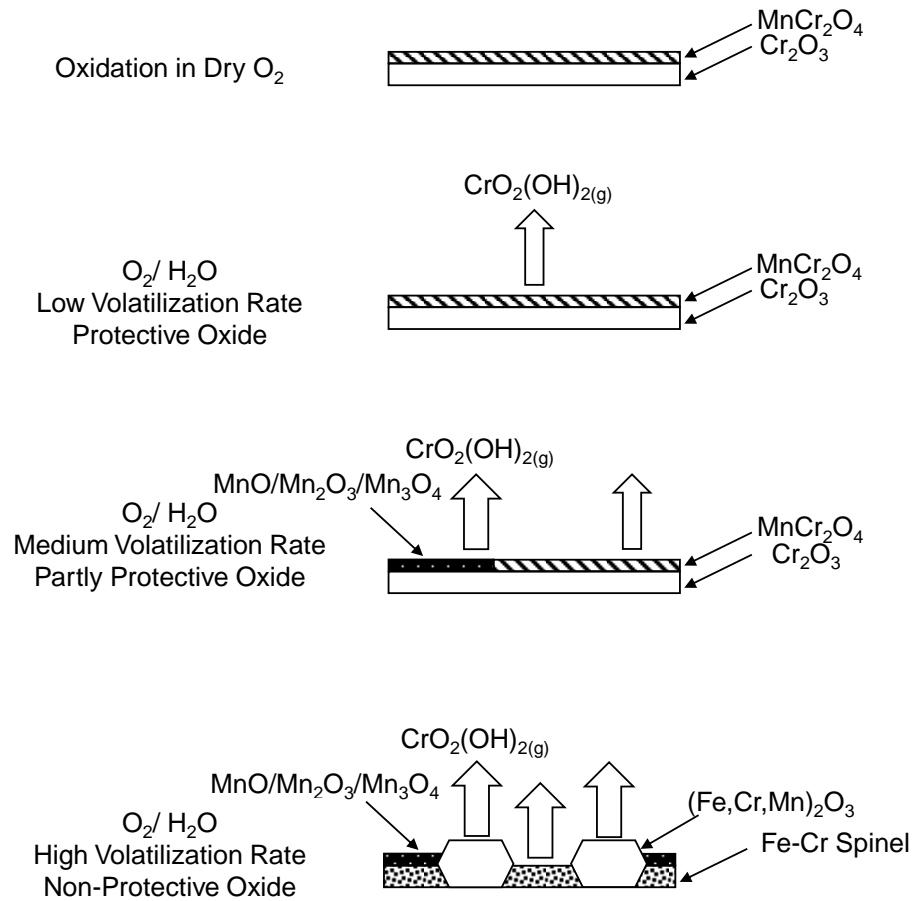


Figure 2-20. Physical description of the $MnCr_2O_4$ scale volatilization.

2.5.5.2. Si Effects

Si in the austenitic Fe-Cr-Ni alloys is shown to be beneficial from a wet oxidation performance perspective.^{108,109} It has been argued that a SiO_2 barrier layer forms below Cr_2O_3 and serves to decrease ionic diffusion, which in turn serves to reduce the overall alloy oxidation rate, albeit in the parabolic oxidation stage.¹¹⁰ The amorphous structure of the SiO_2 layer is the reason it is considered an effective barrier layer.¹¹¹ The amorphous SiO_2 layer lacks grain boundaries responsible for the increase in the outward diffusion rate of cations through the scale.¹¹⁰ The

formation of a continuous SiO_2 layer, rather than a discontinuous layer (precipitates), depends on the alloy Si content and the oxidizing temperature and pressure.¹¹² **Figure 2-21** shows the mechanism of SiO_2 scale formation in dry O_2 . It is shown that when the Si concentration is relatively low, or at low temperatures and low $p\text{O}_2$, SiO_2 forms as precipitates on grain boundaries.¹¹³ At higher temperatures and oxygen partial pressures and/or with higher amounts of Si, SiO_2 forms laterally as a continuous layer underneath Cr_2O_3 .¹¹³ The effect of Si addition on the volatilization tendency of the Cr_2O_3 formed on austenitic stainless steels exposed in steam or air- H_2O mixtures has not been reported in any detail. Given the relatively lower diffusion rate of cations through the SiO_2 layer, it follows that a uniform SiO_2 layer, if formed, would decrease the overall alloy oxidation rate, but any influence of a uniform SiO_2 layer on the onset of linear oxidation as governed by the parabolic rate law needs to be further examined. The Cr diffusion rate has been shown to increase in the alloys containing higher Si content. B. Li et al.¹¹⁰ examined the average effective interdiffusion coefficients of Cr in a set of cast alloys after 7 days of isothermal air oxidation at 1000°C (**Figure 2-22**). They showed that the addition of Si increases the Cr supply rate from the alloy to the alloy/oxide interface serving to maintain the structure and composition of the Cr_2O_3 scale. The effects of Si addition on the high-temperature wet oxidation behaviour of Cr_2O_3 -forming alloys, and in particular its effects on breakaway kinetics has not been well studied until now. It follows that a lower diffusion rate through a SiO_2 layer would affect the onset of linear kinetics that is dictated by the balance

between the parabolic and volatilization terms. Further investigation into whether or not the addition of Si would have any effect on Cr_2O_3 volatilization whatsoever, given the supposedly relatively higher Cr supply rate of the substrate in high Si-containing stainless steel, needs further investigation. This hypothesis is addressed by the research conducted and presented in Chapter 7, as a full-length article submitted to **Corrosion Science** for publication consideration.

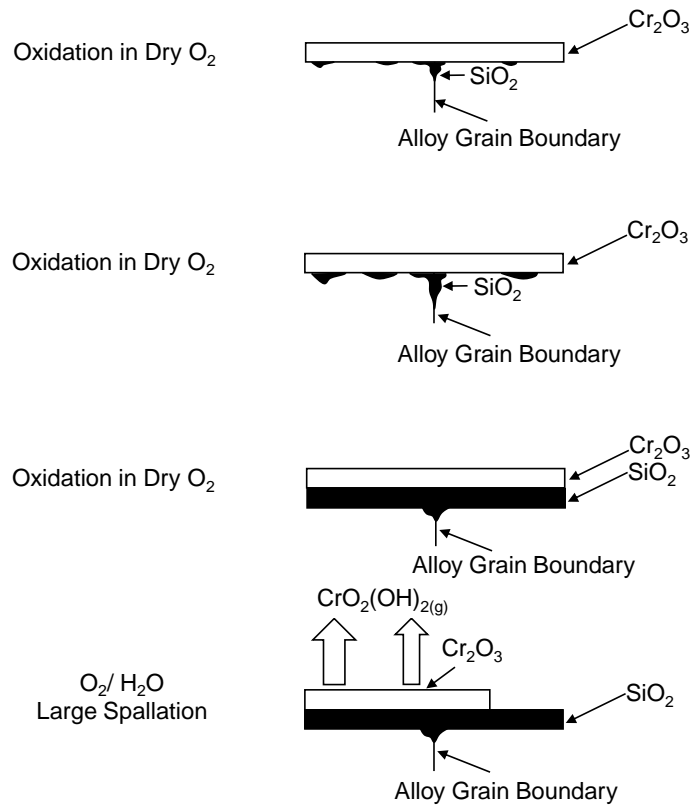


Figure 2-21. Physical description of the Cr_2O_3 volatilization in the presence of SiO_2 .

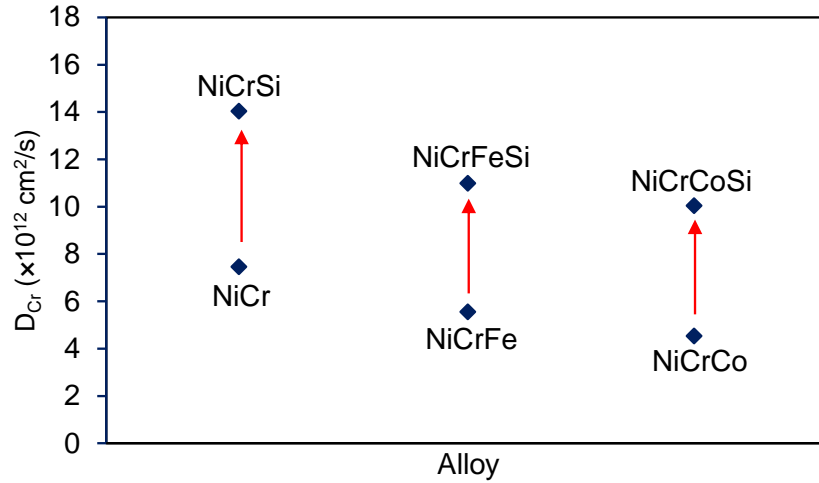


Figure 2-22. Comparison of the average effective interdiffusion coefficients of Cr in the cast alloys after 7 days isothermal air oxidation at 1000°C.¹¹⁰

2.6. References

1. M.J. Garcia-Vargas, L. Lelait, V. Kolarik, H. Fietzek, and M.D.M. Juez-Lorenzo, *Mater. High Temp.* 22 (2005): pp. 245–251.
2. G.R. Holcomb, *J. Electrochem. Soc.* 156 (2009): p. C292.
3. S. Ghali, M. Eissa, and H. El-Faramawy, *Int. J. Stat. Math.* 1 (2014): pp. 24–32.
4. M.I. Sahri, N.K. Othman, Z. Samsu, and A.R. Daud, “Investigation of High Temperature Corrosion Behavior on 304L Austenite Stainless Steel in Corrosive Environments,” *AIP Conf. Proc.* 1614 (2014), pp. 152–157.
5. P. Kofstad, *Mater. Sci. Forum* 154 (1994): pp. 99–108.
6. H.S. Woo, C.W. Na, I.D. Kim, and J.H. Lee, *Nanotechnology* 23 (2012): pp. 1–10.
7. S. Pokhrel, C.E. Simion, V. Quemener, N. Bârsan, and U. Weimar, *Sensors Actuators B* 133 (2008): pp. 78–83.
8. C. Engineering, V. Samsonov, T.O. Handbook, L. Messing, and D. Kingery, *J. Am. Ceram. Soc.* 67 (1984): pp. 111–112.
9. J.A. Crawford, and R.W. Vest, *J. Appl. Phys.* 35 2413 (2014): pp. 2413–2418.

10. J.H. Kim, D.I. Kim, S. Suwas, E. Fleury, and K.W. Yi, *Oxid. Met.* 79 (2013): pp. 239–247.
11. Y. Behnamian, A. Mostafaei, A. Kohandehghan, B.S. Amirkhiz, D. Serate, W. Zheng, D. Guzonas, M. Chmielus, W. Chen, and J.L. Luo, *Mater. Charact.* 120 (2016): pp. 273–284.
12. I. Saeki, Y. Sugiyama, S. Hayashi, A. Yamauchi, T. Doi, Y. Nishiyama, S. Kyo, S. Suzuki, M. Sato, and S. Fujimoto, *Corros. Sci.* 55 (2012): pp. 219–225.
13. L. Mikkelsen, P.H. Larsen, and S. Linderoth, *J. Therm. Anal. Calorim.* 64 (2001): pp. 879–886.
14. L. Jinlong, and L. Hongyun, *Appl. Surf. Sci.* 263 (2012): pp. 29–37.
15. G.A. Acket, and J. Volger, *Physica* 32 (1966): pp. 1543–1550.
16. H.K. Mulmudi, N. Mathews, X.C. Dou, L.F. Xi, S.S. Pramana, Y.M. Lam, and S.G. Mhaisalkar, *Electrochem. Commun.* 13 (2011): pp. 951–954.
17. B.A. Pint, O. Ridge, E.L. Oak, and R. National, *Eng. Issues Turbine Mach. Power Plants Renewables*, Inst. Mater. Miner. Mining, Maney Publ. London, UK (2003): pp. 1057–1073.
18. X. Peng, J. Yan, Y. Zhou, and F. Wang, *Acta Mater.* 53 (2005): pp. 5079–5088.
19. R. Klinger, J. Ensling, H. Jachow, W. Meisel, and E. Schwab, *J. Magn. Magn. Mater.* 150 (1995): pp. 277–283.
20. I.G. Wright, and R.B. Dooley, *Int. Mater. Rev.* 55 (2010): pp. 129–167.
21. D.R. Gaskell, *Introduction to the Thermodynamics of Materials* (Taylor and Francis, 2008).
22. N. Otsuka, Y. Shida, and H. Fujikawa, *Oxid. Met.* 32 (1989): pp. 13–45.
23. C.T. Sims, N.S. Stoloff, and W.C. Hagel, *Superalloys II; High Temperature Materials for Aerospace and Industrial Power*, John Wiley and Sons (1987).
24. C. Wagner, and B. Bunsenges, *Phys. Chem.* 63 (1959): pp. 772–776.

25. N. Birks, G.H. Meier, and F.S. Pettit, *Introduction to the High-Temperature Oxidation of Metals*, 2nd Edition, Cambridge University Press, Technology and Engineering (2006).
26. A.C.S. Sabioni, A.M. Huntz, F. Silva, and F. Jomard, *Mater. Sci. Eng. A* 392 (2005): pp. 254–261.
27. Y. He, J. Ma, Z. Li, and W. Gao, *Mater. Science Forum* 522–523 (2006): pp. 45–52.
28. V.V. Khokhlov, A.G. Rakoch, E.S. Dement, and O.A. Lyzlov, 40 (2004): pp. 62–66.
29. R. Peraldi, and B.A. Pint, *Oxid. Met.* 61 (2004): pp. 463–483.
30. A. Stability, N. Steel, and I.W.H. Zones, *J. Phys. F Met. Phys.* 10 (1980): pp. 383–398.
31. Z. Tókei, K. Hennesen, H. Viehhaus, and H.J. Grabke, *Mater. Sci. Technol.* 16 (2000): pp. 1129–1138.
32. A.C.S. Sabioni, A.M. Huntz, L.C. Borges, and F. Jomard, *Philos. Mag.* 87 (2007): pp. 1921–1937.
33. R.E. Lobnig, H.P. Schmidt, K. Hennesen, and H.J. Grabke, *Oxid. Met.* 37 (1992): pp. 81–93.
34. A.C.S. Sabioni, J.N. V Souza, V. Ji, F. Jomard, V.B. Trindade, and J.F. Carneiro, *Solid State Ionics* 276 (2015): pp. 1–8.
35. T. Sundararajan, S. Kuroda, K. Nishida, T. Itagaki, and F. Abe, *ISIJ Int.* 44 (2004): pp. 139–144.
36. K. Hoshino, and N.L. Peterson, *Commun. Am. Ceram.* (1983): pp. 202–203.
37. P.E. Savage, and C. Rearrangements, *Chem. Rev.* 99 (1999): pp. 603–621.
38. S. Mahboubi, “Effect of Cr content on corrosion resistance of Fe-Cr-Ni alloys exposed in supercritical water (SCW)”, McMaster University (2014).
39. D.A. Guzonas, and W.G. Cook, *Corros. Sci.* 65 (2012): pp. 48–66.

40. T. Schulenberg, L.K.H. Leung, D. Brady, Y. Oka, K. Yamada, and Y. Bae, "Supercritical Water-Cooled Reactor (SCWR) Development through GIF Collaboration," IAEA-CN-164-5S06 (2005).
41. Y. Oka, and S. Koshizuka, Nucl. Technol. 103 (1993): pp. 295–302.
42. M. Nezakat, H. Akhiani, S. Penttilä, and J. Szpunar, J. Nucl. Eng. Radiat. Sci. 2 (2016): pp. 1-8.
43. A.T. Motta, A. Yilmazbayhan, M.J.G. da Silva, R.J. Comstock, G.S. Was, J.T. Busby, E. Gartner, Q. Peng, Y.H. Jeong, and J.Y. Park, J. Nucl. Mater. 371 (2007): pp. 61–75.
44. E.F. Gloyna, L. L., and R.N. McBrayer, Wat. Sci. Tech. 30 (1994): pp. 1–10.
45. D. Bröll, C. Kaul, A. Krämer, P. Krammer, T. Richter, M. Jung, H. Vogel, and P. Zehner, Angew. Chem. Int. Ed. 38 (1999): pp. 2998–3014.
46. Machine Application Corporation, "The Humidity/Moisture Handbook" (Machine Applications Corporation).
47. K. Matsui, A. Ogawa, J. Kikuma, M. Tsunashima, T. Ishikawa, and S. Matsuno, Denver X-Ray Conf. Appl. X-Ray Anal. (1999): pp. 170–178.
48. F.P. Fehlner, and N.F. Mott, Oxid. Met. 2 (1970): pp. 59–99.
49. M. Stern, J. Electrochem. Soc. 106 (1959): pp. 376–381.
50. H.T. Abuluwefa, "Kinetics of High Temperature Oxidation of High Carbon Steels in Multi-Component Gases Approximating Industrial Steel Reheat Furnace Atmospheres," Int. Multiconference Eng. Comput. Sci. (2012), pp. 1–5.
51. C. Wagner, Trans. Faraday Soc. 34 (1938): pp. 851–859.
52. H.E. Evans, Int. Mater. Rev. 40 (1995): pp. 1–40.
53. T. Dudziak, V. Deodeshmukh, L. Backert, N. Sobczak, M. Witkowska, W. Ratuszek, K. Chruściel, A. Zieliński, J. Sobczak, and G. Bruzda, Oxid. Met. 87 (2017): pp. 139–158.
54. H. Asteman, J. Svensson, M. Norell, and L. Johansson, Oxid. Met. 54 (2000): pp. 11–26.

55. K. Segerdahl, J.E. Svensson, M. Halvarsson, I. Panas, and L.G. Johansson, *Mater. High Temp.* 22 (2005): pp. 69–78.
56. X. Cheng, Z. Jiang, B.J. Monaghan, D. Wei, R.J. Longbottom, J. Zhao, J. Peng, M. Luo, L. Ma, S. Luo, and L. Jiang, *Corros. Sci.* 108 (2016): pp. 11–22.
57. H. Ebrahimifar, and M. Zandrahimi, *Indian J. Eng. Mater. Sci.* 18 (2011): pp. 314–320.
58. S. Mahboubi, Y. Jiao, W. Cook, W. Zheng, D.A. Guzonas, G.A. Botton, and J.R. Kish, *Corrosion* 72 (2016): pp. 1170–1180.
59. E.J. Opila, *Journal Am. Ceram. Soc.* 80 (1997): pp. 197–205.
60. B. Pujilaksono, T. Jonsson, M. Halvarsson, I. Panas, J.E. Svensson, and L.G. Johansson, *Oxid. Met.* 70 (2008): pp. 163–188.
61. S. Mahboubi, H.S. Zurob, G.A. Botton, and J.R. Kish, *Can. Metall. Q.* 57 (2018): pp. 89–98.
62. S. Mahboubi, H.S. Zurob, G.A. Botton, and J.R. Kish, “Temperature Effect on the Wet Oxidation Performance of Type 310S Stainless Steel”, Submitted to *Corros. Sci.* (2018)
63. H. Hooshyar, T. Jonsson, J. Hall, J.E. Svensson, L.G. Johansson, and J. Liske, *Oxid. Met.* 85 (2016): pp. 321–342.
64. H.F. Windisch, “Cr Vaporization and Oxide Scale Growth on Interconnects in Solid Oxide Fuel Cells,” Chalmers University of Technology (2015).
65. E.J. Opila, *J. Am. Ceram. Soc.* 86 (2003): pp. 1238–1248.
66. D.J. Young, and B.A. Pint, *Oxid. Met.* 66 (2006): pp. 137–153.
67. Y. Liu, and D.Y. Chen, *Int. J. Hydrogen Energy* 34 (2009): pp. 9220–9226.
68. L.L. Liu, Q.Q. Guo, S. Liu, C.S. Ni, and Y. Niu, *Corros. Sci.* 98 (2015): pp. 507–515.
69. S. Mahboubi, S., H.S. Zurob, G.A. Botton, and J.R. Kish, “Silicon Effects on the Wet Oxidation of Type 310S Stainless Steel”, *Submitt. to Corros. Sci.* (2018).

70. H.E. Evans, and R.C. Lobb, *Corros. Sci.* 24 (1984): pp. 209–222.
71. L. Antoni, J. Mougín, A. Galerie, M. Dupeux, N. Rosman, G. Lucazeau, and A.M. Huntz, *Mater. Corros.* 53 (2002): pp. 486–490.
72. S. Gray, K. Berriche-Bouhanek, and H.E. Evans, *Mater. Sci. Forum* 461 (2004): pp. 755–764.
73. M. Martena, D. Botto, P. Fino, S. Sabbadini, M.M. Gola, and C. Badini, *Eng. Fail. Anal.* 13 (2006): pp. 409–426.
74. P.F. Tortorelli, E.D. Specht, K.L. More, and P.Y. Hou, *Mater. Corros.* 63 (2012): pp. 857–861.
75. J.W. Fergus, C.J. Dileep Kumar, Y. Liu, W. Tilson, A. Dekich, and H. Wang, *ECS Trans.* 50 (2013): pp. 117–126.
76. C. Xu, and W. Gao, *Mater. Res. Innov.* 3 (2000): pp. 231–235.
77. B.J. Spencer, P.W. Voorhees, and J. Tersoff, *Phys. Rev. B - Condens. Matter Mater. Phys.* 64 (2001): pp. 1-31.
78. F.A. Golightly, F.H. Stott, and G.C. Wood, *J. Electrochem. Soc.* 126 (1979): pp. 1035–1042.
79. D.R. Clarke, *Acta Mater.* 51 (2003): pp. 1393–1407.
80. F.N. Rhines, and J.S. Wolf, *Metall. Trans.* 1 (1970): pp. 1701–1710.
81. H. Echsler, E.A. Martinez, L. Singheiser, and W.J. Quadackers, *Mater. Sci. Eng. A* 384 (2004): pp. 1–11.
82. E. Kobeda, *J. Vac. Sci. Technol. B Microelectron. Nanom. Struct.* 4 (1986): pp. 720–722.
83. B. Gleeson, *Oxid. Met.* 49 (1998): pp. 373–399.
84. L. Sun, Q. Zhao, J. Xiang, J. Shi, L. Wang, S. Hu, and S. Su, *J. Cent. Wouth Univ. Technol.* 16 (2009): pp. 0535–0540.
85. B. Kuhn, F.J. Wetzels, J. Malzbender, R.W. Steinbrech, and L. Singheiser, *J. Power Sources* 193 (2009): pp. 199–202.

86. G.H. Meier, M.J. Stiger, J.R. Blachere, F.S. Pettit, C. Sarioglu, R. Janakiraman, E. Schumann, and A. Ashary, *Werkstoffe Und Korrosion* 51 (2000): pp. 358–372.
87. T. Jonsson, S. Canovic, F. Liu, H. Asteman, J.E. Svensson, L.G. Johansson, and M. Halvarsson, *Mater. High Temp.* 22 (2005): pp. 231–243.
88. T. Jonsson, S. Karlsson, H. Hooshyar, M. Sattari, J. Liske, J.E. Svensson, and L.G. Johansson, *Oxid. Met.* 85 (2016): pp. 509–536.
89. J. Zhang, X. Peng, D.J. Young, and F. Wang, *Surf. Coatings Technol.* 217 (2013): pp. 162–171.
90. E. Essuman, G.H. Meier, J. Zurek, M. Hänsel, L. Singheiser, and W.J. Quadackers, *Scr. Mater.* 57 (2007): pp. 845–848.
91. D.J. Young, *Mater. Sci. Forum* 595–598 (2008): pp. 1189–1197.
92. C.T. Fujii, and R.A. Meussner, *J. Electrochem. Soc.* 111 (1964): pp. 1215–1220.
93. A. Fry, S. Osgerby, and M. Wright, *NPL Rep. MATC 90* (2002): pp. 1–39.
94. S. Mahboubi, G.A. Botton, and J.R. Kish, *Corrosion* 71 (2015): pp. 992–1002.
95. A. Galerie, Y. Wouters, and M. Caillet, *Mater. Sci. Forum* 369–372 (2001): pp. 231–238.
96. D. Abriou, and J. Jupille, *Surf. Sci.* 430 (1999): pp. 527–532.
97. J. Ehlers, D.J. Young, E.J. Smaardijk, A.K. Tyagi, H.J. Penkalla, L. Singheiser, and W.J. Quadackers, *Corros. Sci.* 48 (2006): pp. 3428–3454.
98. P. Berthod, *Oxid. Met.* 64 (2005): pp. 235–252.
99. F.-W., Hannes, J. E. Svensson, and J. Froitzheim. *J. Power Sources* 287 (2015): pp. 25–35.
100. B.B. Ebbinghaus, *Combust. Flame* 93 (1993): pp. 119–137.
101. H. Asteman, Svensson, J.-E., and L.-G. Johansson, *Corros. Sci.* 44 (2002): pp. 2635–2649.

102. S. Mahboubi, H.S. Zurob, G.A. Botton, and J.R. Kish, "Environment Effects on the Stability of Chromia (Cr_2O_3)-Based Scale Formed on Type 310S Stainless Steel during Wet Oxidation", Submitt. to Corros. (2018).
103. C. Key, J. Eziashi, J. Froitzheim, R. Amendola, R. Smith, and P. Gannon, J. Electrochem. Soc. 161 (2014): pp. C373–C381.
104. H. Asteman, K. Segerdahl, J.E. Svensson, and L.G. Johansson, Mater. Sci. Forum 369–372 (2001): pp. 277–286.
105. Y. Behnamian, A. Mostafaei, A. Kohandehghan, B.S. Amirkhiz, D. Serate, Y. Sun, S. Liu, E. Aghaie, Y. Zeng, M. Chmielus, W. Zheng, D. Guzonas, W. Chen, and J.L. Luo, Corros. Sci. 106 (2016): pp. 188–207.
106. Y. Behnamian, A. Mostafaei, A. Kohandehghan, B.S. Amirkhiz, D. Serate, W. Zheng, D. Guzonas, M. Chmielus, W. Chen, and J.L. Luo, Mater. Charact. 120 (2016): pp. 273–284.
107. G.R. Holcomb, and D.E. Alman, Scr. Mater. 54 (2006): pp. 1821–1825.
108. B.A. Pint, R. Peraldi, and P.J. Maziasz, Mater. Sci. Forum 461–464 (2004): pp. 815–822.
109. J.S. Dunning, D.E. Alman, and J.C. Rawers, Oxid. Met. 57 (2002): pp. 409–425.
110. B. Li, and B. Gleeson, Oxid. Met. 65 (2006): pp. 101–122.
111. K. Schulmeister, and W. Mader, J. Non. Cryst. Solids 320 (2003): pp. 143–150.
112. D.L. Douglass, and J.S. Armijo, Oxid. Met. 2 (1970): pp. 207–231.
113. F.H. Stott, and F.I. Wei, Oxid. Met. 31 (1989): pp. 369–391.

3. Stability of Chromia (Cr₂O₃)-Based Scales Formed During Corrosion of Austenitic Fe-Cr-Ni Alloys in Flowing Oxygenated Supercritical Water

S. Mahboubi,^{‡*} Y. Jiao,^{*} W. Cook,^{**} W. Zheng,^{***} D.A. Guzonas,^{****} G.A. Botton,^{*}
and J.R. Kish^{*}

Submitted for publication: December 1, 2015. Revised and accepted: May 10, 2016. Preprint available online: May 10, 2016, <http://dx.doi.org/10.5006/1982>.

[‡]Corresponding author. E-mail: mahbos@mcmaster.ca.

^{*}Department of Materials Science and Engineering, McMaster University,
Hamilton, ON, Canada.

^{**}Department of Chemical Engineering, University of New Brunswick, Fredericton,
NB, Canada.

^{***}CanmetMATERIALS, Hamilton, ON, Canada.

^{****}Canadian Nuclear Laboratories, Chalk River, ON, Canada.

3.1. Abstract

The comparative corrosion resistance of two high-chromium austenitic Fe-Cr-Ni alloys, namely Type 310S stainless steel (UNS S31008) and Alloy 33 (UNS R20033), was examined after exposure in supercritical water (25 MPa and 550°C), using a flow-loop autoclave testing facility operated at a flow rate of 200 mL/min. Electron microscopy techniques were used to determine links between the composition and structure of the Cr₂O₃-based oxide scale formed on both alloys and the difference in corrosion resistance observed. The weight change kinetics was distinctly different: progressively positive (weight gain) for Type 310S stainless steel and progressively negative (weight loss) for Alloy 33. The descaled weight loss was lower for Alloy 33, indicating improved corrosion resistance. This improved corrosion resistance was attributed to the improved stability of the Cr₂O₃-based scale that formed on Alloy 33 despite the negative weight change kinetics. The suitability of these alloys as candidate fuel cladding for the Generation IV supercritical water-cooled reactor concept is discussed in light of the findings presented.

Keywords: Alloy 33, corrosion resistance, Cr₂O₃-based oxide scale, oxide, supercritical water, Type 310S stainless steel

3.2. Introduction

The supercritical water-cooled reactor (SCWR) is one of the six Generation IV International Forum's nuclear reactor design concepts under development by the European Union, Japan, Russia, China, and Canada.¹⁻⁵ The inlet coolant (subcritical water) temperature in the various SCWR concepts ranges from 280°C to 350°C (at 25 MPa), whereas the outlet coolant (supercritical water [SCW]) temperature ranges from 500°C to 625°C (at 25 MPa).⁶⁻⁹ In order to produce a SCW of such high temperature, the peak fuel cladding temperature can be as high as 800°C.⁷ Therefore, selection of a suitable fuel cladding material to withstand this high-temperature SCW environment is a challenge, notwithstanding irradiation damage tolerance requirements.

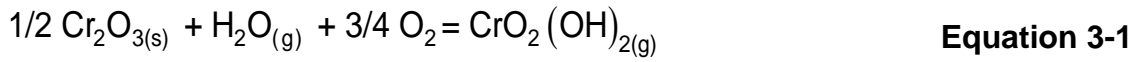
The reasonably high corrosion resistance of high-chromium austenitic Fe-Cr-Ni alloys, such as Type 310S stainless steel (UNS S31008)⁽¹⁾ and INCOLOY Alloy 800H[†] (UNS N08810), in SCW has led to these alloys being short-listed candidates for use as fuel cladding in various SCWR concepts.¹⁰⁻¹² The corrosion resistance in SCW stems from the formation of a more protective chromia (Cr₂O₃)-based scale rather than a spinel (FeCr₂O₄)-based scale.^{10,13-14} An FeCr₂O₄-based scale is believed to be less protective than a Cr₂O₃-based because the diffusion rate of Fe

⁽¹⁾ UNS numbers are listed in *Metals and Alloys in the Unified Numbering System*, published by the Society of Automotive Engineers (SAE International) and cosponsored by ASTM International.

[†] Trade name.

is three times faster than Cr in FeCr_2O_4 ,¹⁵ whereas the diffusion rate of both Fe and Cr are similar in Cr_2O_3 .¹⁶ Thus, a lower corrosion rate in SCW is expected upon formation of a Cr_2O_3 -based scale rather than an FeCr_2O_4 -based scale.

One issue with the formation of a protective Cr_2O_3 -based scale formed on high-chromium alloys is the potential formation of volatile compounds such as: $\text{CrO}_2(\text{OH})$, $\text{Cr}(\text{OH})_3$, CrO_3 , $\text{CrO}(\text{OH})_2$, and $\text{CrO}_2(\text{OH})_2$ if the environment is of an oxidizing nature.¹⁷⁻²⁰ Thermodynamic calculations of partial pressures have shown that the most dominant volatile compound at temperatures below 900°C is $\text{CrO}_2(\text{OH})_2$ in the presence of O_2 and H_2O vapor:^{19,21-24}



The rate of this reaction is highly dependent on the oxidizing parameters, with elevated temperatures, higher amounts of dissolved O_2 (DO), and increased oxidant flow rates increasing the reaction rate.²¹

Volatilization of Cr_2O_3 -based scales in low-pressure water vapor environments at high temperatures ($\sim 600^\circ\text{C}$ to 900°C) is a well-documented phenomenon.^{18,25-26} It has been pointed out that exposure of Cr_2O_3 -based scale-forming alloys in such environments results in larger weight loss.^{19,26} Also, Cr loss from the scale during volatilization may enhance Fe diffusion into the scale,²⁷⁻²⁸ and/or accelerate localized oxidation from oxide scale "breakaway" resulting in formation of an Fe-rich oxide layer/nodule.^{26,29-30} Even though the corrosion resistance exhibited by the selected alloys in SCW has been shown to be similar to that exhibited in low-

pressure superheated steam,³¹⁻³² the mechanism of Cr₂O₃-based scale volatilization in SCW has not been documented yet.

The purpose of this study was to evaluate the stability of Cr₂O₃-based scales formed on two austenitic Fe-Cr-Ni alloys during exposure in flowing oxygenated (8 ppm DO) SCW using a recirculating flow-loop autoclave testing facility. Considering the relatively short in-service life of the Canadian SCWR fuel cladding (~3.5 y), high Ni content of these austenitic alloys could be acceptable from the neutronics perspective.³³ Type 310S stainless steel was chosen for this purpose as it is a short-listed candidate alloy for the Canadian SCWR concept. Nicrofer 3033† (Alloy 33, UNS R20033) was also included on a comparative basis, as it contains a higher Cr content (~33 wt.%) relative to Type 310S stainless steel (~24 wt.%). Recently published studies show that this alloy exhibits promising corrosion resistance in stagnant SCW.³⁴⁻³⁵ Gravimetric measurements coupled with electron microscopy techniques were used to document the mode and extent of corrosion and establish links between the Cr₂O₃-based scale stability and corrosion resistance.

3.3. Experimental Procedures

Rectangular coupons of Alloy 33 (25 mm × 5 mm × 1 mm) and Type 310S stainless steel (20 mm × 10 mm × 2 mm) were prepared from commercial plates, using a diamond wheel saw and mineral oil as lubricant. The chemical composition was analyzed using inductively coupled plasma optical emission spectrometry (ICP-

OES; Varian Spectrometer[†]) and combustion analysis (LECO CS230[†]). The results are listed in **Table 3-1**.

Table 3-1 Composition (wt.%) of Alloy 33 and Type 310S Stainless Steel

| Alloy | Cr | Ni | Mo | Mn | Si | P | S | C | N | Cu | Fe |
|-----------|------|------|-----|-----|------|------|------|------|-----|-----|------|
| 33 | 33.4 | 31.9 | 1.5 | 0.6 | 0.2 | - | - | 0.01 | 0.4 | 0.5 | Bal. |
| Type 310S | 24.3 | 19.6 | 0.3 | 1.0 | 0.76 | 0.04 | 0.03 | 0.06 | - | - | Bal. |

Alloy 33 coupons were exposed in the mill-annealed state. Type 310S stainless steel coupons were solution-annealed at 1,050°C for 1 h followed by water quenching to room temperature prior to exposure. This was done to facilitate a comparison of thermal pretreatment on the stress corrosion cracking resistance of Type 310S stainless steel in SCW as part of a related study.³⁶

Figure 3-1 shows an optical microscopy (LV100-Nikon[†] optical microscope) image of the Alloy 33 and Type 310S stainless steel microstructures in cross section. Alloy 33 was etched using a HCl-HNO₃ mixture with a ratio of 6:1 and 3 drops of glycerol for 200 s. Type 310S stainless steel was etched using a HCl-CH₃COOH-HNO₃ mixture with a ratio of 3:2:1 and 3 drops of glycerol for 40 s. The average grain size (diameter) of Alloy 33 and Type 310S stainless steel was 58±5 μm and 78±33 μm, respectively, as measured using the ASTM Standard E112-96³⁷ linear intercept procedure coupled with ImageJ[†] software. Both materials exhibited an equiaxed grain structure with an appreciable extent of twinning.

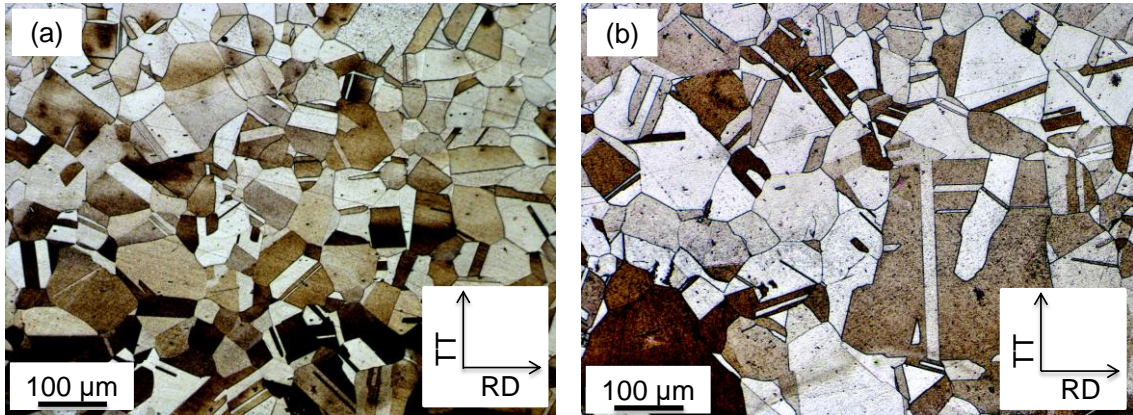


Figure 3-1. Images of the etched (a) Alloy 33 and (b) Type 310S stainless steel in the rolling direction (RD)-through thickness (TT) plane.

A small hole (~2 mm in diameter) was drilled out near the top of each coupon to facilitate mounting on a coupon tree. Coupons were manually ground to an 800 grit surface finish using SiC abrasive papers and water as a lubricant, rinsed with ethanol, and then dried with a warm air stream. This surface finish is agreed upon for corrosion research being conducted in support of developing the Canadian SCWR concept.³² The recirculating flow-loop autoclave testing facility at the University of New Brunswick was used to expose the coupons in the flowing oxygenated SCW. Specific details regarding the design of this facility are published elsewhere.³² The exposure was conducted at 550°C and 25 MPa with a flow rate of 200 mL/min with a constant DO content of 8 ppm (fully air-saturated) as measured at the inlet prior to the pre-heater. The fully air-saturated water was used to simulate the high oxygen potentials from possible water radiolysis products.³² Four coupons of each alloy were suspended on a coupon tree that was placed inside the autoclave. One coupon from each set was removed after 100 h and a

second coupon was removed after 250 h exposure. The remaining two coupons of each set were removed after 542 h exposure.

Each coupon was weighed before and after exposure using a Mettler AT261 DeltaRange[†] analytical mass balance with a precision of 0.001 mg to determine the weight change. A descaled weight loss measurement was also conducted on one of the two coupons exposed for 542 h (longest exposure time). Descaling was achieved by first immersing the coupon in a citric acid (2.0%), dibasic ammonium citrate (5.0%), and disodium EDTA (0.5%) solution at 90°C for 1 h and then immersing in a potassium permanganate (10.0%) and caustic soda (4.0%) solution at 90°C for 1 h. Immersion in the former solution was repeated until the weight loss of the exposed coupon attained a constant value. An unexposed coupon of each alloy was also included to act as the control. The effectiveness of this procedure has been demonstrated elsewhere.³²

Auger electron spectroscopy (AES), used to analyze the corroded surfaces in plan view, was performed with a JEOL JAMP-9500F AUGER/FE-SEM[†]. The analysis consisted of secondary electron imaging and acquiring a sputter depth profile from three distinct areas of the surface. Prior to the AES analysis, surfaces were cleaned to remove any residual hydrocarbon contamination by sputtering the sample with an Ar ion beam with a 3 kV accelerating voltage for ~15 s. A 3 kV Ar ion beam was then used on a 30° tilted sample with a working distance of 20 mm to 23 mm to sputter the surface layers away in successive steps coupled with the use of a 10 kV electron beam to acquire the set of spectra required to build a depth

profile. Standard deconvoluted curves of the expected oxide compounds were used to best fit the element peaks. Atomic percent elemental depth profiles (as a function of the sputtering time) were then constructed from the intensity profile spectra using the microscope software.

Site-specific thin cross-section foils of the oxide scales formed on both alloys after 542 h exposure were extracted using the focused ion beam (FIB, Zeiss NVision 40 CrossBeam Workstation[†]) sample preparation method. Milling was performed using a Ga ion beam with a voltage of 30 kV, a current of 80 pA, and a working distance of 5.6 mm to 5.9 mm. A protective W strap (~2 μm thick) was deposited on the oxide scale at the sites of interest to preserve it during ion milling. The subsequent (scanning) transmission electron microscopy ([S]TEM) examination was conducted using a field emission JEOL 2010F TEM/STEM,[†] equipped with an Oxford INCA[†] energy dispersive x-ray spectroscopy (EDS) system. The operating voltage was 200 kV. Selected area diffraction (SAD) patterns were acquired from areas of interest across the oxide scale/alloy interface to identify the various phases present. SAD patterns of the expected phases were simulated using the JEMS[†] software and published reference patterns.³⁸ As the SAD aperture diameter on the TEM images was larger than 150 nm, relative differences in structure and composition of oxide scales less than 150 nm thick were analyzed using electron energy loss spectroscopy (EELS) instead. This was achieved using a dispersion of 0.2 eV/channel in the dark-field STEM (DF-STEM) mode: the results of which were analyzed using the Gatan DigitalMicrograph[†]

software.³⁹ As the O-K peaks typically show more variation in each oxide type,⁴⁰⁻⁴⁴ the near-edge structure features, along with the published spectra,⁴⁰⁻⁴⁴ were used for phase identification. The EDS analyses (and corresponding images) were obtained using the bright-field STEM (BF-STEM) mode.

3.4. Results

Figure 3-2(a) compares weight change data for the two alloys as a function of exposure time. All three weight change values for Alloy 33 were negative. A detectable negative change was recorded after 100 h exposure. Increasing the exposure time to 250 h had little effect on this initial value. However, a further increase in exposure time to 542 h yielded a more negative weight change value. In contrast, the set of weight change values for Type 310S stainless steel were all positive. No appreciable weight change was observed after 100 h exposure. However, appreciable weight change was observed with increasing exposure time, with a significant increase occurring after 250 h. **Figure 3-2(b)** compares the single weight loss measurement of the descaled coupon of each alloy after 542 h exposure. Alloy 33 exhibited smaller weight loss value despite exhibiting negative weight change kinetics.

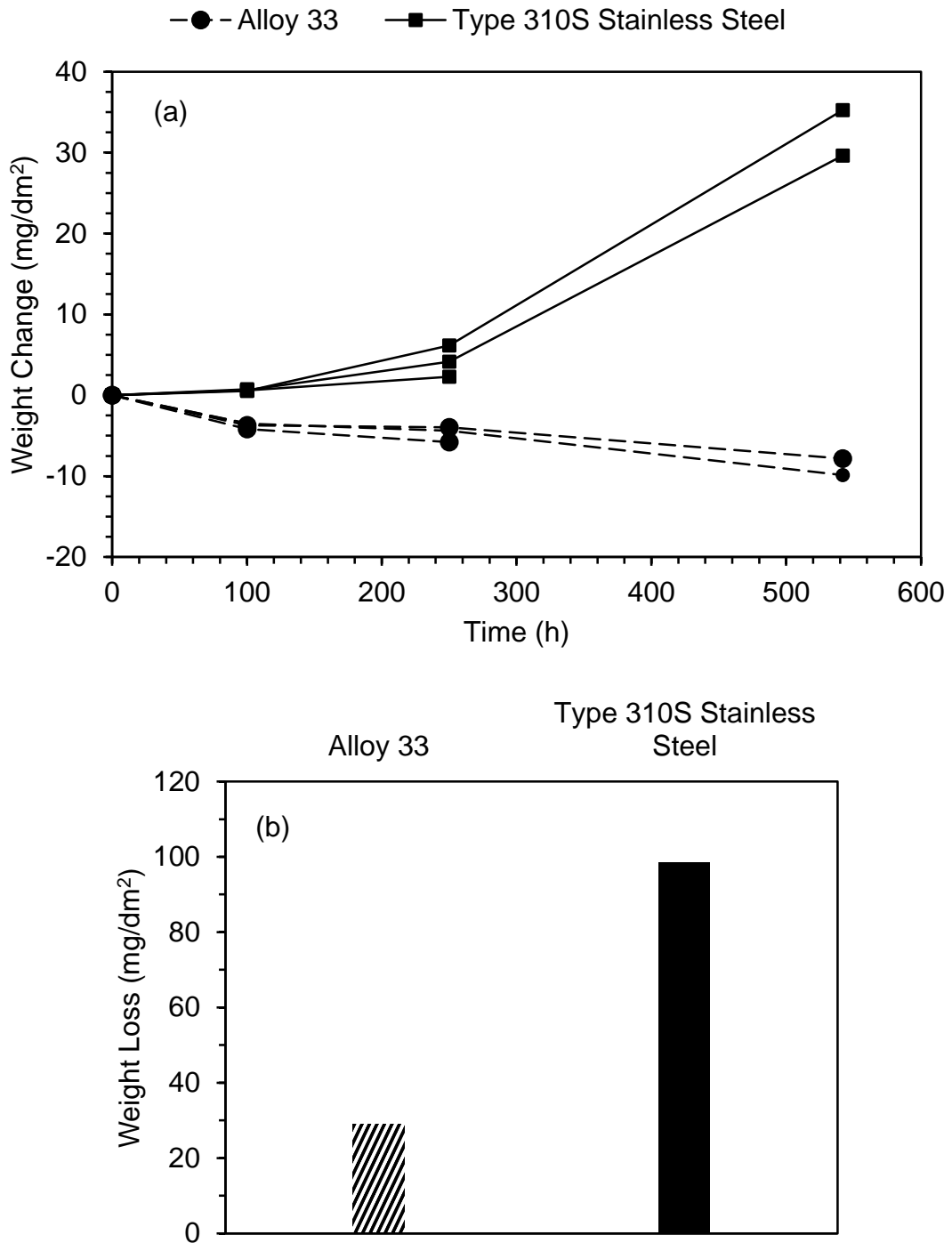


Figure 3-2. (a) Weight change data after 100 h, 250 h, and 542 h exposure and (b) single weight loss data for the descaled coupon of each alloy after 542 h exposure (longest exposure time) in 25 MPa and 550°C flowing oxygenated SCW.

Figure 3-3 shows a set of plan view secondary electron images of the corroded surface of both alloys after each of the three exposure times considered. The Alloy 33 surfaces after all three exposure times (**Figure 3-3[a]** through **[c]**) were essentially indistinguishable and resembled the Type 310S stainless steel surface after 100 h exposure time (**Figure 3-3[d]**). The grinding lines from the mechanical abrasion surface preparation step were clearly visible on these surfaces indicating that the oxide scale was very thin. Also, small (~500 nm) cuboidal/octahedral oxide "nodules" (Type I) were observed to reside on top of a compact, granular, and crack-free "base" scale. These Type I oxide nodules were determined to be a spinel phase $(\text{Mn}_x, \text{Fe}_y)\text{Cr}_2\text{O}_4$, as characterized by EELS and SAD (results not shown here). They were not considered to play a role in scale stabilization during exposure, and thus were not given any further consideration. The base scale formed on Alloy 33 became relatively rougher with increasing exposure time, yet the morphology of the scale after 542 h exposure was not altered, indicating that the oxide crystal structure remained the same during the entire testing time. As for the Type 310S stainless steel surface after 250 h exposure, relatively large ($> 5 \mu\text{m}$) isolated oxide nodules (Type II) accompanying Type I oxide nodules were observed on the base scale (**Figure 3-3[e]**). Type II oxide nodules increased in population and eventually covered almost the entire base scale after 542 h exposure (**Figure 3-3[f]**). No evidence of any significant oxide cracking or spallation was found on any of the surfaces examined.

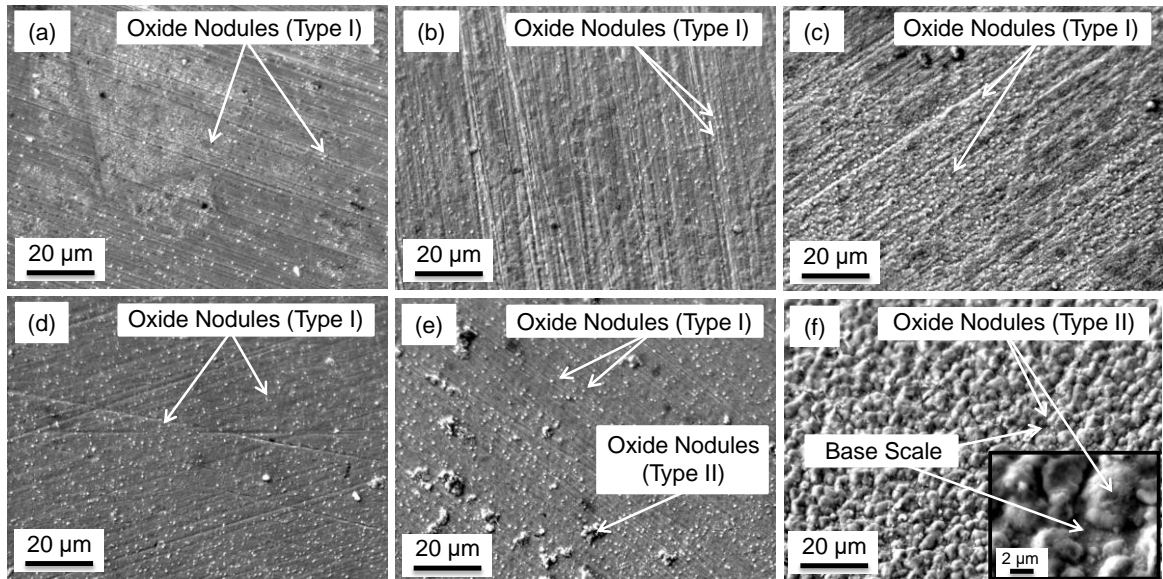


Figure 3-3. Secondary electron images of (a), (b), and (c) Alloy 33 after exposure for 100 h, 250 h, and 542 h, respectively, and (d), (e), and (f) Type 310S stainless steel after exposure for 100 h, 250 h, and 542 h, respectively, in 25 MPa and 550°C flowing oxygenated SCW. Type I oxide nodules in all cases and Type II oxide nodules formed on Type 310S stainless steel coupons after 250 h and 542 h exposure ([e] and [f]) can also be seen.

Average atomic concentration AES depth profiles for O, Cr, Fe, Ni, and Mn for both alloys for the three exposure times are shown in **Figure 3-4**. The base scale formed on Alloy 33 after 100 h exposure was enriched in only Cr and O (**Figure 3-4[a]**). A relatively shallow Cr-depleted zone was also seen just below the Cr₂O₃ scale. After 250 h, the scale consisted of Cr, Fe, and O as major elements and Mn as minor element (yet enriched relative to the alloy) (**Figure 3-4[b]**). The Cr-depleted zone depth also increased compared to that after 100 h exposure. The Fe concentration in the base scale after 542 h exposure increased even more. The scale consisted of Cr, Fe, and O as major elements and Ni and Mn as minor elements (**Figure 3-4[c]**). A much deeper Cr-depleted zone formed below the

scale. The base scale formed on Type 310S stainless steel after 100 h exposure consisted of Cr, Fe, Mn, and O, with a small amount of Ni (**Figure 3-4[d]**). The concentration of Mn was relatively higher at the oxide/SCW interface compared with that at the oxide/alloy interface suggesting the existence of an oxide "cap" enriched in Mn. After 250 h exposure, the scale was enriched in Cr and consisted of Cr, Fe, and O (**Figure 3-4[e]**). The base scale formed after 542 h exposure (**Figure 3-4[f]**) consisted of Cr, Fe, and O as major elements and Mn and Ni as minor elements. It is acknowledged that the oxide scales were not uniform, which may have produced local variations in the oxide composition profiles.

Thin cross-section TEM foils were prepared for Alloy 33 and Type 310S stainless steel after 542 h exposure using the FIB milling sample preparation technique (**Figure 3-5**). The alloy/oxide interface for Alloy 33 was qualitatively rougher than that of Type 310S stainless steel. The thickness of the base scale on Alloy 33 was variable, consisting of both thin and thick regions, whereas the thickness of the base scale on Type 310S stainless steel was more uniform. Recrystallized grains, formed in situ within the plastic deformation zone induced by sample preparation (mechanical-abrasion before exposure), were also apparent in the near-surface region underneath the alloy/oxide interface of both alloys.

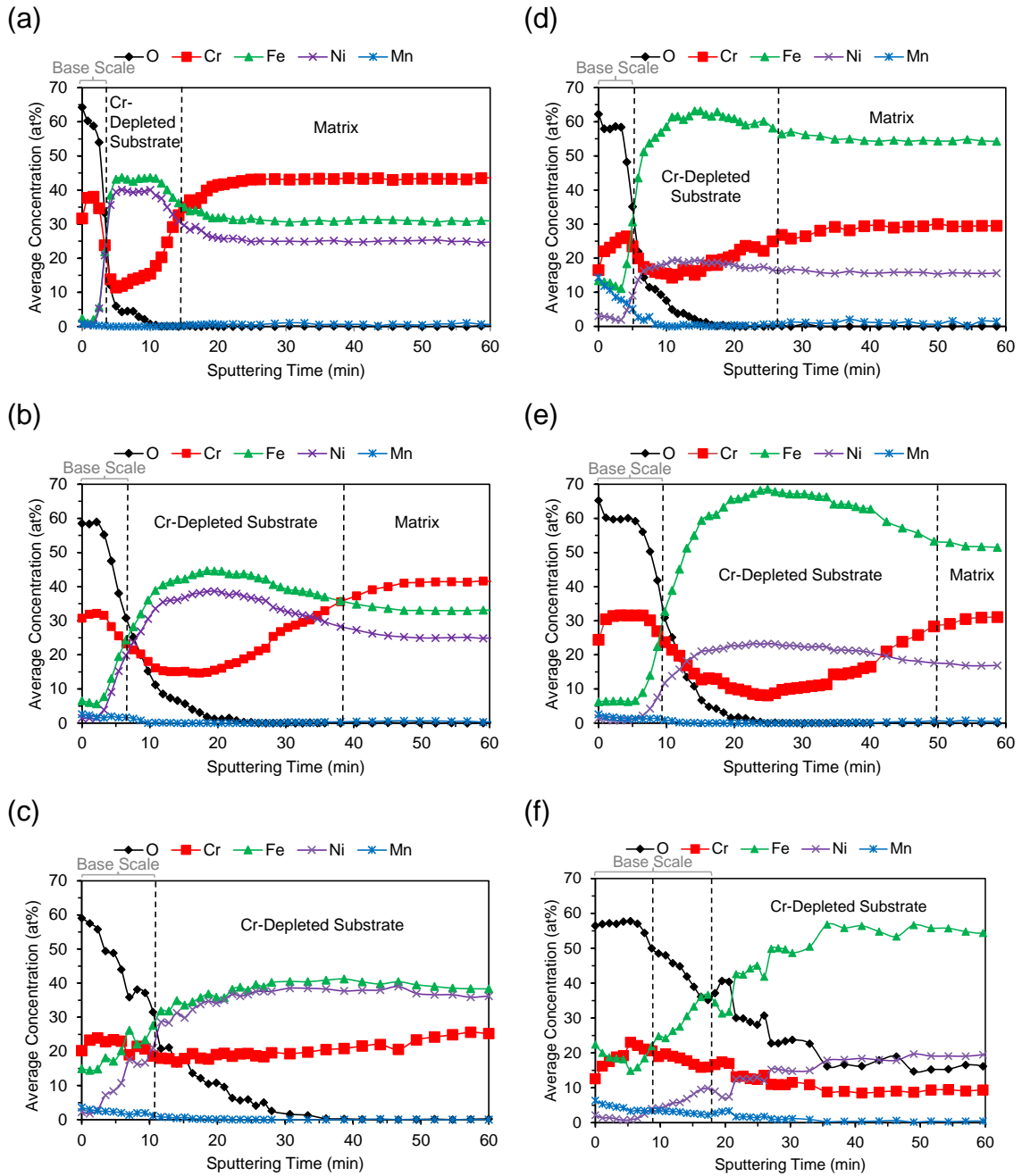


Figure 3-4. Average atomic concentration profile of O, Cr, Fe, Ni, and Mn measured across the base scale/alloy interface of Alloy 33 after (a) 100 h, (b) 250 h, and (c) 542 h exposure and Type 310S stainless steel after (d) 100 h, (e) 250 h, and (f) 542 h exposure in 25 MPa and 550°C flowing oxygenated SCW.

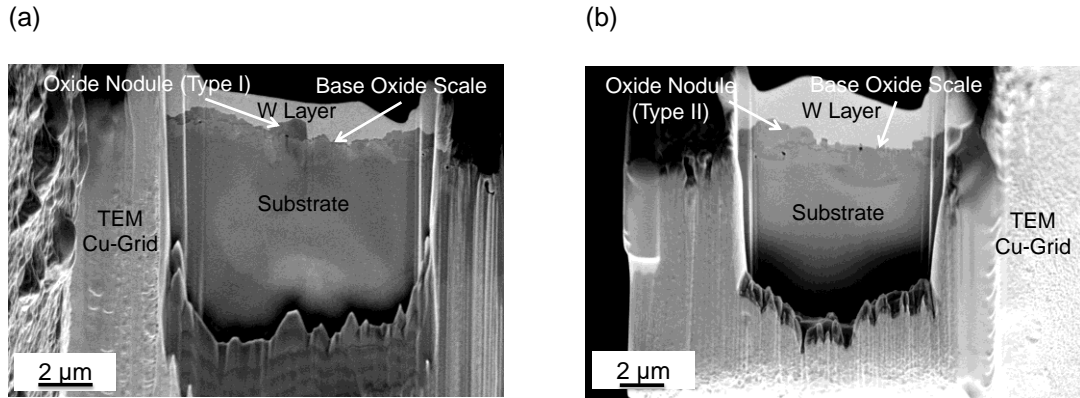


Figure 3-5. Secondary electron images of the FIB-prepared thin cross-section TEM foil of oxide scale formed on (a) Alloy 33 and (b) Type 310S stainless steel after 542 h exposure in 25 MPa and 550°C flowing oxygenated SCW.

Figure 3-6 shows BF-STEM images of the base scale formed on both alloys after 542 h exposure. The corresponding O, Cr, Mn, Fe, and Ni STEM-EDS elemental maps are included as well. The base scale formed on both alloys contained Cr, Fe, and O as major elements and Ni and Mn as minor elements. A relatively thin (~10 nm to 15 nm) Si-oxide layer was also seen below the alloy/oxide interface (results not shown here). The recrystallized grain layer was depleted in Cr and Mn in both alloys, being significantly deeper in Type 310S stainless steel. Both alloys exhibited evidence of incipient intergranular corrosion (IGC) within the recrystallized grain layer, the extent of which was larger in Alloy 33.

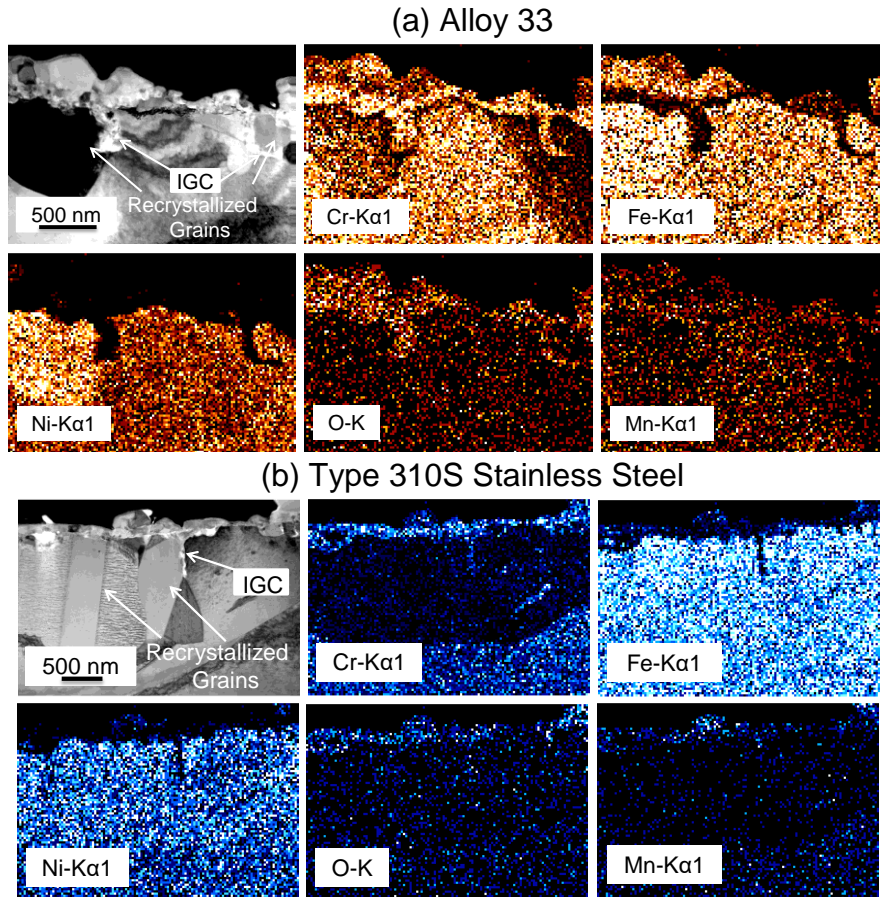


Figure 3-6. BF-STEM image of the substrate and the base scale formed after 542 h exposure in 25 MPa and 550°C flowing oxygenated SCW on (a) Alloy 33 and (b) Type 310S stainless steel in cross section along with their O, Cr, Mn, Fe, and Ni STEM-EDS maps.

Figure 3-7 shows DF-STEM images of the base scale formed on Alloy 33 and Type 310S stainless steel after 542 h exposure. The set of acquired EELS spectra from the base scale is shown in **Figure 3-7(c)** and **(d)** for Alloy 33 and Type 310S stainless steel, respectively. The range of energy loss plotted was restricted to that containing the O-K, Cr-L_{2,3}, and Fe-L_{2,3} peaks, which were used to determine the composition and structure of the oxide phases present. The set of three spectra from both thick and thin areas of the base scale formed on Alloy

33 (**Figure 3-7[c]**) revealed that the base scale comprised mainly Cr, Fe, and O. A small yet significant Mn peak was observed in Area 2. The fine structure of the O-K edge was consistent with $(\text{Cr}_x, \text{Fe}_y)_2\text{O}_3$ ($x \geq y$), where the range of Fe concentration decreased from the oxide/SCW interface to the alloy/oxide interface. The set of two spectra shown in **Figure 3-7(d)** revealed that the Type 310S stainless steel base scale also mainly comprised Cr, Fe, and O. A small Mn peak was also observed in the EELS spectra. The structure of the O-K peaks acquired from Areas 4 and 5 were consistent with $(\text{Fe}_y, \text{Cr}_x)_2\text{O}_3$ ($y > x$) and $(\text{Cr}_x, \text{Fe}_y)_2\text{O}_3$ ($x \sim y$), respectively.

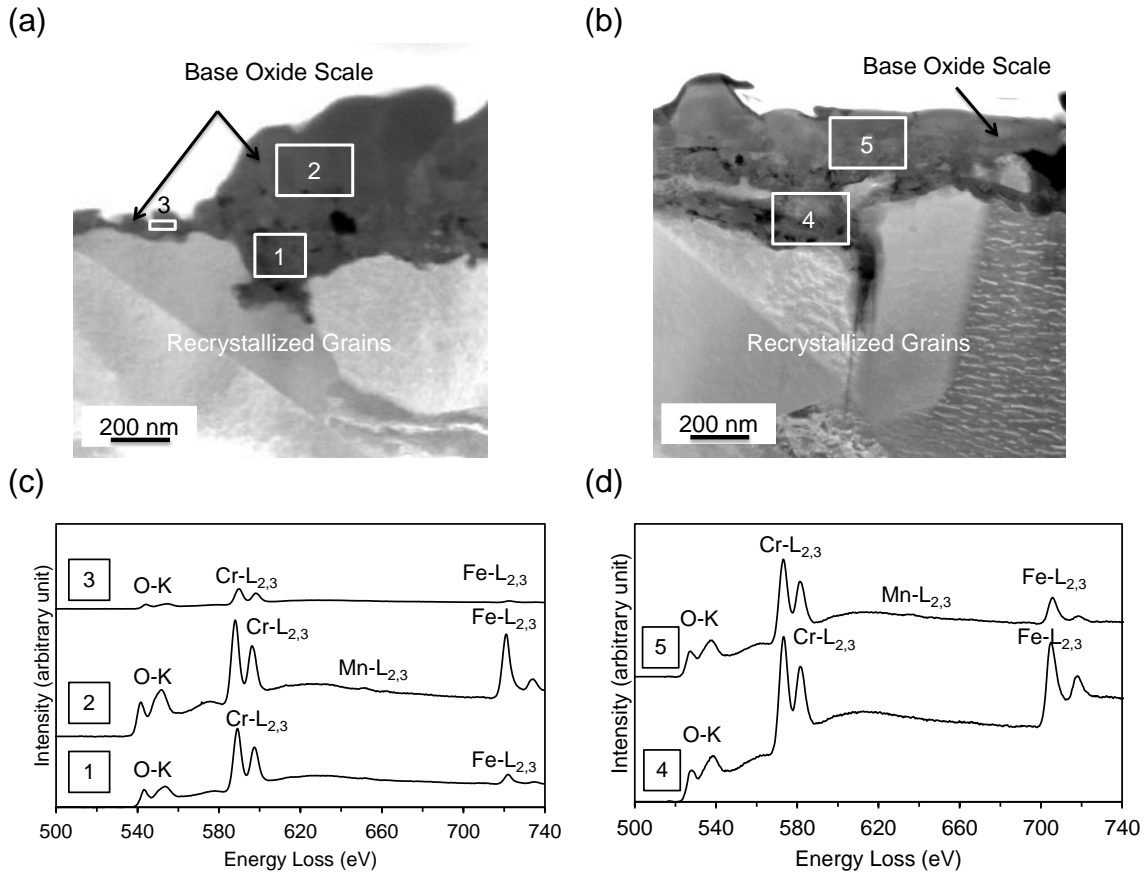


Figure 3-7. DF-STEM image of the base scale formed on (a) Alloy 33 and (b) Type 310S stainless steel after 542 h exposure in 25 MPa and 550°C flowing oxygenated SCW. (c) EELS spectra of Areas 1, 2, and 3 across the base scale on Alloy 33. (d) EELS spectra of Areas 4 and 5 across the base scale on Type 310S stainless steel.

Figure 3-8(a) shows a DF-STEM image of Type II oxide nodules formed on Type 310S stainless steel after 542 h exposure. The framed numbers superimposed on the image identify those regions from which an EELS analysis was conducted [**Figure 3-8(b)**]. The set of two spectra obtained from the Type II nodules (**Figure 3-8(b)**) revealed that the oxide phase mainly consisted of Cr and Fe. The structure obtained from the EELS spectra was consistent with an outer $(\text{Fe}_y, \text{Cr}_x)_2\text{O}_3$ ($y > x$) phase (Type II oxide nodules) residing on an inner $(\text{Cr}_x, \text{Fe}_y)_2\text{O}_3$

($x > y$) layer. The SAD pattern obtained from Area 2 in **Figure 3-8(a)** was also consistent with $(\text{Fe}_y, \text{Cr}_x)_2\text{O}_3$ Type II oxide nodules (**Figure 3-8(c)**).

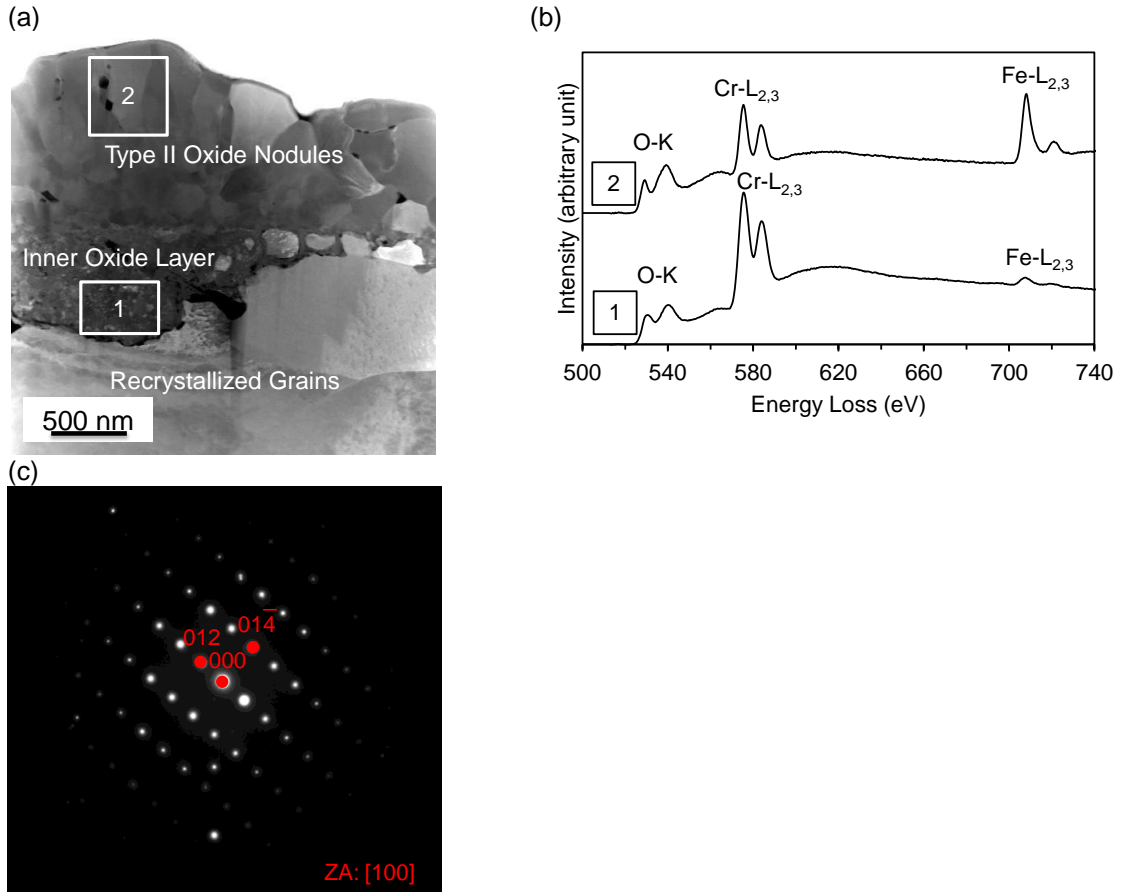


Figure 3-8. (a) DF-STEM image of Type II oxide nodules formed on Type 310S stainless steel after 542 h exposure in flowing oxygenated SCW. (b) EELS spectra of superimposed Areas 1 and 2 in (a), and (c) SAD pattern of Area 2 in (a).

3.5. Discussion

3.5.1. Scale Evolution

Figure 3-9 schematically shows the scale evolution on each alloy during exposure for up to 542 h in 25 MPa and 550°C flowing oxygenated SCW. The structure and composition of the phases are distinguished based on the elemental ratio measurements extracted from the AES and STEM analyses. The base scale formed on Alloy 33 after 100 h exposure was likely Fe-free Cr_2O_3 . After 250 h, a small amount of Fe diffused into the scale, changing the composition to $(\text{Cr}_x, \text{Fe}_y)_2\text{O}_3$ ($x \gg y$) with a small amount of Mn. After 542 h exposure, more Fe diffused into the scale, changing the composition to $(\text{Cr}_x, \text{Fe}_y)_2\text{O}_3$ ($x \geq y$) with a small amount of Ni and Mn. The base scale formed on Type 310S stainless steel after 100 h exposure consisted of a Mn-enriched oxide "cap": $(\text{Mn}_z, \text{Fe}_y, \text{Cr}_x)_2\text{O}_3$ ($z \sim y > x$) on top of the $(\text{Cr}_x, \text{Fe}_y, \text{Mn}_z)_2\text{O}_3$ ($x \geq y, y \sim z$) scale. However, after 250 h exposure, the base scale transformed to $(\text{Cr}_x, \text{Fe}_y)_2\text{O}_3$ ($x \gg y$). No evidence of the Mn-enriched oxide cap was found after 250 h exposure, indicating that the cap was removed (volatilized/dissolved) by that time. Instead, Type II oxide nodules ($(\text{Fe}_y, \text{Cr}_x)_2\text{O}_3$ [$y > x$]) initiated to form on a $(\text{Cr}_x, \text{Fe}_y)_2\text{O}_3$ ($x > y$) base scale. The structure of the base scale after 542 h exposure was $(\text{Cr}_x, \text{Fe}_y)_2\text{O}_3$ with Cr and Fe concentration varying throughout the scale. Also, Type II oxide nodules ($(\text{Fe}_y, \text{Cr}_x)_2\text{O}_3$ [$y > x$]) covered almost the entire base scale. The very thin (~10 nm to 15 nm) layer containing Si and O below the alloy/oxide interface is not shown in

the schematic because such a thin film has been argued not to play a role in stabilizing the Cr_2O_3 -based scales.⁴⁵

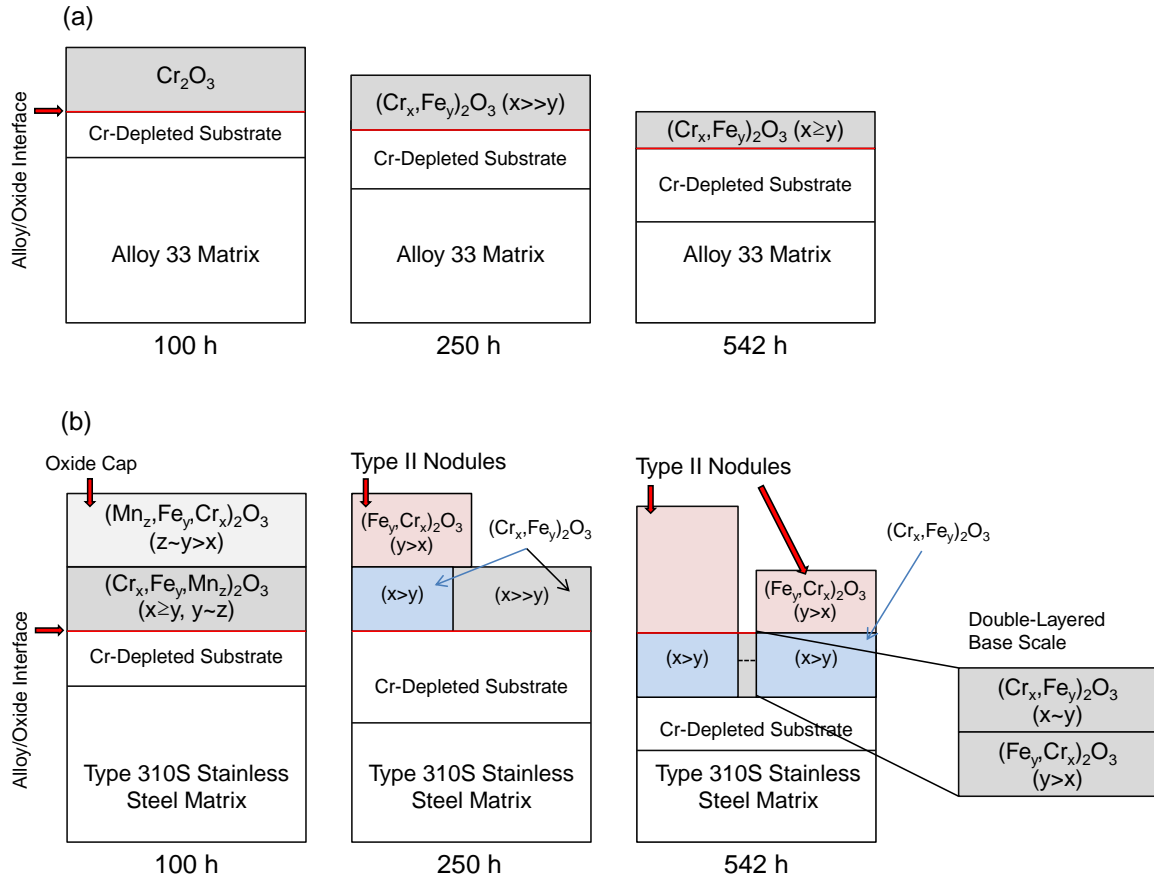
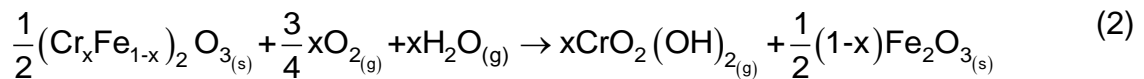


Figure 3-9. Schematic of the scale evolution with time for (a) Alloy 33 and (b) Type 310S stainless steel after exposure in 25 MPa and 550°C flowing oxygenated SCW for 100 h, 250 h, and 542 h. The thicknesses of layers are not to scale.

3.5.2. Mechanism of Scale Volatilization

In previous work,³⁵ it was reported that after 500 h exposure in 25 MPa and 550°C SCW in a static autoclave testing facility (no flow or control of DO), the high Cr content of Alloy 33 resulted in formation of a single-layered Fe-free Cr_2O_3 scale. This is attributed to the fact that Cr-content in Alloy 33 (33.4 wt%) is well above the

critical Cr-content (~20 wt% to 25 wt%) reported to be necessary for the formation of a continuous Cr₂O₃-based scale on an austenitic stainless steel in high-temperature steam environment, albeit this critical value highly depends on alloy grain size and Ni content.⁴⁶ The use of a recirculating flow-loop autoclave to maintain the DO concentration at 8 ppm during exposure is believed to have increased the likelihood of oxide scale volatilization/dissolution. A key observation in support of volatilization is for Cr oxide/hydroxide volatilization to deplete the protective Cr-rich scale in Cr, facilitating Fe diffusion into the base scale to fill in the Cr vacant lattice sites. Depending on the substrate Cr content, the scale then eventually either transforms into a less-protective Fe-rich Cr₂O₃-based scale²⁷⁻²⁸ or starts to locally breakaway to form Fe-rich oxide nodules:^{26,29-30}



The observation that the Cr₂O₃-based scale developed a higher Fe content (lower Cr/Fe) with an increase in exposure time (up to 542 h) is consistent with a volatilization-induced Cr₂O₃ to Fe₂O₃ transformation.

Figure 3-10 compares the average Cr/Fe atomic concentration ratio in the base scale for both alloys after each exposure time considered. Cr/Fe ratios from the previous static autoclave testing of Alloy 33 after 500 h³⁵ and Type 310S stainless steel after 542 h exposure are also shown in Figure 10 for comparison. The very high Cr/Fe ratio in Alloy 33 scale after 100 h exposure indicated that the Cr₂O₃-based scale formed was essentially almost a pure Cr₂O₃, very similar to the

scale found after exposure in stagnant SCW.³⁵ However, the Cr/Fe ratio decreased with an increase in exposure time indicating Cr loss as a result of continuous scale volatilization in flowing oxygenated SCW, which enhanced Fe diffusion into the scale. A progressive decrease in the Cr/Fe ratio with exposure time, coupled with the formation of a roughened oxide/SCW interface and progressive negative weight change, was suggestive of scale volatilization in Alloy 33. Despite this, the volatilization rate was not considered to be high given the relatively low weight loss value measured after 542 h exposure (29 mg/dm²). A linear extrapolation (which assumed the highest possible corrosion rate) of this weight loss value gives a penetration rate of ~21 μm over the in-service lifetime of the cladding (30,660 h [3.5 y]), which is considerably less than the estimated maximum tolerable thickness of the fuel cladding in the Canadian SCWR concept (~200 μm over 3.5 y).^{34,47} The protectiveness of Alloy 33 oxide scale likely relies on the underlying Cr content in the alloy, DO content, and flow rate.²⁰ Ultimately, the stability of the scale relies on whether or not Cr diffusion to the surface offsets the Cr loss by volatilization.

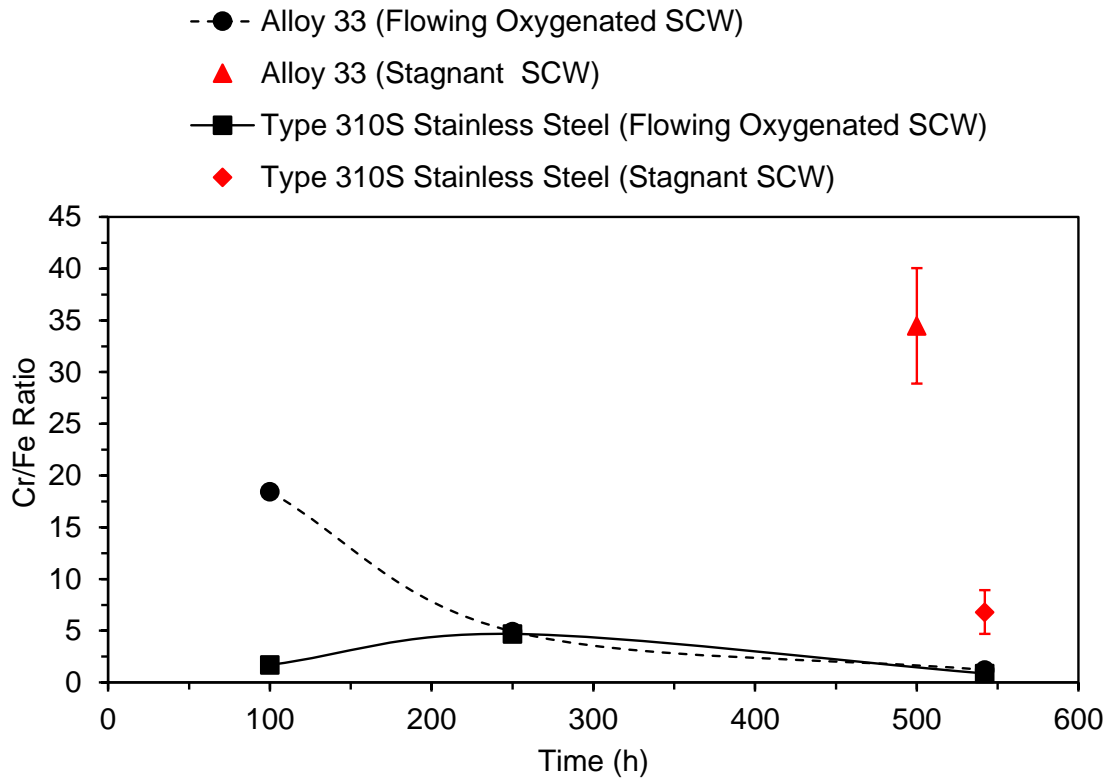


Figure 3-10. Comparison of the average Cr/Fe atomic concentration ratio after 100 h, 250 h, and 542 h exposure in 25 MPa and 550°C flowing oxygenated SCW, 500 h exposure of Alloy 33 in 25 MPa and 550°C stagnant SCW,³⁵ and 542 h exposure of Type 310S stainless steel in 25 MPa and 550°C stagnant SCW.

Examination of the Cr/Fe ratio for Type 310S stainless steel after 100 h, 250 h, and 542 h shows that the Cr/Fe ratio suddenly increased between 100 h and 250 h exposure and then decreased between 250 h and 542 h exposure. This behavior can be explained by a Mn effect on preserving the stability of Cr₂O₃-based scales. As shown in the AES depth profiles, the base scale formed on Type 310S stainless steel after 100 h exposure contained more Fe and Mn at the oxide/SCW interface and less Cr (**Figure 3-4[d]**). Therefore, it is assumed that a protective Mn-enriched oxide cap separated the Cr-rich scale from SCW and prevented it from direct contact with SCW. The scale remained protective up to ~250 h as more

Cr diffused into the scale. The base scale after 250 h exposure was $(Cr_x, Fe_y)_2O_3$ ($x \gg y$), similar to the oxide formed on Alloy 33. The protective Mn-enriched oxide cap no longer existed (volatilized/dissolved in SCW) most likely because the low Mn concentration in the substrate was not sufficient to preserve the cap. Recent on-line measurements of metal release in SCW (at a volumetric flow rate of 0.1 mL/min at 550°C, 650°C, and 700°C at a pressure of 25 MPa) have shown that Mn volatilization/dissolution during the first 161 h exposure was much higher than expected considering the amount in the alloy.⁴⁸ Formation of $(Cr_x, Fe_y)_2O_3$ ($x \gg y$) after 250 h exposure while being in direct contact with SCW enhanced scale volatilization, Fe diffusion into the scale, and consequent oxide scale breakaway. The latter resulted in formation of Type II oxide nodules on the surface after 250 h exposure (**Figure 3-3[e]**). It is plausible that Fe diffusion to form Type II oxide nodules was not only from the alloy substrate, but also from the base scale adjacent to the nodules.²² The latter likely affected Cr/Fe ratio in the base scale along with enhanced Fe diffusion from the Cr-depleted zone yielding values similar to that for Alloy 33 after 250 h and 542 h exposure (**Figure 3-10**). By continuous volatilization of the base scale after 250 h exposure, $(Fe_y, Cr_x)_2O_3$ ($y > x$) Type II nodules covered almost the entire surface, below which an inner $(Cr_x, Fe_y)_2O_3$ ($x > y$) layer was formed.²⁹ The positive weight change of Type 310S stainless steel coupons is attributed to both the base scale formation and accumulation of Type II $(Fe_y, Cr_x)_2O_3$ ($y > x$) nodules on the surface. A linear extrapolation (which assumes the highest possible corrosion rate) of Type 310S stainless steel weight loss value

gives a penetration rate of $\sim 70 \mu\text{m}$ over 3.5 y, which is still below the performance requirement of the fuel cladding in the Canadian SCWR concept ($\sim 200 \mu\text{m}$ at 830°C over 3.5 y).^{34,47} The loss of the protective oxide cap after ~ 100 h in combination with the base scale volatilization, lower Cr content in the substrate, and eventual oxide scale breakaway and formation of Type II $(\text{Fe}_y, \text{Cr}_x)_2\text{O}_3$ ($y > x$) nodules resulted in a much higher metal penetration than that measured for Alloy 33. Therefore, from the perspective of corrosion resistance, Alloy 33 shows promise as a candidate fuel cladding material for Canadian SCWR concept, although the mechanical properties, stress corrosion cracking resistance, and irradiation resistance of this alloy still needs to be studied. One major concern in regard to irradiation damage that needs to be addressed could be the loss of ductility in the higher Ni alloy as He produced from the transmutation of Ni can accumulate along the grain boundaries causing embrittlement.⁴⁹

3.6. Conclusions

The corrosion resistance of Type 310S stainless steel and Alloy 33 (24.3 wt% vs. 33.4 wt% Cr, respectively) in SCW was examined under flowing oxygenated conditions. The results showed that the scale formed on both alloys was Cr_2O_3 -based after up to 542 h exposure. Both gravimetric measurement (negative weight change) and electron microscopy results (decrease in Cr/Fe ratio) confirmed that the scale formed on Alloy 33 volatilized/dissolved in the flowing oxygenated SCW. The preserved protectiveness of Cr_2O_3 -based scale on Alloy 33 was attributed to the higher Cr content of the alloy, which provided sufficient Cr by diffusion to compensate for the Cr lost by volatilization/dissolution. As for Type 310S stainless steel, Mn-enriched oxide cap volatilized/dissolved during the initial ~250 h exposure. Cr_2O_3 -based scale breakaway after ~250 h exposure was supported by lower Cr content in the Type 310S stainless steel substrate and Fe diffusion from both alloy substrate and adjacent (to Type II nodules) base scale. The high weight gain and higher corrosion penetration of Type 310S stainless steel after 542 h exposure were attributed to the accumulation of these nodules. The data suggest that it can take some time for the oxide layers to come to steady-state (depending on bulk alloy Cr content, size of the depleted zone behind the oxide scale, and underlying recrystallized grain size), which should be taken into consideration when planning tests. As well, data obtained for times less than 542 h should probably not be included when predicting long-term corrosion kinetics, as the rate law may change with time.

3.7. Acknowledgements

The authors would like to acknowledge the funding to Canada Gen-IV National Program was provided by Natural Resources Canada through the Office of Energy Research and Development, Atomic Energy of Canada Limited, and Natural Sciences and Engineering Research Council of Canada. The authors would also like to acknowledge VDM metals company for supplying the Alloy 33 sheets. Finally, the authors would like to thank the staff in the Canadian Centre for Electron Microscopy (CCEM), a national facility supported by NSERC, the Canada Foundation for Innovation, and McMaster University, for their technical assistance with sample preparation and electron microscopy assistance.

3.8. References

1. K.H. Chang, S.-M. Chen, T.-K. Yeh, J.-J. Kai, *Corros. Sci.* 81 (2014): p. 21-26.
2. X. Huang, Y. Shen, *J. Nucl. Mater.* 461 (2015): p. 1-9.
3. F. Khatkhatay, L. Jiao, J. Jian, W. Zhang, Z. Jiao, J. Gan, H. Zhang, X. Zhang, H. Wang, *J. Nucl. Mater.* 451 (2014): p. 346-351.
4. Z. Shen, L. Zhang, R. Tang, Q. Zhang, *J. Nucl. Mater.* 458 (2015): p. 206-215.
5. J. Zhong, S.P. Antal, M.Z. Podowski, *J. Power Technol.* 94 (2014): p. 51-60.
6. I. Pioro, P. Kirillov, *Mater. Process. Energy Commun. Curr. Res. Technol. Dev.* (2013): p. 818-830.
7. D. Guzonas, R. Novotny, *Prog. Nucl. Energy* 77 (2014): p. 361-372.
8. T. Schulenberg, L.K.H. Leung, Y. Oka, *Prog. Nucl. Energy* 77 (2014): p. 282-299.
9. G. Locatelli, M. Mancini, N. Todeschini, *Energy Policy* 61 (2013): p. 1503-1520.
10. J. Li, W. Zheng, S. Penttilä, P. Liu, O.T. Woo, D. Guzonas, *J. Nucl. Mater.* 454 (2014): p. 7-11.
11. Z. Shen, L. Zhang, R. Tang, Q. Zhang, *J. Nucl. Mater.* 454 (2014): p. 274-282.
12. G.S. Was, S. Teysseyre, Z. Jiao, *Corrosion* 62 (2006): p. 989-1005.
13. A. Kimura, R. Kasada, N. Iwata, H. Kishimoto, C.H. Zhang, J. Isselin, P. Dou, J.H. Lee, N. Muthukumar, T. Okuda, M. Inoue, S. Ukai, S. Ohnuki, T. Fujisawa, T.F. Abe, *J. Nucl. Mater.* 417 (2011): p. 176-179.
14. L. Tan, T.R. Allen, Y. Yang, *Corros. Sci.* 53 (2011): p. 703-711.
15. O.Y. Goncharov, *Inorg. Mater.* 40 (2004): p. 1476-1482.
16. R.E. Lobnig, H.P. Schmidt, K. Hennesen, H.J. Grabke, *Oxide. Met.* 37 (1992): p.81-93.
17. A. Yamauchi, K. Kurokawa, H. Takahashi, *Oxid. Met.* 59 (2003): p. 517-527.

18. S.I. Castañeda, F.J. Pérez, *Oxid. Met.* 79 (2013): p. 147-166.
19. E.J. Opila, D.L. Myers, N.S. Jacobson, I.M.B. Nielsen, D.F. Johnson, J.K. Olminsky, M.D. Allendor, *J. Phys. Chem. A* 111 (2007): p. 1971-1980.
20. N. Mu, K.Y. Jung, N.M. Yanar, G.H. Meier, F.S. Pettit, G.R. Holcomb, *Oxid. Met.* 78 (2012): p. 221-237.
21. H. Asteman, J. Svensson, M. Norell, L. Johansson, *Oxid. Met.* 54 (2000): p. 11-26.
22. M. Halvarsson, J.E. Tang, H. Asteman, J.E. Svensson, L.G. Johansson, *Corros. Sci.* 48 (2006): p. 2014-2035.
23. X. Zhang, Q. Yan, Y. Yang, Z. Hong, L. Zhang, C. Ge, *Corrosion* 71 (2015): p. 50-56.
24. G.R. Holcomb, *ECS Trans.* 16 (2009): p. 81-92.
25. E.J. Opila, *Mater. Sci. Forum* 461-464 (2004): p. 765-774.
26. H. Asteman, J. Svensson, L. Johansson, *Oxid. Met.* 52 (1999): p. 95-111.
27. R. Peraldi, B.A. Pint, *Oxid. Met.* 61 (2004): p. 463-483.
28. D.J. Young, B.A. Pint, *Oxid. Met.* 66 (2006): p. 137-153.
29. H. Asteman, J.E. Svensson, L.G. Johansson, *Oxid. Met.* 57 (2002): p. 193-216.
30. K. Segerdahl, "The Breakdown of the Protective Oxide on 11% Chromium Steel: The Influence of Water Vapour and Gaseous KCl " (Ph.D. diss., Chalmers University of Technology, 2003).
31. A.T. Motta, A. Yilmazbayhan, M.J.G. da Silva, R.J. Comstock, G.S. Was, J.T. Busby, E. Gartner, Q. Peng, Y.H. Jeong, J.Y. Park, *J. Nucl. Mater.* 371 (2007): p. 61-75.
32. D.A. Guzonas, W.G. Cook, *Corros. Sci.* 65 (2012): p. 48-66.
33. C. Rangacharyulu, D.A. Guzonas, J. Pencer, A. Nava-Dominguez, L.K.H. Leung, "An Integrated Approach to Selecting Materials for Fuel", 19th Pacific Basin Nucl. Conf. (Toronto, Canada: Canadian Nuclear Society, 2014), p. 220-232.

34. S. Mahboubi, G.A. Botton, J.R. Kish, Corrosion 71 (2015): p. 1064-1070.
35. S. Mahboubi, G.A. Botton, J.R. Kish, Corrosion 71 (2015): p. 992-1002.
36. Y. Jiao, J.R. Kish, G. Steeves, W.G. Cook, W. Zheng, D.A. Guzonas, J. Nucl. Eng. Rad. Sci. 2 (2016): p. 011015, 1-9.
37. ASTM E112-13, "Standard Test Methods for Determining Average Grain Size" (West Conshohocken, Pa: ASTM, 2013).
38. P. Stadelmann, "JEMS Software", 2014, <http://www.jems-saas.ch/Home/jemsWebsite/jems.html> (July 11, 2016).
39. "Gatan Digital Micrograph", Garan, 2016, <http://www.gatan.com/products/tem-analysis/gatan-microscopy-suite-software> (July 11, 2016).
40. J. Bischoff, A.T. Motta, J. Nucl. Mater. 430 (2012): p. 171-180.
41. C. Colliex, Phys. Rev. B 44 (1991): p. 11402-11411.
42. D.A. Eustace, D.W. McComb, A.J. Craven, Micron 41 (2010): p. 547-553.
43. C. Colliex, Phys. Rev. B 48 (1993): p. 2102-2108.
44. G.A. Botton, C.C. Appel, A. Horsewell, W.M. Stobbs, J. Microsc. 180 (1995): p. 211-216.
45. H.E. Evans, D.A. Hilton, R.A. Holm, S.J. Webster, Oxid. Met. 19 (1983): p. 1-18.
46. N. Otsuka, Y. Shida, H. Fujikawa, Oxid. Met. 32 (1989): p. 13-45.
47. D. Guzonas, M. Edwards, W. Zheng, J. Nucl. Rad. Sci. 2 (2015): p. 011016.
48. K.I. Choudhry, D.A. Guzonas, D.T. Kallikragas, I.M. Svishchev, "On-line Monitoring of Oxide Formation and Dissolution on Alloy 800H in Supercritical Water", Corros. Sci. 111 (2016): p. 574-582.
49. E.A. Kenik, R.H. Jones, G.E.C. Bell, J. Nucl. Mater. 212-215 (1994): p. 52-59.

4. Environment Effects on the Stability of Chromia (Cr₂O₃) Scale Formed on Type 310S Stainless Steel during Wet Oxidation

S. Mahboubi, H.S. Zurob, G.A. Botton and J.R. Kish*

*Department of Materials Science and Engineering, McMaster University,
Hamilton, ON, Canada*

*Corresponding author: kishjr@mcmaster.ca; 905-525-9140, Extension 21492

Submitted to *Corrosion* on January 30th, 2018

4.1. Abstract

The possibility of surrogating high-pressure supercritical water (SCW) with an ambient pressure air-10% H₂O mixture for studying the wet oxidation resistance of Type 310S stainless steel (UNS S31008) at high temperatures is examined by means of gravimetric measurements and electron microscopy techniques. The kinetics of wet oxidation in the two environments at 550°C is distinctly different: parabolic for the air-10% H₂O mixture and breakaway for SCW. The vapour pressure of Cr-oxy-hydroxide species is estimated to be similar in the two environments, but the rate of the Cr-oxy-hydroxide formation is significantly lower in the air-10% H₂O mixture. The much slower volatilization rate of the oxide scale formed in the air-10% H₂O mixture is attributed to the much lower total pressure of this environment, which serves to prolong the stability of the protective Mn-oxide (MnCr₂O₄) spinel outer layer.

Keywords: Supercritical water, Oxidation, Stainless steels, Pressure

4.2. Introduction

Austenitic stainless steels with a Cr concentration of about 20-25 wt.% (depending on the alloy grain size and surface finish) are well known to exhibit excellent oxidation resistance at high temperatures.¹⁻⁴ The excellent oxidation resistance is imparted by the formation of an external adherent protective chromia (Cr_2O_3) scale.^{2,3,5} It is well known that in the presence of water vapour (H_2O) and oxygen (O_2), the Cr_2O_3 scale reacts to form several gaseous species, among which Cr (VI) oxy-hydroxides [$\text{CrO}_2(\text{OH})_2$] dominate at temperatures below $\sim 1000^\circ\text{C}$.⁶⁻⁹ The volatilization rate of the Cr_2O_3 scale is strongly dependent on temperature, gas flow rate, O_2 and H_2O partial pressures, total pressure of the environment, and the Cr diffusion rate in the alloy.¹⁰⁻¹² Continuous volatilization of, and associated Cr depletion from, the Cr_2O_3 scale promotes Fe diffusion from the alloy into the scale.^{12,13} If the Cr diffusion rate in the alloy to the Cr_2O_3 scale is relatively slow, the incorporation of Fe into the scale can accelerate the Fe-rich oxide formation.^{12,14-19} Accelerated Fe-rich oxide formation (breakaway kinetics) is not desirable from a high-temperature oxidation perspective since the Fe diffusion rate is considerably faster in the porous non-protective Fe-rich oxides than in the protective Cr_2O_3 scale.^{10,20,21} Although volatilization of the Cr_2O_3 scale during wet oxidation has been widely reported in the literature, the mechanism of the breakaway kinetics, particularly in the presence of other oxidizing alloying elements such as Mn and Si is not well-understood since it is unclear if the accelerated Fe-rich oxide formation is as a result of the presence of a Cr-depleted underlying

substrate that contains a Cr content below the critical value required to maintain the Cr supply to the scale, residual stresses in the scale (mechanical spallation), and/or scale volatilization (chemical spallation).^{15,22,23}

Type 310S stainless steel (UNS S31008) has been short-listed as fuel cladding for the Generation IV Canadian supercritical water reactor (SCWR) design concept.^{24–26} The level of stability of the protective Cr_2O_3 scale under the expected oxidizing conditions (outlet temperature of 625°C at 25 MPa) for the supercritical water (SCW) coolant with an associated fuel cladding operating temperature (maximum of 800°C) is a key knowledge gap that needs to be addressed. The stability of Cr_2O_3 scales formed on the candidate fuel cladding alloys in SCW has been given some considerations,^{27–31} but testing has been conducted using sophisticated autoclave testing facilities that typically restrict testing temperatures at or below 625°C.³² Some work has been devoted to using low-pressure (0.1 to 10 MPa) steam as a surrogate for SCW to extend the testing conditions to higher temperatures and/or longer times.^{33–37} The results of these studies have been mixed and it seems that the level of success in using low-pressure steam as a reasonable surrogate for SCW depends on the alloy examined.

Thermodynamic calculations of $\text{CrO}_2(\text{OH})_2$ vapour pressure in steam as a function of inverse temperature show that the $\text{CrO}_2(\text{OH})_2$ partial pressures become significant at the higher steam pressures.^{6,10,38} If the oxygen required for the formation of the $\text{CrO}_2(\text{OH})_2$ species is supplied from a source other than steam dissociation, for example, in case of the air- H_2O mixture, the vapour pressure of

$\text{CrO}_2(\text{OH})_2$ becomes comparable to that for steam at high pressures.¹⁰ The $\text{CrO}_2(\text{OH})_2$ vapour pressure in ambient pressure (0.1 MPa) air-10% H_2O has been estimated to be similar to that in steam at 24-34 MPa.¹⁰ Thus, an air-10% H_2O mixture at 0.1 MPa is a promising possible surrogate for SCW that deserves consideration.¹⁰ The purpose of this study is therefore to examine the suitability of using an ambient pressure air-10% H_2O mixture as a surrogate for high-pressure SCW by directly comparing the oxidation kinetics exhibited by, and the structure and composition of the oxide scale formed on, Type 310S stainless steel in the two oxidizing H_2O -containing environments. We recently showed that the Cr_2O_3 scale formed on Type 310S stainless steel after up to 542 h exposure in flowing oxygenated SCW indicated clear signs of accelerated Fe-rich oxide formation.¹⁹ The results of that study are used as the SCW exposure comparative baseline for the ambient pressure air-10% H_2O mixture exposure reported herein. The oxidation kinetics were characterized by making gravimetric measurements as a function of time, whereas the evolution of the composition and structure of the oxide scale that formed was characterized using electron microscopy techniques.

4.3. Experimental Procedures

4.3.1. Oxidation Testing Apparatus and Conditions

Commercial plate of Type 310S stainless steel was solution annealed at 1150°C for 1 h followed by water quenching to room temperature and then cut into coupons using a diamond wheel saw and mineral oil as lubricant. The chemical composition reproduced from the mill certificate of the plate (in wt.%) is 24.3% Cr, 19.5% Ni, 1.0% Mn, 0.8% Si, 0.3% Mo, 0.06% C, 0.03% S, 0.04% P, and Fe (balance). Coupon dimensions are 15 mm × 9.2 mm × 1.5 mm and the alloy average grain size (diameter) is $78 \pm 33 \mu\text{m}$ (within the 95% confidence interval [CI]) as measured using the ASTM standard E112-13 linear intercept method.³⁹ Coupons were manually ground to 800 grit SiC abrasive paper using water as a lubricant. Prior to each of the exposure tests, coupons were cleaned with ethanol and dried with a warm air stream.

An oxidation testing apparatus was designed for the air-10% H₂O mixture exposure, the layout of which is shown in **Figure 4-1**. Distilled water was held inside a water flask at 46°C. Air as the H₂O carrier was fed inside the flask. At 46°C, a mixture of air-10% H₂O was produced.⁴⁰ The air-10% H₂O mixture with the flow velocity of 4.2 cm/s (measured on both ends of the furnace) entered a quartz tube (with 10 mm inner diameter) positioned inside an 80 cm long horizontal furnace. The horizontal furnace was kept at $550 \pm 5^\circ\text{C}$ and 0.1 MPa during the exposure times of 100 h, 250 h, 500 h and 1000 h. A set of five coupons were fitted in the center of the quartz tube for each exposure with the air-10% H₂O mixture flushing

through the tube and passing the coupon faces which were parallel to the gas flow. After the desired exposure time was attained coupons were removed from the furnace and air cooled. The mass of each coupon was measured prior to and after exposure using an analytical mass balance with a precision of 0.0001 g to determine the weight gain associated with the exposure.

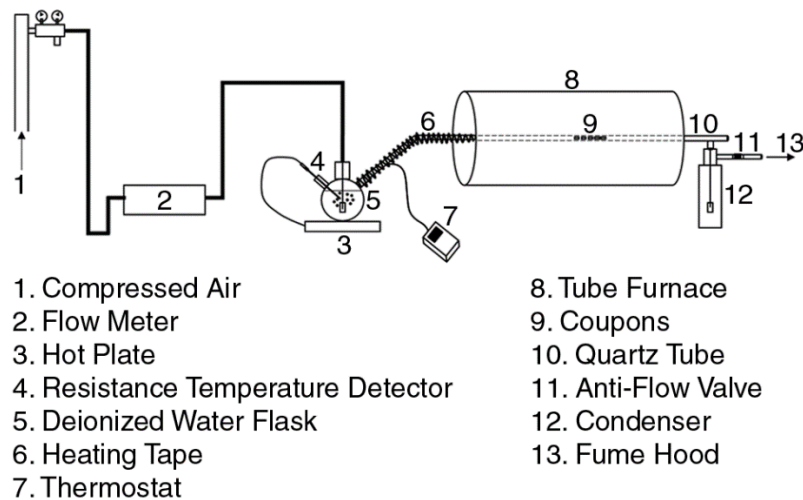


Figure 4-1. Layout of the wet oxidation testing apparatus for exposures in flowing 0.1 MPa air-10% H₂O.

4.3.2. Electron Microscopy Characterization of the Oxidized Coupons

The morphology of the oxide surfaces were examined by secondary electron imaging using a JEOL JAMP-9500F AUGER/FE-SEM* microscope. A 10 kV electron beam and a working distance of 20-24 mm was used for all imaging. Atomic concentration depth profiles through the oxide scales were determined using Auger electron spectroscopy (AES) with the coupons tilted 30° towards the

* Trade name

Auger electron detector. A 3 kV Ar⁺ beam was first used for ~8 s to etch away any surface contamination. A combination of 10 kV electron beam (for Auger electron generation) and 3 kV Ar⁺ beam (for etching) was then used to acquire a concentration depth profile as a function of sputtering time. The acquired deconvoluted curves were then compared with the references using the JEOL^{*} microscope software.

Focused ion beam (FIB, Zeiss NVision 40 CrossBeam® Workstation^{*}) milling was used to prepare a transmission electron microscopy (TEM) cross-sectional sample of the oxide scale formed on the coupon exposed for 1000 h (longest exposure time). Once the site of interest was chosen, two (electron and ion) C layers followed by a W layer were deposited on top of the oxide scale to protect the scale from any damage that could occur during ion milling. A Ga⁺ beam with an incident energy of 30 keV and a current of 90 pA was then used on a coupon loaded at a working distance of 5 mm. Using Ga⁺ beam milling, the TEM sample was separated from the rest of the coupon. The final TEM sample was removed from the coupon and attached to a TEM Cu grid.

Cross-sectional analysis of the FIB prepared TEM sample was done using a field emission JEOL 2010F TEM/STEM^{*}, equipped with an Oxford INCA^{*} energy dispersive X-ray spectroscopy (EDS) system. The TEM analysis was performed using a 200 keV electron beam. Selected area diffraction (SAD) patterns were acquired from regions of interest for phase identification. The patterns were acquired with the smallest SAD aperture available. The JEMS^{*} software was used

to simulate the SAD patterns of the expected phases as a comparative basis for the acquired patterns.⁴¹ To examine the regions of interest smaller than 150 nm, high resolution TEM (HRTEM) and the related Fourier transformed (FT) patterns were obtained using a 200 keV electron beam. FT images were examined using the Gatan DigitalMicrograph* and JEMS* software based on the expected phases as a comparative basis.^{41,42}

Scanning TEM (STEM)-EDS elemental maps were acquired in the bright-field (BF) mode. Complementary electron energy loss spectroscopy (EELS) spectra in the high angle annular dark (HAADF)-STEM mode were also acquired. A 510 eV energy shift and 0.2 eV/channel dispersion were used to include peaks of O, Cr, Mn, Fe, and Ni in one spectrum. A separate energy window with 80 eV drift and 0.2 eV/channel was used for the Si peaks. The EELS results were analyzed using the Gatan DigitalMicrograph* software.⁴² The acquired EELS spectra were benchmarked against the published spectra to help with phase identification.

4.4. Results

Figure 4-2 shows the weight gain data measured as a function of exposure time in 0.1 MPa flowing (4.2 cm/s) air-10% H₂O at 550°C. The error bars represent 95% CI for replicate set of five coupons exposed. A relatively small, yet appreciable, change in weight gain is observed during exposure up to 1000 h. Superimposed onto the plot is the weight gain data measured as a function of exposure time in flowing (0.05 cm/s) oxygenated (8 ppm dissolved oxygen) 25 MPa SCW at 550°C from our previous study.¹⁹ The difference between the coupons weight gain data for short exposure times (< 250 h) in the two environments is negligible. The relatively high weight gain measured after 542 h exposure in SCW starkly contrasts the relatively small weight gain measured after 1000 h exposure in air-10% H₂O. It is clear that the SCW exposure is significantly more aggressive to Type 310S stainless steel than air-10% H₂O at 550°C.

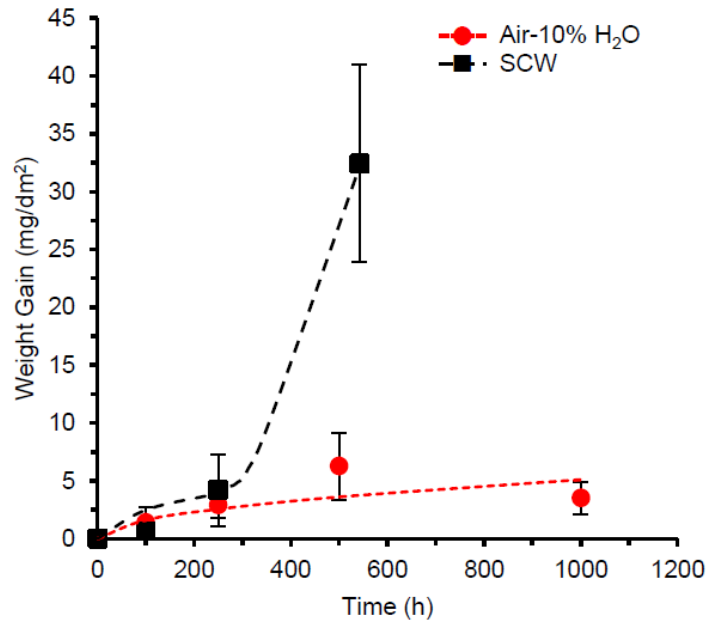


Figure 4-2. Weight gain data of the coupons exposed for up to 1000 h in flowing 0.1 MPa air-10% H₂O at 550°C (dashed red line). Weight gain data of the coupons exposed in flowing oxygenated 25 MPa SCW at 550°C for up to 542 h are also shown for comparison (dashed black line).¹⁹

Plan-view secondary electron images in **Figure 4-3[a]-[d]** show the evolution of the oxide scale during exposure in air-10% H₂O. A compact uniform scale with a smooth topography is formed during the initial 250 h of exposure (**Figure 4-3 [a]** and **Figure 4-3[b]**). The scale formed after 500 h exposure (**Figure 4-3[c]**) is relatively rough. Trigonal oxide nodules form on top of the scale, leading to the rough topography. After 1000 h exposure, a rough scale once again forms on the coupons surface (**Figure 4-3[d]**), presumably by the growth and coalescence of the oxide nodules that are present on the surface after 500 h exposure. Plan-view secondary electron images showing the evolution of the oxide scale during exposure in flowing oxygenated 25 MPa SCW at 550°C after 100 h, 250 h and 542 h exposure are reproduced in **Figure 4-3[e]-[g]** for comparison.¹⁹ After ~250 h

exposure Fe-rich oxide nodules are seen on the oxidized surface. After 542 h exposure, the Fe-rich oxide nodules cover almost the entire surface.¹⁹

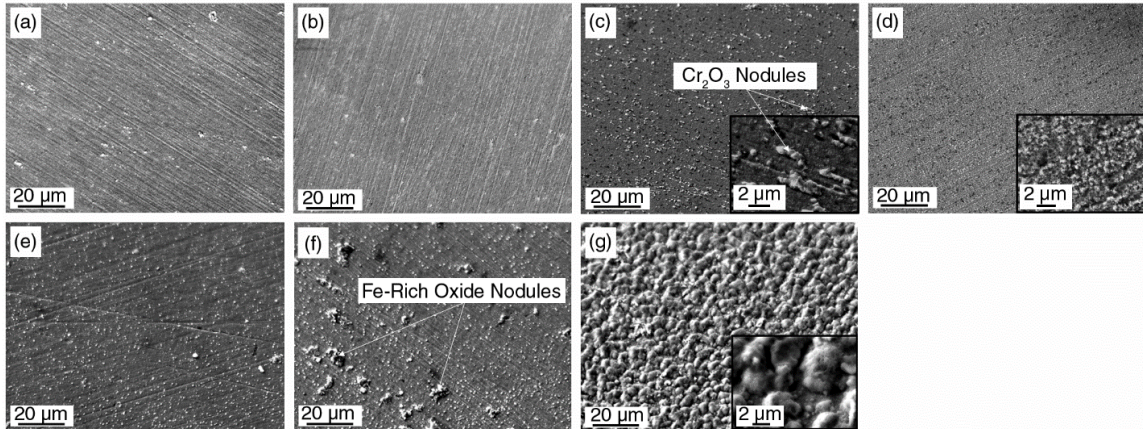


Figure 4-3. Plan-view secondary electron images of the Type 310S stainless steel surface after (a) 100 h, (b) 250 h, (c) 500 h, and (d) 1000 h exposure in flowing 0.1 MPa air-10% H₂O at 550°C. A corresponding set of images obtained after exposure in flowing oxygenated 25 MPa SCW at 550°C for (e) 100 h, (f) 250 h, and (g) 542 h are also shown for comparison.¹⁹

Figure 4-4 shows average atomic concentration depth profiles (acquired using AES) through the scale that forms during the various exposures at three different regions on the surface. A summary of the elemental concentration (at.%) obtained from AES for each of the layers form along with their characterization at different exposure times is shown in **Table 4-1**. The scale that forms after 100 h exposure (**Figure 4-4[a]**) is enriched with Cr and O relative to the unaffected matrix. The layer also contain Fe (less than ~5 at.%) and Mn (less than 8 at.%) as minor elements, being somewhat enriched at the scale/gas interface. The double-layered oxide was best characterized as (Cr,Mn)₂O₃ on top of Cr₂O₃ using the AES concentration quantification. A relatively narrow Cr-depleted zone (an associated Fe- and Ni-enrichment zone) relative to the unaffected matrix is also present in the

matrix adjacent to the scale. The scale that forms after 250 h exposure (**Figure 4-4[b]**) consists of two layers: an outer layer containing Cr, Mn and O as major elements best characterized using the AES concentration quantification as MnCr_2O_4 on top of an inner layer containing just Cr and O as major elements characterized as Cr_2O_3 . Less than ~5 at.% Fe is dissolved in both layers. The depth of the Cr-depleted zone after 250 h exposure is slightly larger than it is after 100 h exposure. After 500 h exposure (**Figure 4-4[c]**), the scale again consists of two layers: an outer layer containing Cr, Mn and O as major elements best characterized as MnCr_2O_4 using the AES concentration quantification on top of an inner layer containing just Cr and O as major elements characterized as Cr_2O_3 . Less than ~5 at.% Fe is dissolved in both layers. The depth of the Cr-depleted zone forms after 500 h exposure is substantially larger than it is after 250 h exposure. The scale after 1000 h exposure (**Figure 4-4[d]**) is thicker than it is after 500 h exposure. Again, the scale consists of two layers: an outer layer containing Cr, Mn and O as major elements best characterized as MnCr_2O_4 using the AES concentration quantification on top of an inner layer containing just Cr and O as major elements. Less than ~5 at.% Fe is again dissolved in both layers. In all of the concentration depth profiles, no detectable change in the Si profiles is found.

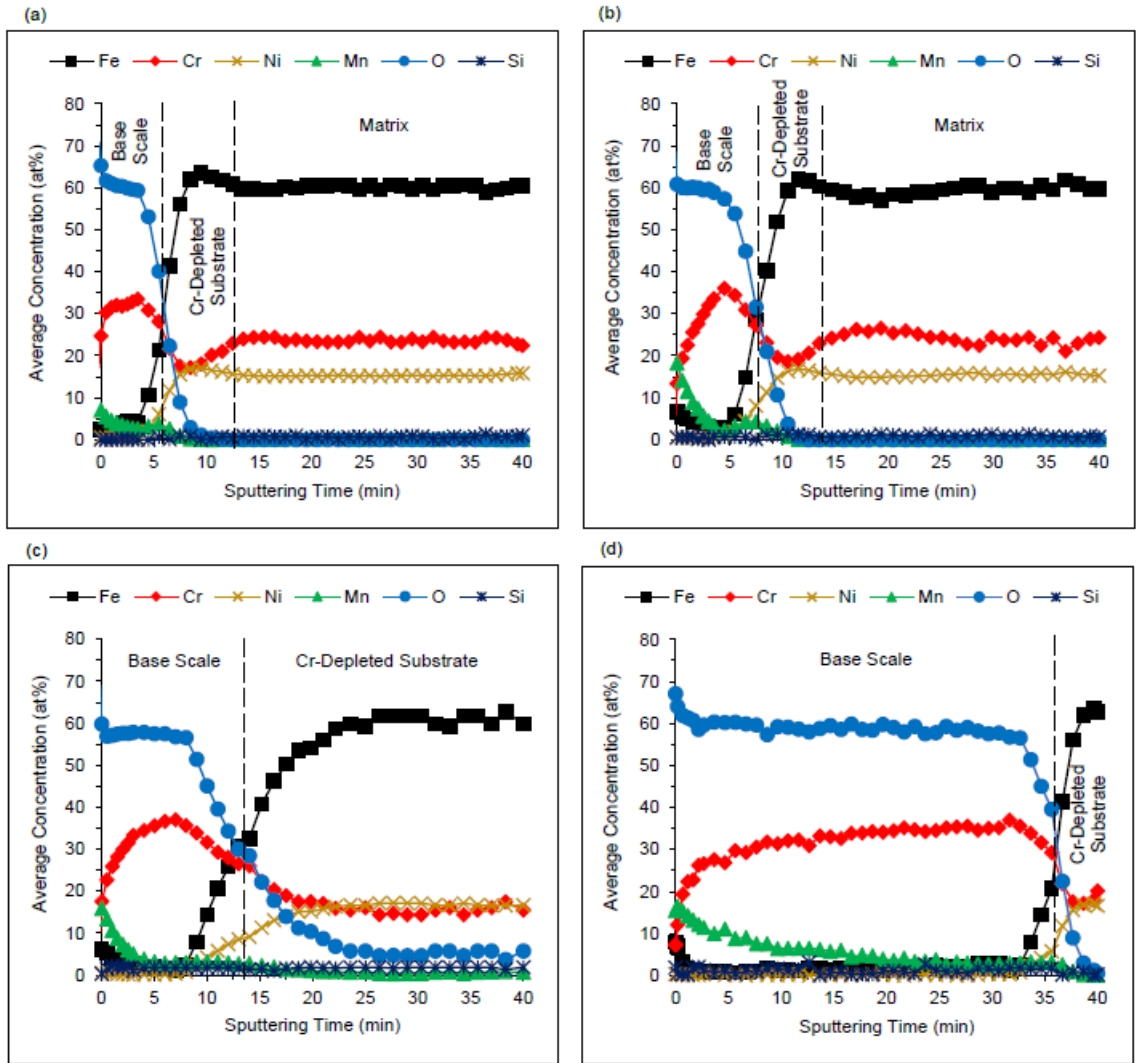


Figure 4-4. Average atomic concentration depth profile of Fe, Cr, Ni, Mn, O, and Si across the scale/alloy interface after (a) 100 h, (b) 250 h, (c) 500 h, and (d) 1000 h exposure in flowing 0.1 MPa air-10% H₂O at 550°C.

Table 4-1 Elemental composition (at.%) of each of the oxide layers, obtained from AES

| Time (h) | Layer Area | Fe | Cr | Ni | Mn | O | Characterized Layer |
|----------|------------|-----|----------|-------|----------|--------|-------------------------------------|
| 100 | Top | <~5 | 30 ± 4 | <~0.5 | 7 ± 1 | 62 ± 4 | (Cr,Mn) ₂ O ₃ |
| | Bottom | <~5 | 32 ± 1 | <~0.5 | <~5 | 60 ± 1 | Cr ₂ O ₃ |
| 250 | Top | <~5 | 22.5 ± 4 | <~0.5 | 11.5 ± 3 | 60 ± 2 | MnCr ₂ O ₄ |
| | Bottom | <~5 | 33 ± 3 | <~0.5 | <~5 | 58 ± 3 | Cr ₂ O ₃ |
| 500 | Top | <~5 | 23 ± 1 | <~0.5 | 14 ± 3 | 57 ± 3 | MnCr ₂ O ₄ |
| | Bottom | <~5 | 36 ± 1 | <~0.5 | <~5 | 57 ± 1 | Cr ₂ O ₃ |
| 1000 | Top | <~5 | 23 ± 4 | <~0.5 | 13 ± 2 | 59 ± 4 | MnCr ₂ O ₄ |
| | Bottom | <~5 | 34 ± 1 | <~0.5 | <~5 | 54 ± 1 | Cr ₂ O ₃ |

*Less than 5 at% dissolved elements in the oxides are not considered in the final scale characterization.

** Si concentration is too low for detection using AES.

Figure 4-5 shows cross-sectional BF-STEM image of the oxide scale formed after 1000 h exposure in flowing 0.1 MPa air-10% H₂O at 550°C along with the STEM-EDS elemental maps of Cr, Mn, O, Fe, Ni, Si, and C. A compact, relatively rough scale with the thickness of $\sim 244 \pm 44$ nm (within 95% CI) is formed on the surface. Recrystallized grains, presumably a consequence of the localized surface plastic deformation incurred from sample preparation (grinding)⁴³ are seen below the scale. Cr- and C-rich regions are visible beneath the recrystallized grains found in the Cr-depleted zone. The scale consists of three layers: an outer layer containing just Mn and O as major elements on top of an intermediate layer containing Cr, Mn and O and major elements on top of a substantially thinner discontinuous (~ 10 nm wide) Si-rich oxide layer. Note that Si and W STEM-EDS peaks overlap and the enrichment seen on top of the Si map originates from the W deposited layer on the TEM sample during FIB milling.

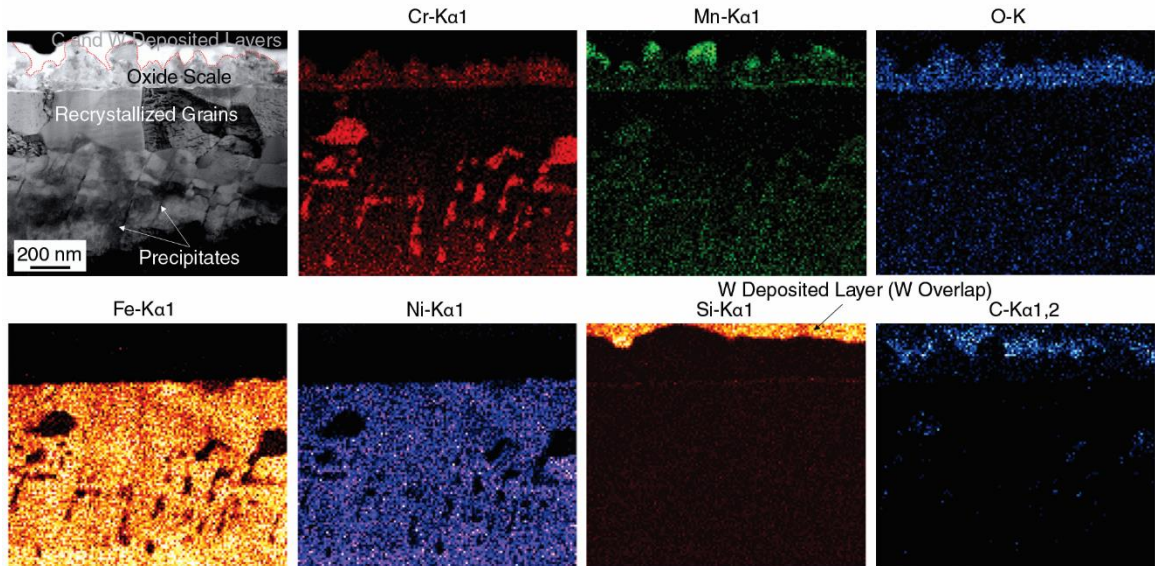


Figure 4-5. BF-STEM cross-sectional image and associated STEM-EDS elemental maps of Cr, Mn, O, Fe, Ni, Si, and C of the oxide scale formed after 1000 h exposure flowing 0.1 MPa air-10% H₂O at 550°C.

Figure 4-6 shows the HAADF-STEM image of the oxide scale formed after 1000 h in flowing 0.1 MPa air-10% H₂O at 550°C and the corresponding EELS spectra from each of the five areas identified. The Mn concentration decreased from *Area 1* (the top surface) to *Area 4* (the bottom interface of the scale). The energy position of each of the major elements peaks for the interested oxide compounds are shown in **Table 4-2**. The integrated peak ratios are also compared in **Table 4-2** with the values in the literature. The structure and composition of the scale from the top to bottom was characterized accordingly as: MnO with minor Fe dissolved (*Area 1*), MnCr₂O₄ with minor Fe dissolved (*Area 2*), Cr₂O₃ with minor Fe dissolved (*Area 3*), (Cr,Mn)₂O₃ with minor Fe dissolved (*Area 4*), and (Cr,Fe,Mn)₂O₃ (*Area 5*).

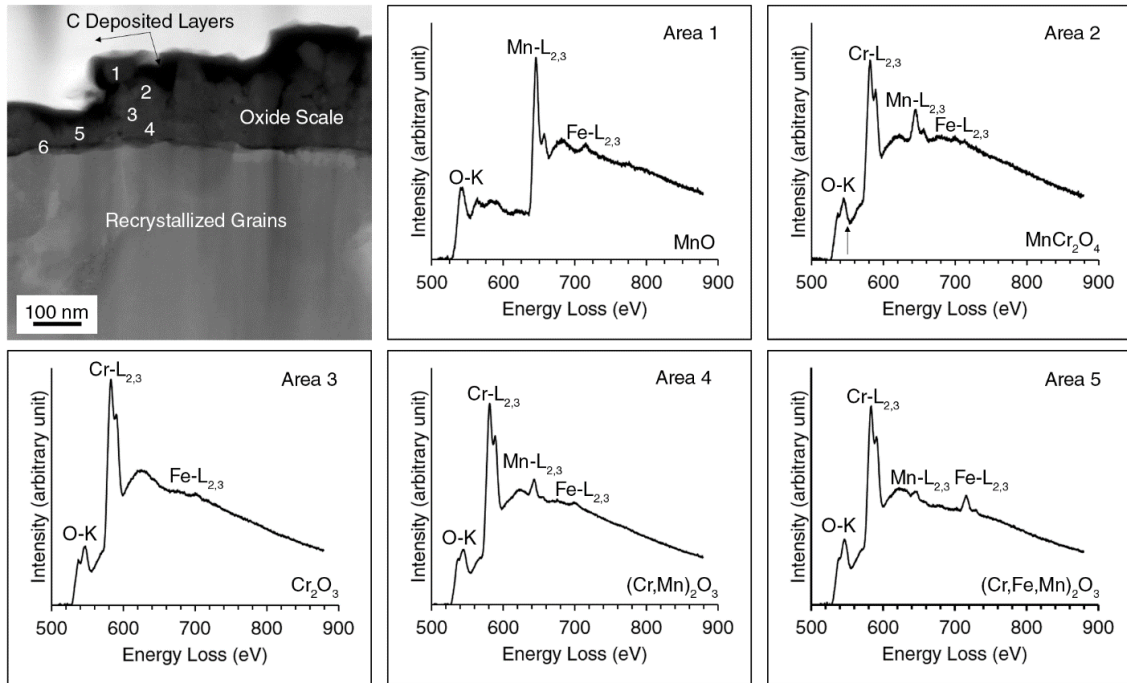


Figure 4-6. HAADF-STEM cross-sectional image of the oxide scale formed after 1000 h exposure in flowing 0.1 MPa air-10% H₂O at 550°C and the corresponding EELS spectra from the areas identified.

Table 4-2 Energy positions (eV) for the major peaks in each of the oxide compounds with ± 0.2 eV error. A comparison of the integrated L₃/L₂ peaks ratio in this study with those reported in the literature is also shown.

| Oxide Type | O | | Cr | | | Mn | | | |
|----------------------------------|----------------|----------------|----------------|--|---|----------------|----------------|--|---|
| | K (first edge) | L ₃ | L ₂ | I _{L₃} /I _{L₂} | (I _{L₃} /I _{L₂}) _{Lit.} | L ₃ | L ₂ | I _{L₃} /I _{L₂} | (I _{L₃} /I _{L₂}) _{Lit.} |
| MnO | 540.2 | - | - | - | - | 645.4 | 656.6 | 1.6±0.3 | ~2-3.9 ⁴² |
| MnCr ₂ O ₄ | 537.0 | 581.6 | 589.0 | 1.2±0.1 | ~1.3 ⁴³ | 644.4 | 656 | 1.2±0.2 | ~1.4 ⁴³ |
| Cr ₂ O ₃ * | 535.8 | 583.2 | 592 | 1.2±0.1 | ~1.4 ⁴⁴ | - | - | - | - |

*The intensity ratio of the peaks for the Cr₂O₃ scales with small amounts of Fe and Mn dissolved is somewhat similar and not shown herein.

Figure 4-7(a) shows the EELS spectrum from Area 6 in the HAADF-STEM image in **Figure 4-6**. The energy position of the L₁ and L_{2,3} Si peaks with ± 0.2 eV error are 158.5, and 108.9 eV, respectively confirming that the oxide layer is SiO₂. The

HRTEM image of the SiO₂ layer (**Figure 4-7[b]**) shows that the discontinuous layer seen in the STEM-EDS maps is amorphous with the width of ~10 nm.

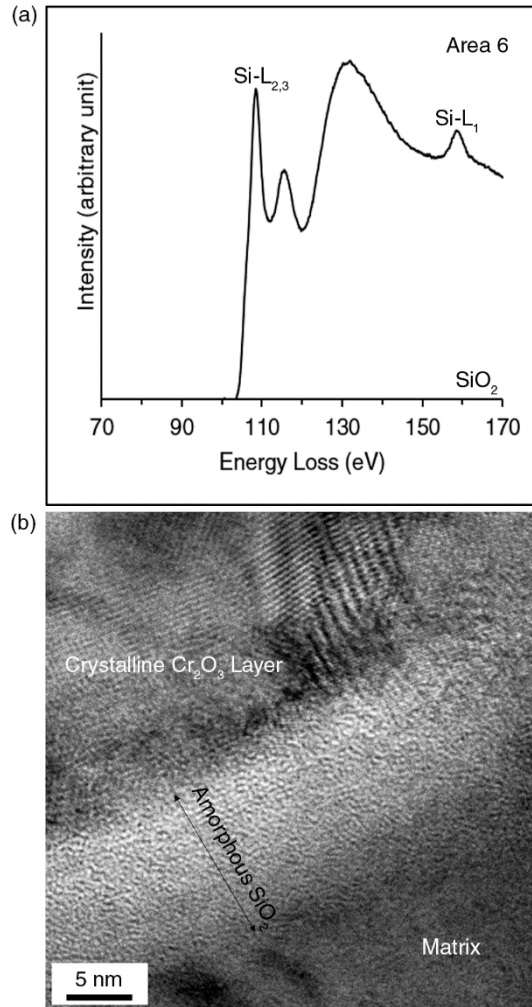


Figure 4-7. (a) EELS spectrum from Area 6 in Figure 6 and (b) HRTEM image of the SiO₂ layer.

Figure 4-8(a) shows a BF-STEM cross-sectional image of the Cr- and C-rich precipitate found in Cr-depleted zone, along with an associated SAD pattern acquired from the precipitate. The region analyzed by SAD has ~150 nm diameter and resides well inside the precipitate. **Figure 4-8(b)** shows the STEM-EDS

intensity profiles from the precipitate and its adjacent matrix. The precipitates are identified as Cr_{23}C_6 with Fe and Ni dissolved.

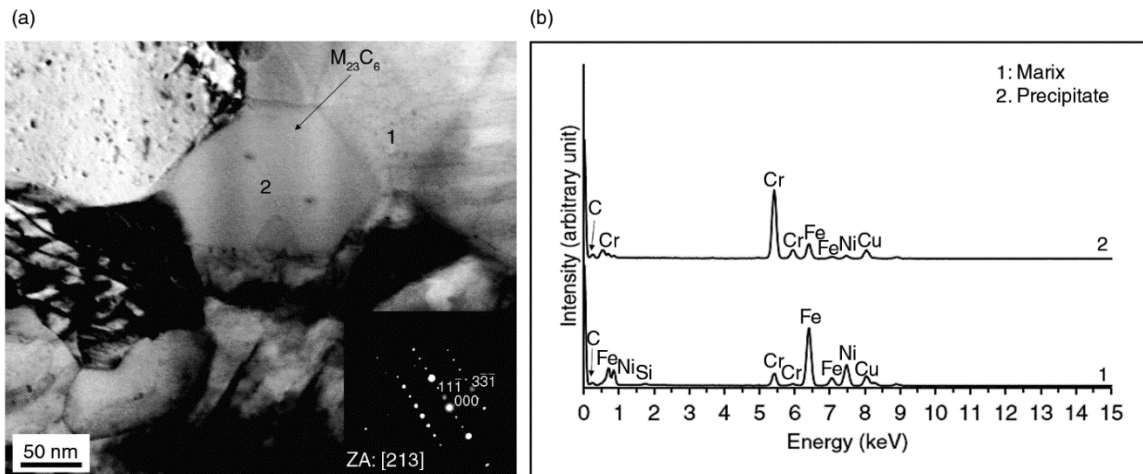


Figure 4-8. (a) BF-STEM cross-sectional image and associated SAD pattern of a Cr-carbide Cr_{23}C_6 precipitate formed in the Cr depleted zone in the coupon exposed for 1000 h in flowing 0.1 MPa air-10% H_2O at 550°C and (b) the STEM-EDS intensity profiles from the precipitate and its adjacent matrix.

4.5. Discussion

4.5.1. Oxidation Kinetics

The relatively small change in the weight gain data of coupons exposed in flowing (4.2 cm/s) 0.1 MPa air-10% H₂O at 550°C for up to 1000 h, considering the error bars, suggests that the oxidation kinetics follow the classic parabolic rate law. No evidence of scale volatilization was found from the kinetics data. The thickness of the oxide scale and Cr-depleted substrate after 1000 h exposure as measured from STEM-EDS images are 244 ± 44 nm and 376 ± 181 nm, respectively. The increase in the oxide thickness with time as shown by the AES results in **Figure 4-4** clearly confirms that the oxidation kinetics follow the parabolic rate law. The weight gain data in the 25 MPa flowing (0.05 cm/s) oxygenated SCW at 550°C for up to 542 h shows an initial parabolic regime that is followed by a linear kinetic regime due to the accelerated Fe-rich oxide formation.¹⁹ The combination of a parabolic and a linear kinetic is the characteristic feature of “breakaway kinetics”: a parabolic regime due to scale accumulation and a linear regime due to scale volatilization resulting in the accelerated formation of Fe-rich oxide nodules.^{44,45} It is plausible that after 542 h exposure in SCW, a plateau is reached in the weight gain results, therefore the conclusion that breakaway kinetics is observed during the 542 h exposure must be validated by exposure of coupons in SCW for longer times.

The thickness of the oxide scale measured from areas without the Fe-rich nodules, and Cr-depleted substrate after 542 h exposure as measured from STEM-

EDS images are 275 ± 68 nm and 1061 ± 120 nm, respectively.¹⁹ It is evident that a large amount of Cr is depleted from the substrate but not incorporated into scale thickening and must be lost due to scale volatilization. It must be noted that the flow velocity in the air-10% H₂O test was chosen to be relatively high (4.2 cm/s) compared to that in the SCW test (0.05 cm/s) to increase the scale volatilization rate. The flow velocity chosen here however is not as high as the values used in the industrial applications (~6 m/s) because of the instrumental limitations.⁴⁶ Even with the difference in the flow rates seen here, the kinetics in air-10% H₂O and SCW is distinctly different, which immediately suggests that the 0.1 MPa air-10% H₂O is not a good surrogate for the 25 MPa SCW at 550°C and relatively small gas velocities.

The thickness of scales and the depth of Cr-depleted substrates formed particularly after 100 h and 250 h exposure in air-10% H₂O mixture and after 100 h and 250 h exposure in SCW are too small for a detailed characterization by SEM-EDS analysis. As a result, a direct comparison between scales thicknesses and the corresponding Cr-depleted depths is not straightforward and requires preparing the samples by FIB followed by STEM-EDS analysis. AES results are therefore used to make this comparison instead. **Figure 4-9** shows a plot of the time required to sputter completely through the Cr₂O₃ scale as a function of time required to sputter completely through the Cr-depleted substrate (obtained from the AES depth profiles) for coupons exposed in 0.1 MPa flowing air-10% H₂O at 550°C and 25 MPa flowing oxygenated SCW at 550°C.¹⁹ The relation between the sputtering time

through the Cr_2O_3 scale and Cr-depleted substrate is linear for the air-10% H_2O test and parabolic for the SCW test. It is evident that regardless of any possible oxide solubility in the two environments, nearly all of the Cr that is depleted from the substrate in the coupons exposed in air-10% H_2O contributes to the scale thickening. The parabolic relationship between the sputtering times of the Cr_2O_3 scale and the Cr-depleted substrate in the SCW suggests that only a fraction of the Cr removed from the substrate contributed in the scale thickening whereas the rest of Cr is lost elsewhere: presumably due to scale volatilization.¹⁹ Comparison of the Cr-depleted substrate depth with respect to the scale thickness in the two environments by STEM analysis confirms that the larger Cr-depleted substrate observed after exposure in SCW is attributed to the higher Cr loss rate from the scale.

The formation of $\text{CrO}_2(\text{OH})_2$ is directly proportional to the total gas pressure of the environment ($p_{\text{CrO}_2(\text{OH})_2} \propto P$).¹⁰ The effect of gas pressure on the wet oxidation kinetics is not well understood and the data reported by laboratories often varies.¹⁰ It is believed that the higher total pressure effect is responsible for the increase in the $\text{CrO}_2(\text{OH})_2$ partial pressure and scale volatilization rate observed in SCW. It is reported that the O_2 partial pressure in the 25 MPa air-saturated flowing SCW test is relatively high which could be responsible for the observed increase in the scale volatilization in SCW.⁴⁷ Additionally, thermodynamic calculations do not consider the effect of time on the $\text{CrO}_2(\text{OH})_2$ formation. Despite the similar calculated $p_{\text{CrO}_2(\text{OH})_2}$ in the air-10% H_2O and SCW, it seems that a very long time

(clearly significantly more than ~1000 h at least) would be needed for the alloy exposed in air-10% H₂O to undergo the same kinetics behaviour observed in SCW.

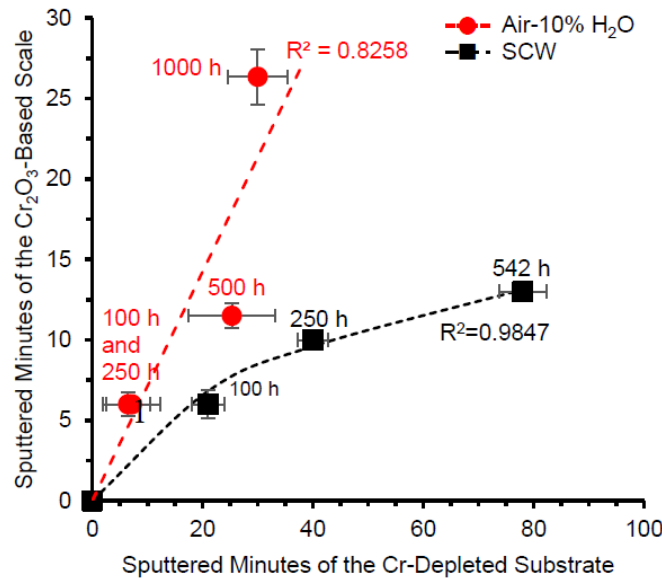
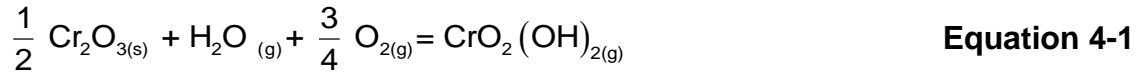


Figure 4-9. Plot of the time required to sputter completely through the minutes of the Cr₂O₃ scale as a function of time required to sputter completely through the minutes of the Cr-depleted substrate (obtained from the AES depth profiles data), for the coupons exposed in flowing 0.1 MPa air-10% H₂O at 550°C and flowing 25 MPa SCW at 550°C.¹⁹

4.5.2. Scale Evolution

Figure 4-10 shows a schematic summary of the scales formed on Type 310S stainless steel after exposure in 0.1 MPa flowing air-10% H₂O at 550°C for up to 1000 h. Note that small amounts of Fe and/or Mn dissolved in the scales are not shown for simplicity. In all of the exposure times, a Mn-rich oxide layer was formed on top of the Cr₂O₃ scale. High-temperature oxidation resistance of Type 310S stainless steel is mainly attributed to the relatively high Cr content of the alloy (24.3 wt%) resulting in the formation of an external protective Cr₂O₃ scale. The presence

of H₂O in the oxidizing environment adversely affects the protectiveness of the Cr₂O₃ scale by forming CrO₂(OH)₂ vapour species through **Equation 4-1**:^{6,12}



Subsequent Cr depletion of the scale and substrate can enhance the scale susceptibility to accelerated Fe-rich oxide formation.^{12,17} It is argued that the significant Cr₂O₃ scale volatilization is accompanied by more Fe diffusion into the scale.^{12,13} Further diffusion of Fe into the Cr₂O₃ scale in the absence of enough Cr supply, can result in the formation of Fe-rich oxide nodules on the surface.¹³ Formation of Fe-rich oxide nodules increases the corresponding weight gain of the alloy after exposure, similar to what is seen in SCW.¹⁹

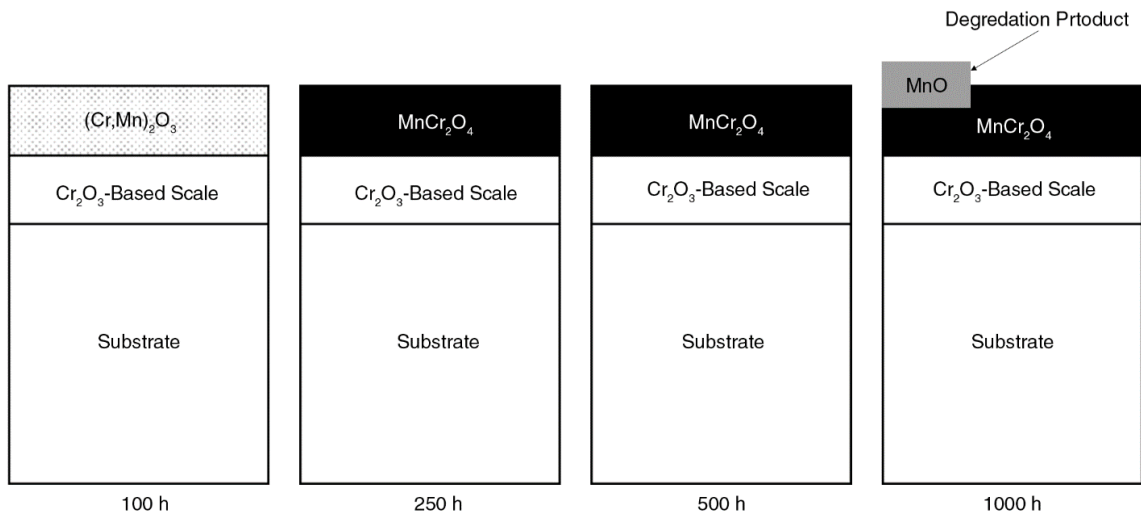
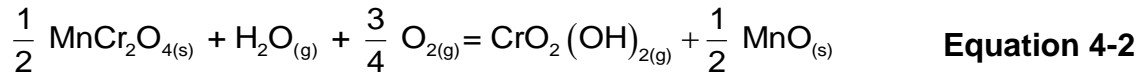


Figure 4-10. Summary of the scale structure and wet oxidation mechanism in flowing 0.1 MPa air-10% H₂O at 550°C. Thicknesses are not set to scale. Note that the SiO₂ layers beneath the Cr-rich scales are not shown.

It is well established that even very small amount of Mn in the alloy can incorporate to the Cr₂O₃ scale during the scale growth.⁴⁸ Because of the very similar affinity of Mn and Cr for O, Mn ions diffuse through the Cr₂O₃ scale forming MnCr₂O₄ layer on the oxide surface.⁴⁸⁻⁵⁰ Cr (VI) volatile species can also form from a MnCr₂O₄ layer in H₂O-containing environments.^{50,51} **Equation 4-2** shows the formation of CrO₂(OH)₂ gas species over a MnCr₂O₄ layer in the presence of H₂O and O₂:⁵¹



Fast diffusion of Mn into the MnCr₂O₄ also assists the formation of MnO.⁵⁰ The MnO degradation products formed can further oxidize to higher oxidation states (e.g. Mn₂O₃ or MnO₂) during the exposure time or cooling of the samples. Measurements of the maximum Cr loss from the MnCr₂O₄ and Cr₂O₃ scale in high-temperature air-3% H₂O has confirmed the effective role of MnCr₂O₄ layer in reducing the Cr₂O₃ scale volatilization rate.⁵¹ The effective role of MnCr₂O₄ is also experimentally shown in the earlier literatures,⁵²⁻⁵⁴ however, no physical evidence of the MnO degradation product has been found. Our STEM-EELS results clearly show that MnO forms on the surface after 1000 h exposure in 0.1 MPa flowing air-10% H₂O at 550°C. MnO is known to be a non-stoichiometric non-protective oxide that can increase ions diffusion and is not considered as a protective oxide.⁵⁵ It must be mentioned that MnO degradation product is only found after 1000 h

exposure in air-10% H₂O, therefore, a relatively long time is needed to see any physical evidence of volatilization whatsoever in air-10% H₂O at 550°C.

The sign of Mn-rich oxide degradation product was indeed found at shorter times in SCW (~100 h), however, Mn-rich oxides disappeared after ~250 h exposure in SCW suggesting that they could be chemically or mechanically removed by the SCW flow as discussed in our previous paper.¹⁹

The influence of the MnCr₂O₄ layer in reducing the volatilization rate of the scale has been discussed by the effect of temperature.⁵¹ Regardless of the pO_2 and pH_2O in the environment, the maximum evaporation ratio of Cr volatile species over a MnCr₂O₄ layer to that over a pure Cr₂O₃ layer is only dependent of temperature and the volatilization reduction factor in the presence of MnCr₂O₄ at 600°C is ~95.⁵¹ It is implied that the formation of an outer MnCr₂O₄ layer on top of a Cr₂O₃ scale is beneficial and can retard the volatilization rate of the latter by decreasing the surface contact area of the Cr₂O₃ scale (physical barrier effect) and the volatilizing environment.^{52,53} The increase in the scale thickness over time, along with the absence of any volatilization induced Fe-rich nodules on the surface, after coupons exposure in 0.1 MPa flowing air-10% H₂O at 550°C for up to 1000 h are in consistent with the effective role of MnCr₂O₄ layer in reducing the Cr₂O₃ scale volatilization rate.

It must be borne in mind that the presence of even small amount of Si in the alloy allows the formation of a SiO₂ layer/precipitates below the Cr₂O₃ scale.⁵⁶⁻⁵⁸

Whether or not the SiO₂ layer/precipitates add protection by serving as a physical barrier to reduce further ion diffusion through the scale depends on the alloy Si content and the SiO₂ layer thickness.⁵⁷⁻⁶⁰ It has been reported that the addition of ~1 wt.% Si to stainless steels when exposed to high temperature (~900°C) wet environments results in the formation of a uniform, protective SiO₂ layer below a Cr₂O₃ layer which reduces the oxidation rate.⁶¹ The very thin discontinuous SiO₂ layer (~10 nm wide) observed in this study are, therefore, not considered to play a major role in controlling the oxidation rate. It should be noted that the scale formed after 500 h exposure in the air-10% H₂O mixture shows variation in the concentration of elements on the surface. AES spot analysis and STEM-EELS results from different parts of the scale showed that Mn concentration is different at each area. It is possible that the Cr loss from the MnCr₂O₄ is a local phenomenon that results in the concentration gradient seen on the scale surface.

It is important to note stresses can generate within the oxide layers during the isothermal oxide formation (growth stress) or cooling from the oxidation temperature (thermal stress).⁶²⁻⁶⁵ For the scales forming at the alloy/oxidizing environment interface, e.g. Cr₂O₃ scales, the growth stress and the corresponding increase in the oxide volume is small and mirrored in the scale thickness.⁶⁶ However, thermal stresses can still generate the amount of which is directly related to the difference between the thermal expansion coefficient of the oxide and alloy or oxide and oxide interface.^{67,68} Since the linear coefficient of thermal expansion difference between MnCr₂O₄ (7.2×10^{-6} 1/°C) and Cr₂O₃ (9.6×10^{-6} 1/°C) at 550°C

after relatively long exposure times is quite small,⁶⁹ it is more likely that the accelerated Fe-rich oxide formation in SCW was as a result of chemical reaction (Mn-rich oxide dissolution) rather than mechanical spallation of MnCr_2O_4 over Cr_2O_3 due to residual stresses.

It should also be noted that the only carbide type found in the current study was Cr_{23}C_6 with small amounts of Fe and Ni, and other common precipitates in the stainless steels namely: Sigma, Laves and Chi phases were not detected in the coupon exposed for 1000 h in 0.1 MPa flowing air-10% H_2O at 550°C. Nevertheless, since no carbide was seen in the Cr-depleted zone and it seems they are dissolved to supply Cr to the scale,⁷⁰ the formation of carbide precipitates seems not to have any effect on the oxidation mechanism, albeit they can affect mechanical properties of the alloy and assist stress corrosion cracking (SCC).^{24,71}

4.5.3. Significance to SCW Testing

Results from this study show that the flowing air-10% H_2O mixture (4.2 cm/s) is not a suitable surrogate for flowing SCW (0.05 cm/s) at 550°C. These findings have meaningful implications regarding testing of suitable high-temperature oxidation resistant fuel cladding materials for the Canadian-SCWR concept. It is possible that increasing the temperature of the air-10% H_2O mixture and using gas velocities closer to the values used in the industrial applications⁴⁶ increase the Cr loss rate from the MnCr_2O_4 oxide cap and the Cr_2O_3 scale and then leads to the similar volatilization kinetics observed at lower temperatures in SCW. The effect of

temperature on the high-temperature wet oxidation kinetics of Type 310S stainless steel in the air-10% H₂O mixture will be presented and discussed in a future publication.

4.6. Conclusions

The possibility of surrogating 25 MPa SCW with an ambient pressure air-10% H₂O mixture for high-temperature oxidation studies is examined within the context of stability of the Cr₂O₃ scale. The vapour pressure of the CrO₂(OH)₂ in SCW is estimated to be similar to that for the ambient pressure air-10% H₂O mixture. Despite this, volatilization is significantly slower in the air-10% H₂O mixture. The main difference between the oxide scales on the two alloys occurs after 250 h exposure when the increase in the volatilization rate in SCW results in the accelerated Fe-rich oxide formation while scale formed in air-10% H₂O mixture stays intact and protective even up to 1000 h exposure. Physical evidence of Cr loss from the MnCr₂O₄ layer along with the formation of the MnO degradation product were found which are in consistent with the previously published studies.⁵¹⁻
⁵⁴ The much slower volatilization of the oxide scale formed in the air-10% H₂O mixture is attributed to the much lower total pressure of this environment, which serves to prolong the stability of the protective MnCr₂O₄ outer layer.

4.7. Acknowledgements

The authors acknowledge the funding to Canada Gen-IV National Program was provided by Natural Resources Canada through the Office of Energy Research and Development, Canadian Nuclear Laboratories, and Natural Sciences and Engineering Research Council of Canada. The authors thank the staff in the Canadian Centre for Electron Microscopy (CCEM), a national facility supported by NSERC, the Canada Foundation for Innovation under the Major Science Initiative and McMaster University, for their technical assistance with sample preparation and electron microscopy assistance.

4.8. References

1. C.T. Fujii, and R.A. Meussner, *J. Electrochem. Soc.* 111 (1964): pp. 1215–1220.
2. N. Otsuka, Y. Shida, and H. Fujikawa, *Oxid. Met.* 32 (1989): pp. 13–45.
3. V.V. Khokhlov, A.G. Rakoch, E.S. Dement, and O.A. Lyzlov, 40 (2004): pp. 62–66.
4. B.A. Pint, R. Peraldi, and P.J. Maziasz, *Mater. Sci. Forum* 461–464 (2004): pp. 815–822.
5. R. Peraldi, and B.A. Pint, *Oxid. Met.* 61 (2004): pp. 463–483.
6. D.J. Young, D.J. and B.A. Pint, *Oxid. Met.* 66 (2006): pp. 137–153.
7. E.J. Opila, D.L. Myers, N.S. Jacobson, I.M.B. Nielsen, D.F. Johnson, J.K. Olminky, and M.D. Allendorf, *J. Phys. Chem. A* 2 (2007): pp. 1971–1980.
8. E.J. Opila, *Mater. Sci. Forum* 461–464 (2004): pp. 765–774.
9. D.J. Young, *Mater. Sci. Forum* 595–598 (2008): pp. 1189–1197.
10. I.G. Wright, and R.B. Dooley, *Int. Mater. Rev.* 55 (2010): pp. 129–167.
11. F.-W., Hannes, J. E. Svensson, and J. Froitzheim. *J. Power Sources* 287 (2015): pp. 25-35.
12. H. Asteman, J. Svensson, M. Norell, and L. Johansson, *Oxid. Met.* 54 (2000): pp. 11–26.
13. H. Asteman, J. Svensson, and L. Johansson, *Oxidatio* 52 (1999): pp. 95–111.
14. L. Zhang, F. Zhu, and R. Tang, *Front. Energy Power Eng. China* 3 (2009): pp. 233–240.
15. K.A. Habib, M.S. Damra, J.J. Saura, I. Cervera, and J. Bellés, *Int. J. Corros.* 2011 (2011).
16. A. Vesel, M. Mozetic, A. Drenik, N. Hauptman, and M. Balat-Pichelin, *Appl. Surf. Sci.* 255 (2008): pp. 1759–1765.

17. A. Yamauchi, K. Kurokawa, and H. Takahashi, *Oxid. Met.* 59 (2003): pp. 517–527.
18. K. Segerdahl, J.E. Svensson, M. Halvarsson, I. Panas, and L.G. Johansson, *Mater. High Temp.* 22 (2005): pp. 69–78.
19. S. Mahboubi, Y. Jiao, W. Cook, W. Zheng, D.A. Guzonas, G.A. Botton, and J.R. Kish, *Corrosion* 72 (2016): pp. 1170–1180.
20. J.E. Tang, F. Liu, H. Asteman, J.E. Svensson, L.G. Johansson, and M. Halvarsson, *Mater. High Temp.* 24 (2007): pp. 27–55.
21. S.E. Sadique, A.H. Mollah, M.S. Islam, M.M. Ali, M.H.H. Megat, and S. Basri, *Oxid. Met.* 54 (2000): pp. 385–400.
22. C. Issartel, H. Buscail, Y. Wang, R. Rolland, M. Vilasi, and L. Aranda, *Oxid. Met.* 76 (2011): pp. 127–147.
23. R. Bauer, M. Baccalaro, L.P.H. Jeurgens, M. Pohl, and E.J. Mittemeijer, *Oxid. Met.* 69 (2008): pp. 265–285.
24. Y. Jiao, W. Zheng, D. Guzonas, and J. Kish, *J. Miner. Met. Mater. Soc.* 68 (2016): pp. 485–489.
25. J. Li, W. Zheng, S. Penttilä, P. Liu, O.T. Woo, and D. Guzonas, *J. Nucl. Mater.* 454 (2014): pp. 7–11.
26. D. Guzonas, M. Edwards, W.Z., *J. Nucl. Eng. Radiat. Sci.* 2 (2016): pp. 1–8.
27. A. Merwin, D. Rodriguez, and D. Chidambaram, *ESC Trans.* 58 (2014): pp. 15–24.
28. R. Wang, Z. Dong, J. Luo, W. Chen, W. Zheng, and D. Guzonas, *Corros. Sci.* 82 (2014): pp. 339–346.
29. Y. Behnamian, A. Mostafaei, A. Kohandehghan, B.S. Amirkhiz, D. Serate, W. Zheng, D. Guzonas, M. Chmielus, W. Chen, and J.L. Luo, *Mater. Charact.* 120 (2016): pp. 273–284.

30. Y. Behnamian, A. Mostafaei, A. Kohandehghan, B.S. Amirkhiz, D. Serate, Y. Sun, S. Liu, E. Aghaie, Y. Zeng, M. Chmielus, W. Zheng, D. Guzonas, W. Chen, and J.L. Luo, *Corros. Sci.* 106 (2016): pp. 188–207.
31. S. Mahboubi, G.A. Botton, and J.R. Kish, *Corrosion* 71 (2015): pp. 992–1002.
32. D.A. Guzonas, and W.G. Cook, *Corros. Sci.* 65 (2012): pp. 48–66.
33. J. Bischoff, A.T. Motta, C. Eichfeld, R.J. Comstock, G. Cao, and T.R. Allen, *J. Nucl. Mater.* 441 (2013): pp. 604–611.
34. A.T. Motta, A. Yilmazbayhan, M.J.G. da Silva, R.J. Comstock, G.S. Was, J.T. Busby, E. Gartner, Q. Peng, Y.H. Jeong, and J.Y. Park, *J. Nucl. Mater.* 371 (2007): pp. 61–75.
35. J. Yuan, X. Wu, W. Wang, S. Zhu, and F. Wang, *Oxid. Met.* 79 (2013): pp. 541–551.
36. P. McClure, “Comparative Study of Materials’ Behaviour in Supercritical Water and Superheated Steam,” Carleton University (2013).
37. X. Huang, J. Li, B.S. Amirkhiz, and P. Liu, *J. Nucl. Mater.* 467 (2015): pp. 758–769.
38. B.B. Ebbinghaus, *Combust. Flame* 93 (1993): pp. 119–137.
39. “ASTM E112-13, ‘Standard Test Methods for Determining Average Grain Size’ (West Conshohocken, PA: ASTM, 2013).”
40. Machine Application Corporation, “The Humidity/Moisture Handbook” (Machine Applications Corporation).
41. “JEMS Software”: <http://www.jems-saas.ch/Home/jemsWebSite/jems.html>.
42. “Digital Micrograph Software”: <http://www.gatan.com/products/tem-analysis/gatan-microscopy-suite-software>.
43. S. Cissé, L. Laffont, B. Tanguy, M.C. Lafont, and E. Andrieu, *Corros. Sci.* 56 (2012): pp. 209–216.
44. S.B. VÉLEZ, “Oxidation Kinetics and Mechanisms in Ht-9 Ferritic/Martensitic Stainless Steel,” Univeristy of Florida, 2005.

45. A. Fry, S. Osgerby, and M. Wright, NPL Rep. MATC 90 (2002): pp. 1–39.
46. P. Huczkowski, W. Lehnert, H.H. Angermann, A. Chyrkin, R. Pillai, D. Gruner, E. Hejrani, and W.J. Quadackers, Mater. Corros. 68 (2017): pp. 159–170.
47. M.D. Bermejo, and M.J. Cocero, VTT Publ. 52 (2006): pp. 3933–3951.
48. A.C.S. Sabioni, A.M. Huntz, L.C. Borges, and F. Jomard, Philos. Mag. 87 (2007): pp. 1921–1937.
49. M.J. Garcia-Vargas, L. Lelait, V. Kolarik, H. Fietzek, and M.D.M. Juez-Lorenzo, Mater. High Temp. 22 (2005): pp. 245–251.
50. F.-W., Hannes, J. E. Svensson, and J. Froitzheim. J. Power Sources 287 (2015): pp. 25-35.
51. G.R. Holcomb, and D.E. Alman, Scr. Mater. 54 (2006): pp. 1821–1825.
52. L. Dongmei, H. Rui, L. Jinshan, L. Yi, K. Hongchao, and F. Hengzhi, Rare Met. Mater. Eng. 37 (2008): pp. 1545–1548.
53. V.P. Deodeshmukh, and S.K. Srivastava, Superalloys 2008 11th Int. Symp. Superalloys (2008): pp. 689–698.
54. G.R. Holcomb, J. Electrochem. Soc. 156 (2009): p. C292.
55. M.J. Radler, J.B. Cohen, G.P. Sykora, T. Mason, D.E. Ellis, and J. Faber, J. Phys. Chem. Solids 53 (1992): pp. 141–154.
56. Y. Behnamian, A. Mostafaei, A. Kohandehghan, B.S. Amirkhiz, J. Li, R. Zahiri, E. Aghaie, W. Zheng, D. Guzonas, M. Chmielus, W. Chen, and J.L. Luo, J. Supercrit. Fluids 120 (2017): pp. 161–172.
57. T. Jonsson, S. Canovic, F. Liu, H. Asteman, J.E. Svensson, L.G. Johansson, and M. Halvarsson, Mater. High Temp. 22 (2005): pp. 231–243.
58. L. Mikkelsen, S. Linderorth, and J.B. Bilde-Sørensen, Mater. Sci. Forum 461–464 (2004): pp. 117–122.
59. S.N. Basu, and G.J. Yurek, Oxid. Met. 36 (1991): pp. 281–315.

60. Y. Wouters, G. Bamba, A. Galerie, M. Mermoux, and J.-P. Petit, *Mater. Sci. Forum* 461 (2004): pp. 839–848.
61. S. Henry, A. Galerie, and L. Antoni, *Mater. Sci. Forum* 369–372 (2001): pp. 353–360.
62. M.J. Kim, and D.B. Lee, *Met. Mater. Int.* 22 (2016): pp. 430–434.
63. X. Cheng, Z. Jiang, D. Wei, J. Zhao, B.J. Monaghan, R.J. Longbottom, and L. Jiang, *Met. Mater. Int.* 21 (2015): pp. 251–259.
64. H.E. Evans, *Int. Mater. Rev.* 40 (1995): pp. 1–40.
65. H.E. Evans, *Mater. High Temp.* 22 (2005): pp. 155–166.
66. P.F. Tortorelli, E.D. Specht, K.L. More, and P.Y. Hou, *Mater. Corros.* 63 (2012): pp. 857–861.
67. K. Ma, X. Tang, and J.M. Schoenung, *J. Wuhan Univ. Technol. Sci. Ed.* 31 (2016): pp. 35–43, <http://link.springer.com/10.1007/s11595-016-1326-7>.
68. J.W. Fergus, C.J. Dileep Kumar, Y. Liu, W. Tilson, A. Dekich, and H. Wang, *ECS Trans.* 50 (2013): pp. 117–126.
69. W. Qu, L. Jian, J.M. Hill, and D.G. Ivey, *J. Power Sources* 153 (2006): pp. 114–124.
70. M.P. Brady, I.G. Wright, and B. Gleeson, *Jom* 52 (2000): pp. 16–21.
71. Y. Jiao, W. Zheng, and J. Kish, *Corros. Sci.* (2018).
72. L. Laffont, and P. Gibot, *Mater. Charact.* 61 (2010): pp. 1268–1273.
73. Y. Chen, Z. Liu, S.P. Ringer, Z. Tong, X. Cui, and Y. Chen, *Cryst. Growth Des.* (2007): pp. 10–12.
74. J. Bischoff, and A.T. Motta, *J. Nucl. Mater.* 430 (2012): pp. 171–180.

5. Effect of Water Vapour Partial Pressure on the Chromia (Cr₂O₃)-Based Scale Stability

S. Mahboubi¹, H.S. Zurob², G.A. Botton³ and J.R. Kish^{4,*}

¹*Shooka Mahboubi, mahbos@mcmaster.ca*

²*Hatem S. Zurob: zurobh@mcmaster.ca*

³*Gianluigi A. Botton: gbotton@mcmaster.ca*

^{4,*}*Joseph R. Kish: corresponding author, kishjr@mcmaster.ca (905)525-9140, ext. 21492*

Department of Materials Science and Engineering, McMaster University, 1280 Main Street West, Hamilton, ON, CA, L9H 4L7

Journal of Canadian Metallurgical Quarterly

Received 06 Apr 2017, Accepted 28 Aug 2017, Published online: 07 Sep 2017

<https://doi-org.libaccess.lib.mcmaster.ca/10.1080/00084433.2017.1373968>

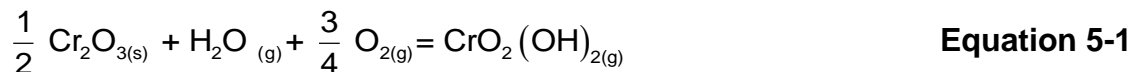
5.1. Abstract

The kinetics of the Cr₂O₃-based scale oxidation and volatilization were studied in the presence of water vapour (H₂O). A commercial Cr₂O₃-based scale forming Type 310S stainless steel was examined at the ambient pressure (0.1 MPa) and 550°C in relatively low and high H₂O-containing environments of air-10% H₂O and air-70% H₂O, respectively. The increase in the partial pressure of H₂O (p_{H_2O}) from 10 to 70% resulted in the transition of the oxidation and volatilization kinetics from the parabolic rate law in air-10% H₂O to the parilinear rate law in air-70% H₂O. The kinetics transition was attributed to the increase in the Cr loss rate from the base scale after coupons exposure in air-70% H₂O. The significant role of Mn alloying element in the base scale protectiveness was also discussed in the context of the Cr₂O₃-based scale stability.

Keywords: Kinetics, Cr₂O₃-based scale, Oxidation, Volatilization, Water vapour, Type 310S stainless steel, Alloying element

5.2. Introduction

High-temperature oxidation and oxide scale volatilization in oxygen (O₂) and H₂O containing environments are unavoidable phenomena that limit the performance of the corrosion-resistant alloys used as structural components for steam-generating applications such as steam boiler power plants, solid oxide fuel cells, nuclear reactors and geothermal power plants.¹⁻⁸ One method to increase the steam oxidation resistance of the alloy structural components is to modify the composition to form a protective external Cr₂O₃-based scale.⁹⁻¹² It is well known that increasing an alloy Cr-content can enhance the formation of a protective external Cr₂O₃-based scale.⁹⁻¹² Even though the increased Cr content in an austenitic Fe-Cr-Ni alloy is desirable from the Cr₂O₃-based scale formation perspective, one major concern exists. The Cr₂O₃ scale is known to form volatile Cr species such as CrO₂(OH), Cr(OH)₃, CrO₃, CrO(OH)₂ and CrO₂(OH)₂.¹³⁻¹⁶ Thermodynamic calculations of volatile Cr species partial pressures have shown that the most dominant phase that is responsible for oxide scale breakaway at temperatures below ~900°C is Cr oxy-hydroxide: CrO₂(OH)₂ (**Equation 5-1**), whereas at temperatures above ~900°C, CrO₃ and CrO₂(OH) species form significantly as well.¹⁴



It is known that the high Cr-containing alloys oxidation and the formation of an external protective Cr₂O₃-based scale follow a parabolic rate law as such scale

reduces further ion diffusion, therefore decreases the oxidation reaction rate.¹ Oxidation kinetics of the Cr₂O₃-based scale forming alloys in the presence of H₂O and any possible transition in the reaction kinetics during scale volatilization, however, is not well understood yet.

The volatile species during the Cr₂O₃-based scale volatilization can be carried away with the oxidizing environment flow and deplete the scale of Cr.¹⁷ Further scale protectiveness relies on the Cr supply from the alloy substrate to the scale.¹⁷ As a result, Fe present at the oxide/alloy interface could diffuse through the vacant lattice sites of Cr in the oxide scale and enhance the formation of a less protective, more Fe-rich Cr₂O₃-based scale.^{18,19}

The oxidation and volatilization rates of the Cr₂O₃-based scale are highly dependent on the oxidizing parameters, with higher p_{H_2O} , higher temperature, higher dissolved oxygen content, and increased environment flow rate, increasing the oxidation and volatilization rates.²⁰ In the case where the environment is not purely steam (e.g. air- H₂O mixture), the oxidation reaction highly depends on the vol.-% O₂ and H₂O existing in the mixture.¹ The calculated vapour pressures of CrO₂(OH)₂ for different total steam pressures and air-10% H₂O mixture as a function of temperature shows that a significantly high vapour pressure of CrO₂(OH)₂ is produced in air-10% H₂O mixture.¹ It is also shown that the increase in the vol.-% H₂O increases the p_{H_2O} that could encourage the Cr₂O₃-based scale breakaway.^{1,20}

In the current study, the high-temperature oxidation behavior of the commercial Type 310S stainless steel (~24 wt.% Cr) is examined in 0.1 MPa and 550°C. The 550°C temperature is used as it is in the operating temperature range for many H₂O containing environments such as those in steam turbines, low-temperature solid oxide fuel cells, and fuel cladding materials in supercritical water cooled reactors.²¹⁻²³ In addition, the importance of the oxidation and volatilization kinetics at the relatively lower 550°C temperature is often underestimated and requires further consideration. To examine the effect of p_{H_2O} on the Cr₂O₃-based scale stability and kinetics of the Cr₂O₃-based scale oxidation and volatilization, two environments were chosen with relatively low (air-10% H₂O) and relatively high (air-70% H₂O) vol.-% H₂O. A more complete physical description of the Cr₂O₃-based scale volatilization mechanism using the targeted commercial alloy and advanced electron microscopy characterization techniques was obtained. The kinetics of oxidation and volatilization in the two environments was also discussed.

5.3. Experimental Procedures

5.3.1. Material

Commercial plate of Type 310S stainless steel (Cr: 24.3 wt.%, Ni: 19.5 wt.%, C: 0.06 wt.%, Mn: 1.0 wt.%, Si: 0.8 wt.%, Mo: 0.8 wt.%, and Fe: balance) was solution annealed at 1150°C for 1 h followed by water quenching to room temperature. Rectangular test coupons with the dimensions of 15 mm × 9.2 mm × 1.5 mm were prepared from the plate using a diamond wheel saw. The provided coupons were then ground to a 400 grit surface finish using SiC abrasive papers with H₂O as a lubricant and cleaned in ethanol. Prior to the coupons exposure in the oxidizing environments, their dimensions and weight were measured using the digital caliper and analytical balance, respectively.

5.3.2. Wet Oxidation Testing

A 120 cm long quartz tube with the inner diameter of 11 mm was fitted inside an 80 cm horizontal furnace. The temperature inside the quartz tube and at the center of its length was kept at 550 ± 3°C. Two exposure conditions were chosen to examine the effect of p_{H_2O} on the scale stability: air-10% H₂O and air-70% H₂O. Deionized water was first heated inside a water flask to 46°C for the air-10% H₂O test and 90°C for the air-70% H₂O test. An air stream was flushed into the heated deionized water flask and the air- H₂O mixture flowed into the quartz tube with the flow rate of 200 mL/min (velocity of 4.2 cm/s). Five coupons (per exposure time and exposure condition) were then inserted in the center of the quartz tube parallel

to the flow direction. Exposure times considered were 100, 250 and 500 h. All coupon weights were measured after exposure using the analytical balance with the precision of ± 0.0001 g to obtain the amount of weight gained due to oxidation.

5.3.3. Oxide Scale Characterization

Scanning electron microscopy (SEM) was initially used in the secondary electron mode for the analysis of the nature and morphology of the oxide scales formed on the coupons in plan-view. This was done using a JEOL JAMP-9500F AUGER/FE-SEM microscope equipped with a Schottky Field Emission Gun filament and an integrated Oxford Synergy system with INCA energy dispersive spectroscopy (EDS) X-ray micro-analysis using an accelerating voltage of 10 kV and a working distance of ~ 20 - 23 mm. Site-specific cross-sectional transmission electron microscopy (TEM) thin film specimens were prepared from the coupons exposed for 500 h (the longest exposure time) in each of the environments considered. This was done using Zeiss NVision 40 focused ion beam (FIB) with a Ga ion beam voltage of 30 kV, a current beam of 80 pA and a working distance of 5.6-5.9 mm. To protect the oxide scales during the ion milling, a ~ 200 nm thick C layer first and a ~ 2 μm thick W strap layer next were deposited on the coupons. TEM analysis was conducted using JEOL 2010F TEM/STEM operating at 200 kV. High-resolution TEM (HRTEM) images were obtained from the base scale and the substrate to characterize the structure of the phases present. The very thin oxide scales formed were characterized using Electron Energy Loss Spectroscopy (EELS) with a dispersion of 0.2 eV/channel while the microscope was operated in

the high angle annular dark field (HAADF)-Scanning (S)TEM mode. EELS qualitative analysis was obtained by comparing the intensity of a specific energy loss (eV) window to each one of the characteristic edges that is observed in a typical EELS spectrum and the position of these edges as compared to reference materials. For characterizing different types of oxides formed on an austenitic Fe-Cr-Ni alloy, O-K, Cr-L_{2,3}, Fe-L_{2,3}, and Ni-L_{2,3} edges can all be used for oxide analysis, however, the O-K edges typically show more variation in each oxide type.

Figure 5-1 shows the reference EELS spectra²⁴⁻²⁹ that were used in the current study as re-plotted using the Plot Digitizer software.³⁰ The red arrow in **Figure 5-1(a)** shows the characteristic feature of a spinel oxide structure: a shoulder peak at ~550 eV.²⁹

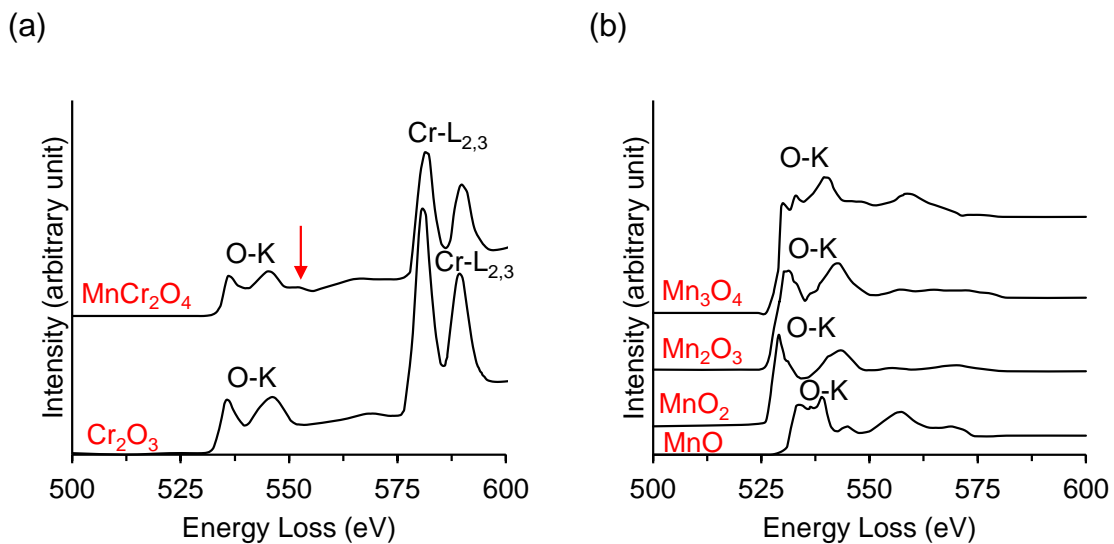


Figure 5-1. EELS spectra in reference compounds for (a) Cr₂O₃ and MnCr₂O₄, and (b) MnO, MnO₂, Mn₂O₃, Mn₃O₄.²⁴⁻²⁹ The red arrow in (a) shows the characteristic feature of a spinel MnCr₂O₄ structure.

5.4. Results and Discussion

Figure 5-2 shows the weight gain comparison of coupons exposed to 0.1 MPa and 550°C flowing air-10% H₂O and air-70% H₂O for up to 500 h. The error bars show the 95% confidence interval for five coupons per exposure condition. The weight gain data for the air-10% H₂O test, considering the error bars did not show a noticeable change over the exposure times considered. The oxidation kinetics followed the parabolic rate law with the alloy parabolic rate constant (k_p) of $\sim 1.7 \times 10^{-12}$ g²/cm⁴/h. The weight gain data for the air-70% H₂O showed a parabolic kinetics, that is the combination of an initial parabolic kinetic rate law (k_p of $\sim 3.5 \times 10^{-13}$ g²/cm⁴/h) followed by a linear kinetic rate law with the alloy negative linear rate constant (k_l) of $\sim 2 \times 10^{-12}$ g/cm²/h. The values measured in this study are comparable with those published in the literature for high Cr-containing Fe-Cr-Ni alloys exposed to air and/or in the presence of H₂O.^{2, 31, 32} The k_p value in the air-70% H₂O test was lower than that of the air-10% H₂O due to the lower p_{O_2} (required for the oxide formation) in this environment.

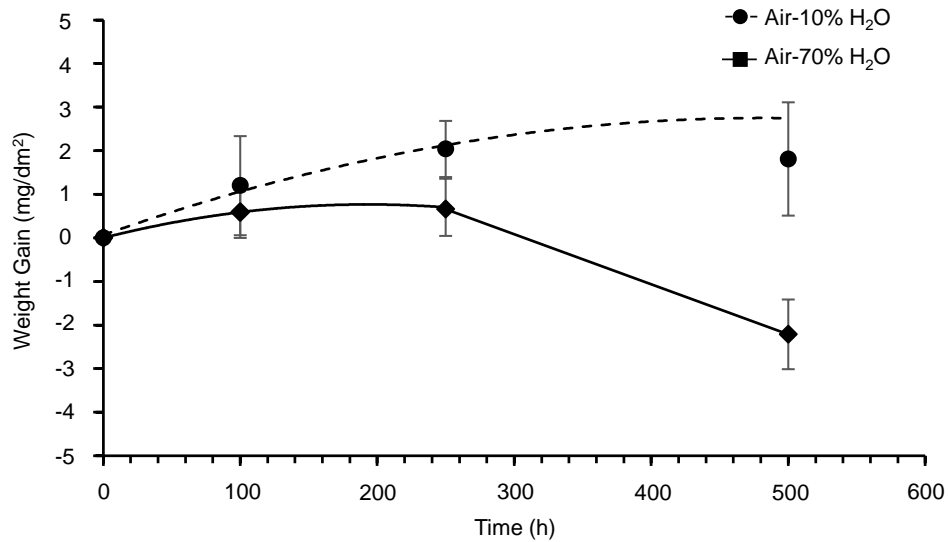


Figure 5-2. Weight gain data of coupons exposed to 0.1 MPa and 550°C air-10% H₂O and air-70% H₂O for up to 500 h. The error bars show the 95% confidence interval for five coupons per data point.

Figure 5-3 shows plan-view secondary electron images of the coupon surfaces after each of the exposure times and conditions considered. The coupon surfaces in all cases consisted of fine-grained oxide scale. The grinding lines from the surface preparation prior to exposure were noticeable on the surface, implying that the scale had very small (~few hundred nanometers) thickness. It should be mentioned that small bright particles were randomly detected on the coupon surface after 250 h exposure in air-70% H₂O (**Figure 5-3[b]**). The SEM-EDS spot analysis showed that these particles were enriched in Mn and O. The presence of the Mn-enriched oxide particles on the coupon surface could be as the result of the outermost oxide layer breakaway.

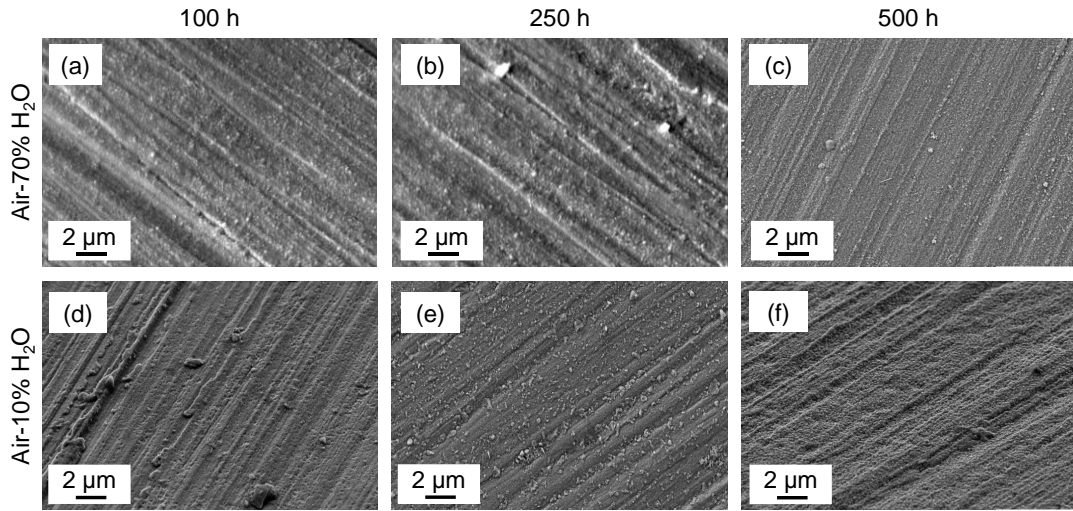


Figure 5-3. Plan-view secondary electron images of coupons exposed to 0.1 MPa and 550°C air-10% H₂O and air-70% H₂O for up to 500 h.

Figure 5-4(a) and **Figure 5-4(b)** show the HAADF-STEM cross section images of coupons exposed for 500 h (the longest exposure time) in air-10% H₂O and air-70% H₂O, respectively. The black and white areas on top of the base scale (as shown with the arrows) are the deposited C and W layers, respectively, during the FIB milling. In both cases, a uniform base scale was formed on the substrate. Recrystallized grains from the surface deformation during the surface preparation were detected below the scale/alloy interface. The base scale thickness in air-10% H₂O was ~68 nm compared with that of the ~50 nm in air-70% H₂O.

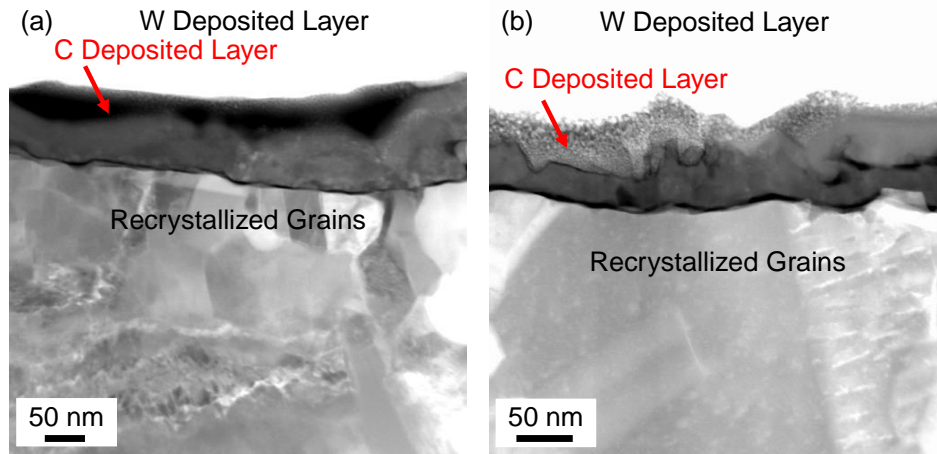


Figure 5-4. Cross-section HAADF-STEM images of coupons after 500 h exposure in 0.1 MPa and 550°C (a) air-10% H₂O and (b) air-70% H₂O for 500 h.

Figure 5-5 shows the cross-section HAADF-STEM image and Fe, Cr, Mn, Ni, and O EELS elemental maps of the base scale formed after 500 h exposure in air-10% H₂O. The black and white areas on top of the base scale in the HAADF-STEM image (as shown with the arrows) are the deposited C and W layers, respectively, during the FIB milling. The base scale was enriched in Cr and Mn. **Figure 5-6** shows the corresponding EELS spectra from Areas 1, 2, and 3 in **Figure 5-5**. The base scale was characterized as the Cr₂O₃ layer with small amounts of dissolved Fe and Mn (Areas 1 and 3). The Mn-enriched layer on top of the Cr₂O₃ layer was characterized as MnCr₂O₄ (Area 2). The formation of a spinel MnCr₂O₄ layer on the Cr₂O₃ layer is well established in Mn containing stainless steels because of the high Mn diffusivity in the Cr₂O₃ layer.³³ It has been shown that a MnCr₂O₄ cap on the Cr₂O₃ layer, depending on the gas flow rate, exposure time and temperature, can reduce the volatilization rate of the base scale since the Cr loss rate from a MnCr₂O₄ layer was much less than that of a Cr₂O₃ layer.³⁴

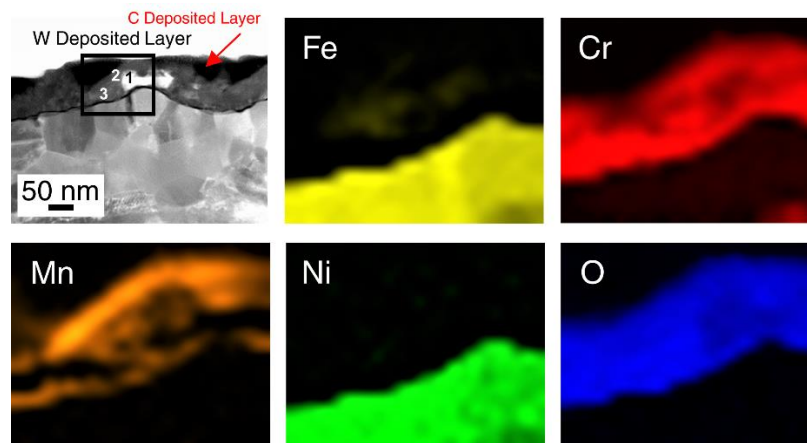
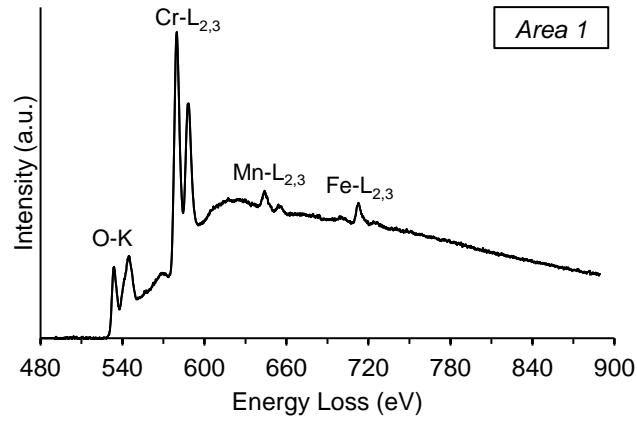
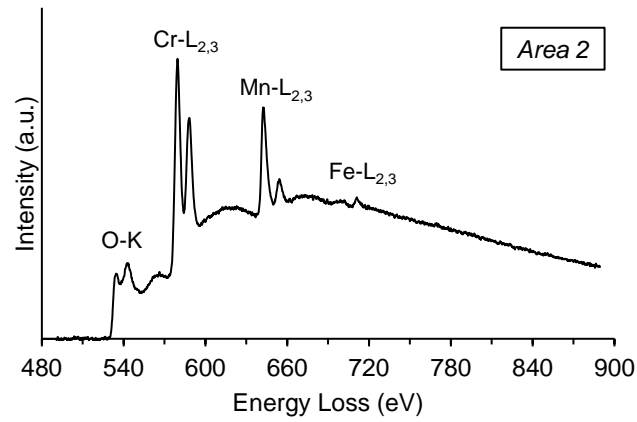


Figure 5-5. Cross-section HAADF-STEM image and EELS Fe, Cr, Mn, Ni, and O elemental maps of the base scale formed on Type 310S stainless steel after 500 h exposure in 0.1 MPa and 550°C air-10% H₂O.

(a)



(b)



(c)

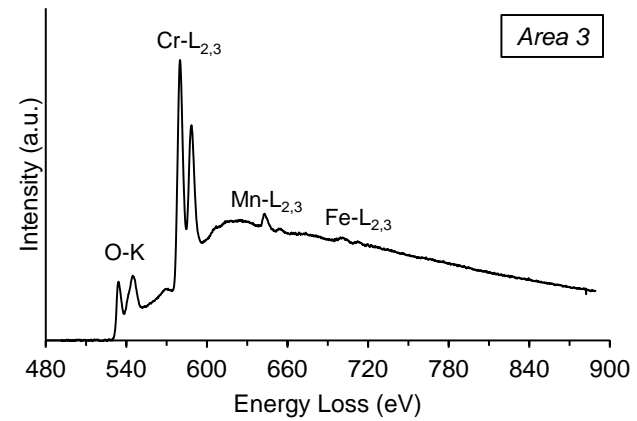


Figure 5-6. EELS spectra of Areas 1, 2, and 3 in the HAADF-STEM image in **Figure 5-5.**

Figure 5-7 shows the cross-section HAADF-STEM image and the Fe, Cr, Mn, Ni, and O EELS elemental maps of the base scale formed after 500 h exposure in air-70% H₂O. The corresponding EELS spectra from areas in the HAADF-STEM image are shown in **Figure 5-8**. The black and white areas on the base scale in the HAADF-STEM image (as shown with the arrows) are the deposited C and W layers, respectively, during the FIB milling. The base scale was enriched in Cr and Mn. The base scale was characterized as Cr₂O₃ layer (*Area 4*). The Mn-enriched layer on top of the Cr₂O₃ layer was identified as MnCr₂O₄ (*Area 5*). *Area 6* contained more Mn, and was identified as Mn₂O₃.

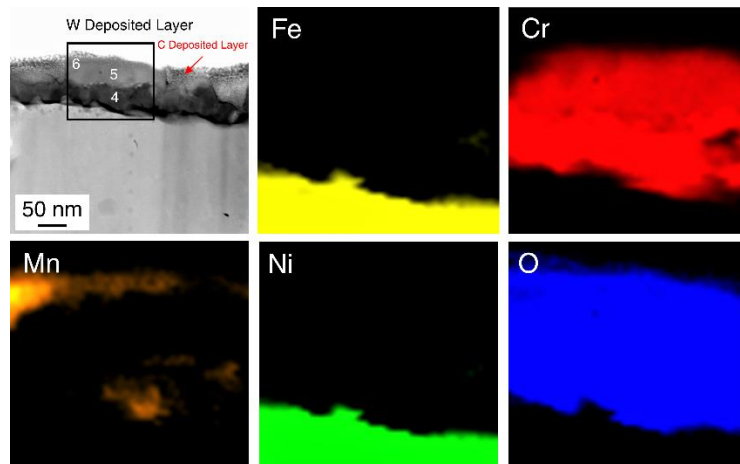
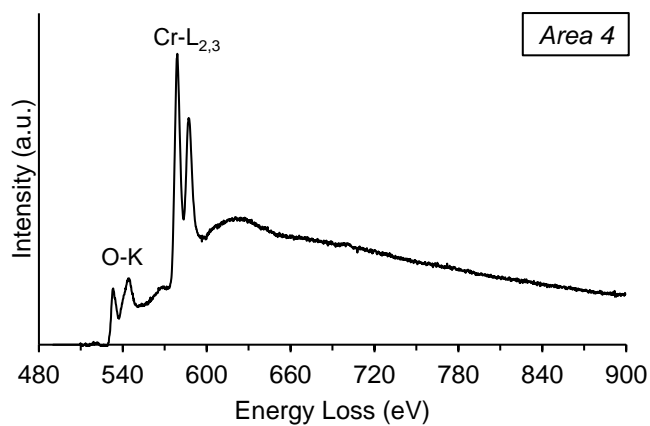
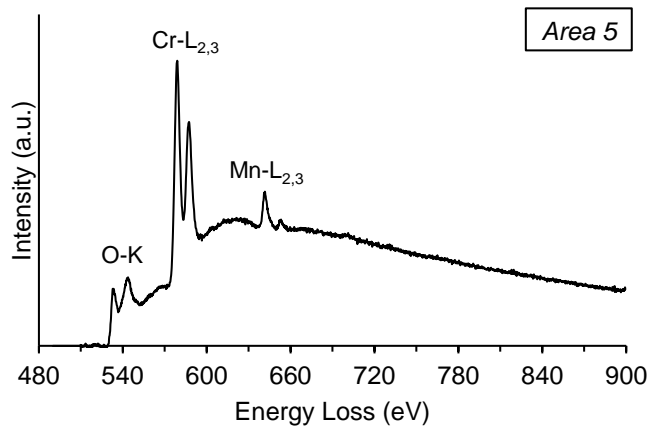


Figure 5-7. Cross-section HAADF-STEM image and EELS Fe, Cr, Mn, Ni, and O elemental maps of the base scale formed on Type 310S stainless steel after 500 h exposure in 0.1 MPa and 550°C air-70% H₂O.

(a)



(b)



(c)

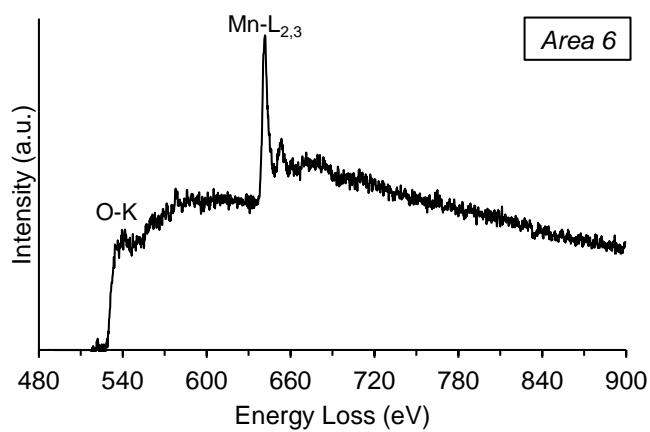
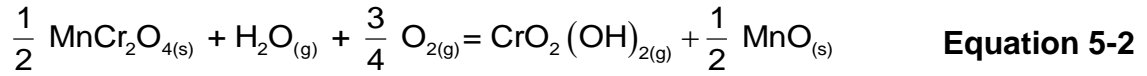


Figure 5-8. EELS spectra of Areas 1, 2, and 3 in the HAADF-STEM image in Figure 5-7.

It has been shown that Cr loss in the presence of H₂O, could also occur from a MnCr₂O₄ layer (**Equation 5-2**):³⁴



Further oxidation of MnO at high temperatures can result in the formation of Mn₂O₃ which is more stable at 550°C.³⁵The physical evidence of Mn₂O₃ degradation products that remained on the Cr₂O₃ layer surface after the loss of CrO₂(OH)₂ from the MnCr₂O₄ layer as was seen in this study (**Figure 5-3(b)** and **Figure 5-7**), after 500 h exposure of coupons in air-70% H₂O, supports the aforementioned thermodynamic theory.

Figure 5-9 shows the cross-section HAADF-STEM image of the alloy after 500 h exposure to air-70% H₂O and the EELS spectra from the corresponding points shown in the image. Points 1-6 EELS spectra were obtained where the Cr loss from the MnCr₂O₄ resulted in the Mn₂O₃ degradation product formation on the oxide surface and transformation of MnCr₂O₄ into a Mn_xCr_{2y}O₄ layer. Points 7-12 EELS spectra were obtained adjacent to points 1-6 for comparison. In points 1-6, the Cr-L_{2,3} peaks in the base scale decreased from the alloy/oxide interface to the oxide-air-70% H₂O interface, which confirmed the Cr depletion of the oxide surface due to base scale volatilization. In the meanwhile, the Mn-L_{2,3} peak increased from the alloy/oxide interface to the oxide/air-70% H₂O interface (points 1-6). Complete disappearance of Cr-L_{2,3} peaks while Mn-L_{2,3} peaks were still present at the oxide-air-70% H₂O interface, confirmed the volatilization of Cr from a MnCr₂O₄ layer and

the formation of Mn_2O_3 , which is in agreement with the previously published thermodynamic theory.³⁴ The adjacent points 7-12, on the other hand, showed that the $MnCr_2O_4$ layer stayed intact on top of the Cr_2O_3 layer. Very small amount of Fe was dissolved in the $MnCr_2O_4$ layer. This suggests that the Cr loss from the $MnCr_2O_4$ layer and formation of Mn_2O_3 , also Fe dissolution in the $MnCr_2O_4$ layer on the surface, are localized phenomena.

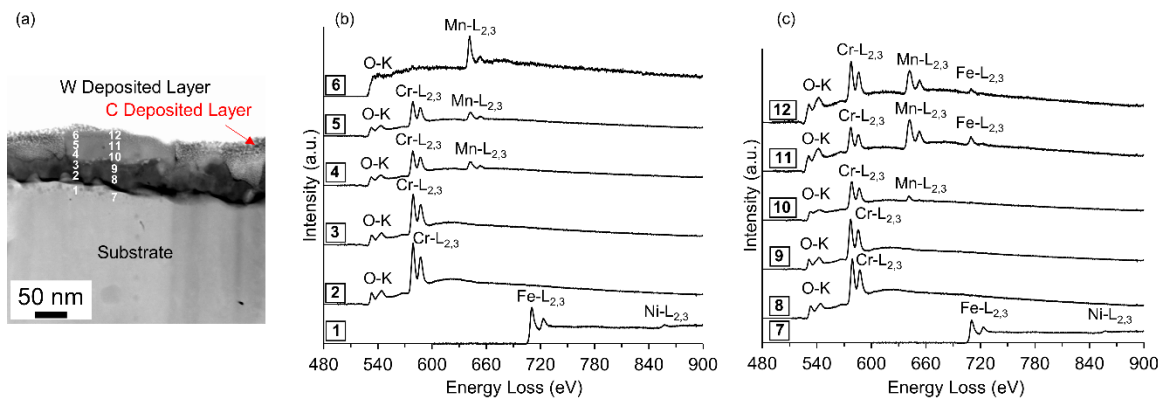


Figure 5-9. (a) Cross-section HAADF-STEM image of Type 310S stainless steel after 500 h exposure in 0.1 MPa and 550°C air-70% H_2O , (b) the corresponding EELS spectra from points 1-6 in (a), and (c) the corresponding EELS spectra from points 7-12 in (a).

Figure 5-10 shows the HRTEM image of the alloy/oxide interface after 500 h exposure of coupons in both environments. The EELS spectra corresponding to the amorphous layers are shown in **Figure 5-10(b)** and **Figure 5-10(d)**. In both environments after 500 h exposure, a ~5 nm thick oxide layer was seen at the scale/alloy interface which was characterized as the SiO_2 layer. The formation of a SiO_2 layer below the base scale in stainless steels during oxidation is very common. The thickness of this layer, however, depends on the Si concentration in the alloy, temperature, pressure and exposure time.³⁶ It is known that the SiO_2

layer might positively enhance the oxidation rate of the alloys at high temperatures by reducing ions diffusion through the scale.³⁶ The protective SiO₂ layer thickness is believed to be ~1 μm therefore the ~5 nm thick SiO₂ layer observed in this study does not seem to play a role in protectiveness of the alloy against high-temperature oxidation.³⁶

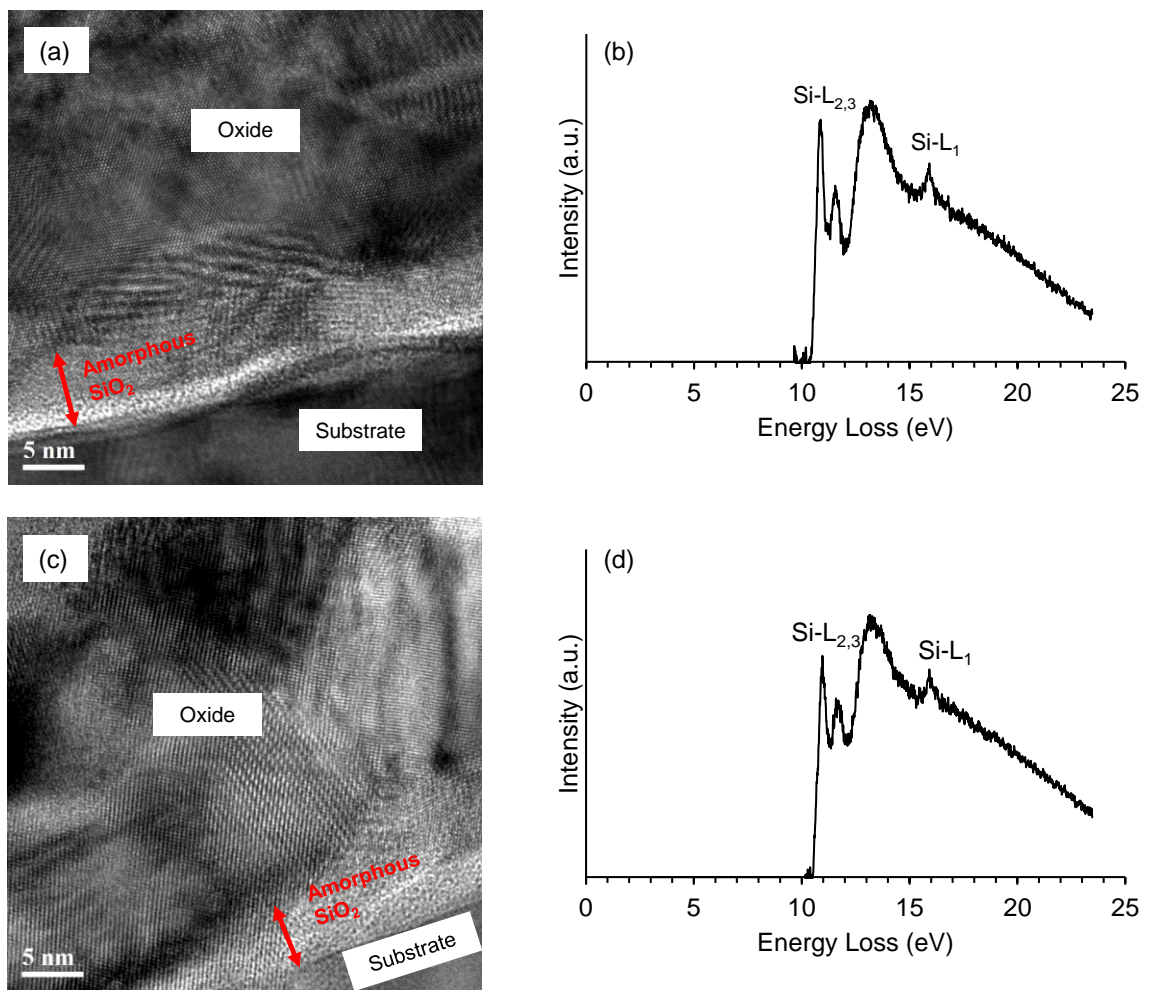


Figure 5-10. HRTEM images of the alloy/oxide interface and the EELS spectra of the amorphous regions (obtained in DF-STEM mode), in Type 310S stainless steel after 500 h exposure in 0.1 MPa and 550°C air-10% H₂O (a) and (b), and air-70% H₂O (c) and (d).

Figure 5-11 shows the summary of the scales characterization after 500 h exposure in 0.1 MPa and 550°C air-10% H₂O and air-70% H₂O. The ~5 nm thick SiO₂ layer underneath the base scale is not shown and the scales thicknesses are not set to scale.

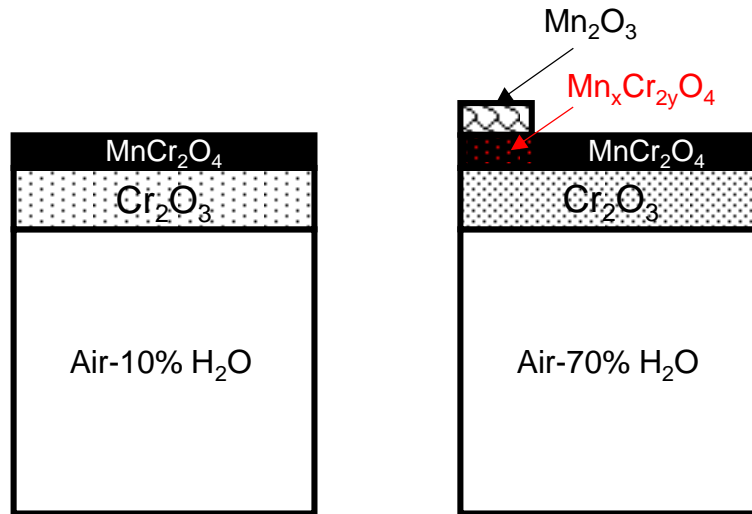


Figure 5-11. Summary of the scale characterization after 500 h exposure of Type 310S stainless steel coupons in 0.1 MPa and 550°C air-10% H₂O and air-70% H₂O. The thicknesses are not set to scale.

In both cases, a MnCr₂O₄ oxide cap formed on top of the Cr₂O₃ layer. The Cr loss rate is known to be much less from the MnCr₂O₄ layer compared with that of the Cr₂O₃ layer,³⁴ which is responsible for the small weight gain values obtained in this study and effective protection of the Cr₂O₃-based scale against breakaway. With the increase of the p_{H_2O} , the kinetics of the reactions changed from parabolic in air-10% H₂O to paralinear in air-70% H₂O. While the Cr₂O₃-based scale remained protected against volatilization in both environments, the Cr loss rate from the MnCr₂O₄ cap was higher in air-70% H₂O. The physical evidence of Mn₂O₃ degradation products as a result of Cr loss from the MnCr₂O₄ layer (**Equation 5-2**,

Figure 5-3(b) and **Figure 5-7)** in air-70% H₂O environment, confirms that the higher p_{H_2O} increased the Cr loss rate from the MnCr₂O₄ layer. Not to mention, further study on the Mn-O enriched particles observed in **Figure 5-3(b)** is suggested. It should be noted that the Mn and Cr concentrations below Mn₂O₃ were different than the areas without Mn₂O₃. This is shown in **Figure 5-11** as Mn_xCr_{2y}O₄. In this study, we showed that the larger content of Mn in the scale formed at air-10% H₂O was in the form of the MnCr₂O₄ uniform layer on the Cr₂O₃ layer, whereas the Mn enrichment on the scale at air-70% H₂O was not uniform: areas in the form of MnCr₂O₄ and areas in the form of Mn₂O₃. The latter is believed to be a degradation product that formed with the loss of CrO₂(OH)₂ from the MnCr₂O₄ layer. Results from this study show that in the presence of the MnCr₂O₄ layer in the 0.1 MPa pressure and 550°C air-10% H₂O and air-70% H₂O, the volatilization rate of the base scale was relatively slower and the Cr₂O₃-based scale breakaway and Fe-rich oxide nodules formation was relatively inhibited.

5.5. Conclusions

The effect of H₂O presence on the oxidation and volatilization mechanisms of commercial Type 310S stainless steel was examined in air- H₂O mixture at 0.1 MPa and 550°C. Comparison of the base scales formed in air-10% H₂O and air-70% H₂O environments, showed that the kinetics of oxidation was different in the two environments: parabolic in air-10% H₂O and paralinear in air-70% H₂O. The transition of oxidation kinetics was attributed to the higher volatilization rate of the scale formed in air-70% H₂O. It was shown that the presence of a uniform MnCr₂O₄ layer on top of the Cr₂O₃-based layer in air-10% H₂O scale reduced the Cr₂O₃ layer volatilization rate, resulting in a parabolic oxidation kinetics of the alloy. The MnCr₂O₄ layer on top of the Cr₂O₃-based layer in air-70% H₂O scale was not uniform and physical evidence of Cr loss from the MnCr₂O₄ and the formation of Mn₂O₃ degradation products were found. The relatively higher Cr loss rate from the MnCr₂O₄ in the higher p_{H_2O} environment (air-70% H₂O) was responsible for the transition of kinetics from parabolic to paralinear rates, therefore, the vapour pressure of the volatile species for the minor alloying elements is important and must not be underrated.

5.6. Acknowledgements

The authors thank the staff at the Canadian Centre for Electron Microscopy (CCEM), a national facility supported by NSERC, the Canada Foundation for Innovation under the MSI program and McMaster University, for their technical assistance with sample preparation and electron microscopy training.

5.7. Disclosure Statement

No potential conflict of interest was reported by the authors.

5.8. Funding

This work was supported by Natural Sciences and Engineering Research Council of Canada under the Discovery Grants program.

5.9. References

1. I.G. Wright and R.B. Dooley: "A review of the oxidation behaviour of structural alloys in steam", *Int. Mater. Rev.* 55 (2010): pp.129–167.
2. N. Otsuka and H. Fujikawa: "Scaling of austenitic stainless steels and nickel-based alloys in high-temperature steam at 973 K", *Corros.* 47 (1991): pp. 240–248.
3. J. Stringer and I.G. Wright: "Current limitations of high-temperature alloys in practical applications", *Oxid. Met.* 44 (1995): pp. 265–308.
4. W.H. Yeo, A.T. Fry, J. Purbolaksono, S. Ramesh, J.I. Inayat-Hussain, H.L. Liew, and M. Hamdi, *J. Supercrit. Fluids* 92 (2014): pp. 215–222.
5. Z. Shao, and S.M. Haile: "A high-performance cathode for the next generation of solid-oxide fuel cells", *Nature* 431 (2004): pp. 170–173.
6. Z. Shen, L. Zhang, R. Tang, and Q. Zhang, *J. Nucl. Mater.* 458 (2015): pp. 206–215.

7. S.N. Karlsdottir, K.R. Ragnarsdottir, I.O. Thorbjornsson, and A. Einarsson, *Geothermics*. 53 (2015): pp. 281–290.
8. Y. Alipour, P. Henderson, and P. Szakálos, *Mater. Corros.* 65 (2014): pp. 217–225.
9. M. Lukaszewicz, N.J. Simms, T. Dudziak, and J.R. Nicholls, *Oxid. Met.* 79 (2013): pp. 473–483.
10. R. Peraldi and B.A. Pint, *Oxid. Met.* 61 (2004): pp. 463–483.
11. N. Otsuka, Y. Shida, and H. Fujikawa, *Oxid. Met.* 32 (1989): pp. 13–45.
12. M. Lukaszewicz, N.J. Simms, T. Dudziak, and J.R. Nicholls, *Mater. High Temp.* 29 (2012): pp. 210–218.
13. A. Yamauchi, K. Kurokawa, and H. Takahashi, *Oxid. Met.* 59 (2003): pp. 517–527.
14. E.J. Opila, D.L. Myers, N.S. Jacobson, I.M.B. Nielsen, D.F. Johnson, J.K. Olminky, and M.D. Allendor, *J. Phys. Chem. A.* 111 (2007): pp. 1971–1980.
15. S.I. Castañeda, and F.J. Pérez, *Oxid. Met.* (2013) 79: pp. 147–166.
16. N. Mu, K.Y. Jung, N.M. Yanar, G.H. Meier, F.S. Pettit, and G.R. Holcomb, *Oxid. Met.* 78 (2012): pp. 221–237.
17. H. Asteman, J.E. Svensson, and L.G. Johansson, *Oxid. Met.* 57 (2002): pp.193–216.
18. D.J. Young and B. A. Pint, *Oxid. Met.* 66 (2006): pp. 137–153.
19. M. Halvarsson, J.E. Tang, H. Asteman, J.E. Svensson, and L.G. Johansson, *Corros. Sci.* 48 (2006): pp. 2014–2035.
20. H. Asteman, J. Svensson, M. Norell, and L. Johansson, *Oxid. Met.* 54 (2000): pp. 11-26.
21. Alina Agüero, Raúl Muelas, Ana Pastor, Steve Osgerby, *Surf. Coat. Technol.* 200 (2005): pp. 1219-1224.
22. Eric D. Wachsman and Kang Taek Lee, *Sci.* 334 (2011): pp. 935-939.

23. S. Mahboubi, Y. Jiao, W. Cook, W. Zheng, D. Guzonas, G.A. Botton and J.R. Kish, *Corros.* 72 (2016): pp. 1170-1180.
24. Y. Chen, Z. Liu, S. P. Ringer, Z. Tong, X. Cui, and Y. Chen, *Crys. Growth Des.* 7 (2007): pp. 2279-2281.
25. J. Bischoff and A.T. Motta, *J. Nucl. Mater.* 430 (2012): pp. 171–180.
26. H.K. Schmid and W. Mader, *Micron.* 37 (2006): pp. 426–432.
27. H. Kurata and C. Colliex, *Phys. Rev. B*, 48 (1993) pp. 2102–2108.
28. G.A. Botton, C.C. Appel, A. Horsewell, and W.M. Stobbs, *J. Microsc.* 180 (1995): pp. 211–216.
29. S. Mahboubi: “Effect of Cr content on corrosion resistance of Fe-Cr-Ni alloys exposed in supercritical water (SCW)”, M.A.Sc. thesis, McMaster University, 2014.
30. “Plot Digitizer Software”, <http://sourceforge.net/projects/plotdigitizer/>.
31. A. Paúl, R. Sánchez, O. M. Montes, and J. A. Odriozola, *Oxid. Met.* 67 (2007): pp. 87–105.
32. B.A. Pint, K.A. Terrani, M.P. Brady, T. Cheng, J.R. Keiser, *J. Nucl. Mater.*, 440 (2013): pp. 420–427.
33. A.C.S. Sabioni, A.M. Huntz, L.C. Borges, and F. Jomard, *Philos. Mag.*, 87 (2007) pp. 1921–1937.
34. G.R. Holcomb and D.E. Alman, *Scr. Mater.* 54 (2006): pp. 1821–1825.
35. E.R. Stobbe, B.A. de Boer, and J.W. Geus, *Catalysis Today*, 47 (1999): pp. 161-167.
36. H.E. Evans, D.A. Hilton, R.A. Holm, and S.J. Webster, *Oxid. Met.* 19 (1983): pp. 1-18.

6. Temperature Effect on the Wet Oxidation Performance of Type 310S Stainless Steel

Shooka Mahboubi¹, Hatem S. Zurob², Gianluigi A. Botton³, and Joseph R. Kish^{4,*}

¹Shooka Mahboubi, mahbos@mcmaster.ca

²Hatem S. Zurob: zurobh@mcmaster.ca

³Gianluigi A. Botton: gbotton@mcmaster.ca

^{4,*}Joseph R. Kish: corresponding author, kishjr@mcmaster.ca (905)525-9140, ext. 21492

Department of Materials Science and Engineering, McMaster University, 1280 Main Street West, Hamilton, ON, CA

Submitted to *Corrosion Science* on March 25th, 2018

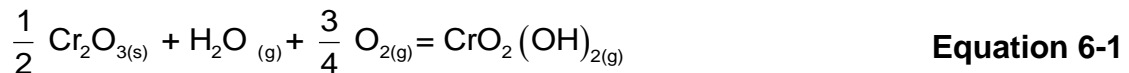
6.1. Abstract

Effect of temperature on wet oxidation kinetics of Type 310S stainless steel exposed in air-10% H₂O was investigated to develop a more complete physical description linking structure and composition of scales formed to changes in oxidation kinetics. The governing kinetic rate law is parabolic at 550°C, paralinear at 675°C and breakaway (paralinear) at 800°C. Beneficial effects of an outer MnCr₂O₄ layer is lost at 800°C as the rate of oxidized Cr volatilization is sufficiently high. Increasing the alloyed Si content to promote formation of a continuous SiO₂ layer at the alloy/scale interface is identified as a promising wet oxidation control strategy.

Keywords: Oxidation, Stainless steel, STEM

6.2. Introduction

The application of high Cr-containing (> 20 wt.% Cr) austenitic stainless steels in the high-temperature water vapour-containing (wet) environments is favored from an oxidation resistance perspective.¹⁻³ The generally acceptable oxidation resistance of these alloys is attributed to the formation of a continuous, compact and protective Cr₂O₃ scale that forms externally on the original alloy surface.^{4,5} In general, the formation kinetics of the protective Cr₂O₃ scale follows a parabolic rate law in dry oxidation environments, in which the mass gain from the oxide growth, controlled by outward diffusion of Cr cations through the oxide, is proportional to the square root of time.⁶⁻⁸ However, the presence of water vapour has a detrimental effect on the oxidation resistance of Cr₂O₃-forming stainless steels.⁹⁻¹¹ A volatilization reaction between the Cr₂O₃ scale and O₂ and H₂O vapour components occurs in the wet environment producing oxidized Cr vapour compounds (**Equation 6-1**).¹²⁻¹⁴ In wet air environments, Cr-oxy-hydroxide [CrO₂(OH)₂] is the stable oxidized Cr vapour compound at temperatures below ~1000 °C, due to the relatively high vapour pressure.^{13,15-17}



Continuous volatilization of the Cr₂O₃ scale depletes the oxide of Cr, which serves to enhance the diffusion of other alloying elements cations, Fe in particular, through the oxide.¹⁸ Continuous diffusion of Fe cations through the scale promotes the formation of a thick, porous non-protective hematite (Fe₂O₃) or magnetite

(Fe₃O₄).¹⁸⁻²¹ From a practical perspective, this accelerated thickening of the oxide scale is undesirable since it can reduce the heat transfer rate of the thin-walled components and/or increase the tendency for spallation of the oxide scale in high-temperature applications.^{22,23} The tendency for the accelerated formation of Fe-rich oxides on Fe-Cr-Ni alloys during wet oxidation increases considerably with temperature due to the concomitant increase in the rate of oxidized Cr lost from a Cr₂O₃ layer to volatilization.²⁴

The presence of Mn in the Cr₂O₃-forming alloys has been shown to have a beneficial effect on the high-temperature wet oxidation resistance.²⁵⁻²⁷ The relatively high diffusivity of Mn cations in the Cr₂O₃ scale promotes the formation of a Mn-spinel oxide (MnCr₂O₄) outer layer.²⁸⁻³¹ As the MnCr₂O₄ contains oxidized Cr, it follows that the CrO₂(OH)₂ vapour compound still forms by reaction of the MnCr₂O₄ outer layer with oxygen and water vapour components in the environments.^{32,33} Measurements of the maximum Cr loss rate over pure Cr₂O₃ and MnCr₂O₄ in air-3% H₂O show that the rate of oxidized Cr volatilization is decreased by a factor of 95 at 600 °C and a factor of 35 at 800°C by MnCr₂O₄.³⁴ Thus, the formation of a MnCr₂O₄ outer layer on top of a Cr₂O₃ scale is viewed a means to improve the wet oxidation resistance.³²⁻³⁵ However, the role of Mn in providing increased wet oxidation resistance of Cr₂O₃-forming stainless steels is often overlooked due the relatively low content in the alloy (present as a minor alloying element).

The purpose of this study is to investigate the effect of temperature on the wet oxidation kinetics of Type 310S stainless steel exposed in a flowing air-10% H₂O mixture to develop a more complete physical description linking changes in the structure and composition of the oxide scale formed to changes in the oxidation kinetics. Weight change measurements were made at various exposure times up to 1000 h to identify the governing rate law. Both scanning and transmission electron microscopy (SEM and TEM) and associated techniques were then used to characterize how the structure and composition of the oxide scale changes with both time and temperature. We previously showed that a MnC₂O₄ outer layer forms on Type 310S stainless steel when exposed in the same flowing air-10% H₂O mixture at 550°C up to 500 h exposure.^{36,37} It is of both fundamental and practical interest to better understand the inhibiting effect the MnCr₂O₄ outer layer has on the wet oxidation at higher temperatures.

6.3. Experimental Procedures

A cold-rolled and mill annealed plate of ASTM A240 Type 310S stainless steel with the dimensions of 30 cm × 30 cm × 1.5 mm was provided from Columbus Stainless Ltd.³⁸ Annealing was achieved by heat treating the alloy to a temperature between 1030°C and 1150°C for 60 minutes (2.5 mm/min) followed by water quenching to ensure the dissolution of carbide precipitates into the solution.³⁸ The average alloy grain diameter is 34 ± 4 μm as measured (within the 95% confidence interval [CI]) using the ASTM standard E112-13 linear intercept method.³⁹ The chemical composition (wt.%) of the alloy, reproduced from the associated mill certificate, is:

Cr: 24.7, Ni: 20.2, Mn: 1.9, Si: 0.6, C: 0.05, P: 0.02, Mo: 0.07, N: 0.03, Cu: 0.06, and Fe: balance. The plate was cut into 15 mm × 9.2 mm × 1.5 mm coupons and these coupons were ground to 400 grit SiC paper, cleaned in ethanol, and dried using warm air stream. Coupon weights were measured using a Mettler Toledo balance with the precision of 0.0001 g prior to being inserted into the high-temperature tube furnace and exposed to the wet oxidation environment. A detailed description of the wet air oxidation testing apparatus used is provided elsewhere.³⁶

Five coupons per exposure time and temperature were positioned in the center of the horizontal quartz tube inside the tube furnace. Three temperatures were chosen for study: 550°C, 675°C, and 800°C. A mixture of the air-10 vol.-% H₂O ($p_{O_2} = 0.1890$ atm and $p_{H_2O} = 0.0996$ atm) passed across the surface of the coupons with the flow velocity of 4.0 ± 0.2 cm/s. Coupons were exposed at each temperature for various times, namely 24 h, 50 h, 100 h, 250 h, 500 h, and 1000 h. Coupons were then cooled down to room temperature inside the furnace with an estimated cooling rate of 0.05°C/s to minimize any thermal shock induced to the oxides formed. Gravimetric measurements were then performed by measuring the coupons weight gain (change in weight divided by the surface area) to study any transitions in the high-temperature kinetics of oxidation. The oxides formed were then removed using a descaling solution to examine the amount of alloy weight loss due to oxidation. A detailed description of the descaling procedure is provided elsewhere.⁴⁰

The morphology, composition and structure of the oxides formed on the coupons after 100 h, 250 h, 500 h, and 1000 h exposure were examined in plan-view using a JEOL JAMP-9500 AUGER/FESEM microscope equipped with a Schottky field emission gun (FEG). An electron beam energy of 10 kV and the working distance of ~20 mm were used for this purpose. Auger electron spectroscopy (AES) was used to determine the elemental composition (in at.%) of the oxide scale surface. This was achieved by tilting the coupons 30° towards the Auger electron hemispherical electrostatic energy analyzer, with similar electron beam energy and working distance as mentioned above. Coupon surfaces were sputter cleaned using an Ar⁺ ion beam operating at 3 kV prior to the AES analysis. A quantitative analysis was then conducted by the direct comparison of the spectra acquired with the published reference spectra.

Focused ion beam (FIB) was used to prepare a site-specific cross-sectional thin foil of the oxide scale formed after 500 h at each of the three temperatures for subsequent transmission electron microscopy analysis. This was done using a Zeiss NVision40 dual beam FIB microscope equipped with FEG. A protective coating consisting of a carbon (inner layer) and a tungsten (outer layer) was applied to sites of interest by electron deposition. A Ga⁺ ion beam operating at a 30 kV and a beam current of ~80 pA was used at a working distance of ~5 mm to prepare the cross-section foils at the sites of interest. Scanning TEM (STEM) analysis was performed using a JEOL 2010F equipped with X-ray energy dispersive spectrometer (EDS) for elemental analysis. Imaging was done in the bright-field

(BF) and the high-angle annular dark-field (HAADF) modes. STEM-EDS was first used to obtain elemental maps and information on the elements distribution across the oxide/alloy interface. The composition and structure of the oxide layers were then characterized using electron energy loss spectroscopy (EELS). The EELS spectra achieved were compared with those previously published in the literature.^{36,37} Selected area diffraction (SAD) patterns were also acquired from the regions of interest within the oxide scale. JEMS software⁴¹ was then used to compare the SAD patterns acquired with the reference patterns in the literature for indexing.

6.4. Results

6.4.1. Wet Oxidation Kinetics

Figure 6-1 shows the average weight gain of Type 310S stainless steel exposed in flowing air-10% H₂O at 550°C, 675°C, and 800°C for up to 1000 h. The error bars represent 95% CI for replicate set of coupons exposed. Superimposed into the plots are the trend lines corresponding to the governing oxidation kinetics at each temperature, as discussed in more detail later. At 550°C, the weight gain exhibited at all exposure times considered is relatively small and considering the error bars, only a small increase at a decreasing rate (consistent with a parabolic rate law) is observed up to 1000 h. The weight gain at 675°C first increases at a decreasing rate with time to 250 h (consistent with parabolic rate law) and then decreases at a constant rate with time after 250 h (consistent with a linear rate

law). The weight gain at 800°C exhibits a more complex time dependence. It first increases at a decreasing rate with time to 250 h (consistent with a parabolic rate law), thereafter it further increases at a constant rate with time to 500 h (consistent with a linear rate law) and then the weight gain decreases at a constant rate with time to 1000 h (again consistent with a linear rate law).

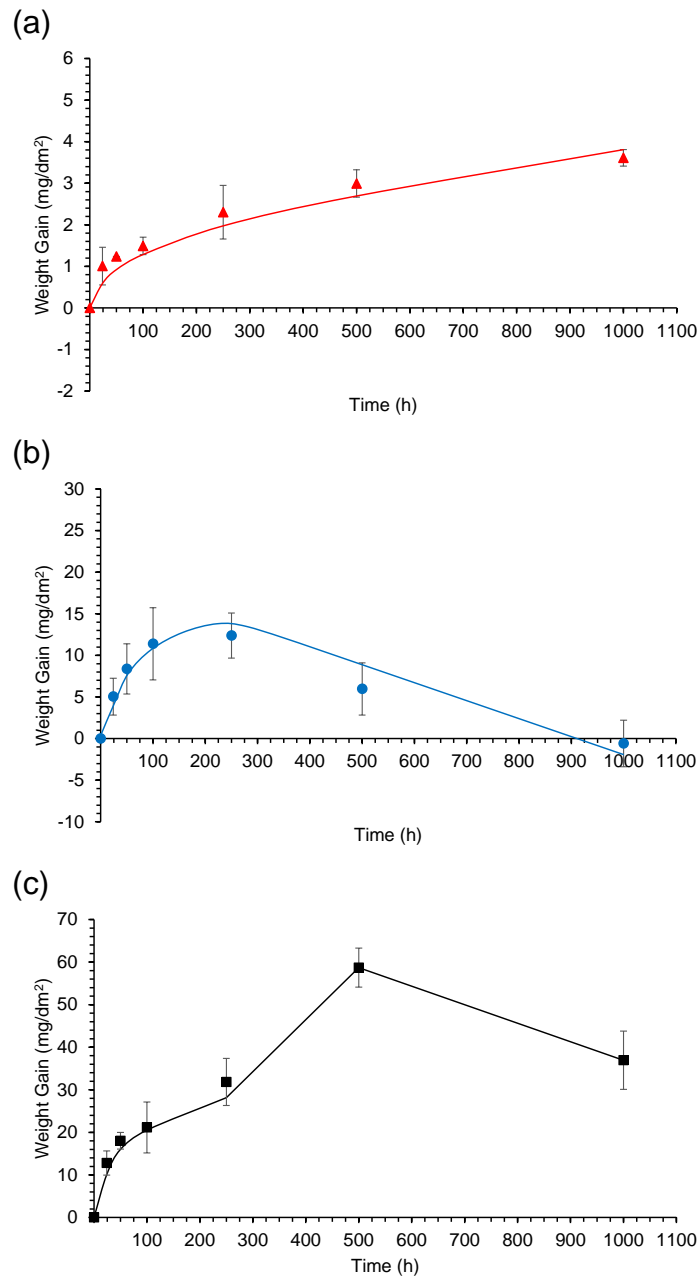


Figure 6-1. Weight gain of Type 310S stainless steel exposed for 24 h, 50 h, 100 h, 250 h, 500 h, and 1000 h in flowing air-10% H₂O at (a) 550°C, (b) 675°C, and (c) 800°C.

Figure 6-2 shows the average weight loss of Type 310S stainless steel exposed in the flowing air-10% H₂O at 550°C, 675°C, and 800°C up to 1000 h. The error bars represent 95% CI for replicate set of coupons exposed. Again superimposed into the plots are trend lines corresponding to the likely governing rate laws (solid lines). The dashed lines in the 675°C and 800°C plots represent the extension of the parabolic rate law over the entire 1000 h. The significance of the deviation between the parabolic rate law extension and the linear rate law is discussed in detail later. The variation in weight loss as a function of time at both 550°C and 675°C is similar to that observed for the respective weight gain dependence shown in **Figure 6-1** for these two temperatures. It is acknowledged that the deviation of the presumed linear kinetics regime from the parabolic kinetics regime in the weight loss exhibited beyond 250 h at 675°C is quite small considering the error bars. However, the clear discontinuity of the weight gain data supports a presumption of a transition in the controlling governing kinetic rate law. In contrast, the variation of weight loss as a function of time at 800°C is not similar to variation in weight gain. The weight loss first increases at a decreasing rate with time to 250 h (consistent with a parabolic rate law), thereafter it further increases at a constant rate with time to 1000 h (consistent with a linear rate law). In other words, there are only two kinetics regimes in the weight loss dependence, as opposed to three kinetics regimes in the weight gain dependence. It is clear that the weight loss is a strong function of temperature, with the highest extent occurring at the highest temperature considered.

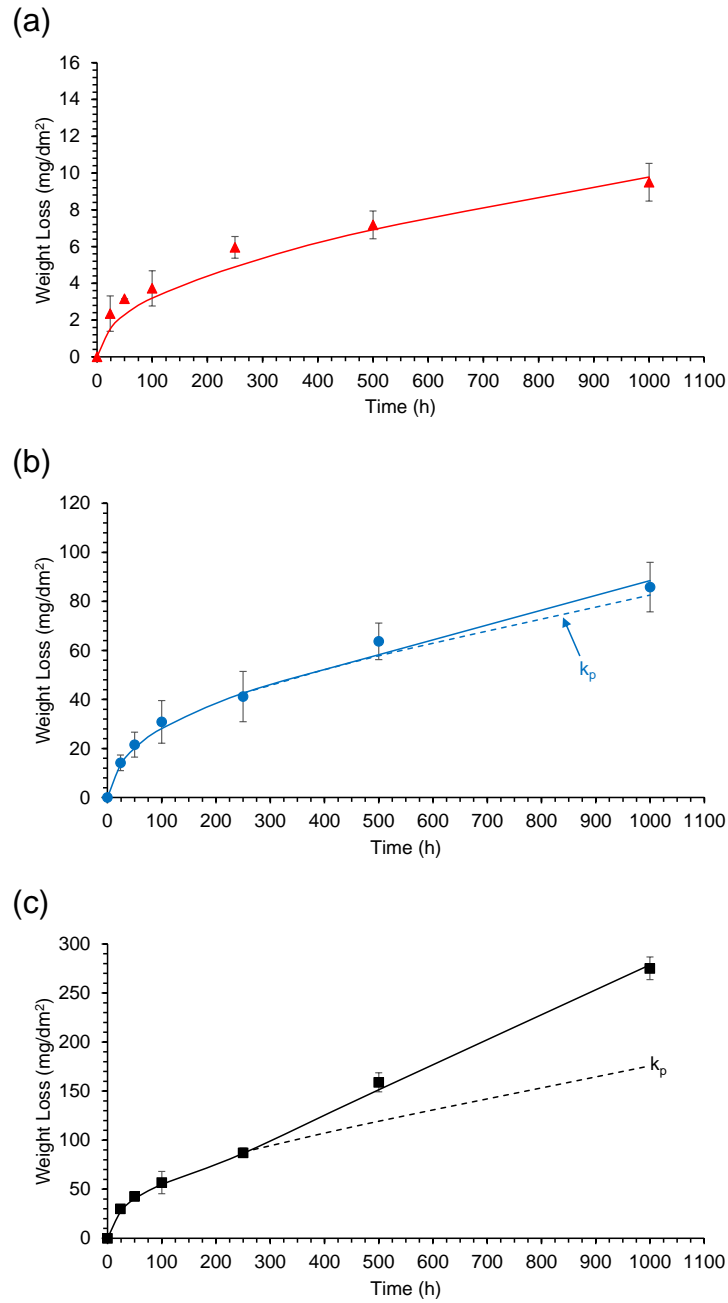


Figure 6-2. Weight loss of Type 310S stainless steel exposed for 24 h, 50 h, 100 h, 250 h, 500 h, and 1000 h in flowing air-10% H₂O at (a) 550°C, (b) 675°C, and (c) 800°C.

As **Figure 6-1** and **Figure 6-2** show, the wet oxidation kinetics is likely better described in terms of weight loss (metal loss) given the complex kinetics indicated by the weight gain measurements. **Table 6-1** lists the parabolic (k_p) and linear (k_l) rate constants determined from fitting the trend in weight loss with time shown in **Figure 6-2** for the three temperatures. The regression values (R^2) for each rate law fit is also listed. The value of k_p is lowest for the 550°C exposure and highest for the 800°C exposure (as expected). The k_l values for the 675°C and 800°C exposures were determined by fitting the weight loss data for the latter three exposure times (250 h, 500 h, and 1000 h). The value is higher at the higher exposure temperature (also as expected).

Table 6-1 k_p and k_l oxidation rate constants (within the 95% CI) for Type 310S stainless steel after up to 1000 h exposure in flowing air-10% H₂O

| Temperature (°C) | k_p (g ² /cm ⁴ /s) | R_p^2 | k_l (g/cm ² /s) | R_l^2 |
|------------------|--|---------|---------------------------------|---------|
| 550 | $(2.7 \pm 1.5) \times 10^{-15}$ | 0.963 | - | - |
| 675 | $(2.1 \pm 0.1) \times 10^{-13}$ | 0.996 | $(1.6 \pm 1.1) \times 10^{-10}$ | 0.963 |
| 800 | $(9.3 \pm 2.7) \times 10^{-13}$ | 0.992 | $(7.1 \pm 0.1) \times 10^{-10}$ | 0.997 |

6.4.2. Oxide Scales Characterization

Figure 6-3 shows a set of plan-view secondary electron images of oxide scale formed after 100 h, 250 h, 500 h, and 1000 h exposure in flowing air-10% H₂O at each of the three temperatures considered. Starting with the set of images corresponding to the 550°C exposure, the images show the same features, regardless of the exposure time. The oxide is relatively thin as the grinding lines from surface preparation prior to exposure are visible. Bright particles are observed

to decorate the surface in what appears as random distribution. These particles are Mn-rich as identified by SEM-EDS. After 1000 h exposure, the oxide scale appears to be somewhat rougher relative to others formed after shorter exposure times. The set of images corresponding to the oxide scale formed during the 675°C exposure also shows similar features regardless of the exposure time. The oxide scale is relatively compact and consists of relatively small grains. Bright particles are also observed on the surface: the density of which is significantly greater relative to that observed during the 550°C exposure. In contrast, the oxide scale formed during the 800°C exposure shows distinctly different features after the various exposure times considered. After 100 h exposure, a fine granular oxide scale is observed, similar in appearance to that formed during the 675°C exposure. After 250 h exposure, relatively small nodules have formed on top of the “base scale”. These particles are Fe-rich as identified by SEM-EDS. After 500 h exposure, the nodules presumably have coalesced to form a continuous outer layer with a plate-like morphology. After 1000 h exposure, the oxide scale is discontinuous as spalled regions are clearly visible. These spalled regions likely account for the observed transition from positive weight gain to negative weight gain after 500 h, as shown in **Figure 6-1(c)**.

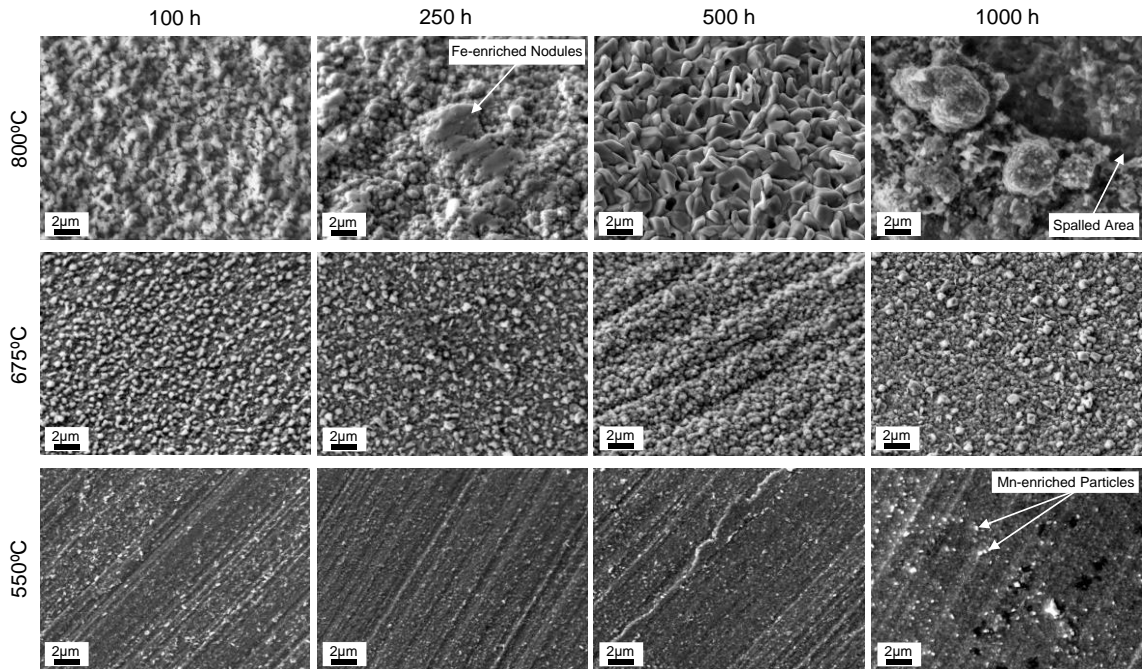


Figure 6-3. Plan-view secondary electron images of coupons exposed for 100 h, 250 h, 500 h, and 1000 h in flowing 0.1 MPa air-10% H₂O at 550°C, 675°C, and 800°C.

Table 6-2 shows the average atomic concentrations of Fe, Cr, Ni, Mn, and O of the oxide surfaces (~4 nm deep), as acquired from three different locations using AES. The average values are listed along with the 95% CI as the associated error. The Ni concentration is excluded from consideration as is not detected in any of the spectra acquired (less than ~0.5 at.% in each case). For the 550°C exposure, the oxide scale surface is comprised of Cr, Mn and O after all four exposure times considered. Both the Cr and Mn concentrations do not vary with exposure time up to 500 h. Of the two metallic elements, Cr is the dominant element. After 1000 h exposure, Mn becomes the dominant metallic element. The atomic concentration ratio (Mn:Cr:O) of the oxide scale surface formed after exposure times up to 500 h are consistent with MnCr₂O₄, whereas the ratio after an exposure time of 1000 h is

consistent with $(\text{Mn,Cr})_2\text{O}_3$. The oxide scale surface formed after all four exposure times is also comprised of Cr, Mn and O for the 675°C exposure. However, Cr is the dominant metallic element only after 100 h exposure, whereas Mn is the dominant metallic element after the remaining three exposure times. The atomic concentration ratio (Mn:Cr:O) of the oxide surface formed after 100 h exposure is consistent with MnCr_2O_4 , whereas the ratio is consistent with $(\text{Mn,Cr})_2\text{O}_3$ for the remaining three exposure times. In contrast, the composition of the oxide scale surface formed after exposure at 800°C significantly varies with exposure time. The composition of the scale surface formed after 100 h consists of Cr, Mn and O and the atomic concentration ratio is again consistent with MnCr_2O_4 . The relatively small Fe-rich nodules observed to have formed after 250 h exposure are comprised of 32 ± 5 at.% Fe, 9 ± 3 at.% Cr, 57 ± 4 at.% O, and less than ~ 5 at.% Mn, and were characterized as $(\text{Fe,Cr})_2\text{O}_3$. The underlying “base scale” is comprised of Mn, Cr and O, with the atomic concentration ratio consistent with $(\text{Mn,Cr})_2\text{O}_3$. After 500 h exposure, the oxide scale surface is comprised of Fe, Cr and O, with the atomic concentration ratio consistent with $(\text{Fe,Cr})_2\text{O}_3$. The intact oxide surface formed after 1000 h is comprised of Fe, Cr and O, with the atomic concentration ratio consistent with $(\text{Fe,Cr})_2\text{O}_3$. The analysis of the spalled region surface yields a similar composition as the intact oxide surface.

Table 6-2 Average elemental composition (at.%) obtained from the oxide scale surface formed in flowing air-10% H₂O

| Time (h) | 550°C | | | | 675°C | | | | 800°C | | | |
|----------|-------|------|------|------|-------|------|------|------|-------|------|------|------|
| | Fe | Cr | Mn | O | Fe | Cr | Mn | O | Fe | Cr | Mn | O |
| 100 | <~1 | 26±2 | 15±3 | 59±4 | <~5 | 26±3 | 15±3 | 59±3 | <~8 | 22±4 | 12±2 | 57±3 |
| 250 | <~1 | 29±3 | 13±3 | 58±1 | <~5 | 15±1 | 22±3 | 55±1 | <~8 | 15±2 | 25±3 | 56±2 |
| 500 | <~5 | 24±4 | 14±2 | 57±3 | <~5 | 12±1 | 29±1 | 54±1 | 22±3 | 13±1 | <~5 | 57±1 |
| 1000* | <~5 | 15±1 | 24±3 | 55±2 | <~5 | 15±1 | 26±2 | 55±1 | 22±2 | 14±3 | <~5 | 58±1 |

*The compositions for the 1000 h exposure at 800°C are from the intact base oxide surface.

Figure 6-4 shows a set of cross-sectional back-scattered electron images of scales formed after the selected times of 100 h, 250 h, 500 h, and 1000 h exposure in flowing air-10% H₂O at 800°C. Similar results are not reported for the scales formed at 550°C and 675°C since they are too thin for such an examination. The composition and structure of those scales were analyzed in detail using TEM the results of which are presented later for comparison. The scale formed after 100 h is relatively thin and is formed externally on the metal surface. The scale contains Cr, Mn, Fe and O as major elements. The Fe content is variable: being highest at the scale/metal interface. A discontinuous layer containing Si and O is found to reside underneath the external scale (formed at the scale/metal interface). After 250 h exposure, the scale is thicker relative to that formed after 100 h and it contains Cr, Mn, Fe and O as major elements. The layer containing Si and O found to reside underneath the external scale (formed at the scale/metal interface) remains discontinuous. A significantly thicker scale forms after 500 h exposure. The scale is multi-layered consisting of a porous outer Fe-Cr-O layer formed on an inner Cr-Mn-Fe-containing inner layer. The Fe content is higher in the outer layer relative to the inner layer, whereas the Cr content is lower in the outer layer relative

to the inner layer. There is clear Ni-enrichment at the scale/metal interface. However, Ni is also clearly present within the scale itself, located at the outer layer/inner layer interface. As Ni typically does not participate in scale formation during wet oxidation,⁴² the results suggest that there is a change from external scale growth to internal scale growth during the 800°C exposure. Two distinct discontinuous layers containing Si and O are found: one layer residing at the scale/metal interface and the other layer residing at the inner layer/outer layer interface. The structure and composition of the scale formed after 1000 h is similar to that formed after 500 h with more Fe enrichment in the outer layer. However the scale is thicker and the interfaces within the multi-layered scale are more sharply defined.

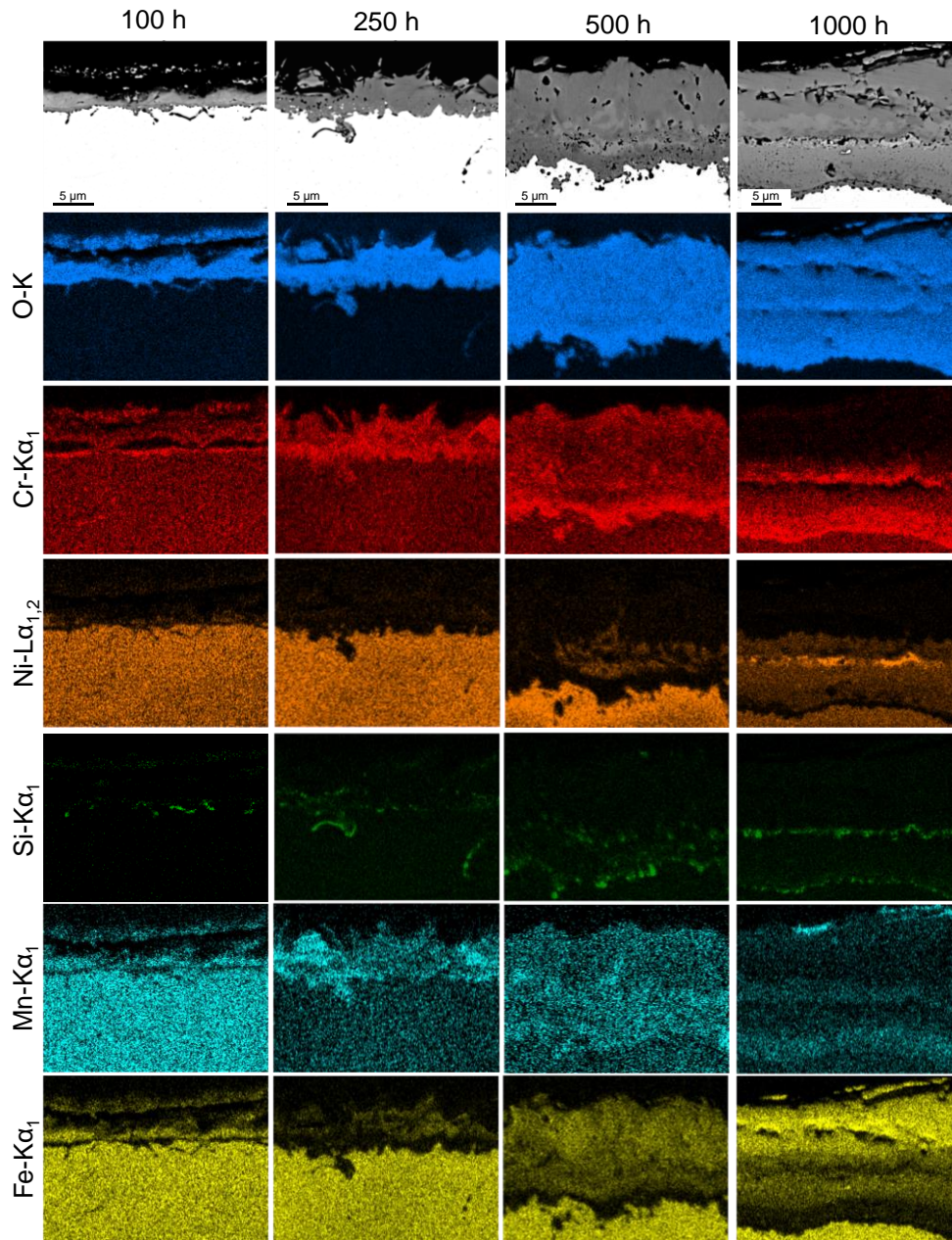


Figure 6-4. Cross-sectional back-scattered electron images of the oxidized coupons exposed for 100 h, 250 h, 500 h, and 1000 h in flowing 0.1 MPa air-10% H₂O at 800°C, and the corresponding SEM-EDS elemental maps of O, Cr, Ni, Si, Mn, and Fe.

Figure 6-5 shows secondary electron images of the site-specific FIB-prepared TEM cross-sectional samples extracted. These scales were formed after 500 h exposure at the three temperatures. The deposited protective W and C layers are identified to differentiate the scale from these layers. The extracted scale formed during the 500°C exposure is 76 ± 17 nm thick (**Figure 6-5[a]**). A layer of recrystallized grains has formed at the metal surface, the formation of which presumably is a consequence of the accumulated mechanical deformation acquired during surface preparation and the subsequent exposure to high temperature.^{43,44} The extracted scale formed during 675°C exposure is 578 ± 243 nm thick (**Figure 6-5[b]**). Second phase particles are visible in the metal. The large dark region below the scale is a damage artifact from FIB milling due to the detachment of material. The extracted scale formed during the 800°C exposure is $13,300 \pm 900$ nm thick (**Figure 6-5[c]**). The multi-layered structure is revealed by the difference in brightness in the image, which arises from a difference in composition. The dashed line indicates the location of the starting alloy surface (prior to wet oxidation exposure) based on the SEM-EDS examination presented earlier. Pores are readily observed in both the outer layer and inner layer of the scale, with the size being larger in the outer layer. Second phase particles are also visible in the metal. The embedded roman numbers on **Figure 6-5(c)** show the selected areas from which a detailed fine-structure STEM analysis was carried out (as described below).

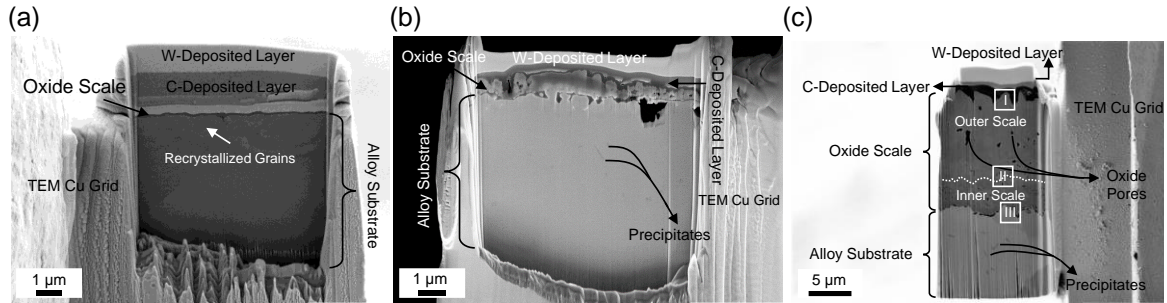


Figure 6-5. Secondary electron images of the FIB-prepared cross-sectional TEM samples of the oxide scale formed after 500 h exposure in flowing air-10% H₂O at (a) 550°C, (b) 675°C, and (c) 800°C.

Figure 6-6 shows a cross-sectional HAADF-STEM image of the oxide scale formed after 500 h exposure at 550°C along with an associated set of STEM-EELS elemental maps and spectra. Both Fe and Ni are enriched at the metal surface and are not noticeably incorporated into the scale (less than ~2 at.%). Si-rich “islands” (about 10 nm wide) have formed at the scale/metal interface. The scale itself contains Cr, Mn and O as major elements. Mn is segregated, being preferentially located at the outer surface and at the scale/metal interface, with the content being higher at the outer surface. Although Cr is detected throughout the scale, it is enriched in the middle region (region of low Mn). Superimposed onto the HAADF-STEM image are numbers that show areas from which the EELS spectra presented were acquired. The phases present in the scale were identified using peak structure in the EELS spectra by comparing the position of the elemental peaks and the relative ratio of the L₃/L₂ edge intensities. A tabulation of the required reference data is published elsewhere.³⁶ From the EELS maps and peak structures in the acquired spectra, it is concluded that this scale consists of three oxides: (i) Si- rich oxide islands at the scale/metal interface (Area 1), (ii) an inner Cr-rich oxide layer

with small amount of Mn in the middle (Area 2), and (iii) an outer Mn-Cr-rich oxide layer on the top (Area 3). The Mn concentration is indeed higher at the alloy/oxide interface compared with Area 2 but the scale structure and phase is still the same. The Si-rich “islands” are consistent with SiO_2 . The inner layer is consistent with Cr_2O_3 with small amount of Mn dissolved and the outer layer is consistent with MnCr_2O_4 . The EELS spectra represented herein match well with those published in the literature.³⁶

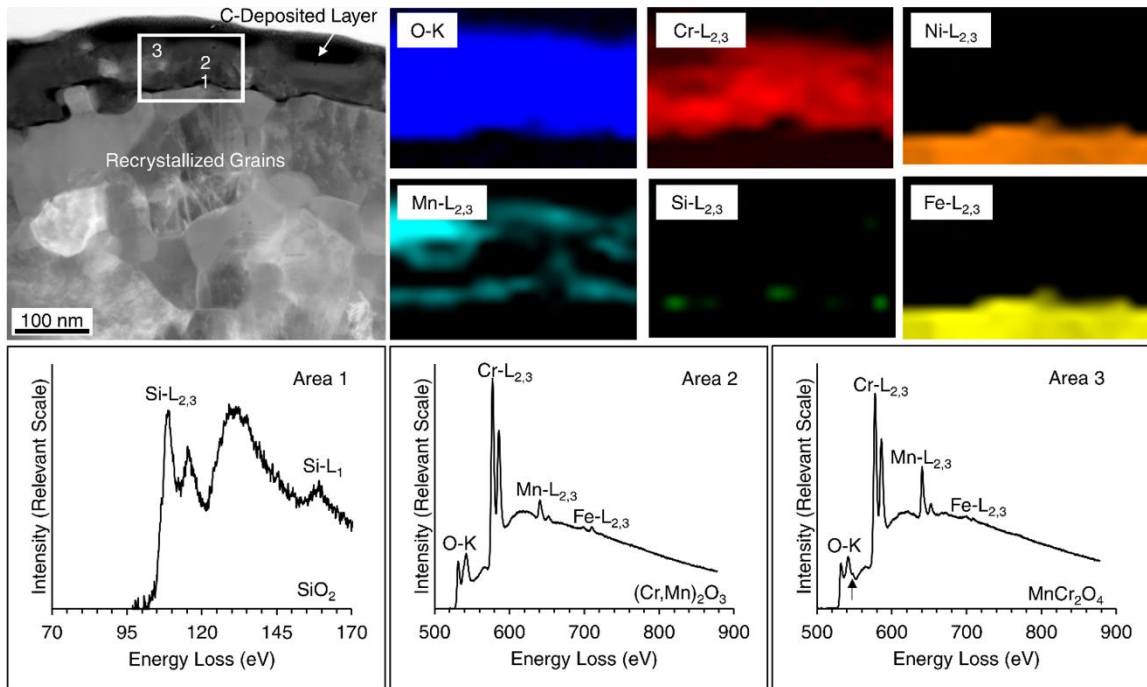


Figure 6-6. Cross-sectional HAADF-STEM image of the oxide scale formed after 500 h exposure in flowing air-10% H_2O at 550°C along with an associated set of STEM-EELS elemental maps and spectra.

Figure 6-7 shows a cross-sectional HAADF-STEM image of the oxide scale formed after 500 h exposure at 675°C along with an associated set of STEM-EELS elemental maps and spectra. The external scale consists of a Mn-rich oxide layer

residing on top of a Cr-rich oxide layer. A close examination of the outer Mn-rich oxide layer shows that the Mn content in this layer is variable, as identified by variations in brightness (intensity) across the layer. An internal Si-rich layer has formed on the recrystallized grain boundaries of the metal underneath the external scale. As the STEM-EDS Si and W peaks overlap, care must be exercised in interpreting the results. The upper bright layer is found to be located just above the external oxide scale and, thus, presumably associated with the protective W layer deposited during the FIB milling procedure. Superimposed onto the HAADF-STEM image are numbers that show areas from which the EELS spectra presented were acquired. The peak structure of the spectrum acquired from Area 4 indicates that the Si-rich layer is consistent with SiO_2 . The outer Mn-rich oxide layer and the inner Cr-rich oxide layer is consistent with $(\text{Mn,Cr})_2\text{O}_3$ and Cr_2O_3 based on the peak structure in the spectrum acquired from Area 6 and 5 respectively. The peak structure in the spectrum acquired from Area 7 (a local region with less Mn enrichment in the outer layer) is consistent with MnCr_2O_4 .

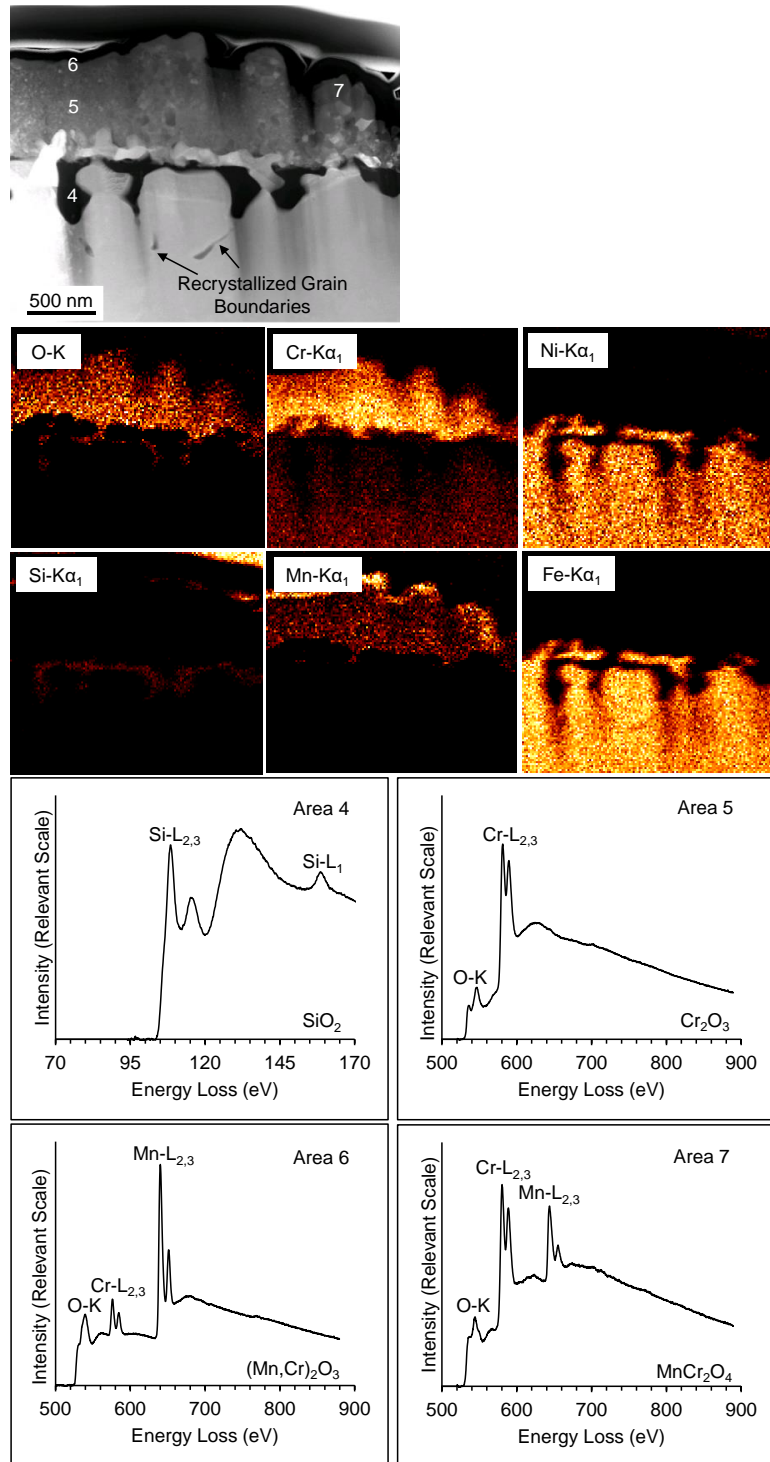


Figure 6-7. Cross-sectional HAADF-STEM image of the oxide scale formed after 500 h exposure in flowing air-10% H $_2$ O at 675°C along with an associated set of STEM-EDS elemental maps and EELS spectra (acquired from Areas 4, 5, 6 and 7 shown on the image).

Figure 6-8 shows a cross-sectional HAADF-STEM image of the outer layer (obtained from site I in **Figure 6-5[c]**) of the scale formed after 500 h exposure at 800°C along with an associated set of STEM-EDS elemental maps for O, Cr, Mn, and Fe and an EELS spectrum (acquired from Area 8 shown on the image). The outer layer is comprised of a columnar grain structure. The STEM-EDS elemental maps show that this layer consists of Fe, Cr and O as major elements and Mn as a minor element. The EELS spectrum matches well with $(\text{Fe,Cr})_2\text{O}_3$ after comparison of the spectrum with those previously published in the literature.³⁶ The relatively large size of the columnar grains provide an opportunity to acquire the selected area diffraction (SAD) pattern from Area 9 shown on the image. SAD pattern clearly confirmed the M_2O_3 (M= Cr and Fe) rhombohedral unit cell of the scale which is in support of the EELS result.

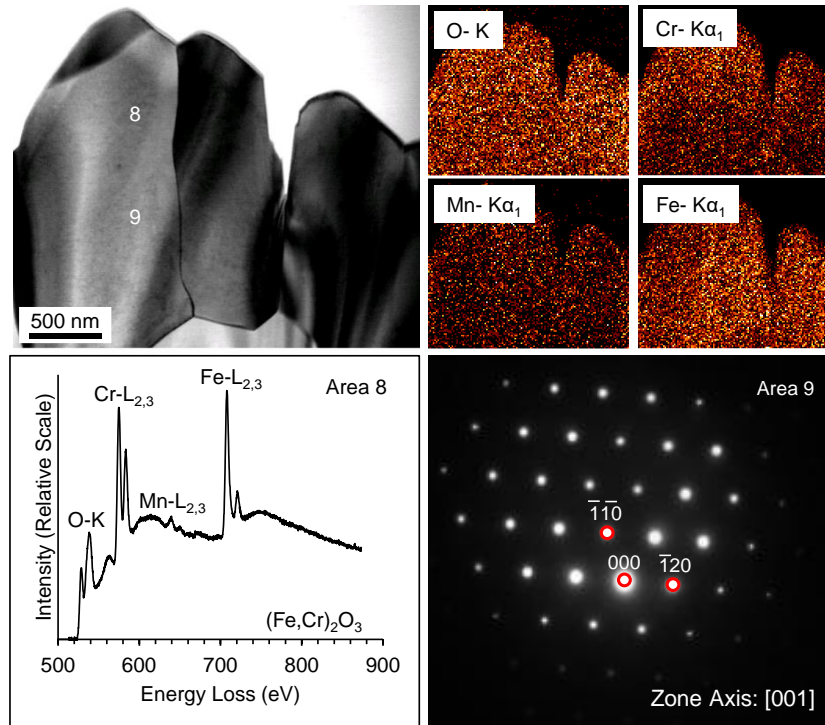


Figure 6-8. Cross-sectional HAADF-STEM image of the outer layer of the scale formed after 500 h exposure at 800°C along with an associated set of STEM-EDS elemental maps, an EELS spectrum (acquired from Area 8 shown on the image) and a SAD pattern (acquired from Area 9 shown on the image).

Figure 6-9 shows the cross-sectional HAADF-STEM image of the outer layer/inner layer interface in the scale formed after 500 h exposure at 800 °C (obtained from site II in **Figure 6-5[c]**) along with associated STEM-EDS elemental maps and EELS spectra (acquired from Area 10 and 11 shown on the image). The interface region consists of a fine-grained structure. The EDS maps reveal that composition of this region varies from grain to grain: some are Cr-Mn-rich, whereas others are Fe-Ni-rich. Localized regions of Si enrichment are also observed between some of the grains. The EELS spectrum from Area 10 matches well with the Cr_2O_3 phase with small amounts of Mn and Fe, whilst the EELS spectrum in

Area 11 shows the characteristic features of a spinel oxide (an O-K shoulder peak shown with the arrow)³⁷ and is consistent with $(\text{Mn,Ni})(\text{Fe,Cr})_2\text{O}_4$.

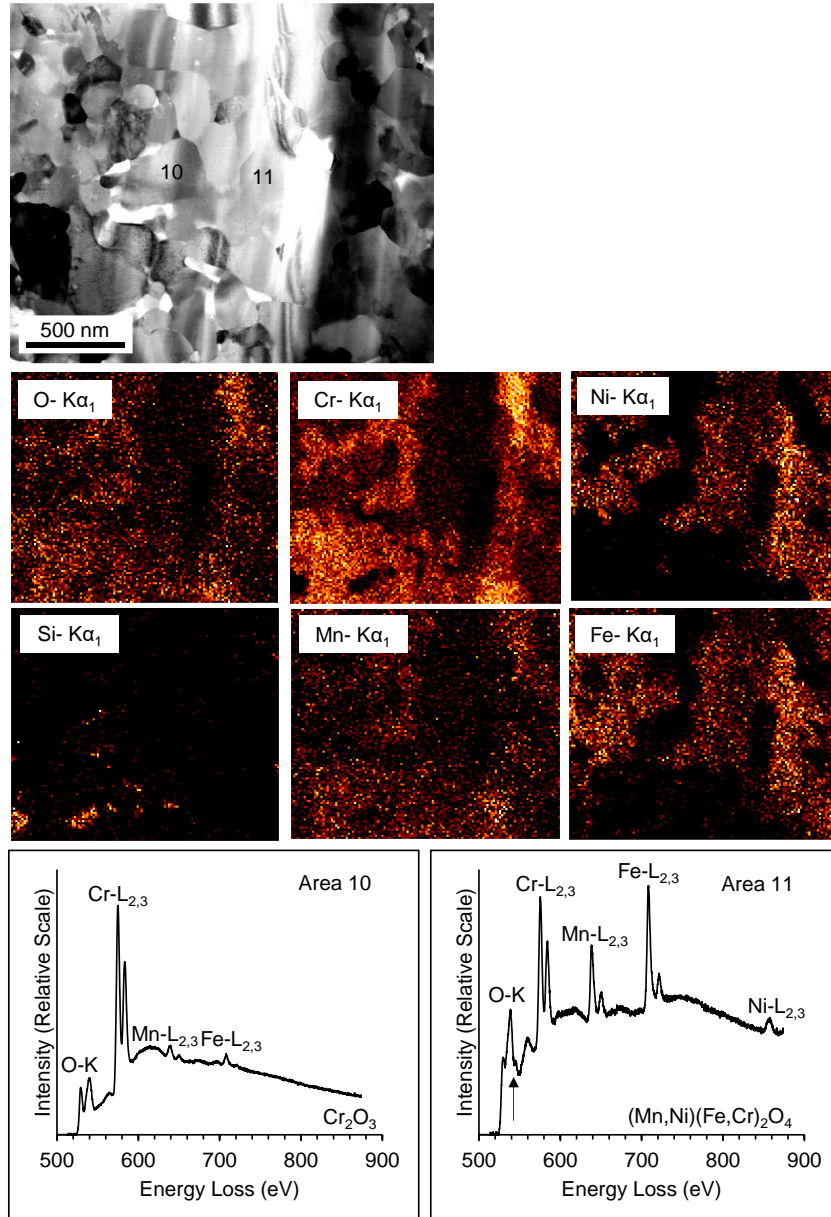


Figure 6-9. Cross-sectional HAADF-STEM image of the outer layer/inner layer interface in the scale formed after 500 h exposure at 800°C along with an associated set of STEM-EDS elemental maps and EELS spectra (acquired from Area 10 and 11 shown on the image).

Figure 6-10 shows a cross-sectional HAADF-STEM image of inner layer (near the scale/metal interface) of the scale formed after 500 h exposure at 800 °C (obtained from site III in **Figure 6-5[c]**) along with an associated set of STEM-EDS elemental maps and EELS spectra (acquired from Areas 12, 13 and 14 shown on the image). This region also consists of a fine-grained structure. However, the EDS maps reveal significantly less variation in composition. This region consists of a Cr-rich oxide layer residing on the underlying metal. A discontinuous SiO₂ layer has formed at the oxide/metal interface (Area 12). Based on the peak structure in the EELS spectra acquired from Area 13, the oxide adjacent to the interface is consistent with Cr₂O₃. In contrast, the peak structure in the EELS spectra acquired from Area 14 reveals that the oxide is consistent with FeCr₂O₄ (likely with some dissolved Mn and Ni).

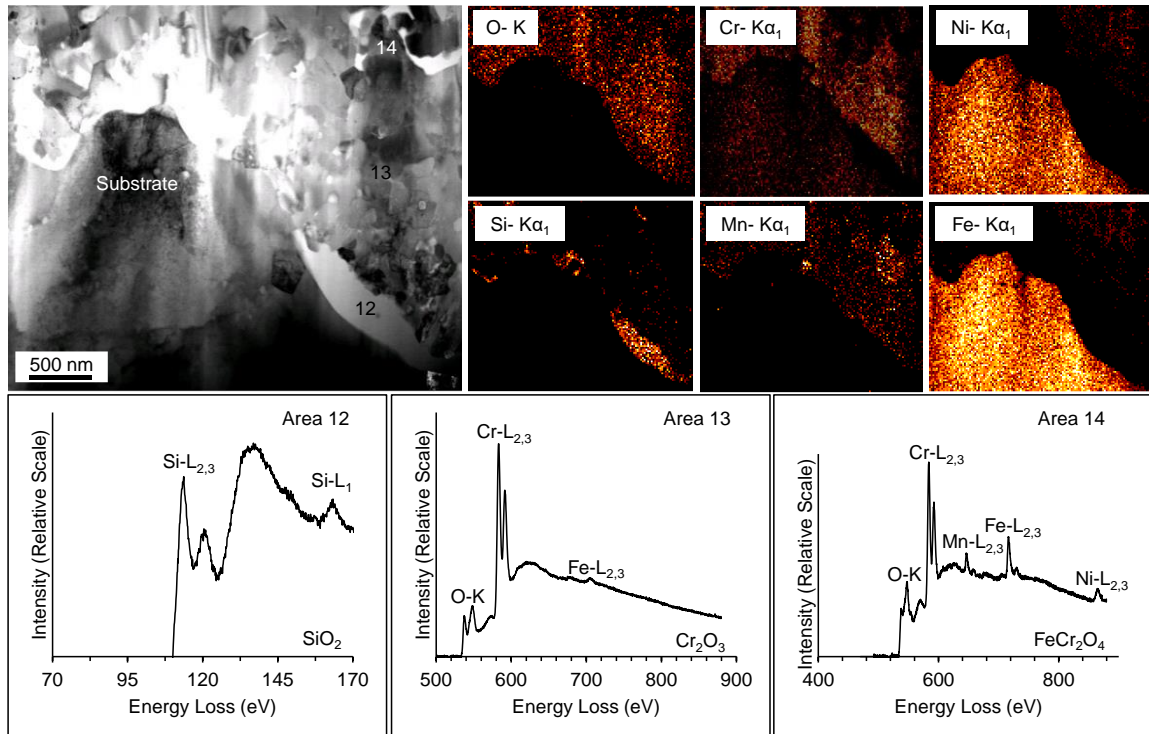


Figure 6-10. Cross-sectional HAADF-STEM image of the inner layer (near the scale/metal interface) of the scale formed after 500 h exposure at 800°C along with an associated set of STEM-EDS elemental maps and EELS spectra (acquired from Area 12, 13 and 14 shown on the image).

6.5. Discussion

Wet oxidation involving volatilization of a protective Cr_2O_3 scale is typically governed by a parabolic rate equation of the form:⁴⁵⁻⁴⁸

$$m \times \frac{dm}{dt} = k_p - k_l \times m \quad \text{Equation 6-2}$$

where m is the mass of the metal consumed per surface area, t is the time, k_p is the parabolic rate constant capturing the diffusion controlled accumulation of the scale and k_l is the linear rate constant capturing the loss of scale due to volatilization.⁴⁵⁻⁴⁸ The weight loss data in **Figure 6-2** has been fitted with

Equation 6-2 using the k_p and k_l values listed in **Table 6-1**. Parabolic kinetics is observed during the 1000 h exposure at 675°C and 800°C exposure, but only the parabolic kinetic regime is observed during the 1000 h at 550°C. A deviation from the linear kinetic regime and the extrapolated parabolic kinetic regime is clearly observed at 800°C. At 675°C, the deviation is not so apparent. However, the transition observed in the corresponding weight gain data (**Figure 6-1[b]**) and the change in the composition and structure of the oxide scale formed suggest that the deviation is real and that volatilization controls the weight loss after 250 h exposure at this temperature.

Figure 6-11 shows a simplified physical description of the scale/metal interface formed on Type 310S stainless steel during the parabolic kinetic regime (scale accumulation) and the linear kinetic regime (scale loss by volatilization) for the various exposures in flowing air-10% H₂O. The composition and structure of the oxide scale that forms during the parabolic kinetic regime is the same for each temperature. It is comprised of a relatively thin MnCr₂O₄ layer formed on top of a thicker Cr₂O₃ layer. A discontinuous SiO₂ layer is also formed at the scale/metal interface. In contrast, the composition and structure of the oxide scale formed during the linear kinetic regime is distinctly different for the two elevated temperatures. A linear kinetic regime is not observed during the 1000 h exposure at 550°C. At 675°C, the scale is comprised of a relatively thin (Mn,Cr)₂O₃ layer formed on top of a thicker Cr₂O₃ layer. **Figure 6-7** indicates that the formation of (Mn,Cr)₂O₃ is a localized phenomenon and that some small local regions with less

Mn enrichment corresponding to MnCr_2O_4 still exist. This localized phenomenon is not shown in **Figure 6-11(b)** due to its small area fraction. At 800°C , the scale is more complex as contains multiple layers. It mainly consists of a relatively thick porous Fe_2O_3 layer formed on top of an internal FeCr_2O_4 layer. The outer layer still contains some amount of Cr which is not shown here. Also the Cr_2O_3 grains seen in the inner layer in **Figure 6-10** are not shown due to their small area fraction. The discontinuous SiO_2 layer, formed during shorter exposure times at these elevated temperatures, remains largely unaffected other than growing to a limited extent. A detail discussion on the scale growth mechanism in each case is described in more detail below.

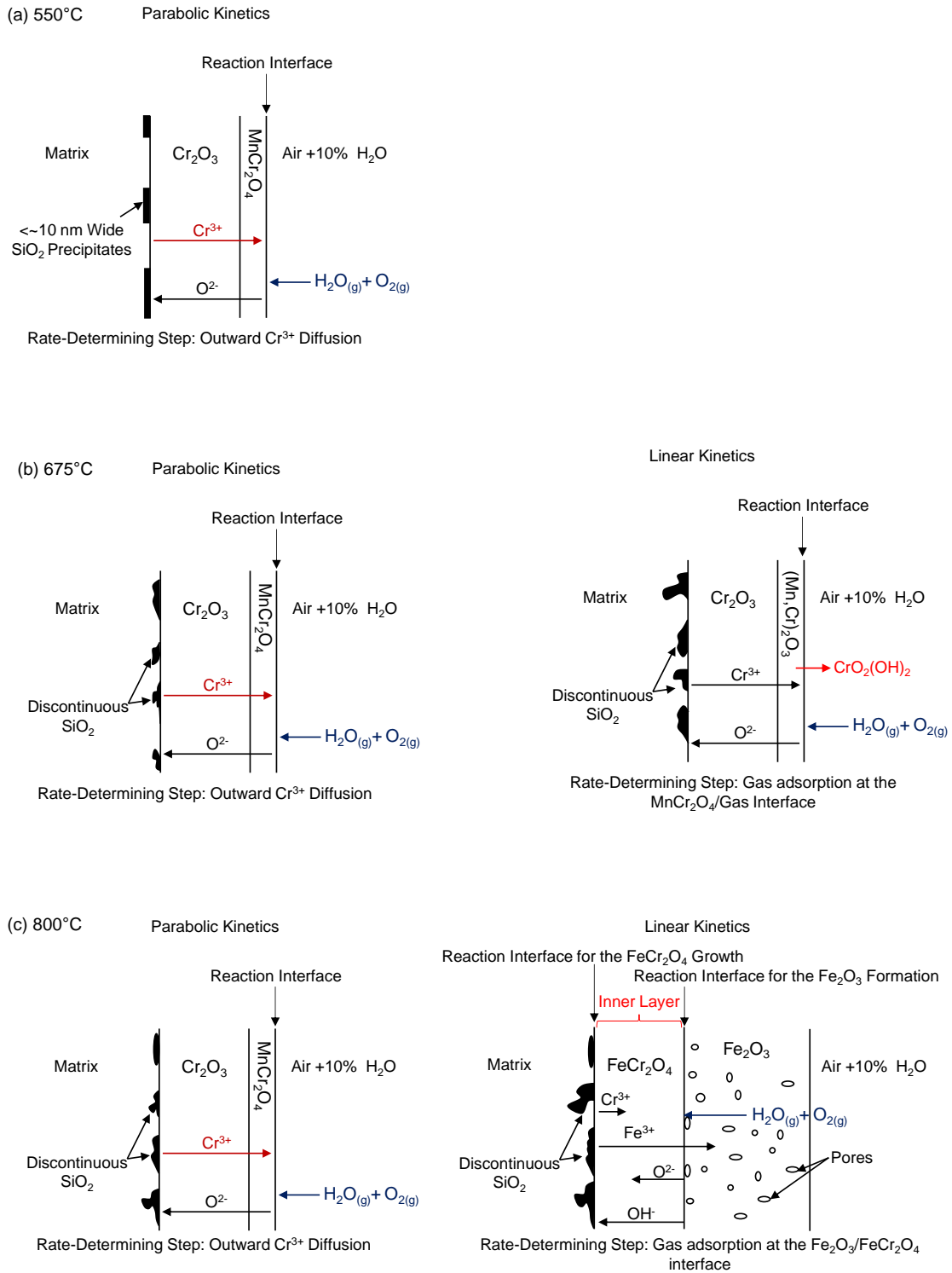
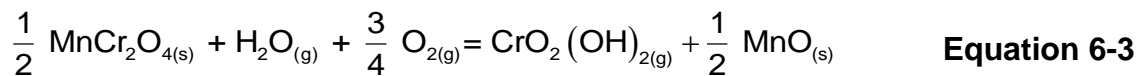


Figure 6-11. Simplified physical description of the oxidation and volatilization mechanistics for Type 310S stainless steel after up to 500 h exposure in flowing 0.1 MPa air-10% H_2O at 550°C, 675°C and 800°C.

The initial formation of a Cr₂O₃ scale in each case is expected since the Type 310S stainless steel under study has a starting bulk Cr content of 24.7 wt.%, which is well in excess of the critical value of ~20 wt.% required for such formation in austenitic Fe-Cr-Ni alloys.⁴⁹⁻⁵¹ As mentioned above, the parabolic kinetic regime is diffusion controlled with the diffusion process inside the Cr₂O₃ layer being the rate-controlling step. This step (for Cr₂O₃ scale growth) is well-established to be the outward diffusion of Cr cations (Cr³⁺).^{52,53} The formation of the outer MnCr₂O₄ is also expected given the thermodynamic stability of the spinel with respect to the binary MnO and Cr₂O₃ oxides at elevated temperatures coupled with the rapid diffusion of Mn cations (relative to Cr and Fe) through Cr₂O₃.^{33,54,55} Thus, given the outward diffusion, oxide growth occurs at the scale/gas interface. The activation energy determined from the k_p values listed in **Table 6-1** is 340 ± 37 kJ/mol, which compares favorably with the reported values of 323 kJ/mol⁵⁶ and 380 ± 51 kJ/mol⁵² for the bi-layer MnCr₂O₄ and Cr₂O₃ forming alloys.

Volatilization of oxidized Cr from MnCr₂O₄ occurs according to **Equation 6-3**:³⁴



Removal of oxidized Cr from MnCr₂O₄ coincides with the formation of porous non-protective MnO on the scale surface.^{34,57} This reaction occurs at the scale/gas interface, with the adsorption of the oxidizing gas species being the rate-controlling step.⁵⁸⁻⁶⁰ Further oxidation of MnO during extended exposure times (or even by cooling to room temperature) can form other types of Mn-oxide products such as

Mn_3O_4 and Mn_2O_3 .^{61,62} The AES analysis of the scale surface after 1000 h exposure at 550°C indicates the presence of $(\text{Mn,Cr})_2\text{O}_3$, rather than MnCr_2O_4 (as observed after shorter exposure times). This finding suggests that volatilization occurred during the exposure at 550°C, but the relatively low rate requires extended exposure times to be resolved with the experimental methodology employed.

The change in the oxide scale composition and structure associated with the transition to the linear kinetic regime (volatilization control) is temperature dependent, at least for the 1000 h exposure considered. The accelerated formation of Fe-rich oxides occurs at 800°C, but not at 675°C. At 800°C, a thick porous Fe_2O_3 layer forms on top of an internal layer that mainly consists of FeCr_2O_4 . It has been vastly discussed that the excess growth of the Fe_2O_3 layer cannot be explained by a diffusion controlled process (parabolic oxidation) and adsorption of the oxidizing gas species on the oxide surfaces must play a role.^{10,63-65} Penetration of the oxidizing species through a Fe-rich oxide layer also has been widely discussed in the literature.⁶⁶⁻⁶⁸ It is argued that the outer porous Fe-rich oxide layer and the inner Cr-rich FeCr_2O_4 layer are separated at the original alloy surface by a large amount of voids present as the result of stresses in the oxides.^{69,70} Transport of oxidizing species through the outer layer to the $\text{Fe}_2\text{O}_3/\text{FeCr}_2\text{O}_4$ interface and their adsorption and dissociation at this interface is therefore highly plausible similar to a mechanism explained by Ehlers et al.,⁶⁸ and can be considered as the slowest reaction step (rate-controlling step).^{66,68,71} It is important to acknowledge that the

$\text{Fe}_2\text{O}_3/\text{FeCr}_2\text{O}_4$ interface is rich in Cr that is susceptible to volatilization therefore it follows to consider that the $\text{Fe}_2\text{O}_3/\text{FeCr}_2\text{O}_4$ interface controls the volatilization rate. H_2O can penetrate through the oxides and reach to the $\text{Fe}_2\text{O}_3/\text{FeCr}_2\text{O}_4$ interface providing the necessary agent to oxidize the metal to form an inner layer further from the interface that is controlling volatilization.¹⁰ Many attempts have thus far been done to understand the transport mechanism of species through oxides. The mechanisms reported however, often vary for different oxides and in different oxidizing conditions.^{63,65} Gaseous hydroxyl compounds have very high transport rate through an oxide scale during steam oxidation since their effective radius is smaller than that for O_2 anions.⁷² It is argued that H_2O adsorbs at the interface on the sites that are free of adsorbed O_2 and decomposes to form hydroxyls.⁷² The H_2 generated from this reaction either dissolves in the metal or is transported back to the gas mixture (hydrogen evolution).^{72,73} The inward growing FeCr_2O_4 is then formed by transport of oxidizing anions from the interface of the oxides to the inner oxide layer whilst the reaction interface for the growth of the FeCr_2O_4 layer is the $\text{FeCr}_2\text{O}_4/\text{alloy}$ interface in this case.^{10,21} The combined SEM and STEM results show that the inner layer has different compositions of elements and the Cr, Mn, and Fe concentrations even in adjacent oxide grains vary. The observed variations in the composition within the inner oxide layer is consistent with the reported literature.⁷⁴ It has been argued that those oxide grains that have less than 60 wt.% Cr can transform into a porous Fe-Cr spinel-type oxide.^{21,74} As the diffusivity of Fe

is much higher relative to Cr into a porous Fe-Cr spinel oxide, Fe more easily contributes to the growth of the outer Fe-rich oxide layer with time.^{21,74}

The accelerated formation of Fe-rich oxides (so called “breakaway” oxidation) is typically what is observed during wet oxidation of Fe-Cr-Ni alloys.^{19,75,76} In this case, the Cr content within the Cr-depleted zone in the alloy is less than a critical value required to maintain Cr₂O₃ (or MnCr₂O₄) by replacing the oxidized Cr lost to volatilization and, thus, Fe becomes the dominant diffusing metal leading to the rapid formation of Fe-rich oxides.^{19,20,77} The change in the dominant diffusing metal from Cr to Fe is coupled with the formation of less protective Mn-rich oxide degradation products from the volatilization reaction.^{32,78} The AES results show that Mn-rich oxide products are detected after 250 h exposure at 800°C, which coincides with the transition from the parabolic regime to the linear kinetic region. **Figure 6-12** compares the average minimum Cr content present in the Cr-depleted zone within the alloy as a function of exposure time at 550°C, 675°C and 800°C. From **Figure 6-12** and our electron microscopy results, it is evident that a critical Cr content of 11.2 ± 1.8 wt.% is required to be present in the Cr-depleted zone to maintain the original Cr₂O₃/MnCr₂O₄ scale whilst any value lower than that results in the accelerated Fe-rich oxide formation. Our reported critical Cr content in the Cr-depleted zone is close to the previously reported value of 13 ± 1 wt.% by B. Bauer et al.⁷⁹ for the austenitic Cr₂O₃ forming Fe–25Cr–20Ni–2.8Si alloy at ~1000°C.

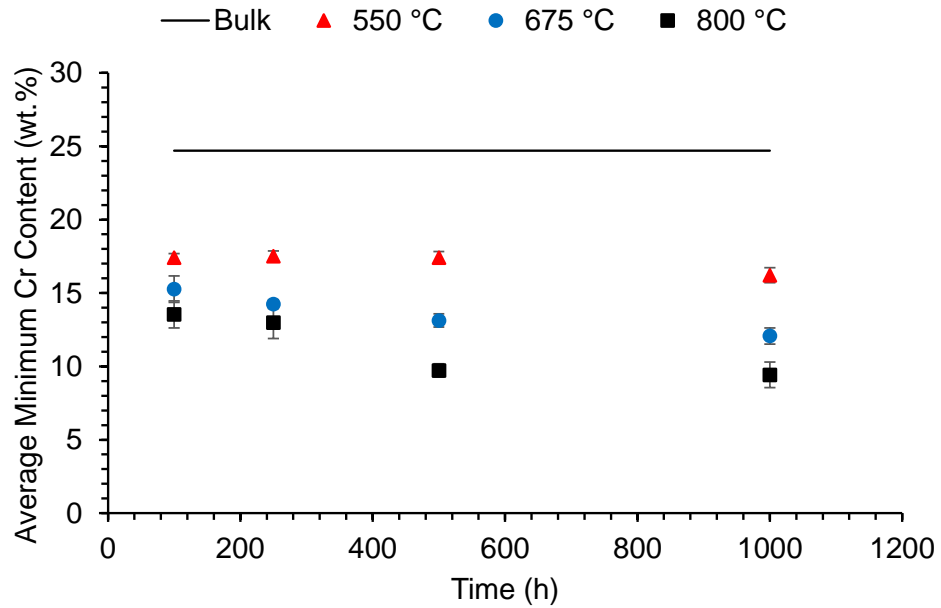


Figure 6-12. Average minimum Cr content (wt.%) present in the Cr-depleted zone as a function of exposure time at 550°C,³⁶ 675°C, and 800°C.

Figure 6-13 compares the depth of the Cr-depleted zone within the alloy as a function of time during the exposure at 675°C and 800°C. The depths of the Cr-depleted zone at 550°C measured in this study after 500 h and in our previous work after 100 h, 250 h and 1000 h are also shown for comparison.³⁶ The depth of the Cr-depleted zone after all of the exposure times is insignificant at 550°C albeit slightly increases with time (consistent with the parabolic rate). At 675°C a deviation from the parabolic law is observed after ~250 h which is consistent with the higher amount of weight loss associated with the volatilization controlled kinetic regime. It is evident that at 800°C up to 250 h the depth is still small and follows a parabolic law yet it increases to ~27 μm after 500 h which is significantly large. We saw that after 500 h exposure, Fe incorporates more into the scale formation therefore it is plausible that the Cr-depleted depth remains the same after 1000 h

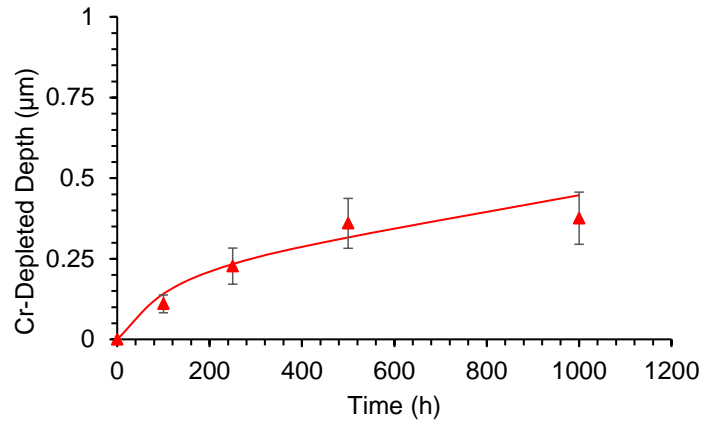
exposure. The findings from **Figure 6-13** are in consistent with the observed kinetics suggesting that a large Cr-depleted depth with the average minimum Cr content less than the critical value reported earlier is needed for the breakaway oxidation to occur.

The lack of Fe-rich oxide formation at 675°C is also consistent with the weight gain data exhibited in **Figure 6-1(b)**. **Equation 6-4** predicts that the oxide scale thickness (X) increases with time during accumulation, but decreases with time during volatilization until the scale thickness reaches a critical (steady-state) thickness (in the absence of accelerated Fe-rich oxide formation).⁶⁴ Note that k'_p and k'_l here are the parabolic and linear rate constants with the units of cm^2/s and cm/s , respectively. The negative slope observed after 250 h exposure at 675°C (initial parabolic kinetic regime) is consistent with this prediction as the scale thickness would remain constant, but metal consumption would continue at a constant rate.

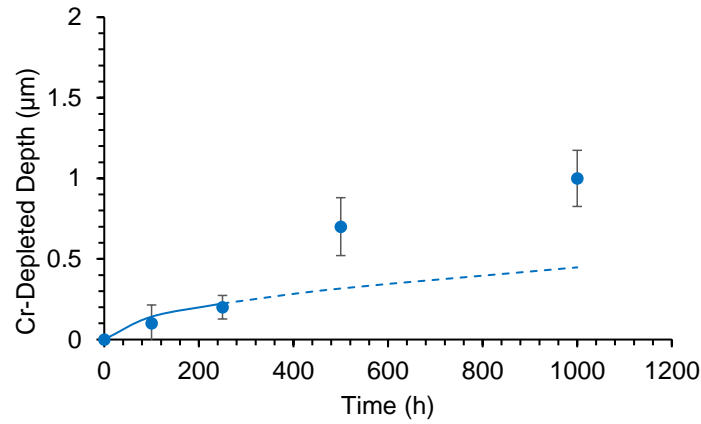
$$\frac{dX}{dt} = \frac{k'_p}{X} - k'_l$$

Equation 6-4

(a)



(b)



(c)

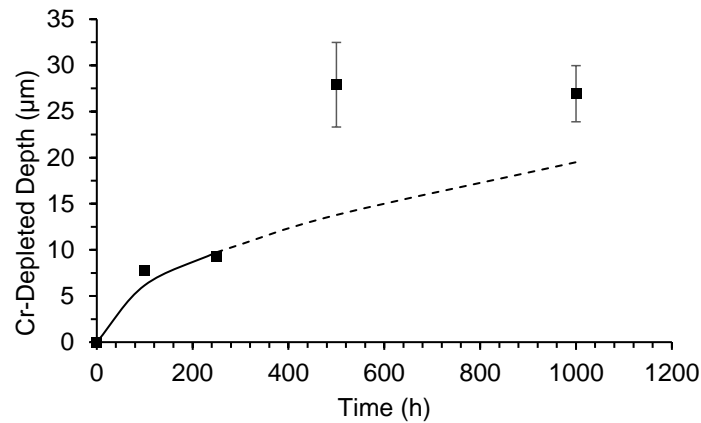


Figure 6-13. Graph of the Cr-depleted depth (µm) formed in Type 310S stainless steel matrix after up to 1000 h exposure in flowing 0.1 MPa air-10% H₂O at (a) 550°C,³⁶ (b) 675°C, and (c) 800°C.

Figure 6-14 plots the thickness of the Cr_2O_3 layer formed on Type 310S stainless steel after up to 1000 h exposure at 675°C . The Cr_2O_3 layer thickness increases parabolically up to 250 h with the k_p of $3.9 \times 10^{-15} \text{ cm}^2/\text{s}$ ($R^2 = 0.985$) however significantly deviates from the parabolic kinetics after 250 h exposure. The scale thickness considering the error bars is somewhat the same after 250 h and reaches to the steady-state thickness. The similar oxide thickness observed between 250 h and 1000 h exposure confirms the assumption that the Cr supply from the alloy is sufficient to supply the oxidized Cr lost to volatilization.

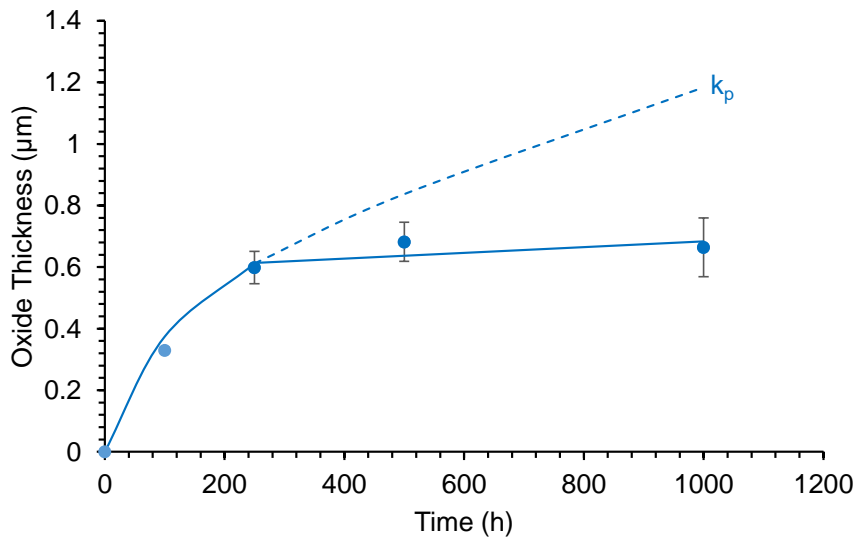


Figure 6-14. Variation in the thickness of the oxide scale formed on Type 310S stainless steel after up to 1000 h exposure in flowing 0.1 MPa air-10% H_2O at 675°C .

The volatilization rate of oxidized Cr from MnCr_2O_4 is believed to be lower than from Cr_2O_3 scale, therefore MnCr_2O_4 is considered to be a protective oxide relative to Cr_2O_3 , when present as an outer layer.^{32,34} Holcomb et al.³⁴ showed that the rate of oxidized Cr loss from MnCr_2O_4 is strongly dependent on temperature,

regardless of the partial pressures of H₂O and O₂ in the environment, as the volatilization rate increases exponentially with temperature. Young and Pint⁸⁰ estimated the flux of oxidized Cr lost to volatilization in a flowing (~1.4 cm/s) air-10% H₂O mixture at 500°C, 600°C and 800°C. Their flux equations can be used to estimate the flux of Cr lost (g/cm²/s) at the 675°C and 800°C exposures considered in this study, the value of which can be compared to a flux of Cr lost from the metal estimated from the depth of the Cr-depleted zone and the associated Cr content. Such a comparison provides some insights into the degree of protection offered by the MnCr₂O₄ cap in each case. The estimated fluxes are listed and compared in **Table 6-3**. The partial pressure of CrO₂(OH)₂ listed, as required in the volatilization flux estimation, was calculated using the Gibbs free energy of **Equation 6-1** that is reported in the literature.⁸⁰ The procedure used to estimate the oxidized Cr flux from STEM results as well as the flux equations used to estimate the oxidized Cr loss are provided in **Appendix A**. From **Table 6-3**, it is evident that the flux estimated from Cr metal consumption is slightly smaller than the flux estimated from volatilization at 675°C, which supports the idea that MnCr₂O₄ is indeed protective and slows down the rate of oxidized Cr lost to volatilization. However, the flux estimated from Cr metal consumption is significantly higher than the flux estimated from volatilization at 800°C. The discrepancy is likely related to the fact that the Cr-depleted zone overestimates the Cr metal flux available for volatilization because of the formation of the FeCr₂O₄ layer underneath the original oxide scale formed during the accumulation (parabolic kinetic) stage.

Table 6-3 Estimated and measured Cr loss flux (g/cm²/s) in air-10% H₂O

| Temperature (°C) | pCrO ₂ (OH) ₂ (atm) | Estimated J _{Cr} (g/cm ² /s) | Cr-Depleted Depth (µm)* | Average Cr Content of the Depleted Zone (wt.%)* | Measured J _{Cr} (g/cm ² /s) |
|------------------|---|--|-------------------------|---|---|
| 675 | 1.4 × 10 ⁻⁷ | 8.5 × 10 ⁻¹¹ | 0.9±0.2 | 12.6±0.8 | (4.9 ± 1.4) × 10 ⁻¹¹ |
| 800 | 3.0 × 10 ⁻⁷ | 1.7 × 10 ⁻¹⁰ | 27.4±2.1 | 9.6±0.6 | (2.1 ± 1.1) × 10 ⁻⁹ |

*Values shown here are for 500 h and 1000 h exposure times.

From a wet oxidation performance perspective, the results indicate that Mn (as an alloying element) has a beneficial effect on the performance (weight loss) of Type 310S stainless, but the effect is only temporary. The beneficial effect stems from the formation of a protective MnCr₂O₄ cap that is more resistant to oxidized Cr loss by volatilization. However, oxidized Cr loss by volatilization will occur from this cap leading to the accelerated formation of non-protective Fe-rich oxides at elevated temperatures. The results also indicate that Si (as an alloying element) may have a beneficial effect on the wet oxidation performance by forming a barrier layer at the scale/metal interface. The formation of a discontinuous SiO₂ layer (precipitates) underneath a Cr₂O₃ scale, as observed in this study, and the associated effect on reducing diffusion into the Cr₂O₃ scale has been given some consideration.^{81,82} The ability of SiO₂ to reduce diffusion is attributed to the amorphous structure.^{83,84} The wet oxidation exposure at 550°C coincided with the formation of a discontinuous SiO₂ layer, within which the spacing between individual precipitates is larger than the width (~10 nm wide). Such a formation is not considered to be an effective barrier,⁴⁰ as an effective barrier requires the formation of a continuous layer.^{85,86} The exposures at both 675°C and 800°C, also coincided with the formation of a discontinuous SiO₂ layer, albeit with larger individual precipitates. It is considered worthwhile to investigate the wet oxidation

performance of Type 310S stainless steel with an intentionally higher alloyed Si as a control strategy. If it is true that a continuous SiO_2 layer can serve as an effective barrier layer, then both a slower parabolic oxidation rate and a delay in the onset of accelerated formation of non-protective Fe-rich oxides are expected.

6.6. Conclusions

The wet oxidation performance of Type 310S stainless steel was examined in a flowing air-10% H_2O mixture to develop a more complete physical description linking changes in the structure and composition of the oxide scale formed to changes in the oxidation kinetics. Major conclusions drawn from this study are summarized below.

- Wet oxidation is governed by a parabolic rate law, which includes a diffusion-controlled scale accumulation term and a constant volatilization loss term. Scale accumulation involves the formation of a thinner MnCr_2O_4 outer layer on a thicker Cr_2O_3 inner layer, whereas volatilization involves the loss of oxidized Cr from the MnCr_2O_4 cap as the initiating process, as confirmed by the formation of Mn-rich oxide reaction products.
- The onset of accelerated formation of non-protective Fe-rich oxides during the linear kinetic regime is temperature dependent for the 1000 h exposure time considered: forming only at 800 °C. The delayed onset at 675°C is attributed to the Cr content within the depleted zone in the alloy being

sufficiently higher than the critical content (11.2 ± 1.8 wt.% Cr) required to maintain the original $\text{Cr}_2\text{O}_3/\text{MnCr}_2\text{O}_4$ scale.

- Mn (as an alloying element) has a beneficial effect on performance, but the effect is only temporary. The beneficial effect stems from the formation of a protective MnCr_2O_4 cap that is more resistant to oxidized Cr loss by volatilization. However, oxidized Cr loss by volatilization will occur from this cap leading to the accelerated formation of non-protective Fe-rich oxides at elevated temperatures.

6.7. Acknowledgements

Funding was provided by Natural Sciences and Engineering Research Council of Canada (NSERC) through the Discovery Grants program. The technical support provided by the Canadian Centre for Electron Microscopy (CCEM) is greatly appreciated. The CCEM is a national facility supported by NSERC, Canada Foundation for Innovation (CFI) through the Major Science Initiative MSI fund and McMaster University.

6.8. Appendix A

The mass transfer of Cr from a Cr₂O₃ scale to a flowing gas is discussed using the gas transport theory in the viscous flow regime by Gaskell⁸⁷ and is further explained by Young and Pint.⁸⁰ The molar flux of the Cr species, J_{Cr}, is given by **Equation 6-5** in which k_m is the mass-transfer coefficient, R is the universal gas constant, T is the temperature and p_i and p₀ are the partial pressure of CrO₂(OH)₂ gas species (pCrO₂(OH)₂) at the oxide surface and alloy/oxide interface, respectively:⁸⁰

$$J_{Cr} = \frac{k_m}{RT} (p_i - p_0) \quad \text{Equation 6-5}$$

To measure the pCrO₂(OH)₂, the thermodynamic data discussed by Opila⁸⁸ for **Equation 6-1** is used:

$$\Delta G^\circ = 53,500 + 45.5T \text{ (J)} \quad \text{Equation 6-6}$$

The value of k_m in **Equation 6-5** can be measured using **Equation 7** in which D_{AB} is the binary gas diffusion coefficient, ν is the kinematic viscosity, V is the linear gas velocity and l is the coupon length:

$$k_m = 0.664 \left(\frac{D_{AB}^4}{\nu} \right)^{1/6} \left(\frac{V}{l} \right)^{1/2} \quad \text{Equation 6-7}$$

Considering that the measured D_{AB} is ~1 cm²/s at temperatures between 600-800°C⁸⁰, and using the flow velocity and coupon length of 4.0 ± 0.2 cm/s and 1.5 cm, respectively the value of k_m can be measured for the temperatures considered in this study. It should be noted that the values for ν at the temperature range between 600-800°C are also reported elsewhere and can be considered to be

approximately $1 \text{ cm}^2/\text{s}$.⁸⁰ The J_{Cr} is then simply estimated by replacing the k_m value in **Equation 6-5**.

The procedure for measuring Cr cations flux lost to oxidation and volatilization during exposure of Type 310S stainless steel after 500 h and 1000 h exposure (longest exposure times) in air-10% H₂O at 675°C and 800°C based on the STEM and SEM results is explained as follows.

First, the depth of the Cr depleted zone (d) was measured at 675°C and 800°C after 500 h and 1000 h using STEM and SEM results. The average of these values within the 95% CI are presented in **Table 6-3**. Using the known coupons dimensions, length (l) and width (w) in particular, and d , the volume of the Cr depleted zone ($V_{\text{Cr-depleted zone}}$) was estimated:

$$V_{\text{Cr-depleted zone}} (\text{cm}^3) = l \times w \times d \quad \text{Equation 6-8}$$

Knowing that the density of Type 310S stainless steel (ρ) is 7.89 g/cm^3 according to its mill test certificate,³⁸ and that 24.7 wt.% of the alloy is consisted of Cr, the mass of Cr in the Cr depleted depth (m_1) is estimated:

$$m_1 (\text{g}) = 0.247 \times \rho \times V_{\text{Cr-depleted zone}} \quad \text{Equation 6-9}$$

It is important to note that not all of the mass measured in **Equation 6-9** incorporates into the scale formation and volatilization. STEM-EDS results show that some Cr still remains in the Cr-depleted zone regardless of the Cr-depleted depth, after exposure in all cases. The average minimum Cr content left in the Cr-depleted zone is shown in **Figure 6-12**. If the amount of Cr remained in the

substrate below the scale is x wt.%, the mass of Cr lost from the depleted zone to oxidation and volatilization (m_2) is estimated as:

$$m_2 (g) = (1 - [x\%]) m_1 \quad \text{Equation 6-10}$$

To measure the flux of oxidized Cr lost to oxidation and volatilization (J_{Cr}), **Equation 6-11** is used where A and t are the cross sectional area for transport of Cr cations (cm^2) and time of exposure (s), respectively. A can be measured knowing the l and w of the coupons. Estimated flux values measured using this equation are presented in **Table 6-3**.

$$J_{Cr} = \frac{m_2}{At} \quad \text{Equation 6-11}$$

6.9. References

1. J.H. Kim, D.I. Kim, S. Suwas, E. Fleury, and K.W. Yi, *Oxid. Met.* 79 (2013): pp. 239–247.
2. H. Asteman, J.-E. Svensson, and L.-G. Johansson, *J. Electrochem. Soc.* 151 (2004): p. B141.
3. Y. Behnamian, A. Mostafaei, A. Kohandehghan, B.S. Amirkhiz, D. Serate, W. Zheng, D. Guzonas, M. Chmielus, W. Chen, and J.L. Luo, *Mater. Charact.* 120 (2016): pp. 273–284.
4. S. Zhang, H. Yang, and L. Singh, *CEUR Workshop Proc.* 1225 (2014): pp. 41–42.
5. R. Peraldi, and B.A. Pint, *Oxid. Met.* 61 (2004): pp. 463–483.
6. B. Li, and B. Gleeson, *Oxid. Met.* 62 (2004): pp. 45–69.
7. A.C.S. Sabioni, J.N. V Souza, V. Ji, F. Jomard, V.B. Trindade, and J.F. Carneiro, *Solid State Ionics* 276 (2015): pp. 1–8.
8. E. Schmucker, C. Petitjean, L. Martinelli, P.J. Panteix, S. Ben Lagha, and M. Vilasi, *Corros. Sci.* 111 (2016): pp. 474–485.
9. W.J. Nowak, P. Wierzba, D. Naumenko, W.J. Quadackers, J. Sieniawski, Water vapour effect on high temperature oxidation behaviour of superalloy Rene 80, *Advances. Manufacturing Sci. and Technol.* 40 (2016) 1-12.
10. H. Hooshyar, T. Jonsson, J. Hall, J.E. Svensson, L.G. Johansson, and J. Liske, *Oxid. Met.* 85 (2016): pp. 321–342.
11. J. Yuan, W. Wang, H. Zhang, L. Zhu, S. Zhu, and F. Wang, *Corros. Sci.* 109 (2016): pp. 36–42.
12. T. Dudziak, V. Deodeshmukh, L. Backert, N. Sobczak, M. Witkowska, W. Ratuszek, K. Chruściel, A. Zieliński, J. Sobczak, and G. Bruzda, *Oxid. Met.* 87 (2017): pp. 139–158.
13. E.J. Opila, D.L. Myers, N.S. Jacobson, I.M.B. Nielsen, D.F. Johnson, J.K. Olminky, and M.D. Allendorf, *J. Phys. Chem. A* 2 (2007): pp. 1971–1980.

14. P. Huczowski, W. Lehnert, H.H. Angermann, A. Chyrkin, R. Pillai, D. Gruner, E. Hejrani, and W.J. Quadackers, *Mater. Corros.* 68 (2017): pp. 159–170.
15. E.J. Opila, N.S. Jacobson, D.L. Myers, and E.H. Copland, *J. Miner. Met. Mater. Soc.* 58 (2006): pp. 22–28.
16. E.J. Opila, *Mater. Sci. Forum* 461–464 (2004): pp. 765–774.
17. E. Bucher, *Berg- Und Hüttenmännische Monatshefte* 156 (2011): pp. 423–428.
18. J. Froitzheim, and J.E. Svensson, *Electrochem. Soc.* 35 (2011): pp. 2503–2508.
19. H. Asteman, J. Svensson, M. Norell, and L. Johansson, *Oxid. Met.* 54 (2000): pp. 11–26.
20. K. Segerdahl, J.E. Svensson, M. Halvarsson, I. Panas, and L.G. Johansson, *Mater. High Temp.* 22 (2005): pp. 69–78.
21. T. Jonsson, S. Karlsson, H. Hooshyar, M. Sattari, J. Liske, J.E. Svensson, and L.G. Johansson, *Oxid. Met.* 85 (2016): pp. 509–536.
22. P.J. Ennis, and W.J. Quadackers, *Int. J. Press. Vessel. Pip.* 84 (2007): pp. 82–87.
23. I.G. Wright, and R.B. Dooley, *Int. Mater. Rev.* 55 (2010): pp. 129–167.
24. H. Asteman, J.-E. Sevensson, and L.-G. Johansson, *Oxid. Met.* 57 (2002): pp. 193–216.
25. V.P. Deodshmukh, and S.K. Srivastava, *JOM* 61 (2009): pp. 56–59.
26. J.S. Dunning, D.E. Alman, and J.C. Rawers, *Oxid. Met.* 57 (2002): pp. 409–425.
27. A. Takei, and K. Nii, *Trans. Tapan Inst. Met.* 22 (1981): pp. 118–126.
28. R. Sachitanand, M. Sattari, J.E. Svensson, and J. Froitzheim, *Int. J. Hydrogen Energy* 38 (2013): pp. 15328–15334.
29. H.M. Tawancy, *Mater. High Temp.* 34 (2017): pp. 22–32.

30. M.J. Garcia-Vargas, L. Lelait, V. Kolarik, H. Fietzek, and M.D.M. Juez-Lorenzo, *Mater. High Temp.* 22 (2005): pp. 245–251.
31. V.F.C. Lins, M.M.R. Castro, R.Z. Domingues, and T. Matencio, *Chem. Eng. Technol.* 33 (2010): pp. 334–340.
32. H. Falk-Windisch, J.E. Svensson, and J. Froitzheim, *J. Power Sources* 287 (2015): pp. 25–35.
33. A.N. Hansson, and M.A.J. Somers, *Mater. High Temp.* 22 (2005): pp. 223–229.
34. G.R. Holcomb, and D.E. Alman, *Scr. Mater.* 54 (2006): pp. 1821–1825.
35. M.J. Garcia Vargas, L. Lelait, V. Kolarik, H. Fietzek, and M. Juez-Lorenzo, *Mater. Sci. Forum* 461–464 (2004): pp. 823–830.
36. S. Mahboubi, H.S. Zurob, G.A. Botton, J.R. Kish, Environment effects on the stability of chromia (Cr_2O_3)-based scale formed on Type 310S stainless steel during wet oxidation, Submitted to *Corros.* (2018).
37. S. Mahboubi, H.S. Zurob, G.A. Botton, and J.R. Kish, *Can. Metall. Q.* 57 (2018): pp. 89–98.
38. ASTM A240, "Standard Specification for Chromium and Chromium-Nickel Stainless Steel Plate, Sheet, and Strip for Pressure Vessels and for General Applications"
39. "ASTM E112-13, 'Standard Test Methods for Determining Average Grain Size' (West Conshohocken, PA: ASTM, 2013)."
40. S. Mahboubi, "Effect of Cr Content on Corrosion Resistance of Fe-Cr-Ni Alloys Exposed in Supercritical Water (SCW)," McMaster University, 2014.
41. JEMS Software: <http://www.jems-saas.ch/Home/jemsWebSite/jems.html>.
42. A.C.S. Sabioni, A.M. Huntz, J.N.V. Souza, M.D. Martins, and F. Jomard, *Philos. Mag.* 88 (2008): pp. 391–405.
43. I. Altenberger, B. Scholtes, U. Martin, and H. Oettel, *Mater. Sci. Eng. A* 264 (1999): pp. 1–16.
44. S. Cissé, L. Laffont, B. Tanguy, M.C. Lafont, and E. Andrieu, *Corros. Sci.* 56

(2012): pp. 209–216.

45. L. Aranda, and P. Berthod, *Comput. Sci. Eng.* 3 (2001): pp. 14–15.

46. P. Berthod, L. Aranda, and C. Heil, *Open Corros. J.* 2 (2009): pp. 150–156.

47. E. Conrath, and P. Berthod, *Oxid. Met.* 81 (2014): pp. 393–405.

48. A. Dieye, E. Conrath, and P. Berthod, *Mater. Sci.* 13 (2015): pp. 370–376.

49. S. Mahboubi, Y. Jiao, W. Cook, W. Zheng, D.A. Guzonas, G.A. Botton, and J.R. Kish, *Corrosion* 72 (2016): pp. 1170–1180.

50. V.V. Khokhlov, A.G. Rakoch, E.S. Dement, and O.A. Lyzlov, 40 (2004): pp. 62–66.

51. N. Otsuka, Y. Shida, and H. Fujikawa, *Oxid. Met.* 32 (1989): pp. 13–45.

52. T. Brylewski, J. Dąbek, and K. Przybylski, *J. Therm. Anal. Calorim.* 77 (2004): pp. 207–216.

53. J.S. Dunning, D.E. Alman, and J.C. Rawers, *Oxid. Met.* 57 (2002): pp. 409–425.

54. G.R. Holcomb, J.H. Tylczak, and R. Hua, “Materials Performance in USC Steam,” in *25th Annu. Conf. Foss. Energy Mater.* (Portland, OR, United States, 2011).

55. A.C.S. Sabioni, A.M. Huntz, L.C. Borges, and F. Jomard, *Philos. Mag.* 87 (2007): pp. 1921–1937.

56. A.M. Huntz, A. Reckmann, C. Haut, C. Sévérac, M. Herbst, F.C.T. Resende, and A.C.S. Sabioni, *Mater. Sci. Eng. A* 447 (2007): pp. 266–276.

57. J.M. Rakowski, C.P. Stinner, M. Lipschutz, and J.P. Montague, *TMS (The Miner. Met. Mater. Soc.)* (2005): pp. 271–286.

58. S.J. Bonner, “A Microstructural and Kinetic Study of Molten Aluminium Oxidation in Relation to Dross Formation,” *The University of Queensland*, 2015.

59. K. Onal, M.C. Maris-Sida, G.H. Meier, and F.S. Pettit, *Mater. High Temp.* 20 (2003): pp. 327–337.

60. T. Cheng, and P.F. Tortorelli, *J. Am. Ceram. Soc.* 96 (2013): pp. 2330–2337.
61. E. Alonso, C. Hutter, M. Romero, A. Steinfeld, and J. Gonzalez-Aguilar, *Energy & Fuels* 27 (2013): pp. 4884–4890.
62. M.A. Langell, C.W. Hutchings, G. a Carson, and M.H. Nassir, 14 (1996): pp. 1656–1661.
63. A. Fry, S. Osgerby, and M. Wright, *NPL Rep. MATC 90* (2002): pp. 1–39.
64. D.J. Young, *Mater. Sci. Forum* 595–598 (2008): pp. 1189–1197.
65. H. Hooshyar, T. Jonsson, J. Hall, J.E. Svensson, L.G. Johansson, and J. Liske, *Oxid. Met.* 85 (2016): pp. 321–342.
66. C. Issartel, H. Buscail, Y. Wang, R. Rolland, M. Vilasi, and L. Aranda, *Oxid. Met.* 76 (2011): pp. 127–147.
67. H. Buscail, S. El Messki, F. Riffard, S. Perrier, R. Cueff, E. Caudron, and C. Issartel, *Mater. Chem. Phys.* 111 (2008): pp. 491–496.
68. J. Ehlers, D.J. Young, E.J. Smaardijk, A.K. Tyagi, H.J. Penkalla, L. Singheiser, and W.J. Quadackers, *Corros. Sci.* 48 (2006): pp. 3428–3454.
69. A. Kaderi, A.Z.M. Zainal, H. Ani, R. Othman, Observation on void formed in oxide scale of Fe-Cr-Ni alloy at 1073 K in dry and humid environments, *IIUM Eng. J.* 12 (2011) 69–78.
70. S.E. Sadique, A.H. Mollah, M.S. Islam, M.M. Ali, M.H.H. Megat, and S. Basri, *Oxid. Met.* 54 (2000): pp. 385–400.
71. A. Galerie, S. Henry, Y. Wouters, M. Mermoux, J.P. Petit, and L. Antoni, *Mater. High Temp.* 22 (2005): pp. 105–112.
72. E. Essuman, G.H. Meier, J. Zurek, M. Hänsel, L. Singheiser, and W.J. Quadackers, *Scr. Mater.* 57 (2007): pp. 845–848.
73. C.T. Fujii, and R.A. Meussner, *J. Electrochem. Soc.* 111 (1964): pp. 1215–1220.
74. H. Hooshyar, “High Temperature Corrosion of Stainless Steels in Low Oxygen Activity Environments The Effect of H₂ and H₂O,” Chalmers University of

Technology, 2016.

75. X. Cheng, Z. Jiang, B.J. Monaghan, D. Wei, R.J. Longbottom, J. Zhao, J. Peng, M. Luo, L. Ma, S. Luo, and L. Jiang, *Corros. Sci.* 108 (2016): pp. 11–22.

76. X. Peng, J. Yan, Y. Zhou, and F. Wang, *Acta Mater.* 53 (2005): pp. 5079–5088.

77. H.E. Evans, D.A. Hilton, and R.A. Holm, *Oxid. Met.* 11 (1977): pp. 1–21.

78. A. Ramírez, P. Hillebrand, D. Stellmach, M.M. May, P. Bogdanoff, and S. Fiechter, *J. Phys. Chem. C* 118 (2014): pp. 14073–14081.

79. R. Bauer, M. Baccalaro, L.P.H. Jeurgens, M. Pohl, and E.J. Mittemeijer, *Oxid. Met.* 69 (2008): pp. 265–285.

80. D.J. Young, and B.A. Pint, *Oxid. Met.* 66 (2006): pp. 137–153.

81. R. Wang, Z. Dong, J. Luo, W. Chen, W. Zheng, and D. Guzonas, *Corros. Sci.* 82 (2014): pp. 339–346.

82. Y. Wouters, G. Bamba, A. Galerie, M. Mermoux, and J.-P. Petit, *Mater. Sci. Forum* 461 (2004): pp. 839–848.

83. A. Paúl, S. Elmrabet, L.C. Alves, M.F. Da Silva, J.C. Soares, and J.A. Odriozola, *Nucl. Instruments Methods Phys. Res. Sect. B Beam Interact. with Mater. Atoms* 181 (2001): pp. 394–398.

84. K. Schulmeister, and W. Mader, *J. Non. Cryst. Solids* 320 (2003): pp. 143–150.

85. S.N. Basu, and G.J. Yurek, *Oxid. Met.* 36 (1991): pp. 281–315.

86. T. Jonsson, S. Canovic, F. Liu, H. Asteman, J.E. Svensson, L.G. Johansson, and M. Halvarsson, *Mater. High Temp.* 22 (2005): pp. 231–243.

87. D.R. Gaskell, *An Introduction to Transport Phenomena in Materials Engineering* (New York, 1992).

88. E.J. Opila, D.L. Myers, N.S. Jacobson, I.M.B. Nielsen, D.F. Johnson, J.K. Olminky, and M.D. Allendor, *J. Phys. Chem. A* 111 (2007): pp. 1971–1980.

7. Silicon Effects on the Wet Oxidation of Type 310S Stainless Steel

Shooka Mahboubi¹, Hatem S. Zurob², Gianluigi A. Botton³, and Joseph R. Kish^{4,*}

¹Shooka Mahboubi, mahbos@mcmaster.ca

²Hatem S. Zurob: zurobh@mcmaster.ca

³Gianluigi A. Botton: gbotton@mcmaster.ca,

^{4,*}Joseph R. Kish: corresponding author, kishjr@mcmaster.ca (905)525-9140,
ext. 21492

*Department of Materials Science and Engineering, McMaster University, 1280
Main Street West, Hamilton, ON, CA*

Submitted to Corrosion Science on February 13th, 2018

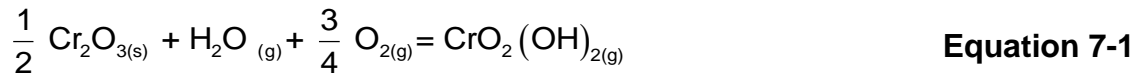
7.1. Abstract

The wet oxidation kinetics of high-Si (5.9 wt.%) Type 310 stainless steel exposed in a flowing air-10% H₂O mixture at 800°C was investigated. The parabolic kinetics and the associated benefits of the high Si content alloyed is linked to the structure and composition of the oxide scale formed relative to that formed on conventional low-Si (0.6 wt.%) Type 310 stainless steel. Accelerated formation of Fe-rich oxides is not observed due to Cr-rich silicide intermetallic phases present in the starting as-cast microstructure serving as reservoirs to sufficiently supply Cr from the alloy to replace oxidized Cr lost to volatilization.

Keywords: Oxidation, Stainless Steel, STEM

7.2. Introduction

High Cr-containing austenitic stainless steels have been widely used in high-temperature water vapour (H₂O)-containing environments such as those in boiler pipes, coal gasification industries, and gas turbines.¹⁻³ Relatively high Cr content of these alloys promotes the formation of an adherent, compact, external chromia (Cr₂O₃) scale that better protects the alloy against oxidation than the formation of Fe-rich oxide scales.⁴⁻⁶ It is well known that in the presence of O₂ and H₂O (wet oxidation), Cr₂O₃ scale volatilizes and forms Cr-O-H gas species, among which Cr-oxy-hydroxides (CrO₂(OH)₂) are more stable at temperatures below ~1000°C (**Equation 7-1**).⁷⁻¹⁰



If the rate of Cr loss from the Cr₂O₃ scale during volatilization becomes greater than the rate of Cr supply from the alloy to the scale, the Cr₂O₃ scale becomes more defective allowing easier transport of Fe through to form a new external scale.¹¹ Continuous transport of Fe into the Cr₂O₃ scale can accelerate the oxidation rate resulting in linear (non-protective) kinetics associated with the growth of a porous Fe₂O₃ external scale that is prone to thickening.¹¹⁻¹⁴ The rate controlling step for parabolic or “breakaway” kinetics (contribution of both parabolic and linear regimes) is argued to be the surface chemical reactions such as adsorption and decomposition of H₂O gas species on the Fe-rich oxide surface.¹⁵⁻¹⁷ Thickening of the oxide scale during Fe-rich oxide formation reduces

the heat transfer rate from alloy to its adjacent environment, which can then result in catastrophic failure of operating components.^{18,19} From a high-temperature oxidation resistance perspective, initiation of the linear kinetic has important engineering implications as any means that can delay this point can help extend component life.^{12,20,21}

The majority of commercial stainless steels capable of forming a protective Cr_2O_3 scale contain some amount of Si. It has been argued that Si is beneficial from a general oxidation resistance viewpoint as it serves to promote the formation of a silica (SiO_2) barrier layer below the Cr_2O_3 scale, and, thus, reduces the parabolic rate constant.²²⁻²⁹ Due to relatively small diffusion rate of Si in austenitic alloys, SiO_2 often forms at the alloy/oxide interface by inward diffusion of O^{2-} .³⁰⁻³² Studies have shown that the formation of SiO_2 can occur as precipitates, as opposed to a continuous SiO_2 layer, at the Cr_2O_3 scale/metal interface.³³⁻³⁵ The formation of a continuous SiO_2 layer depends on the alloyed Si content and exposure conditions.³⁶ It has been argued that the morphology of the SiO_2 inner layer plays a key role in providing enhanced protection with a continuous SiO_2 layer serving to reduce the outward diffusion of metal cations, to a greater extent than a discontinuous SiO_2 layer (present as precipitates at the scale/metal interface).^{37,38} The formation of a continuous SiO_2 layer, rather than a discontinuous one, has been implicated more often than not as being detrimental to the general oxidation resistance by serving to promote mechanical spallation of the oxide scale.^{22,23,39-41} The SiO_2 layer/precipitates is/are expected to be in compression as the ratio of the

volumes of SiO₂ layer relative to the underlying austenitic matrix (Pilling-Bedworth ratio) is greater than one, which implies a tendency for spallation during oxidation.⁴² Moreover, SiO₂ has a much lower coefficient of thermal expansion (CTE) than Cr₂O₃, again implying a tendency for spallation during any temperature cycling.⁴¹

Some work has been done to better understand the effect of alloyed Si content on the high-temperature oxidation of Cr₂O₃ scale-forming alloys by intentionally adding higher amounts of Si to these alloys. Li et al.⁴¹ studied the effect of addition of up to 2.7 wt.% Si to a set of cast Cr₂O₃ scale-forming alloys exposed in dry air at 1000°C. Their results show that Si additions weakens the metallic bond strength in the alloys, which serves to increase the atomic volume of the Ni-based alloys by 2% and, in turn, significantly increases the effective diffusion coefficient of Cr. They discussed that, even with the presence of Fe in the alloys, the effective diffusion coefficient of Cr in the alloy is still higher with higher amounts of Si since Cr has a smaller atomic radius than Fe. It is also argued that the SiO₂ layer formed can hinder Fe diffusion.^{33,41} The larger atomic size of Fe than Cr means it is easier to transport Cr through a SiO₂ layer than Fe.

Not a lot of studies have thus far been done to understand the effect of Si additions on the high-temperature wet oxidation behaviour of Cr₂O₃-forming alloys, and its particular effect on breakaway kinetics. It is plausible that, since Fe diffusion rate through a SiO₂ layer is relatively slow, the onset of linear kinetics that is dictated by the balance between the parabolic and volatilization terms might be delayed with higher amounts of Si. Therefore, it is worthy to examine whether the

increase in the alloy Cr supply rate and decrease in Fe diffusion rate through the SiO_2 layer prevents or postpones the onset of linear kinetics resulting from the volatilization of the Cr_2O_3 scale by compensating for the Cr loss of the scale.

The objective of this study is to investigate the effect alloyed Si has on the wet oxidation of Type 310 stainless steel, a high temperature austenitic stainless steel that is capable of forming a protective Cr_2O_3 scale. In particular we are interested in better understanding how the structure and composition of the scale formed evolves with time during wet oxidation and how this evolution, in turn, affects the onset of the accelerated linear kinetic. A gravimetric study exposing a modified Type 310 stainless steel with intentional Si alloying (6 wt.%) in an air-10 vol.% H_2O mixture at 800°C was used for this purpose. The oxide scale formed as a function of exposure time was characterized using scanning electron microscopy (SEM) and transmission electron microscopy (TEM) techniques. Site specific cross-sectional TEM foils were prepared using the focused ion beam (FIB) milling technique, which allowed us to isolate localized regions of scale breakdown for a subsequent high resolution structure and chemistry analyses. The results are compared with those acquired for conventional Type 310S stainless steel exposure under identical conditions, the results of which have been reported elsewhere.¹⁵ As our previous results show, Type 310 stainless steel is prone to linear oxidation in this environment.¹⁵

7.3. Experimental Procedures

7.3.1. Materials

Sections of a developmental centrifugally-casted Si-containing (6 wt.%) Type 310 stainless steel (Type 310-6Si) pipe were received in the as-cast condition from Kubota Ltd. (Orillia, ON). Thermocalc simulations were used which predict a fully austenitic structure with 6 wt.% Si for Type 310 stainless steel. The pipe was cast with an external diameter of 20.5 cm and the wall thickness of 1.5 cm. **Table 7-1** lists the chemical composition (wt.%) of the Type 310-6Si stainless steel pipe, which is reproduced from the associated mill test certificate. Also included in **Table 7-1** is the chemical composition (reproduced from the mill certificate) of the commercial Type 310S stainless steel plate product that was used as the comparative basis. The plate sample was provided by Columbus Stainless Ltd. in the cold-rolled and mill-annealed condition.

Table 7-1 Chemical composition (wt.%) of the stainless steels

| Alloy | Fe | Cr | Ni | Si | Mn | C | N | P | Cu | S |
|---------------------|------|------|------|-----|-----|------|------|------|------|-------|
| Type 310-6Si | Bal. | 24.7 | 19.2 | 5.9 | 0.7 | 0.01 | 0.05 | 0.01 | 0.01 | 0.005 |
| Type 310S | Bal. | 24.7 | 20.2 | 0.6 | 1.9 | 0.05 | 0.03 | 0.02 | 0.06 | 0.001 |

Rectangular test coupons (10 mm × 10 mm × 1.5 mm) were prepared from the as-cast Type 310-6Si stainless steel pipe sections, with the long axis of the coupon being parallel to the longitudinal axis of the pipe. Care was taken to extract the coupons from the mid-wall location to ensure a consistent microstructure among the test coupons. The starting microstructure of the Type 310-6Si material was characterized using both light optical microscopy (LV100-Nikon optical

microscope) and scanning electron microscopy (SEM), equipped with X-ray energy dispersive spectroscopy (JEOL JSM-7000F scanning electron microscope). A rectangular test coupon was cold mounted in cross-section (with the normal of plane examined being parallel to the longitudinal axis of the pipe) using epoxy resin. The working surface was prepared using standard metallographic procedures to create a mirror finish.

7.3.2. Wet Oxidation Exposure

All surfaces of the rectangular test coupons were ground to 400 grit SiC paper, cleaned in ethanol, and dried using a warm air stream. Coupon weights were then measured using a Mettler Toledo digital balance with the precision of 0.0001 g prior to insertion into the furnace. Wet oxidation was conducted in a flowing air-10 vol.-% H₂O mixture ($p_{O_2} = 0.1890$ atm and $p_{H_2O} = 0.099$ atm) heated to 800°C using a horizontal tube furnace apparatus. Specific details of the wet oxidation testing apparatus employed are published elsewhere.⁴³ In particular, six coupons of Type 310-6Si stainless steel per exposure time were positioned in the center of a quartz tube in a horizontal furnace kept at $800 \pm 5^\circ\text{C}$. A mixture of air-10% H₂O passed the surface of coupons with the flow velocity of 4 ± 0.2 cm/s. Five exposure times were chosen to study: 24 h, 50 h, 100 h, 250 h and 500 h. After each of the exposure time, the set of six coupons were cooled to room temperature inside the furnace, with an estimated cooling rate of about 0.05°C/s to help minimize thermal stress accumulation within the oxide scale formed. Coupons were re-weighed once removed from the furnace using the same digital balance (weight gain

measurement). Three of the exposed coupons were set aside for de-scaling and subsequent re-weighing (weight loss measurement). De-scaling involved immersing the sub-set of coupons in a solution containing citric acid (2.0%), dibasic ammonium citrate (5.0%) and disodium EDTA (0.5%) at 90°C for 1 h and then immersing in a solution containing potassium permanganate (10.0%) and caustic soda (4.0%) at 90°C for 1 h.^{44,45} The latter step was repeated until a constant weight was measured and remnants of oxide scale were no longer visible on the surface. An unexposed coupon was included in each de-scaling step as a control to ensure minimal metal was lost during the process.

Oxide Scale Characterization

The set of oxide scales that formed on Type 310-6Si stainless steel after the various exposure times was first imaged in plan-view using secondary electrons using a JEOL JAMP-9500F FE-Auger microscope operating as an SEM with an accelerating voltage of 10 kV and a working distance of ~20 mm. The set of oxide scales were then analyzed in cross-section using a JEOL JSM-7000F scanning electron microscope with the accelerating voltage of 10 kV and the working distance of 10 mm. Images were acquired in both secondary electron and backscattered electron modes. One coupon from each exposure cold mounted in cross-section (with the normal of plane examined being parallel to the longitudinal axis of the pipe) using epoxy resin was used for this purpose. The working surface was prepared using standard metallographic procedures to create a mirror finish.

EDS-generated elemental maps of the scale/metal interface were acquired to examine the elemental distribution in the oxide scale as well as in the matrix.

An X-ray diffraction (XRD) examination of the oxide scales formed at the various exposure times was also conducted to provide complementary information regarding the composition of the oxide scales formed. The XRD examination was performed with a Bruker D8 DISCOVER diffractometer, equipped with DAVINCI.DESIGN, and a Co-Sealed Tube Source ($\lambda = 1.79026$ angstrom), using an energy of 35 kV and current of 45 mA. An XRD examination of the starting material was also performed using this instrument. A pattern search and match was then executed in DIFFRAC.EVA (Bruker AXS) using the integrated international centre for diffraction data (ICDD) PDF-4+ 2016 powder database. The search was constrained to database results containing the elements of O, Fe, Cr, Ni, Mn, C and Si.

A Zeiss NVision 40 FIB dual platform instrument was used to prepare and extract a thin cross-sectional foil of the scale/metal interface from the one of the 500 h coupons for subsequent examination using TEM techniques. Using the SEM mode, a site of interest with obvious oxide scale breakdown was selected for foil preparation and extraction. The site was deposited first with a carbon layer (~ 1 μm thick) then a tungsten layer (~ 2 μm thick) to protect the site from the adjacent ion milling action. Milling was done using a Ga^+ beam with a voltage of 30 kV and a working distance of 5 mm.

The TEM examination was conducted in a JEOL 2010F microscope using an accelerating voltage of 200 kV. EDS-generated elemental maps of the oxide scale/metal interface were obtained in bright field (BF) scanning TEM (STEM) mode (BF-STEM mode). A complementary set of electron energy loss spectroscopy (EELS)-generated maps and spectra were acquired using the high-angle annular dark field (HAADF)-STEM mode for a higher spatial resolution characterization of the oxide scale chemistry and structure. A dispersion of 0.2 eV/pixel was used to acquire the O, Fe, Mn, and Ni edges, whereas a dispersion of 0.1 eV/pixel was used to acquire the Si-L_{2,3} and L₁ edges. The intensity ratios of the peaks, and possible peak shifts due to the changes in the chemical compositions of the oxides, were compared with the values published in the literature for expected oxide phases.

7.4. Results

7.4.1. Starting Material Characterization

Figure 7-1 shows a light microscopy image of the starting microstructure of the as-cast Type 310-6Si stainless steel. The as-cast microstructure consists of a dendritic network (dark phase) embedded in the presumably austenitic matrix (bright phase). A corresponding light microscopy image of the starting microstructure of the Type 310S stainless steel plate material used as the comparative basis is also shown. The wrought microstructure consists of an equiaxed grain structure with a considerable amount of twinning present. The average grain size (diameter) is $34 \pm 4 \mu\text{m}$, as measured using the ASTM E112-96 linear intercept procedure⁴⁶ coupled with the ImageJ software. Chemical etching of the Type 310-6Si stainless steel was achieved using a HCl-HNO₃ (aq) mixture with a volume ratio of 6:1 for 20 seconds, whereas the Type 310S stainless steel was etched using a HCl-CH₃COOH-HNO₃ (aq) mixture with a volume ratio of 3:2:1 and 3 drops of glycerol for 45 seconds.

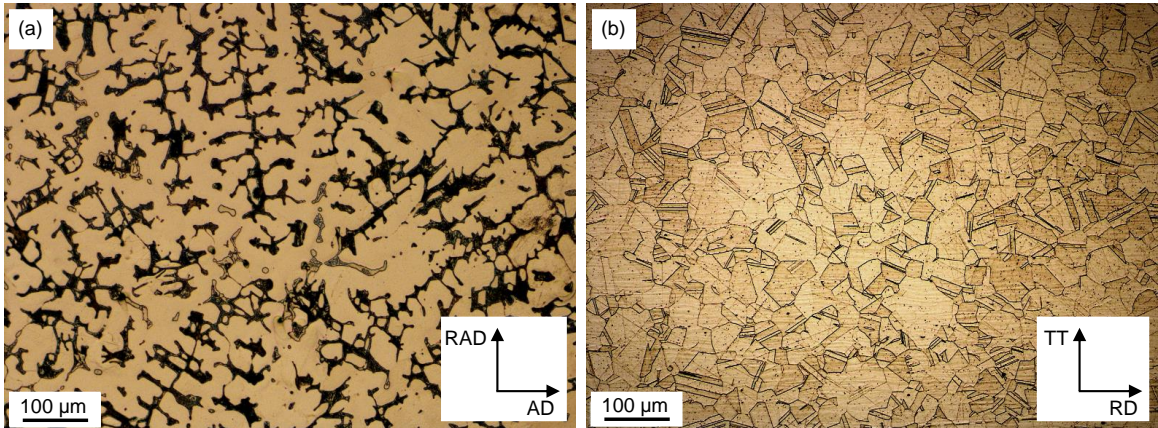


Figure 7-1. Images of the etched (a) as-cast Type 310-6Si stainless steel in the axial direction (AD)-radial direction (RAD) plane and (b) cold rolled and mill annealed Type 310S stainless steel in the rolling direction (RD)-through thickness (TT) plane.

Figure 7-2 shows back-scattered electron images and an associated set of EDS maps of the starting microstructure of the as-cast Type 310-6Si stainless steel. The lower magnification image (**Figure 7-2[a]**) shows the typical characteristic of dendrites (long network of dendrite branches from which smaller branches grow) embedded in the austenite matrix. The higher magnification image (**Figure 7-2[b]**) shows that the dendritic network phase is not monolithic as it consists of interdendritic phase that co-exists with the matrix phase. The set of EDS maps from the high magnification image show that the dendritic network is enriched in Cr and Si relative to the matrix and depleted in Fe and Ni relative to the matrix phase.

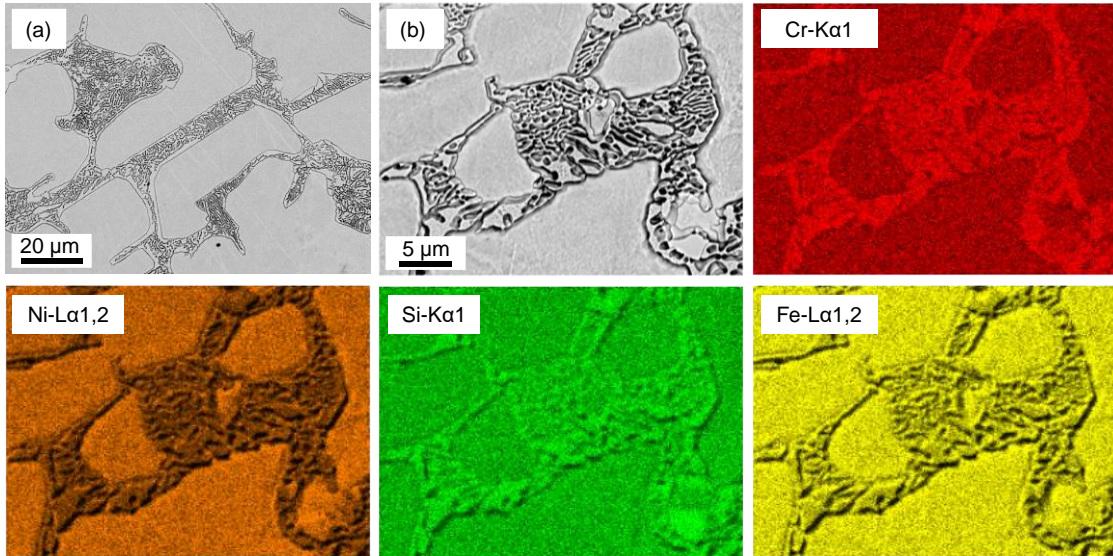


Figure 7-2. (a) Low and (b) high magnification back-scattered electron images and an associated set of EDS maps of the starting microstructure of the as-cast Type 310-6Si stainless steel.

Figure 7-3 shows the result of the XRD examination of the starting as-cast Type 310-6Si stainless steel. Two sets of peaks are identified: one set corresponding to the austenite matrix and a second set corresponding to the $\text{Cr}_{0.65}\text{Ni}_{0.25}\text{Si}_{0.1}$ intermetallic phase. The positive identification of the $\text{Cr}_{0.65}\text{Ni}_{0.25}\text{Si}_{0.1}$ intermetallic phase is consistent with what the EDS maps presented in **Figure 7-2** imply: the formation of a Cr-rich-Si intermetallic phase.

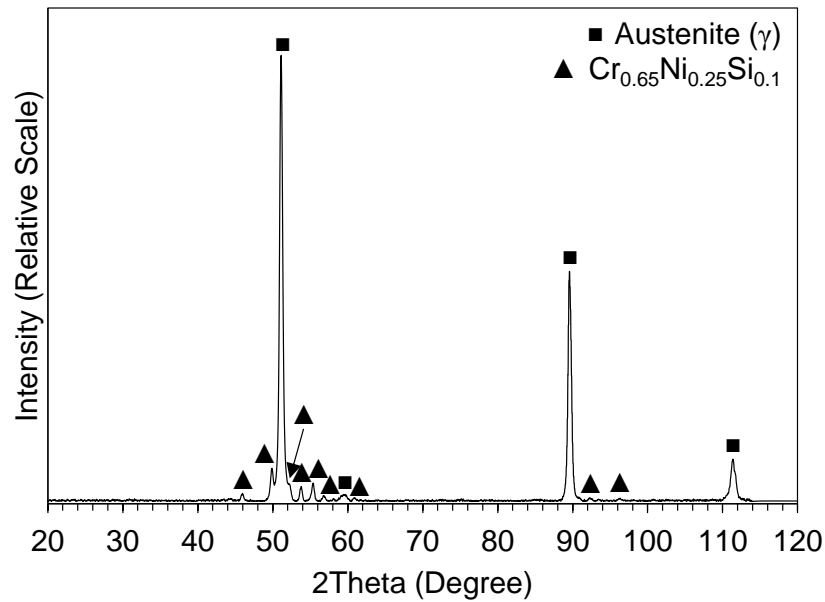


Figure 7-3. XRD pattern of Type 310-6Si stainless steel in the as-cast condition.

7.4.2. Wet Oxidation Kinetics

Figure 7-4(a) shows the weight gain (mg/dm^2) of Type 310-6Si stainless steel exposed in flowing air-10% H_2O mixture at 800°C up to 500 h. The weight gain (mg/dm^2) for Type 310S stainless steel from our previous study is also plotted here for comparative purposes.¹⁵ The weight gain is the average of the set of coupons exposed and the error bars represent the associated 95% confidence interval. The trend lines superimposed onto the plot correspond to kinetic models derived using the derived rate constants as described in more detail later. The weight gain of Type 310-6Si stainless steel first increases at a decreasing rate up to ~ 250 h, then decreases at a constant rate from ~ 250 h to 500 h. Oxide scale spallation, as will be shown later in the SEM images (**Figure 7-5**), could be responsible for the negative weight gain trend of Type 310-6Si stainless steel at longer times. In stark

contrast, the weight gain of Type 310S stainless steel increases at a decreasing rate up to ~250 h and then increases at a constant rate from ~250 h to 500 h.

Since some of the scales formed on Type 310-6Si stainless steel coupons spalled off, weight loss measurements need to be considered as more accurate indication of the actual metal oxidation rate.⁴⁴ **Figure 7-4(b)** shows the weight loss data (mg/dm^2) of Type 310-6Si stainless steel and Type 310S stainless steel for the set of exposure times considered. The weight gain is the average of the set of coupons exposed and the error bars represent the associated 95% confidence interval. Again, the trend lines correspond to kinetic models derived using the rate constants. Weight loss for Type 310-6Si stainless steel first increases at a decreasing rate up to ~250 h, then it increases at a constant rate between ~250 h to 500 h. The weight loss of Type 310S stainless steel also first increases at a decreasing rate up to ~250 h, then it also increases at a constant rate from ~250 h to 500 h. Type 310-6Si stainless steel consistently exhibits the lower weight loss of the two stainless steels, clearly indicating a beneficial effect of alloyed Si on the wet oxidation kinetics.

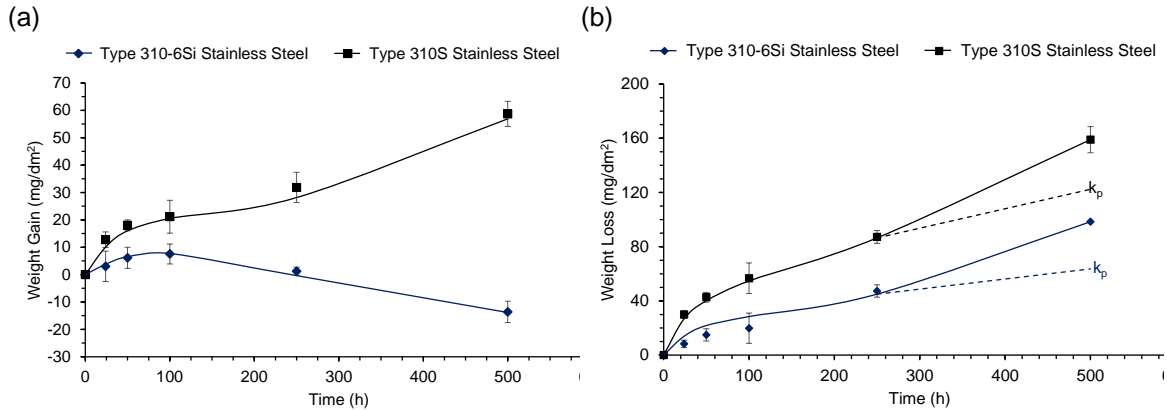


Figure 7-4. Average (a) weight gain and (b) weight loss of coupons exposed for up to 500 h in flowing 0.1 MPa air-10% H₂O at 800°C. The error bars represent 95% confidence interval for replicate set of coupons exposed.

7.4.3. Oxide Scale Characterization

Figure 7-5 shows a set of plan-view secondary electron images of the oxidized surfaces of Type 310-6Si (**Figure 7-5[a]**) and Type 310S (**Figure 7-5[c]**) stainless steels after exposure in the flowing air-10% H₂O mixture at 800°C for the various times considered. A set of high-magnification plan-view secondary electron images of the oxidized surfaces of Type 310-6Si stainless steel from the superimposed boxes in **Figure 7-5[a]** is shown in **Figure 7-5[b]**. The scale formed on Type 310-6Si stainless steel after 24 h exposure is relatively thin as the grinding lines from surface preparation prior to exposure are still visible. After 50 h exposure, the oxide scale consists of relatively larger oxide grains, which are closely packed. After 100 h exposure, the oxide scale surface is rough. A negligible number of regions of spalled oxides are also seen. After 250 h exposure, the oxide scale consists of spalled regions that leave behind a surface with pit-like features visible. After 500 h exposure, the oxide scale consists of spalled regions that leave behind a surface

with pit-like features. In contrast, the oxide scale formed on Type 310S stainless steel after each exposure time considered is compact, without showing any evidence of spallation. We previously showed that the oxide scale formed on Type 310S stainless steel incorporates a large amount of Fe to form Fe-rich $(\text{Fe,Cr})_2\text{O}_3$ after 250 h exposure in the flowing air-10% H_2O mixture at 800°C .¹⁵ Therefore, despite the alloyed Si having a beneficial effect on the metal oxidation rate, the Si appears to have a detrimental effect on the oxide scale stability in terms of the tendency for spallation. Clearly, alloyed Si affects the structure and composition of the oxide scale formed on Type 310 stainless steel.

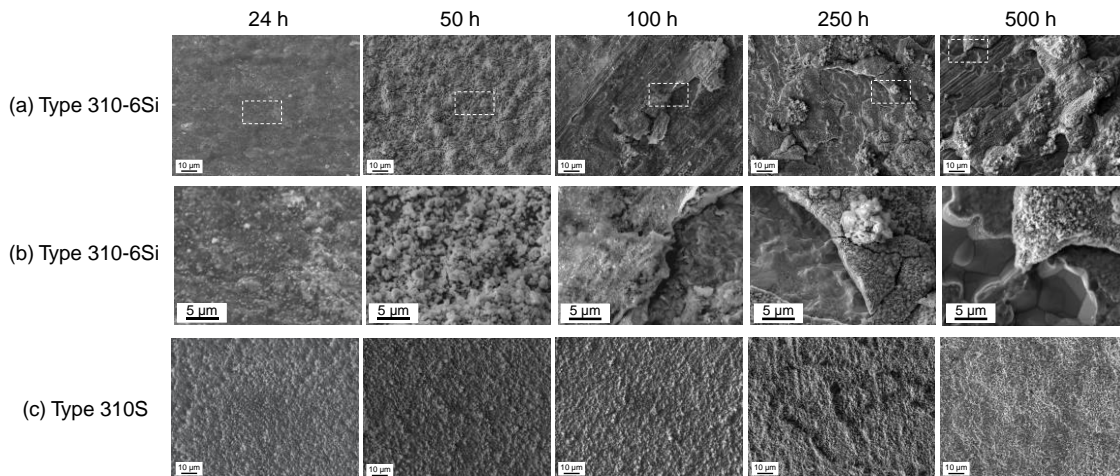


Figure 7-5. Low magnification plan-view secondary electron images of the oxidized surfaces of (a) Type 310-6Si and (c) Type 310S stainless steel after exposure for up to 500 h in flowing 0.1 MPa air-10% H_2O at 800°C . (b) High magnification plan-view secondary electron images of the oxidized surfaces of Type 310-6Si stainless steel obtained from the superimposed boxes in Figure 7-5(a).

Figure 7-6 shows a set of secondary electron images of etched Type 310-6Si stainless steel in cross-section after exposure for up to 500 h in flowing 0.1 MPa air-10% H₂O at 800°C. A set of SEM-EDS elemental maps for O, Cr, Ni, Si, Mn, and Fe corresponding to each of SEM image provided is also shown. The oxide scale formed after each exposure time consists of large amount of Si at the alloy/oxide interface, and Cr and Mn. The oxide scale is not well-attached to the metal, especially after 250 h and 500 h as decohesion at the scale/metal interface is clearly visible in both cases. The oxide scale thickness is relatively uniform up to 100 h exposure. However, after 250 h and 500 h exposure, the oxide scale thickness becomes more variable due to the spallation that occurred.

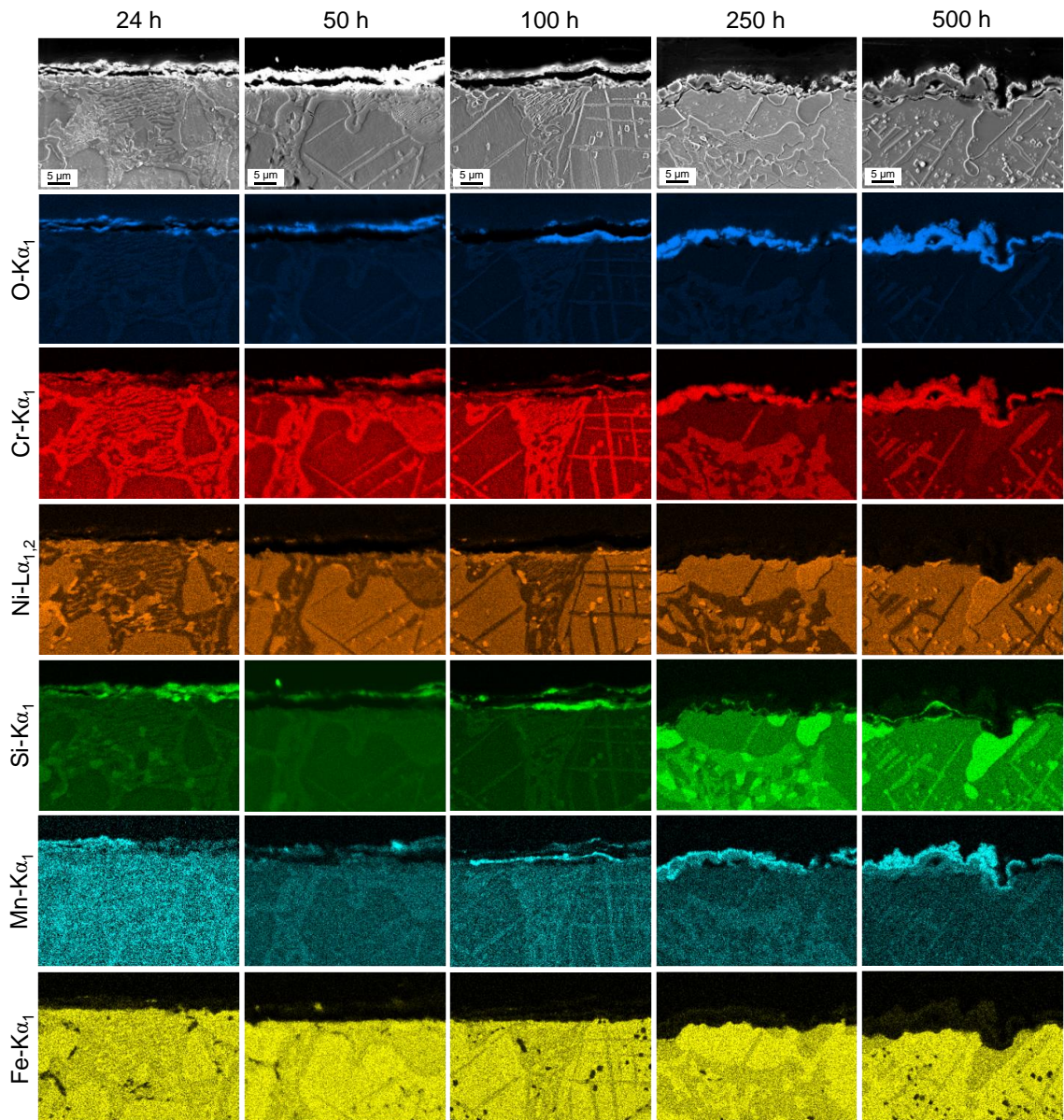


Figure 7-6. Cross-sectional secondary electron images of the oxidized coupons exposed for 24 h, 50 h, 100 h, 250 h, and 500 h in flowing 0.1 MPa air-10% H₂O at 800°C, and the corresponding SEM-EDS elemental maps of O, Cr, Ni, Si, Mn, and Fe.

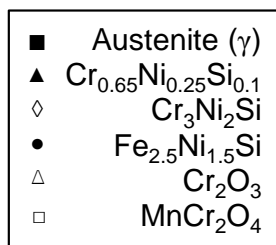
Figure 7-7 shows the set of XRD patterns of Type 310-6Si stainless steel after exposure in the flowing 0.1 MPa air-10% H₂O mixture at 800°C for the various times considered. Peaks associated with oxide phases are not observed after 24 h exposure (**Figure 7-7[a]**). It is likely that the oxide scale is too thin to be captured in the XRD pattern. In contrast, oxide phase peaks for MnCr₂O₄ and Cr₂O₃ are clearly observed in the set of XRD patterns acquired after the remaining exposure times considered (50 h, 100 h, 250 h, and 500 h). The inner Si-rich oxide layer in each case is not captured in the associated XRD pattern suggesting it is amorphous.

In addition to the oxide phase peaks, the XRD patterns shown in **Figure 7-7** contain a set of peaks associated with various Si-containing intermetallic phases within the metal. Referring back to **Figure 7-6**, the near-surface microstructure of Type 310-6Si stainless steel, the dendritic network in particular, is observed to evolve with time during the high temperature exposure. In short, the morphology and composition of the dendritic structure changes with time at temperature (ageing). Specifically, the long network of dendrites change into sharp-edged smaller intermetallics. After 24 h exposure, the dendritic network is enriched in Cr and Si relative to the matrix, which is similar to what is observed in the starting as-cast microstructure (**Figure 7-2**). The associated XRD pattern after 24 h exposure indicates that the dominant intermetallic phase within the dendritic network is Cr_{0.65}Ni_{0.25}Si_{0.1}. However, peaks associated with the Fe_{2.5}Ni_{1.5}Si and Cr₃Ni₂Si intermetallic phases are also detected after 24 h, indicating that the chemistry of

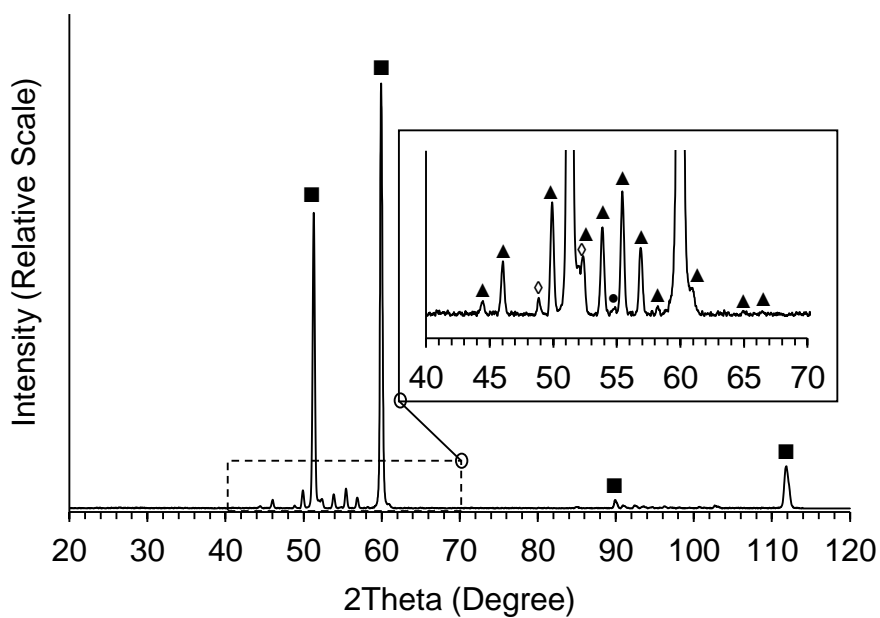
the dendritic phase did indeed change. Simply comparing the Cr content in the various intermetallic phases indicates that the Cr is likely being depleted from the starting dendritic phase during the wet oxidation exposure. The starting dendritic $\text{Cr}_{0.65}\text{Ni}_{0.25}\text{Si}_{0.1}$ intermetallic phase remains intact after 50 h and 100 h exposure along with the $\text{Fe}_{2.5}\text{Ni}_{1.5}\text{Si}$ and $\text{Cr}_3\text{Ni}_2\text{Si}$ intermetallic phases. The SEM cross-sectional images in **Figure 7-6** indicate that intermetallic phase formation within the austenite matrix has occurred after these exposure times. The associated EDS maps indicate that the intermetallic phase is rich in Cr and Si relative to the matrix and depleted in Fe and Ni relative to the matrix. After 250 h and 500 h exposure, the starting dendritic $\text{Cr}_{0.65}\text{Ni}_{0.25}\text{Si}_{0.1}$ intermetallic phase is depleted of Cr and has been replaced in large part by the intermetallic phase formation within the austenite matrix. The dominant peak now is associated with the Cr-free $\text{Fe}_{2.5}\text{Ni}_{1.5}\text{Si}$ intermetallic phase, albeit the small peaks of the Cr-lean $\text{Cr}_3\text{Ni}_2\text{Si}$ intermetallic phase are also still detected by XRD.

The SEM cross-sectional images of the oxide scale/metal interface after 250 h and 500 h exposure in **Figure 7-6** reveals another interesting feature: the pit-like features occur within the silicide intermetallic phases that intersect the surface. We believe that these features are a consequence of the brittle phase fracturing under either a mechanical stress developed by a growing oxide scale during exposure or a thermal stress developed upon cooling. The formation of a layered oxide scale on the presumably fractured silicide intermetallic phase surface suggests that fracture occurred during exposure. However, the unaffected linear weight loss

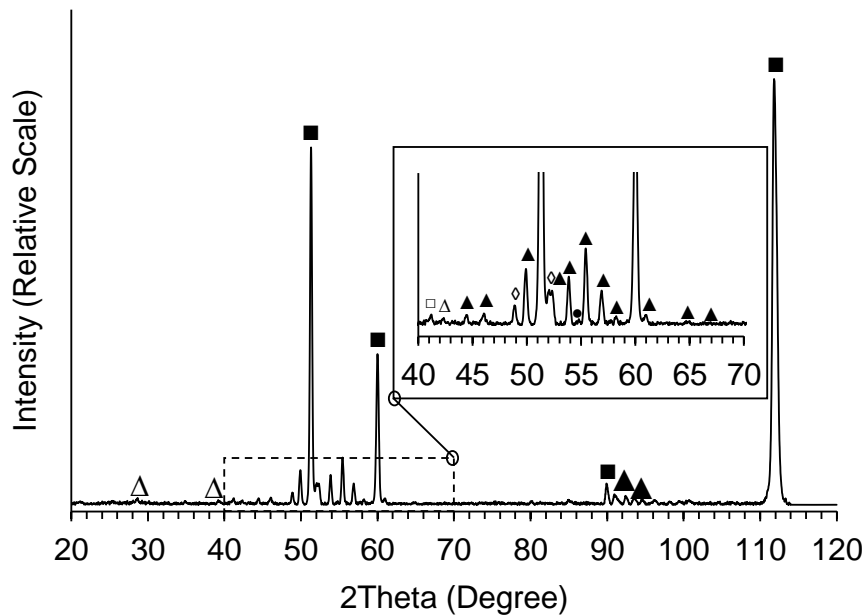
kinetics observed, at the longer times for which oxide scale spallation occurred, suggests otherwise. Either way, scale spallation is undesirable from a practical perspective.



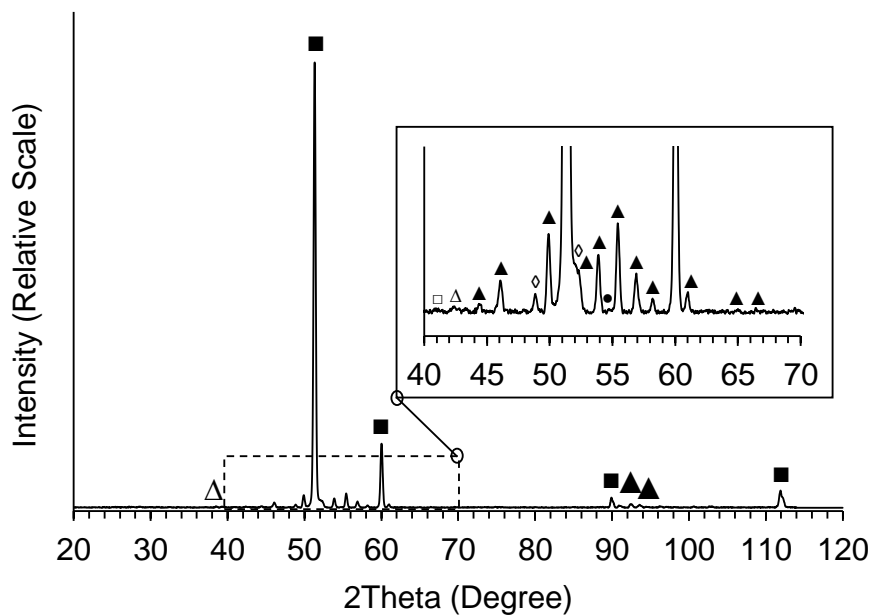
(a) 24 h



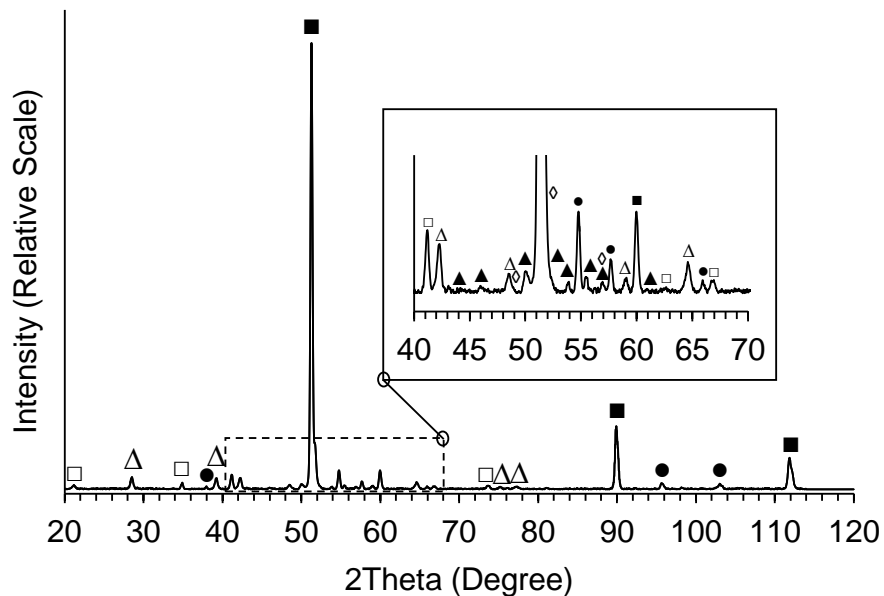
(b) 50 h



(c) 100 h



(d) 250 h



(e) 500 h

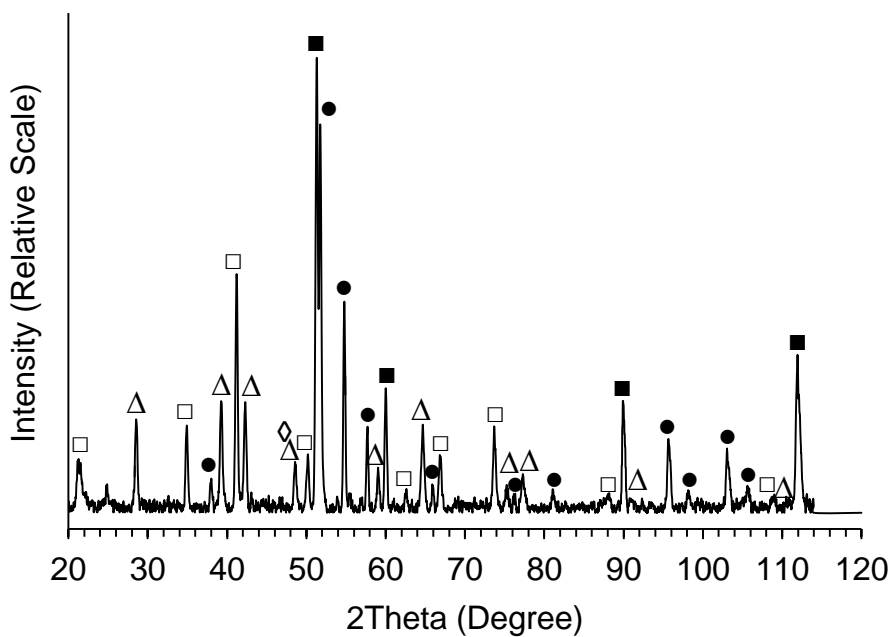


Figure 7-7. XRD patterns of Type 310-6Si stainless steel coupons exposed for 24 h, 50 h, 100 h, 250 h, and 500 h in flowing 0.1 MPa air-10% H₂O at 800°C.

Figure 7-8(a) shows the plan-view secondary electron image of Type 310-6Si stainless steel after 500 h exposure in the flowing air-10% H₂O mixture at 800°C. The superimposed red box represents the site-specific area from which a TEM sample was extracted. The site was chosen so that it included both the intact oxide scale and adjacent spalled region close by. **Figure 7-8(b)** shows the cross-sectional secondary electron image of the FIB-prepared thin foil attached to a TEM Cu grid. The carbon and tungsten deposited layers are labelled on the surface.

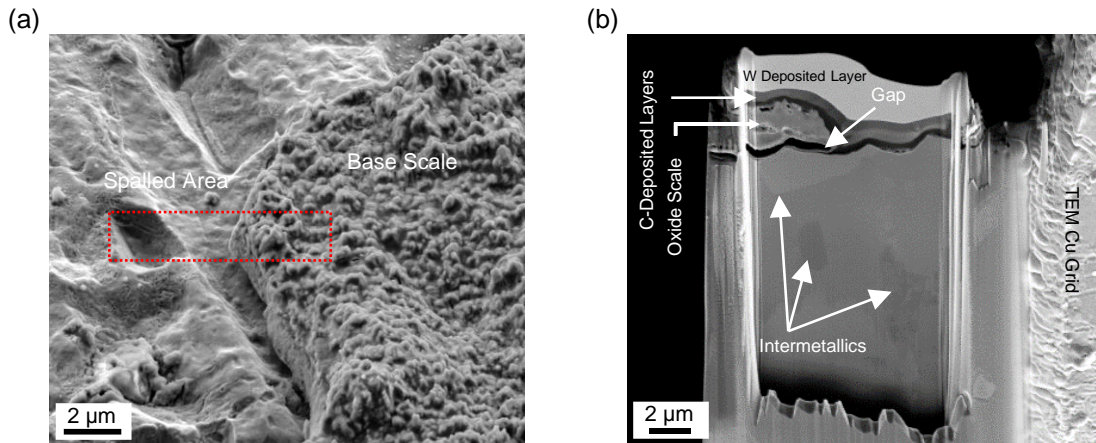


Figure 7-8. (a) Plan-view secondary electron image of the coupon exposed for 500 h in flowing 0.1 MPa air-10% H₂O at 800°C. The red box on the image shows the area from which a TEM thin foil was extracted by FIB. (b) Secondary electron image of the as-prepared TEM sample in cross-section.

Figure 7-9 shows the cross-sectional BF-STEM image of the intact oxide scale region of the thin foil along with the STEM-EDS elemental maps of O, Cr, Ni, Si, Mn, Fe, and C. The elemental distribution in the scale is consistent with the SEM-EDS results described above. The oxide scale consists of three layers: a Si-rich inner layer, a Cr-rich intermediate layer with small equiaxed grains and a Mn-rich outer layer with relatively large columnar grains. A small amount of Fe is also

present in the intermediate and outer layers. The oxide scale is separated from an underlying fractured intermetallic embedded in the matrix by a large gap that is indexed on the STEM image.

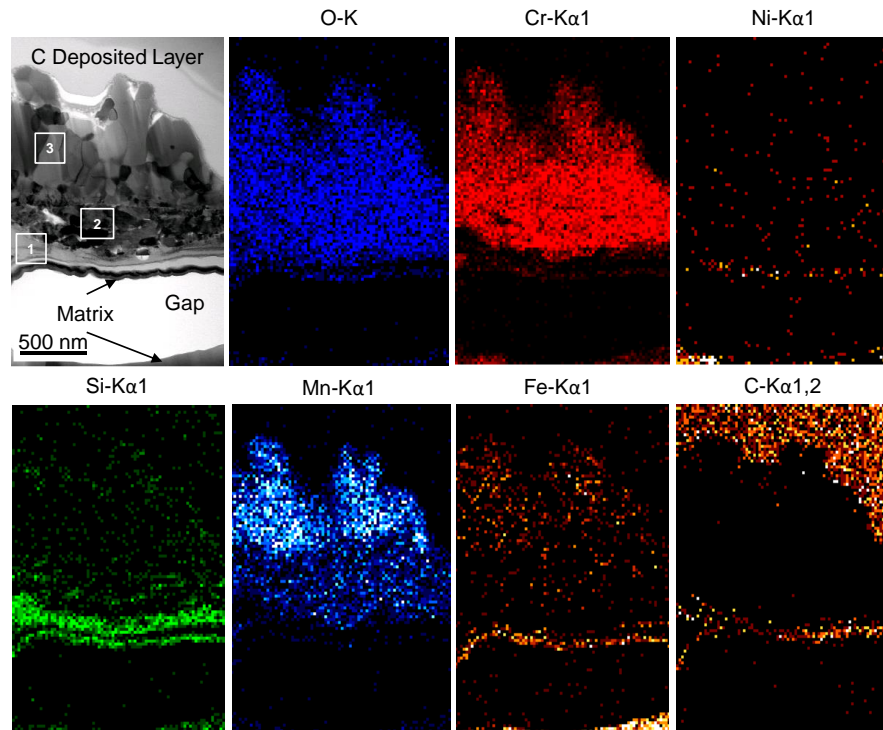


Figure 7-9. BF-STEM image of the scale formed on Type 310-6Si stainless steel after 500 h exposure in flowing 0.1 MPa air-10% H₂O at 800°C and the STEM-EDS elemental maps of O, Cr, Ni, Si, Mn, Fe and C.

Figure 7-10 shows the corresponding EELS spectra obtained from the superimposed areas (numbers) on the BF-STEM image in **Figure 7-9**. The EELS spectra were compared with those published in the literature. **Table 7-2** summarizes the major EELS intensity ratio of peaks used for characterizing the oxides formed in this study and those reported elsewhere. The EELS spectrum of the Si-rich oxide inner layer (Area 1) is consistent with the one of SiO₂.^{25,43} From **Table 7-2**, the EELS spectrum of the fine-grain crystalline Cr-rich oxide

intermediate layer (Area 2) is consistent with the Cr_2O_3 phase, whereas the EELS spectrum of the columnar-grain Mn-rich oxide outer layer (Area 3) is consistent with MnCr_2O_4 . The shoulder peak in the Area 3 EELS spectrum at ~ 548 eV (indicated by arrow) clearly confirms the spinel structure based on reference data in the literature.⁴⁷⁻⁵⁰

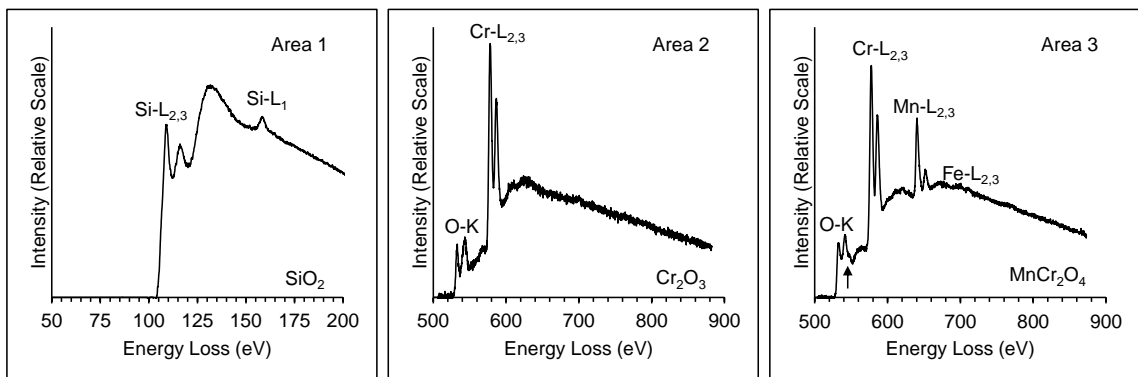


Figure 7-10. The corresponding EELS spectra from the numbers superimposed on the BF-STEM image in **Figure 7-9**.

Table 7-2 Comparison of the integrated L_3/L_2 peaks ratio in this study with those reported in the literature

| Area | Oxide Type | Cr | | Mn | | Fe | |
|------|------------------------------|-------------------|----------------------------|-------------------|----------------------------|-------------------|----------------------------|
| | | I_{L_3}/I_{L_2} | $(I_{L_3}/I_{L_2})_{Lit.}$ | I_{L_3}/I_{L_2} | $(I_{L_3}/I_{L_2})_{Lit.}$ | I_{L_3}/I_{L_2} | $(I_{L_3}/I_{L_2})_{Lit.}$ |
| 2 | Cr_2O_3 | 1.3 ± 0.2 | $\sim 1.4^{49}$ | - | - | - | - |
| 3 | MnCr_2O_4 | 1.2 ± 0.2 | $\sim 1.3^{50}$ | 1.3 ± 0.2 | $\sim 1.4^{50}$ | - | - |
| 5 | $(\text{Cr,Fe})_2\text{O}_3$ | 1.2 ± 0.2 | $\sim 1.4^{49}$ | - | - | 1.1 ± 0.2 | $\sim 1.3^{49}$ |

Figure 7-11 shows the HAADF-STEM image of the spalled oxide surface. The superimposed box on the image shows an area from which the associated EELS elemental maps of O, Cr, Ni, Si, and Fe were obtained and the numbers superimposed show the corresponding EELS spectra locations. The EELS map show the presence of a thin oxide scale on the presumably spalled oxide surface. The EELS maps indicate that the scale consists of two layers: a Si-rich oxide inner

layer and a Cr-rich oxide outer layer. The EELS spectrum acquired from the inner layer (Area 4) is consistent with SiO_2 , whereas the EELS spectrum acquired from the outer layer (Area 5) is consistent with $(\text{Cr,Fe})_2\text{O}_3$. The experimental ratio of the L_3 and L_2 peaks of the transition metal edges is in good agreement with those reported in the literature (**Table 7-2**). A Mn peak is not observed in the spectrum from Area 4, suggesting that there is likely insufficient Mn available in the matrix to promote the formation of a MnCr_2O_4 outer layer.

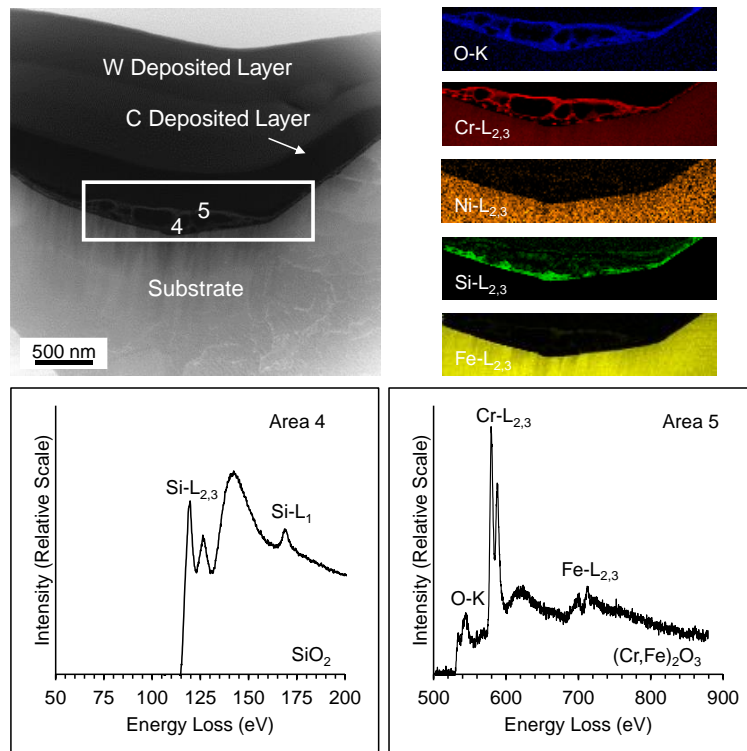


Figure 7-11. Cross-sectional HAADF-STEM image of the scale formed on the oxide surface on Type 310-6Si stainless steel exposed for 500 h in flowing 0.1 MPa air-10% H_2O at 800°C and the O, Cr, Ni, Si, and Fe EELS elemental maps. The corresponding EELS spectra from the areas identified with numbers superimposed on the HAADF-STEM image are also shown.

7.5. Discussion

The exposure times in this study were chosen in such a manner that would allow the determination of the wet oxidation rate constant(s). It is clear that there are two kinetic regimes in the weight loss kinetics exhibited by the low-Si and high-Si Type 310 stainless steel during wet oxidation exposure, as shown in **Figure 7-4(b)**. The expected parabolic kinetic model based on the current state of knowledge works for the first 250 h of exposure, whereas the time dependence of the remaining weight loss data are best fit with a linear kinetic model. Parabolic oxidation kinetic implies that the diffusion through the oxide scale is the rate controlling step in the overall oxidation mechanism, which typically involves the outward diffusion of Cr cations.^{7,51} Linear kinetic implies that interfacial reaction sequence is the rate controlling step in the overall oxidation mechanism. Although linear kinetic has been associated with the Fe-rich scale formation during volatilization of oxidized Cr in the protective oxide scale, the mechanism (rate controlling step) is still being debated. Determined values of the parabolic (k_p) and linear (k_l) rate constant, as well as the associated R-squared values (R_p^2) for parabolic fits are listed in **Table 7-3**. The k_l rate constant is measured using two data points of 250 h and 500 h. The k_p and k_l values reported for both the low-Si and high-Si Type 310 stainless steel agree well with values published in the literature for Cr_2O_3 -forming Fe-Cr-Ni alloys. **Table 7-3** also shows the previously published k_p and k_l values in the temperature range of 800°C to 1100°C for Cr_2O_3 -forming Fe-Cr-Ni alloys.⁵²⁻⁵⁴

Table 7-3 Kinetic rate constants determined in flowing air-10% H₂O mixture at 800°C. Previously published k_p and k_l values are also shown for comparison

| Alloy | k_p (g ² /cm ⁴ /s) | $k_{p(\text{lit.})}$ (g ² /cm ⁴ /s) | R_p^2 | k_l (g/cm ² /s) | $k_{l(\text{lit.})}$ (g/cm ² /s) |
|---------|--|---|---------|--------------------------------|---|
| 310-6Si | $(1.1 \pm 0.5) \times 10^{-13}$ | $\left(\begin{array}{l} 2.2 \times 10^{-12} \text{ ref.51} \\ \sim 1 \times 10^{-13} \text{ ref.50} \end{array} \right)$ | 0.986 | $(5.5 \pm 0.1) \times 10^{-9}$ | $\left(\begin{array}{l} 0.9 \times 10^{-10} \text{ ref.53} \\ 4.9 \times 10^{-9} \text{ ref.52} \end{array} \right)$ |
| 310S | $(9.3 \pm 2.7) \times 10^{-13}$ | | 0.992 | $(5.8 \pm 0.8) \times 10^{-9}$ | |

Contribution of parabolic and linear kinetics is well explained using the overall parabolic kinetic model (**Equation 7-2**). The scale thickness (X) simultaneously increases with time (t) because of outward diffusion of Cr cations and decreases because of oxidized Cr loss during volatilization until the thickness reaches to a critical thickness ($X_{\text{crit.}}$) after which the linear kinetics becomes dominant.⁵⁵

$$\frac{dX}{dt} = \frac{k_p}{X} - k_l$$

Equation 7-2

7.5.1. Parabolic Kinetic Regime

The k_p value of high-Si Type 310-6Si stainless steel is smaller than it is for the low-Si Type 310S stainless steel. The difference can be rationalized by considering the oxide scale composition and structure, as characterized by electron microscopy.

Figure 7-12 schematically compares the oxide scale formed on the high-Si Type 310-6Si stainless steel with that formed on Type 310S stainless steel during the parabolic kinetic regime. Both scales consist of an outer MnCr₂O₄ layer, and Cr₂O₃ intermediate layer and a SiO₂ inner layer. The major difference between the two is the morphology of the SiO₂ inner layer, which is continuous and much thicker in the high-Si Type 310-Si stainless steel. Therefore, the difference in the k_p is likely

related to the high-Si content, and the associated formation of a continuous, rather than a discontinuous (precipitate), SiO_2 inner layer.

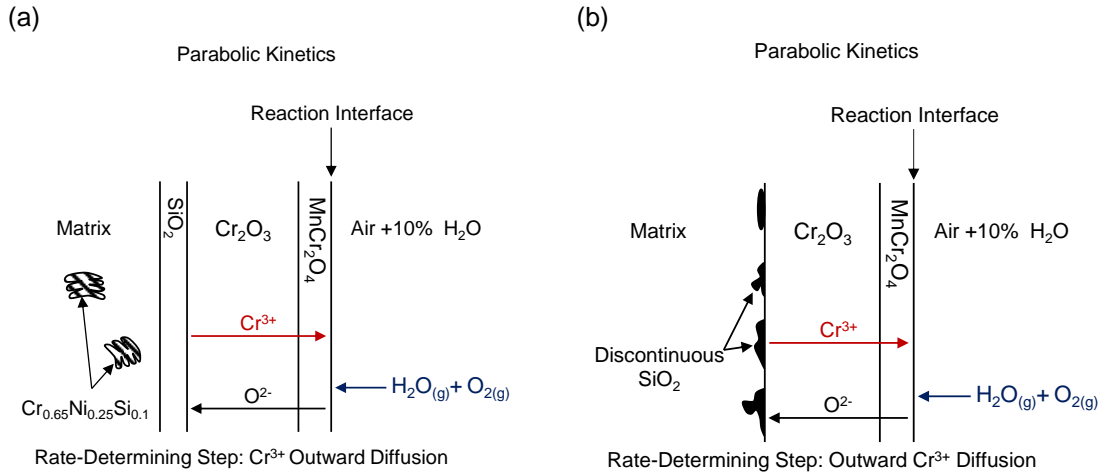


Figure 7-12. Schematic diagrams showing the composition and structure of the oxide scale formed on the (a) high-Si Type 310-Si stainless steel and (b) low-Si Type 310S stainless steel¹⁵ associated with the parabolic kinetic regime.

SiO_2 is thermodynamically far more stable than Cr_2O_3 and tends to form underneath the latter either in the form of a uniform layer or precipitates.⁵⁶⁻⁵⁸ The growth rate of the SiO_2 layer is slower than that for the Cr_2O_3 layer and highly depends on the inward diffusion rate of O anions into the alloy substrate.^{56,59} The inward diffusion of O anions is faster across the alloy grain boundaries.^{29,59} It follows then that the formation of a continuous, rather than a discontinuous, SiO_2 layer depends not only on the alloyed Si content and oxidizing parameters such as temperature and oxygen partial pressure, but also on the morphology of the oxide scale formed on top of the SiO_2 layer, as the outer layers affect the inward diffusion rate of O anions to the alloy/oxide interface.^{60,61} The SiO_2 phase that forms in Fe-Cr-Ni alloys during high temperature oxidation most often has a long range atomic

disorder (is amorphous).⁶² An amorphous SiO₂ layer/precipitate typically has a lower density of defects and lacks grain boundaries.⁴¹ The relatively low defect density and the absence of grain boundaries in the amorphous SiO₂ layer are believed to combine to significantly hinder the outward diffusion rate of scale forming metals (within the alloy) through the SiO₂ layer, and, thus, decrease in the overall alloy high-temperature oxidation rate.^{22,41,63,64}

7.5.2. Linear Kinetic Regime

From **Table 7-3**, the linear rate constants (k_l) presumably of both stainless steels is the same within experimental error. Again the difference can be rationalized by considering the oxide scale composition and structure, as characterized by electron microscopy. **Figure 7-13** schematically compares the oxide scale formed on the high-Si Type 310-6Si stainless steel with that formed on Type 310S stainless steel during the linear kinetic regime. The high-Si Type 310-6Si stainless steel retains a continuous MnCr₂O₄ outer layer residing on a Cr₂O₃ intermediate layer during the linear kinetic regime, whereas the low-Si Type 310S stainless steel forms a relatively thick Fe-rich (Fe,Cr)₂O₃ outer layer residing on a Fe-rich spinel (FeCr₂O₄) inner layer.

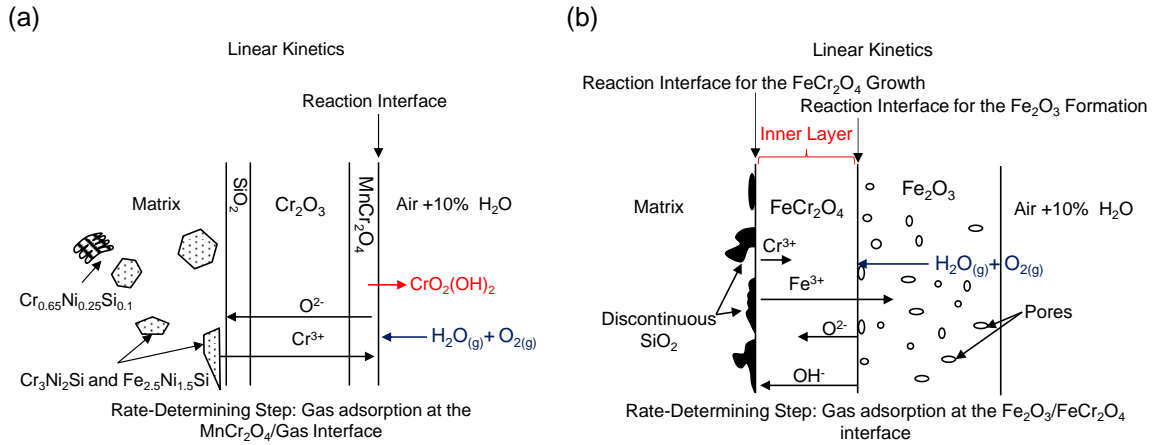


Figure 7-13. Schematic diagrams showing the composition and structure of the oxide scale formed on the (a) high-Si Type 310-6Si stainless steel and (b) low-Si Type 310S stainless steel¹⁵ associated with the linear kinetic regime.

We previously argued that the presence of the continuous MnCr_2O_4 outer layer is beneficial in reducing the overall volatilization rate since the rate of oxidized Cr loss from the MnCr_2O_4 is less than that for the Cr_2O_3 scale formed on the low-Si Type 310S stainless steel.¹⁵ However, we showed that this benefit is lost at higher temperatures as the protective $\text{MnCr}_2\text{O}_4/\text{Cr}_2\text{O}_3$ scale is depleted of Cr and forms a more porous non-protective Fe_2O_3 scale in this wet oxidizing environment.¹⁵ Oxidized Cr is lost to form a protective Cr_2O_3 scale during volatilization (**Equation 7-1**).^{7,25,65} If the Cr supply rate from the alloy to alloy/oxide interface is not sufficient to compensate for the oxidized Cr lost from the scale during volatilization, the Cr_2O_3 scale becomes defective, which serves to promote the outward diffusion of Fe available at the alloy/oxide interface.^{25,65-67} Fe diffusion into the scale and formation of Fe_2O_3 scale increases the overall alloy oxidation rate (linear kinetics).⁴⁵ As implied in **Figure 7-13**, the partially protective MnCr_2O_4 outer layer (with a lower oxidized Cr volatilization rate) is still intact on the high-Si

Type 310S stainless steel after 500 h exposure, which suggests that the outward diffusion of Cr in alloy is still sufficient to replace oxidized Cr in the scale lost to volatilization. **Figure 7-14** shows a plot of the Fe/Cr concentration ratio (at.%) in the Cr_2O_3 intermediate layer formed on the high-Si Type 310-6Si stainless steel after the set of exposure times considered. The Fe/Cr ratio is relatively low and is independent of exposure time (average of 0.04 ± 0.02 with 95% confidence interval). This implies that the rate of Cr supply to the alloy/oxide interface is sufficient to replace the oxidized Cr in the scale that is lost to volatilization.

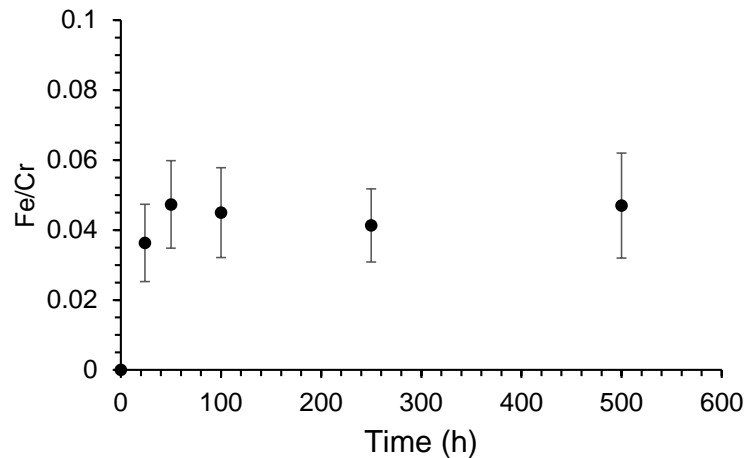


Figure 7-14. Variation in the Fe/Cr concentration ratio (at.%) as a function of exposure time in the flowing air-10% H_2O mixture at 800°C .

We argue here that the starting Cr-rich silicide intermetallic phase ($\text{Cr}_{0.65}\text{Ni}_{0.25}\text{Si}_{0.1}$) that forms the dendritic network in the starting as-cast structure of the high-Si Type 310-6Si stainless steel plays a controlling role in the overall oxidation mechanism. During the course of the high temperature exposure, the starting Cr-rich silicide intermetallic phase ($\text{Cr}_{0.65}\text{Ni}_{0.25}\text{Si}_{0.1}$) transforms into a Cr-

lean silicide intermetallic phase ($\text{Cr}_3\text{Ni}_2\text{Si}$) and a Cr-free silicide intermetallic ($\text{Fe}_{2.5}\text{Ni}_{1.5}\text{Si}$) phase. We believe the Cr that presumably dissolves in the matrix from the transformation of the starting $\text{Cr}_{0.65}\text{Ni}_{0.25}\text{Si}_{0.1}$ replenishes some of the Cr content in the depleted zone that is lost to scale formation. In other words, the starting $\text{Cr}_{0.65}\text{Ni}_{0.25}\text{Si}_{0.1}$ phase is believed to serve as Cr reservoirs that serve to maintain a sufficient Cr supply to the scale to replace the oxidized Cr lost in the scale due to volatilization. Given the rather high fraction of silicide intermetallic phase precipitation, it was rather difficult to measure the depth (and extent) of the Cr depleted zone in the high-Si Type 310-Si stainless steel. Having said that, it is expected to be significantly less than the depth of the Cr depleted zone in the low-Si Type 310S stainless steel, which is measured to be $27.9 \pm 4.6 \mu\text{m}$ after 500 h exposure.¹⁵ If the starting $\text{Cr}_{0.65}\text{Ni}_{0.25}\text{Si}_{0.1}$ phase can serve as an effective Cr reservoir, then, as predicted from parabolic rate equation (**Equation 7-2**), the Cr_2O_3 intermediate layer should reach a steady state thickness. **Figure 7-15** plots the thickness of the Cr_2O_3 intermediate layer formed on the high-Si Type 310-6Si stainless steel the various exposure times considered. The thickness varies with exposure time in the parabolic manner up to 250 h ($k_p = 1.9 \times 10^{-13} \text{ cm}^2/\text{s}$ with a R^2 value of 0.960). The thickness measured after 500 h exposure clearly deviates from value predicted if parabolic kinetics was still maintained, and is the same as the value measured after 250 h with experimental error. This finding is consistent with the belief that the Cr supply from the alloy is sufficient in replacing the oxidized Cr lost in the scale to volatilization.

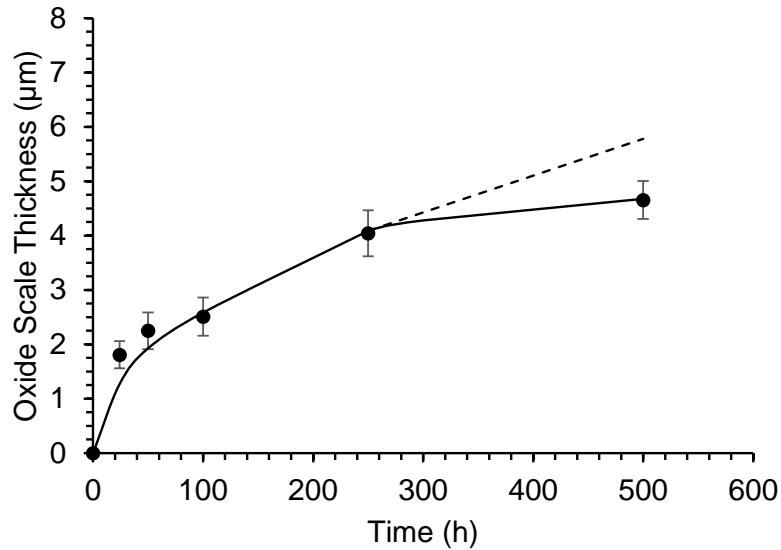


Figure 7-15. Variation in the thickness of the Cr_2O_3 intermediate layer formed on the high-Si Type 310-6Si stainless steel as a function of exposed time in the flowing air-10% H_2O mixture at 800°C .

The finding that both the high-Si and low-Si Type 310 stainless steel exhibit essentially the same k_L value indicates that the same rate-determining step is controlling the volatilization, despite the difference in oxide scale composition and structure. As indicated in **Figure 7-13**, the alloy/oxide layer interface from which oxidized Cr is volatilizing is believed to be rate controlling interface, with the adsorption of oxidizing gas component at that controlling interface being the rate determining step. It is implied that in the presence of H_2O gas molecules in the oxidizing environment, preferential adsorption of H_2O species on the surfaces is favored.⁵⁵ Transport of H_2O species throughout the scales is much easier than O_2 since H_2O is known to form hydroxide ions upon adsorption that have radius of 95 pm, much smaller than that for O_2 (152 pm).^{14,68}

The findings discussed above have several practical implications. Si alloying can have a beneficial effect on the wet oxidation performance of Type 310 stainless steel. Si alloying can reduce the overall metal loss by reducing the metal loss that occurs during the initial parabolic kinetic regime. Silicon alloying can also significantly delay the onset of accelerated Fe-rich oxide formation. This is achieved by the formation of Cr-rich silicide intermetallic phases that can serve as Cr reservoirs, which maintain a sufficient Cr supply to the scale to replace the oxidized Cr lost in the scale to volatilization. However, Si alloying can have a detrimental effect on the wet oxidation performance of Type 310 stainless steel as the oxide scale is prone to spallation upon cooling. Moreover, the formation of brittle silicide intermetallic phases has a detrimental effect on the mechanical properties, high-temperature creep strength and ductility in particular.⁶⁹ A promising strategy to improve the wet oxidation performance may be one in which the morphology of the Cr-rich silicide intermetallic phase can be controlled in such a manner that it minimizes the detrimental impact on mechanical properties and the tendency for oxide scale spallation as initiated by fracture of starting brittle Cr-rich silicide dendritic phase network.

7.6. Conclusions

Silicon effects (up to 6 wt.%) on the wet oxidation kinetics of Type 310 stainless steel in a flowing air-10% H₂O mixture at 800°C are quite distinct and are related to the manner in which the structure and composition of the oxide scale formed affect the kinetics. The wet oxidation kinetics of both the high-Si (5.9 wt.%) and the low-Si (0.6 wt.%) Type 310 stainless steels follow a parabolic rate law that involves the diffusion-controlled accumulation and a constant volatilization loss of oxidized Cr oxide scale. Si alloying reduces the overall metal loss by forming a continuous layer underneath the protective Cr₂O₃ intermediate layer serving to reduce the parabolic rate constant whilst having no effect on the volatilization rate constant. Accelerated formation of Fe-rich oxides on the high-Si Type 310 stainless steel concomitant with the linear rate law regime is not observed at exposure times considered. The formation of the Cr-rich silicide intermetallic dendritic phase (Cr_{0.65}Ni_{0.25}Si_{0.1}) in the starting as-cast microstructure of the high-Si Type 310 stainless steel is believed to act as reservoirs serving to ensure the Cr supply from the alloy to the alloy/oxide interface is sufficient to replace the oxidized Cr in the scale lost to volatilization. Despite the lower wet oxidation kinetics exhibited by the high-Si Type 310 stainless steel, the oxide scale is susceptible to spallation.

7.7. Acknowledgements

The authors acknowledge the funding from Natural Sciences and Engineering Research Council of Canada under the Discovery Grants program. The authors also thank the staff in the Canadian Centre for Electron Microscopy (CCEM), a national facility supported by NSERC, the Canada Foundation for Innovation under the MSI program and McMaster University, for their technical assistance with sample preparation and electron microscopy.

7.8. References

1. J. Yuan, W. Wang, H. Zhang, L. Zhu, S. Zhu, and F. Wang, *Corros. Sci.* 109 (2016): pp. 36–42.
2. X. Peng, J. Yan, Y. Zhou, and F. Wang, *Acta Mater.* 53 (2005): pp. 5079–5088.
3. M.I. Sahri, N.K. Othman, Z. Samsu, and A.R. Daud, *AIP Conf. Proc.* 1614 152 (2014): pp. 152–157.
4. M.S. Elbakhshwan, S.K. Gill, A.K. Rumaiz, J. Bai, S. Ghose, R.B. Rebak, and L.E. Ecker, *Appl. Surf. Sci.* 426 (2017): pp. 562–571.
5. A.C.S. Sabioni, R.P.B. Ramos, V. Ji, F. Jomard, W.A. De Almeida MacEdo, P.L. Gastelois, and V.B. Trindade, *Oxid. Met.* 78 (2012): pp. 211–220.
6. M. Calmunger, R. Eriksson, G. Chai, S. Johansson, and J.J. Moverare, *Corros. Sci.* 100 (2015): pp. 524–534.
7. Y. Li, S. Wang, P. Sun, D. Xu, M. Ren, Y. Guo, and G. Lin, *Corros. Sci.* 128 (2017): pp. 241–252.
8. Z. Yu, M. Chen, C. Shen, S. Zhu, and F. Wang, *Corros. Sci.* 121 (2017): pp. 105–115.
9. W. Wongpromrat, G. Berthomé, V. Parry, S. Chandra-ambhorn, W. Chandra-ambhorn, C. Pascal, A. Galerie, and Y. Wouters, *Corros. Sci.* 106 (2016): pp. 172–178.
10. H. Asteman, Svensson, J.-E., and L.-G. Johansson, *Corros. Sci.* 44 (2002): pp. 2635–2649.
11. X. Cheng, Z. Jiang, B.J. Monaghan, D. Wei, R.J. Longbottom, J. Zhao, J. Peng, M. Luo, L. Ma, S. Luo, and L. Jiang, *Corros. Sci.* 108 (2016): pp. 11–22.
12. J. Zhang, X. Peng, D.J. Young, and F. Wang, *Surf. Coatings Technol.* 217 (2013): pp. 162–171.
13. H. Asteman, J.-E. Sevensson, and L.-G. Johansson, *Oxid. Met.* 57 (2002): pp. 193–216.

14. J. Yuan, X. Wu, W. Wang, S. Zhu, and F. Wang, *Materials (Basel)*. 7 (2014): pp. 2772–2783.
15. S. Mahboubi, H.S. Zurob, G.A. Botton, and J.R. Kish, “Temperature Effect on the Wet Oxidation Performance of Type 310S Stainless Steel”, Submitted to *Corr. Sci.* (2018).
16. A. Galerie, S. Henry, Y. Wouters, M. Mermoux, J.P. Petit, and L. Antoni, *Mater. High Temp.* 22 (2005): pp. 105–112.
17. H. Hooshyar, T. Jonsson, J. Hall, J.E. Svensson, L.G. Johansson, and J. Liske, *Oxid. Met.* 85 (2016): pp. 321–342.
18. I.G. Wright, and R.B. Dooley, *Int. Mater. Rev.* 55 (2010): pp. 129–167.
19. P.J. Ennis, and W.J. Quadackers, *Int. J. Press. Vessel. Pip.* 84 (2007): pp. 82–87.
20. B.A. Pint, O. Ridge, E.L. Oak, and R. National, *Eng. Issues Turbine Mach. Power Plants Renewables*, Inst. Mater. Miner. Mining, Maney Publ. London, UK (2003): pp. 1057–1073.
21. X. Cheng, Z. Jiang, D. Wei, J. Zhao, B.J. Monaghan, R.J. Longbottom, and L. Jiang, *Met. Mater. Int.* 21 (2015): pp. 251–259.
22. H. Buscail, S. El Messki, F. Riffard, S. Perrier, R. Cueff, E. Caudron, and C. Issartel, *Mater. Chem. Phys.* 111 (2008): pp. 491–496.
23. R. Pettersson, L. Liu, and J. Sund, *Corros. Eng. Sci. Technol.* 40 (2005): pp. 211–216.
24. J.S. Dunning, D.E. Alman, and J.C. Rawers, *Oxid. Met.* 57 (2002): pp. 409–425.
25. S. Mahboubi, H.S. Zurob, G.A. Botton, and J.R. Kish, *Can. Metall. Q.* 57:1 (2018): pp. 89-98.
26. H.E. Evans, D.A. Hilton, R.A. Holm, and S.J. Webster, *Oxid. Met.* 19 (1983): pp. 1–18.

27. G. Bamba, Y. Wouters, A. Galerie, F. Charlot, and A. Dellali, *Acta Mater.* 54 (2006): pp. 3917–3922.
28. S. Mahboubi, “Effect of Cr Content on Corrosion Resistance of Fe-Cr-Ni Alloys Exposed in Supercritical Water (SCW),” McMaster University, 2014.
29. F.H. Stott, and F.I. Wei, *Oxid. Met.* 31 (1989): pp. 369–391.
30. S. Gray, K. Berriche-Bouhanek, and H.E. Evans, *Mater. Sci. Forum* 461 (2004): pp. 755–764.
31. Z. Yang, J. tao Lu, Z. Yang, Y. Li, Y. Yuan, and Y. feng Gu, *Corros. Sci.* 125 (2017): pp. 106–113.
32. T. Jonsson, S. Canovic, F. Liu, H. Asteman, J.E. Svensson, L.G. Johansson, and M. Halvarsson, *Mater. High Temp.* 22 (2005): pp. 231–243.
33. X.-W. Cheng, Z.-Y. Jiang, B.J. Monaghan, R.J. Longbottom, D.-B. Wei, A.C. Hee, and L.-Z. Jiang, *Mater. Corros.* 69 (2018).
34. T. Amano, *ECS Trans.* 25 (2010): pp. 3–19.
35. R.N. Durham, B.M. Gleeson, and D. Young, *Oxid. Met.* 50 (1998): pp. 139–165.
36. Y.-X. Xu, X.-T. Luo, C.-X. Li, G.-J. Yang, and C.-J. Li, *Surf. Eng.* 33 (2017): pp. 210–216.
37. V. Badin, E. Diamanti, P. Forêt, and E. Darque-Ceretti, *Procedia Mater. Sci.* 9 (2015): pp. 48–53.
38. X. Cheng, Z. Jiang, B.J. Monaghan, D. Wei, R.J. Longbottom, J. Zhao, J. Peng, M. Luo, L. Ma, S. Luo, and L. Jiang, *Corros. Sci.* 108 (2016): pp. 11–22.
39. A. Paúl, S. Elmrabet, L.C. Alves, M.F. Da Silva, J.C. Soares, and J.A. Odriozola, *Nucl. Instruments Methods Phys. Res. Sect. B Beam Interact. with Mater. Atoms* 181 (2001): pp. 394–398.
40. D.L. Douglass, and J.S. Armijo, *Oxid. Met.* 2 (1970): pp. 207–231.
41. B. Li, and B. Gleeson, *Oxid. Met.* 65 (2006): pp. 101–122.

42. T. Ohashi, and T. Haradat, *Oxid. Met.* 46 (1996): pp. 235–254.
43. S. Mahboubi, H.S. Zurob, G.A. Botton, and J.R. Kish, Submitted to *Corros.* January 2018.
44. D.A. Guzonas, and W.G. Cook, *Corros. Sci.* 65 (2012): pp. 48–66.
45. S. Mahboubi, Y. Jiao, W. Cook, W. Zheng, D.A. Guzonas, G.A. Botton, and J.R. Kish, *Corros.* 72 (2016): pp. 1170–1180.
46. “ASTM E112-13, ‘Standard Test Methods for Determining Average Grain Size’ (West Conshohocken, PA: ASTM, 2013).”
47. B.R. Knappett, P. Abdulkin, E. Ringe, D.A. Jefferson, S. Lozano-Perez, T.C. Rojas, A. Fernández, and A.E.H. Wheatley, *Nanoscale* 5 (2013): p. 5765.
48. Y.-L. Chueh, M.-W. Lai, J.-Q. Liang, L.-J. Chou, and Z.L. Wang, *Adv. Funct. Mater.* 16 (2006): pp. 2243–2251.
49. J. Bischoff, and A.T. Motta, *J. Nucl. Mater.* 430 (2012): pp. 171–180.
50. Y. Chen, Z. Liu, S.P. Ringer, Z. Tong, X. Cui, and Y. Chen, *Cryst. Growth Des.* (2007): pp. 10–12.
51. E. Schmucker, C. Petitjean, L. Martinelli, P. Panteix, S. Ben, and M. Vilasi, *Corros. Sci.* 111 (2016): pp. 474–485.
52. B.A. Pint, K.A. Terrani, M.P. Brady, T. Cheng, and J.R. Keiser, *J. Nucl. Mater.* 440 (2013): pp. 420–427.
53. D. Lussana, D. Baldissin, M. Massazza, and M. Baricco, *Oxid. Met.* 81 (2014): pp. 515–528.
54. L. Aranda, T. Schweitzer, L. Mouton, S. Mathieu, O. Rouer, P. Villegier, P. Berthod, and E. Conrath, *Mater. High Temp.* 32 (2015): pp. 530–538.
55. D.J. Young, *Mater. Sci. Forum* 595–598 (2008): pp. 1189–1197.
56. R. Bauer, M. Baccalaro, L.P.H. Jeurgens, M. Pohl, and E.J. Mittemeijer, *Oxid. Met.* 69 (2008): pp. 265–285.

57. W.J. Quadakkers, V. Shemet, and L. Singheiser, *Mater. High Temp.* 20 (2003): pp. 115–127.
58. L. Mikkelsen, S. Linderoth, and J.B. Bilde-Sørensen, *Mater. Sci. Forum* 461–464 (2004): pp. 117–122.
59. J. Guo, C. Cheng, H. Li, J. Zhao, and X. Min, *Eng. Fail. Anal.* 79 (2017): pp. 625–633.
60. S.N. Basu, and G.J. Yurek, *Oxid. Met.* 36 (1991): pp. 281–315.
61. H. Shibata, K. Kimura, T. Tanaka, and S. Kitamura, *ISIJ Int.* 51 (2011): pp. 1944–1950.
62. H.X Chen, X.H. Ma, S.S. Bo, and J.B. Chen, *Corros. Eng. Sci. Technol.* 45 (2010): pp. 475–479.
63. H.-W. Hsu, and W.-T. Tsai, *Mater. Chem. Phys.* 64 (2000): pp. 147–155.
64. T.D. Nguyen, J. Zhang, and D.J. Young, *Oxid. Met.* 81 (2014): pp. 549–574.
65. K. Bawane, K. Ning, and K. Lu, *Corros. Sci.* (2017): pp. 0–1.
66. G.R. Holcomb, *J. Electrochem. Soc.* 156 (2009): p. C292.
67. H. Buscail, R. Rolland, and S. Perrier, *Ann. Chim. Sci. Des Mater.* 39 (2015).
68. H. Hooshyar, T. Jonsson, J. Hall, J.E. Svensson, L.G. Johansson, and J. Liske, *Oxid. Met.* 85 (2016): pp. 321–342.
69. S. Vujic, R. Sandström, and C. Sommitsch, *Mater. High Temp.* 32 (2015): pp. 607–618.

8. Conclusions and Outlooks

High-temperature wet oxidation performance of Type 310S stainless steel was examined within the context of the stability and protectiveness of the Cr_2O_3 scale formed. In particular, the effects of total gas pressure, water vapour partial pressure and Si and Mn minor alloying elements on the wet oxidation performance of the alloy were investigated. Emphasis was placed on establishing links between changes in the structure and composition of the protective Cr_2O_3 scale and accelerated Fe-rich oxidation using advanced electron microscopy techniques. From a fundamental interest perspective, the motivations for this study are the current knowledge gaps that exist regarding mechanistic aspects of breakaway oxidation as governed by the balance between the initial parabolic oxidation stage and the final linear oxidation stage and the means to control the onset of the latter stage through modifying the structure and composition of the oxide scales formed. The onset of the final linear oxidation stage has paramount practical importance as if delayed the accelerated oxidation rate is prohibited which increases the lifetime of components used at high temperatures significantly.

The effect of Cr content on the wet oxidation behaviour of Type 310S stainless steel was evaluated in high-pressure (25 MPa) flowing oxygenated SCW (a condition that has practical significance affecting the selection of a candidate fuel cladding material for the Canadian Gen IV SCWR design concept). The main contribution of this work is the evidence in support that accelerated Fe-rich oxidation is indeed a performance concern of Cr_2O_3 forming engineering alloys in

SCW at the predicted temperatures associated with the coolant outlet conditions that needs to be considered in the selection of a suitable material for fuel claddings. The research conducted in this study is presented and discussed in Chapter 3. This article is published in ***Corrosion*** (Vol. 72, No. 9 (2016), pp: 1170-1180, <https://doi.org/10.5006/1982>). The major findings are summarized as follows:

- The Cr₂O₃ scale formed on Type 310S stainless steel remains protective up to ~250 h exposure in flowing oxygenated SCW at 550°C (parabolic oxidation). An accelerated linear oxidation stage is observed thereafter, which occurs in concomitant with the formation of Fe-rich oxides. The key factor promoting changes to the structure and composition of the Cr₂O₃ scale is the relatively deep Cr-depleted zone formed in the metal.
- Increase in the bulk alloy Cr content to ~33 wt.% (Alloy 33) is effective in maintaining a compact Cr₂O₃ scale, which significantly delays the onset of accelerated Fe-rich oxide formation (not observed during the exposure times considered). The Cr content in the Cr-depleted zone in the metal is sufficiently high to maintain a Cr supply that in turn maintains a compact Cr₂O₃ scale despite the loss of oxidized Cr to volatilization.

The possibility of using an ambient pressure air-10% H₂O mixture as a surrogate for high-pressure SCW was then examined in details. Based on thermodynamic predictions, it has been argued that the partial pressure of Cr(VI) vapour species is sufficiently similar in the two environments and a similar wet oxidation performance can be expected. The results from Chapter 3 served as the

comparative basis for the results obtained by exposing Type 310S stainless steel in a flowing air-10% H₂O mixture at 550°C. The wet oxidation kinetics exhibited by, and the structure and composition of the oxide scale formed on, Type 310S stainless steel were directly compared in the two wet environments. This article is the first in the literature that makes such a direct comparison to validate such a prediction based on thermodynamic calculations. The research conducted in this study is presented and discussed in Chapter 4. This article is submitted to **Corrosion** for publication consideration. The major findings are summarized as follows:

- Volatilization is significantly slower in the air-10% H₂O mixture despite that the vapour pressure of the CrO₂(OH)₂ in SCW is estimated to be similar to that of the ambient pressure air-10% H₂O mixture.
- The main difference between the oxide scales formed on Type 310S stainless steel in the two environments occurs after 250 h exposure when the increase in the volatilization rate in SCW results in the accelerated linear oxidation associated with Fe-rich oxide formation, whereas the oxide scale formed in air-10% H₂O mixture stays intact and protective even up to 1000 h exposure.
- The presence of a MnCr₂O₄ layer on top of the Cr₂O₃ scale, as formed on Type 310S stainless steel exposed in the air-10% H₂O mixture, is beneficial in reducing the oxidized Cr volatilization rate. The much slower volatilization

rate of the oxidized Cr from the MnCr_2O_4 cap is attributed to the much lower total pressure of this environment.

- For the first time in the literature, physical evidence of oxidized Cr loss from the MnCr_2O_4 layer along with the formation of the MnO degradation product was found using advanced electron microscopy techniques, which is consistent with the previously published thermodynamic predictions.

In the remainder of this collective study, the wet oxidation performance of Type 310S stainless steel was examined in the ambient pressure wet air. First, the effects of water vapour partial pressure on the wet oxidation performance of Type 310S stainless steel was examined at 550°C . Two wet gas mixtures, namely air-10% H_2O and air-70% H_2O , were chosen for this comparative study. This article was submitted to the Conference of Metallurgist for presentation, which was then invited by MetSoc of CIM for publication in the ***Canadian Metallurgical Quarterly*** (CMQ) journal on August 2017 (Vol. 57, No. 1 (2018), pp: 89-98, <https://doi.org/10.1080/00084433.2017.1373968>). The research conducted in this study is presented and discussed in Chapter 5. The major findings are summarized as follows:

- The wet oxidation kinetics exhibited by Type 310S stainless steel in the two environments were distinctly different: parabolic oxidation in air-10% H_2O and paralinear oxidation in air-70% H_2O . The difference in the oxidation

kinetics is attributed to the increase in the rate of oxidized Cr loss during volatilization when partial pressure of water vapour increases.

- It was shown that uniform MnCr_2O_4 layer on top of the Cr_2O_3 scale as formed after 500 h exposure in air-10% H_2O reduces the Cr_2O_3 scale volatilization rate, resulting in parabolic oxidation kinetics. The MnCr_2O_4 layer on top of the Cr_2O_3 scale as formed in air-70% H_2O was discontinuous and physical evidence of oxidized Cr loss from the MnCr_2O_4 layer (Mn_2O_3 degradation product) was found.
- Based on thermodynamics, the vapour pressure of Cr(VI) gas species measured over MnCr_2O_4 and Cr_2O_3 is important and highly depends on the water vapour partial pressure of the gas.

The effect of temperature on the wet oxidation performance of Type 310S stainless steel in the flowing air-10% H_2O mixture was then examined considering the influence temperature has on the stability of the MnCr_2O_4 layer. Type 310S stainless steel was exposed for up to 1000 h in a 0.1 MPa flowing air-10% H_2O mixture at 550°C, 675°C, and 800°C. Links between changes in the structure and composition of the protective Cr_2O_3 scale and the oxidation kinetics were made. In particular the mechanism of breakaway oxidation (observed at 800°C) along with the rate-controlling steps during oxidation were proposed. In addition, the role of Mn alloying element on changing the structure, composition and morphology of the scales formed is discussed. The results of this study are presented and discussed

in Chapter 6. This article is submitted to **Corrosion Science** for publication consideration. The major findings are summarized as follows:

- At 550°C only parabolic oxidation is observed during the 1000 h exposure which is associated with the presence of the MnCr_2O_4 cap on the Cr_2O_3 scale.
- At 675°C, parabolic oxidation kinetics is observed after the 1000 h exposure. Initial parabolic oxidation stage involves formation of a protective MnCr_2O_4 cap on top of the Cr_2O_3 scale that reduces oxidized Cr loss rate. The measured flux of Cr lost to volatilization is relatively small at 675°C. No accelerated Fe-rich oxide formation is observed for the 1000 h exposure implying the scale is still protective. The lean linear oxidation stage is associated with relatively small rate of oxidized Cr lost to volatilization resulting in the formation of Mn_2O_3 degradation product.
- At 800°C breakaway oxidation is observed with an increase in the linear rate constant. Formation of a MnCr_2O_4 cap on the Cr_2O_3 scale can only delay the onset of accelerated linear oxidation at low temperatures. The rate of oxidized Cr loss from the MnCr_2O_4 layer during volatilization at 800°C is measured and is much higher than that at lower temperatures, which makes the MnCr_2O_4 layer itself to be prone to volatilization. The measured flux of oxidized Cr lost to volatilization is considerably high at 800°C leading to the accelerated Fe-rich oxide formation in this case.

- A mechanism of scales formation and rate-determining steps at each temperature is proposed. At 550°C, outward diffusion of Cr cations through the scale is the rate-determining step. At 675°C, after relatively long exposure times, adsorption of gas species is the rate-determining step and the controlling interface is the outer MnCr_2O_4 /gas while it moves to the Cr-rich internal oxide surface at 800°C making the adsorption of gas species at the surface of the Cr-rich scale to be rate-determining.
- The change in the oxidation kinetics is attributed to the rate of oxidized Cr lost to volatilization over MnCr_2O_4 and Cr_2O_3 . Evidence of Mn_2O_3 degradation products was found at 550°C and 675°C. The MnCr_2O_4 layer itself becomes much more prone to volatilization at 800°C and the porous degradation products formed also transport Fe cations through.
- The discontinuous SiO_2 layer that forms underneath the Cr_2O_3 scale at each temperature is not effective in reducing the volatilization rate of the oxidized Cr. Addition of alloyed Si to enhance the formation of a continuous SiO_2 layer is identified to be likely a meaningful wet oxidation control strategy.

Building upon the insights acquired from the research presented and discussed in Chapter 6, the effects of alloyed Si on the wet oxidation performance of Type 310 stainless steel was studied to better understand how the structure and composition of the oxide scale formed evolves with time during wet oxidation and how this evolution affects the kinetics. The wet oxidation performance of a high-Si cast Type 310 stainless steel (5.9 wt.% Si) in the flowing air-10% H_2O mixture at

800°C was investigated for this purpose. The results obtained presented and discussed for Type 310S stainless steel (the low-Si counterpart) in Chapter 6 were used as a comparative basis. Chapter 7 presents and discusses the results of this study. This article is submitted to **Corrosion Science** for publication considerations. The major findings are summarized as follows:

- The wet oxidation kinetics of both high-Si (5.9 wt.%) and low-Si (0.6 wt.%) Type 310 stainless steels follow a parabolic rate law according to weight loss kinetics which involves the diffusion-controlled accumulation and a constant volatilization of oxidized Cr.
- Si alloying can reduce the overall metal loss by reducing the metal lost during the initial parabolic kinetic stage.
- Si alloying does not have any effect whatsoever on the linear rate of oxidation associated with the volatilization of the oxidized Cr.
- Si alloying can significantly delay the onset of accelerated Fe-rich oxide formation, therefore, prohibits the oxide thickening albeit the oxide scale formed is prone to spallation upon cooling.
- Presence of Cr-rich silicide intermetallic phases in the initial cast microstructure that eventually become depleted of Cr is beneficial in supplying Cr needed by the scale during volatilization.

Breakaway oxidation associated with Fe-rich oxide formation is a matter of concern in many of the high-temperature structural alloys. Mn addition to the alloy and formation of a MnCr_2O_4 layer on the Cr_2O_3 scale is only effective at lower temperatures and pressure, also at relatively shorter exposure times. A more promising logic for inhibiting the accelerated linear oxidation of the alloy associated with Fe-rich oxide formation is considered to be increasing the alloyed Si content. It is proposed herein that a worthy effective approach to improve the wet oxidation performance of Type 310S stainless steel, is finding a thermal process that controls the morphology of the Cr-rich silicide intermetallic phases: one that reduces the detrimental impact on mechanical properties followed by the tendency for oxide scale spallation, yet retains Cr supply during oxidation and volatilization.

It is worth mentioning that data obtained from this collective study shows times less than at least 250 h should probably not be included when predicting long-term oxidation kinetics for candidate fuel cladding alloys in Gen IV SCWR as well as structural alloys used in high-temperature environments since the rate law may change significantly at longer time.